Towards Scalable Quantum Communication and Computation: Novel Approaches and Realizations

A dissertation presented

by

Liang Jiang

to

The Department of Physics

in partial fulfillment of the requirements

for the degree of

Doctor of Philosophy

in the subject of

Physics

Harvard University

Cambridge, Massachusetts

May 2009

Thesis advisor

Mikhail D. Lukin

Author

Liang Jiang

Towards Scalable Quantum Communication and Computation: Novel Approaches and Realizations

Abstract

Quantum information science involves exploration of fundamental laws of quantum mechanics for information processing tasks. This thesis presents several new approaches towards scalable quantum information processing.

First, we consider a hybrid approach to scalable quantum computation, based on an optically connected network of few-qubit quantum registers. Specifically, we develop a novel scheme for scalable quantum computation that is robust against various imperfections. To justify that nitrogen-vacancy (NV) color centers in diamond can be a promising realization of the few-qubit quantum register, we show how to isolate a few proximal nuclear spins from the rest of the environment and use them for the quantum register. We also demonstrate experimentally that the nuclear spin coherence is only weakly perturbed under optical illumination, which allows us to implement quantum logical operations that use the nuclear spins to assist the repetitive-readout of the electronic spin. Using this technique, we demonstrate more than two-fold improvement in signal-to-noise ratio. Apart from direct application to enhance the sensitivity of the NV-based nano-magnetometer, this experiment represents an important step towards the realization of robust quantum information processors using electronic and nuclear spin qubits.

We then study realizations of quantum repeaters for long distance quantum communication. Specifically, we develop an efficient scheme for quantum repeaters based on atomic ensembles. We use dynamic programming to optimize various quantum repeater protocols. In addition, we propose a new protocol of quantum repeater with encoding, which efficiently uses local resources (about 100 qubits) to identify and correct errors, to achieve fast one-way quantum communication over long distances.

Finally, we explore quantum systems with topological order. Such systems can exhibit remarkable phenomena such as quasiparticles with anyonic statistics and have been proposed as candidates for naturally error-free quantum computation. We propose a scheme to unambiguously detect the anyonic statistics in spin lattice realizations using ultra-cold atoms in an optical lattice. We show how to reliably read and write topologically protected quantum memory using an atomic or photonic qubit.

Contents

List of Figures

List of Tables

Citations to Previously Published Work

Most of the chapters of this thesis have appeared in print elsewhere. By chapter number, they are:

- Chapter 2: "Scalable Quantum Networks based on Few-Qubit Registers," L. Jiang, J. M. Taylor, A. S. Sorensen, and M. D. Lukin (e-print: quant-ph/0703029), and "Distributed Quantum Computation Based-on Small Quantum Registers," L. Jiang, J. M. Taylor, A. S. Sorensen, and M. D. Lukin, *Phys. Rev. A* **76**, 062323 (2007).

  Related experimental work: "Quantum Register Based on Individual Electronic and Nuclear Spin Qubits in Diamond," M. V. G. Dutt, L. Childress, L. Jiang, E. Togan, J. Maze, F. Jelezko, A. S. Zibrov, P. R. Hemmer, and M. D. Lukin, *Science* **316**, 1312 (2007).

- Chapter 3: "Coherence and Control of Quantum Registers Based on Electronic Spin in a Nuclear Spin Bath," P. Cappellaro, L. Jiang, J. S. Hodges, and M. D. Lukin, *Phys. Rev. Lett.* (to be published, 2009).

- Chapter 4: "Coherence of an Optically Illuminated Single Nuclear Spin Qubit," L. Jiang, M. V. G. Dutt, E. Togan, L. Childress, P. Cappellaro, J. M. Taylor, and M. D. Lukin, *Phys. Rev. Lett.* **100**, 073001 (2008).

- Chapter 5: "Repetitive Readout of Single Electronic Spin via Quantum Logic with Nuclear Spin Ancillae," L. Jiang, J. S. Hodges, J. Maze, P. Maurer, J. M. Taylor, D. G. Cory, P. R. Hemmer, R. L. Walsworth, A. Yacoby, A. S. Zibrov, and M. D. Lukin, to be submitted to Science.

- Chapter 6: "Fast and Robust Approach to Long-Distance Quantum Communication with Atomic Ensembles," L. Jiang, J. M. Taylor, and M. D. Lukin, *Phys. Rev. A* **76**, 012301 (2007).

- Chapter 7: "Optimal approach to quantum communication algorithms using dynamic programming," L. Jiang, J. M. Taylor, N. Khaneja, and M. D. Lukin, *Proc. Natl. Acad. Sci. U. S. A.* **104**, 17291 (2007).

- Chapter 8: "Quantum Repeater with Encoding," L. Jiang, J. M. Taylor, K. Nemoto, W. J. Munro, R. Van Meter, and M. D. Lukin, *Phys. Rev. A* **79**, 032335 (2009).

- Chapter 9: "Anyonic Interferometry and Protected Memories in Atomic Spin Lattices," L. Jiang, G. K. Brennen, A. Gorshkov, K. Hammerer, M. Hafezi, E. Demler, M. D. Lukin, and P. Zoller, *Nature Physics* **4**, 482 (2008).

Acknowledgments

First of all, I would like to thank my advisor, Prof. Mikhail Lukin, for his support and encouragement. In the past five years I have been inspired by Misha's deep insights and constant flow of new ideas.

I would like to thank other members of my thesis committee, Prof. Navin Khaneja and Prof. Charles Marcus. It is Navin's brilliant insight that leads to the project of optimal approach to quantum communication algorithms using dynamic programming. It is Charlie's illuminating course of mesoscopic physics that stimulated the project of hybrid approach to distributed quantum computation. I feel very fortunate to have such a helpful thesis committee.

I would also like to acknowledge several other faculty members both at Harvard and elsewhere who have helped me pursue my studies. Prof. Eugene Demler, Prof. Efthimios Kaxiras, Prof. Ron Walsworth and Prof. Amir Yacoby all bring up new ideas and stimulating comments during the discussions at Harvard. Collaborations and visits with Prof. Ignacio Cirac at MPQ, with Prof. Peter Zoller and Prof. Hans Briegel at Innsbruck expanded my vision of quantum science. It is also great pleasure to collaborate with Prof. Juan Jose Garcia-Ripoll from Madrid, Prof. William Munro from HP, Prof. Kae Nemoto from NII, Prof. Ana Sanpera from Barcelona, and Prof. Anders Sorensen from Copenhagen.

In addition to fruitful scientific discussions, I would like to thank my fellow coworkers. In particular, I would like to acknowledge Jake Taylor for helping me orient to life in the group, as well as working together on many research projects. I would also like to thank Jonathan Hodges and Jero Maze who taught me how to operate the NV center experiment. It is my great pleasure to share office with Alexey Gor-

shkov, as we both know "what is going on with our computers at 2 am." I feel very lucky to work with many wonderful people, including Misho Bajcsy, Jonatan Bohr Brask, Gavin Brennen, Paola Cappellaro, Darrick Chang, Lily Childress, Yiwen Chu, Gurudev Dutt, Dirk Englund, Christian Flindt, Simon Folling, Maria Fyta, Adam Gali, Garry Goldstein, Michael Gullans, Mohammad Hafezi, Sebastian Hofferberth, Michael Hohensee, Sungkun Hong, Tao Hong, Takuya Kitagawa, Frank Koppens, Peter Maurer, Susanne Pielawa, Qimin Quan, Peter Rabl, Ana Maria Rey, Oriol Romero-Isart, Brendan Shields, Paul Stanwix, Jeff Thompson, Emre Togan, Alexei Trifonov, Rodney Van Meter, Philip Walther, Tun Wang, Yanhong Xiao, Norman Yao, and Alexander Zibrov.

The Physics Department staff has been an invaluable resource. I would like to thank Adam Ackerman, Sheila Ferguson, Vickie Green, Stuart McNeil, William Walker, Jean O'Connor, and Marilyn O'Connor for all their help.

I have many friends who have encouraged and supported me during the five years of graduate school. Thanks to Shasha Chong, Jonathan Fan, Gene-Wei Li, Xiaofeng Li, Yi-Chia Lin, Yanyan Liu, Linjiao Luo, Wei Min, Jia Niu, Yuqi Qin, Ruifang Song, Meng Su, Jingtao Sun, Bolu Wang, Fan Yang, Jing Yang, Yiming Zhang, and Hong Zhong.

Finally, I would like to thank my parents for their persistent support and sacrifice for my education and research, I cannot thank you enough. This thesis is dedicated to you.

Dedicated to my parents
Ailing Pang and Dazhong Jiang

Chapter 1

Introduction and Motivation

1.1 Overview and Structure

As one of the most successful theories of nature, quantum mechanics keeps surprising us with its exotic behavior and profound power. The discovery of the unprecedented computational power of quantum mechanical resources opens a new chapter of quantum information science. For example, Shor's quantum factorizing algorithms can give an exponential speed-up compared to all known classical algorithms. Quantum communication protocols between two remote parties can be unconditionally secure against eavesdropping.

All these promising applications have attracted many researchers from various disciplines to explore the field of quantum information science. However, this field is still confronted with both practical and conceptual challenges. In particular, various decoherence mechanisms prevent us from realizing a well isolated quantum systems with more than 10 controllable quantum bits (qubits). Usually, the larger the quan-

tum system, the faster it decoheres. This motivates the study of efficient approaches to achieve large scale quantum computation. Chapters 2, 3 and 4 will discuss a hybrid approach to achieve distributed, scalable quantum computation. The idea is to decompose a large quantum computer into many small, few-qubit quantum information processors, which can be connected using the resources of quantum entanglement.

Quantum communication has been realized up to 150 km by sending single photons directly. However, it become very difficult to extend the communication distance further, because the communication rate decreases exponentially with the distance, due to photon loss in optical fibers. Quantum repeaters can resolve the fiber attenuation problem, reducing the exponential scaling to polynomial scaling by introducing repeater stations to store intermediate quantum states. Chapters 6, 7 and 8 will discuss several promising approaches to efficient, long-distance quantum communication using quantum repeaters.

What else can we do with the quantum nature of physics? As discussed in Chapter 5, we can use quantum logic to improve the signal-to-noise ratio (SNR) for precision measurement of magnetic field, such as the nano-magnetometer using defect color centers in diamond.

In addition, many-body quantum systems can exhibit exotic behaviors, such as the topological order. Topological order is often characterized by ground state degeneracy robust against local perturbations, and it can be used to overcome local decoherence. Chapter 9 presents a proposal to probe such topological order with atomic, molecular and optical (AMO) systems and use it for robust quantum memory.

1.2 Distributed Quantum Computation

In order to achieve large scale quantum computation, it is crucial to be able to progressively build larger controllable quantum systems with many qubits. In addition, the quantum gates among these qubits should have sufficiently small error probability, so that these imperfections can be actively suppressed using quantum error correction [154]. In practice, however, it is an extremely challenging task to build a controllable quantum system with many qubits (e.g. > 10), as well as high fidelity quantum gates.

One approach to alleviate such a challenge is to decompose the many-qubit quantum computer into smaller few-qubit, highly-controllable elementary units, which will be called quantum registers in this thesis. We define a *quantum register* as a few-qubit device that contains one *communication* qubit, with a photonic interface; one *storage* qubit, with very good coherence times; and several *auxiliary* qubits, used for purification and error correction. A critical requirement for a quantum register is high-fidelity unitary operations between the qubits within the register. The photonic interface can be used to generate entanglement between communications qubits from any two quantum registers. In Chapter 2, we justify that the distributed quantum computation scheme with quantum registers can be very robust against various imperfections in the photonic interface, including photon loss and bit-flip/dephasing errors.

We identify two promising physical implementations for quantum registers. First, recent experiments have demonstrated quantum registers composed of few trapped ions, which can support high-fidelity local operations [124, 85, 169]. The ion qubits

can couple to light efficiently [20] and were recognized early for their potential in an optically coupled component [60, 55]. Probabilistic entanglement of remote ion qubits mediated by photons has also been demonstrated [149, 139, 138].

The second physical implementation uses the nitrogen-vacancy (NV) color centers in diamond. The NV centers are very common and stable defects, which can be regarded as naturally built ion-traps. The electronic spin of the NV center can be used as the communication qubit. It can be initialized and readout optically and also manipulated with electron spin resonance (ESR) pulses. Similar to ion traps, it is feasible to optically generate entanglement between the electronic spins from two remote registers. The proximal nuclear spins provide the memory or ancillary qubits, which have extraordinarily long coherence times [63] and can be manipulated with high precision using techniques from nuclear magnetic resonance (NMR) [194, 34].

Different from those well-isolated qubits associated with each ion, the nuclear spins proximal to the NV centers are always couple to the nuclear spin bath. In Chapter 3, we show how to isolate a few proximal nuclear spins from the rest of the environment and use them to construct a quantum register, together with the NV electronic spin. We describe how coherent control techniques based on magnetic resonance methods can be adapted to these electronic-nuclear solid state spin systems, to provide not only efficient, high fidelity manipulation of the registers, but also decoupling from the spin bath. As an example, we analyze feasible performances and practical limitations in a realistic setting associated with NV centers in diamond.

Another difference from the trapped ions is that the nuclear spins proximal to the NV centers always couple to the electronic spin via hyperfine interaction. When

we optically excite the electronic spin for initialization, readout, or entanglement generation, the nuclear spin dynamics are governed by time-dependent hyperfine interaction associated with rapid electronic transitions. In Chapter 4, we introduce the spin-fluctuator model to describe the nuclear spin dynamics induced by the stochastic hyperfine interaction. We show that due to a process analogous to motional averaging in NMR, the nuclear spin coherence can be preserved after a large number of optical excitation cycles. Our theoretical analysis is in good agreement with experimental results. It indicates a novel approach that could potentially isolate the nuclear spin system completely from the electronic environment.

1.3 Repetitive Readout Assisted with Nuclear Spin Ancillae

Besides being a promising candidate for a quantum register, a single NV center can also be used as a room-temperature nano-magnetometer, because the electronic spin associated with the NV center can be used as a very good magnetic sensor. Recently, NV-based nano-magnetometer with high sensitivity has been proposed theoretically [186] and demonstrated experimentally [141, 6]. The magnetometer sensitivity, however, is currently limited by the signal-to-noise ratio associated with the electronic spin readout [141]. About 10^4 averages are needed in order to distinguish the signal from the background noise.

In Chapter 5, we describe and demonstrate experimentally a new method to improve readout of single spins in solid state. According to our study from Chapter 4,

the nuclear spins has a relatively slow depolarization rate (up to a few 10 μs), compared to the fast optical readout/polarization of the electronic spin (only $\sim$ 200 ns). This motivates us to use quantum logic operations on a quantum system composed of a single electronic spin and several proximal nuclear spin ancillae to repetitively readout the state of the electronic spin.

Using coherent manipulation of single NV center in room temperature diamond, we first demonstrate full quantum control of three-spin system. Then, we make use of the nuclear spin memory and quantum logic operations to demonstrate ten-fold enhancement in the total fluorescent signal of the electronic spin readout, as well as more than two-fold improvement in signal-to-noise ratio. Finally, we demonstrate an extended procedure to further improve the readout using two nuclear spins. Such a technique can be directly applied to improve the sensitivity of spin-based nanoscale diamond magnetometers. In addition, this demonstration represents an important step towards realization of robust quantum information processors using electronic and nuclear spin qubits in solid state systems.

1.4 Quantum Repeaters

The goal of quantum key distribution is to generate a shared string of bits between two distant locations (a key) whose security is ensured by quantum mechanics rather than computational complexity [79]. Recently, quantum key distribution over 150 km has been demonstrated [190], but the key generation rate decreases exponentially with the distance due to the fiber attenuation. Quantum repeaters can resolve the fiber attenuation problem, reducing the exponential scaling to polynomial scaling by

introducing repeater stations to store intermediate quantum states [26, 59, 39, 191].

The underlying idea of quantum repeater [26, 61] is to generate a backbone of entangled pairs over much shorter distances, store them in a set of distributed nodes (called repeater stations), and perform a sequence of quantum operations which only succeed with finite probability. *Entanglement purification* operations [11, 51] improve the fidelity of the entanglement in the backbone, while *entanglement connection* operations join two shorter distance entangled pairs of the backbone to form a single, longer distance entangled pair. By relying on a quantum memory at each repeater station to let different sections of the repeater re-attempt failed operations independently, a high fidelity entangled state between two remote quantum systems can be produced in polynomial time.

The Duan-Lukin-Cirac-Zoller (DLCZ) quantum repeater protocol [59] uses atomic ensembles as the quantum memories at repeater stations. Recently, there are many experimental progress [41, 35, 65] towards realization of the DLCZ protocol. The challenge for the DLCZ protocol is now shifting towards the realization of scalable quantum repeater systems which could yield a reasonable communication rate at continental distances ($\gtrsim 1000km$). Thus, the DLCZ protocol should be examined and adapted to practical experimental considerations, allowing to remove imperfections such as the finite efficiency of retrieval and single-photon detection and fiber length fluctuations. In Chapter 6, we present an extension of the DLCZ protocol, keeping the experimental simplicity of the original scheme while avoiding fundamental difficulties due to these expected experimental imperfections.

Besides the DLCZ protocol, there are two other representative quantum repeater

schemes. They are the Briegel-Dur-Cirac-Zoller scheme (BDCZ scheme) [26, 61], and the Childress-Taylor-Sorensen-Lukin scheme (CTSL scheme) [38, 39]. Different from the DLCZ protocol with limited controllability and at most 50% success probability for each entanglement connection operation, the BDCZ and CTSL schemes assume deterministic (i.e, 100% success probability) entanglement connection (which can be achieved with physical systems like quantum dots, ion traps, or NV centers). It is of both theoretical and practical interests to find the optimal implementation within a given quantum repeater scheme.

In Chapter 7, we introduce a method for systematically optimizing existing repeater schemes and developing new, more efficient schemes. Our approach makes use of a dynamic programming-based searching algorithm, the complexity of which scales only polynomially with the communication distance, letting us efficiently determine near-optimal solutions. We find significant improvements in both the speed and the final state fidelity for preparing long distance entangled states.

As far as we know, all quantum repeater schemes (e.g., Ref. [59, 26, 61, 38, 39, 191]) will be ultimately limited by the coherence time of the quantum memory [93]. This is because they all require two-way classical communication. Two-way classical communication is needed for the DLCZ scheme to verify the successful entanglement connection; it is also indispensable for the BDCZ and CTSL schemes to verify successful entanglement purification before proceeding to the next nesting level over longer distances. For two-way classical communication, however, the time to generation a key should be at least the communication time between the remote repeater stations, which unfortunately increases at least linearly with the communication distance due

to the finite speed of light. Consequently, quantum repeaters with two-way classical communication have their key generation rates (i.e., the inverse of the key generation time) decreasing at least linearly with the distance. Thus, the finite coherence time of the quantum memory ultimately limits the communication distance [93].

Can we design a new quantum repeater protocol that is not limited by the coherence time of the quantum memory? In Chapter 8, we present a new, fast quantum repeater protocol in which the communication distance is *not* limited by the memory coherence time. Our protocol encodes logical qubits with small CSS codes [154], applies entanglement connection at the encoded level, and uses classical error correction to boost the fidelity of entanglement connection. It is important that the number of qubits at each repeater station has a favorable scaling with distance, which turns out to be Poly(Log(L)) for our new repeater with encoding, where L is the number of repeater stations.

1.5 Anyons and Topological Order

Strongly correlated quantum systems can exhibit exotic behavior called topological order which is characterized by non-local correlations that depend on the system topology. Such systems can exhibit remarkable phenomena such as quasi-particles with anyonic statistics and have been proposed as candidates for naturally error-free quantum computation.

In our three-dimensional world, there are only two types of indistinguishable particles – bosons and fermions – which are symmetric and anti-symmetric under exchange. One can show [199] that bosons and fermions are the only two types of indistinguish-

able particles in the three-dimensional world. For two-dimensional systems, however, indistinguishable particles can be something other than bosons or fermions, and they are called anyons [200]. For bosons or fermions, we will always obtain the trivial identity operation by moving one particle around the other. In contrast, anyons have the exotic property that moving one particle around a second particle can induce a unitary evolution that is different from identity. For abelian anyons, the unitary evolution induces an overall phase. For non-abelian anyons, the unitary can evolve the system from one state to a different state [151]. Such unitary evolutions can be used to implement quantum gates and achieve intrinsically fault-tolerant quantum computation [113, 49, 151].

Despite these remarkable properties, anyons have never been observed in nature directly. In Chapter 9, we describe how to unambiguously detect and characterize such states in recently proposed spin lattice realizations using ultra-cold atoms or molecules trapped in an optical lattice. We propose an experimentally feasible technique to access non-local degrees of freedom by performing global operations on trapped spins mediated by an optical cavity mode. We show how to reliably read and write topologically protected quantum memory using an atomic or photonic qubit. Furthermore, our technique can be used to probe statistics and dynamics of anyonic excitations.

Chapter 2

Scalable Quantum Networks based on Few-Qubit Registers

2.1 Introduction

The key challenge in experimental quantum information science is to identify isolated quantum mechanical systems with good coherence properties that can be manipulated and coupled together in a scalable fashion. Substantial progress has been made towards the physical implementation of few-qubit quantum registers using systems of coupled trapped ions [43, 124, 85, 169], superconducting islands [204, 196], solid-state qubits based on electronic spins in semiconductors [162], and color centers in diamond [203, 98, 37, 63, 153]. While the precise manipulation of large, multi-qubit systems still remains an outstanding challenge, approaches for connecting such few qubit registers into large scale circuits are currently being explored both theoretically [44, 60, 130, 155, 193, 55] and experimentally [122, 18]. Of specific

importance are approaches which can yield fault-tolerant operations with minimal resources and realistic (high) error rates.

In Ref. [60] a novel technique to scalable quantum computation was suggested, where high fidelity local operations can be used to correct low fidelity non-local operations, using techniques that are currently being explored for quantum communication [26, 61, 38]. In this Letter, we present a hybrid approach, which requires only 5 (or fewer)-qubit registers with local determinstic coupling. The small registers are connected by optical photons, which enables non-local coupling gates and reduces the requirement for fault tolerant quantum computation [185]. Besides providing additional improvements over the earlier protocol [60] (suppressed measurement errors, more efficient entanglement purification, and higher final entanglement fidelity), we perform a reality check for our network-based scheme. Specifically, we analyze two physical systems where our approach is very effective. We consider an architecture where pairwise non-local entanglement can be created in parallel, as indicated in Fig. 2.1. This is achieved via simultaneous optical excitation of the selected register pairs followed by photon-detection in specific channel. We use a Markov chain analysis to estimate the overhead in time and operational errors, and discuss the feasibility of large scale, fault-tolerant quantum computation using this approach.

The present work is motivated by experimental advances in two specific physical systems. Recent experiments have demonstrated quantum registers composed of few trapped ions, which can support high-fidelity local operations [124, 85, 169]. The ion qubits can couple to light efficiently [20] and were recognized early for their potential in an optically coupled component [60, 55]. Probabilistic entanglement of remote ion

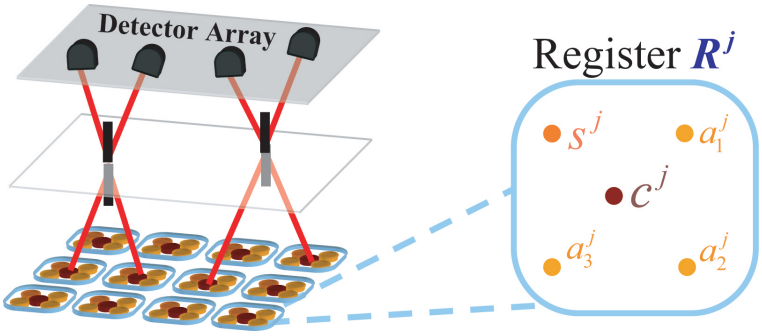

Figure 2.1: Illustration of distributed quantum computer based on many quantum registers. Each register has five physical qubits, including one communication qubit (c), one storage qubit (s), and three auxiliary qubits ($a_{1,2,3}$). Local operations for qubits from the same register have high fidelity. Entanglement between remote registers can be generated probabilistically [38, 57, 178]. Optical MEMS devices [111] can efficiently route photons and couple arbitrary pair of registers. Detector array can *simultaneously* generate entanglement for many pairs of registers.

qubits mediated by photons has also been demonstrated [149, 139]. At the same time, few-qubit quantum registers have been recently implemented in high-purity diamond samples [98, 37, 63, 153]. Here, quantum bits are encoded in individual nuclear spins, which are extraordinarily good quantum memories [63] and can also be manipulated with high precision using techniques from NMR [194]. The electronic spin associated with a nitrogen-vacancy (NV) color center enables addressing and polarization of nuclei, and entanglement generation between remote registers. While for systems of trapped ions there exist several approaches for coupling remote few-qubit registers (such as those based on moving the ions [110]), for NV centers in diamond it is difficult to conceive a direct construction of large scale multi-qubit systems without major advances in fabrication technology. For the latter scenario the hybrid approach developed here is required. Furthermore the use of light has the major advantage that it allows for connecting spatially separated qubits, which reduces the requirement for

fault-tolerant quantum computation [185].

2.2 Quantum Registers

We define a *quantum register* as a few-qubit device that contains one *communication* qubit, with a photonic interface; one *storage* qubit, with very good coherence times; and several *auxiliary* qubits, used for purification and error correction (described below). A critical requirement for a quantum register is high-fidelity unitary operations between the qubits within the register.

The simplest quantum register requires only two qubits: one for storage and the other for communication. Entanglement between two remote registers may be generated using probabilistic approaches from quantum communication ([38] and references therein). In general, such entanglement generation produces a Bell state of the communication qubits from different registers, conditioned on certain measurement outcomes. If state generation fails, it can be re-attempted until success, with an exponentially decreasing chance of continued failure. When the communication qubits (c^1 and c^2) are prepared in the Bell state, we can immediately perform the remote C-NOT gate on the storage qubits (s^1 and s^2) using the gate-teleportation circuit between registers R^1 and R^2. This can be accomplished [82, 67, 55] via a sequence of local C-NOTs within each register, followed by measurement of two communication qubits and subsequent local rotations. Since arbitrary rotations on a single qubit can be performed within a register, the C-NOT operation between different quantum registers is in principle sufficient for universal quantum computation. Similar approaches are also known for deterministic generation of graph states [9] —an essential resource

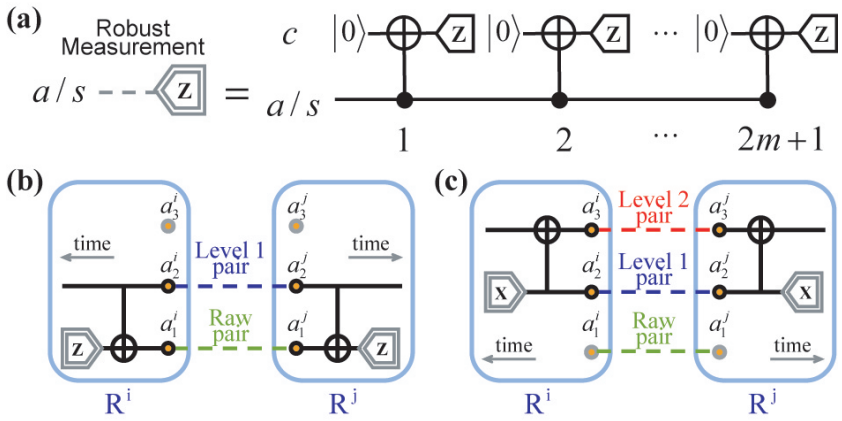

Figure 2.2: Circuits for robust operations. (a) Robust measurement of the auxiliary/storage qubit, a/s, based on majority vote from $2m+1$ outcomes of the communication qubit, c. Robust measurement is denoted by the box shown in the upper left corner. (b)(c) Using entanglement pumping to create high fidelity entangled pairs between two registers R^i and R^j. The entanglement pumping is achieved by local operation and classical communication. Within each register, a local CNOT coupling gate is applied, and then a robust measurement is performed to one of the auxiliary qubit. If the two outcomes from both registers are the same, it indicates a successful step of pumping; otherwise generate new pairs and restart the pumping operation from the beginning. The two circuits are for the first level pumping and the second level pumping, purifying bit- and phase-errors, respectively.

for one-way quantum computation [166].

2.3 Robust Operations with Five-Qubit Quantum Registers

In practice, the qubit measurement, initialization, and entanglement generation can be fairly noisy with error probabilities as high as a few percent, due to practical limitations such as finite collection efficiency and poor interferometric stability. As a result the corresponding error probability in non-local gate circuit will also be

very high. In contrast, local unitary operations may fail infrequently ($p_L \lesssim 10^{-4}$) when quantum control techniques for small quantum system are utilized [194, 124]. We now show that the most important sources of imperfections, such as imperfect initialization, measurement errors for individual qubits in each quantum register, and entanglement generation errors between registers, can be corrected with a modest increase in register size. We determine that with just *three* additional auxiliary qubits and high-fidelity local unitary operations, all these errors can be efficiently suppressed by bit-verification and entanglement purification [26, 61]. This provides an extension of Ref. [60] that mostly focused on suppressing errors from entanglement generation.

We are assuming in the following a separation of error probabilities: any internal, unitary operation of the register fails with low probability, p_L, while all operations connecting the communication qubit to the outside world (initialization, measurement, and entanglement generation) fail with error probabilities that can be several orders of magnitude higher. For specificity, we set these error probabilities to p_I, p_M, and $1 - F$, respectively. In terms of these quantities the error probability in the non-local C-NOT gate circuit is of order $p_{CNOT} \sim (1-F)+2p_L+2p_M$. We now show how this fidelity can be greatly increased.

Robust measurement can be implemented by bit-verification: a majority vote among the measurement outcomes (Fig. 2.2a), following a sequence of C-NOT operations between the auxiliary/storage qubit and the communication qubit. This also allows *robust initialization* by measurement. High-fidelity *robust entanglement generation* is achieved via entanglement purification [26, 61, 60] (Fig. 2.2bc), in which lower fidelity entanglement between the communication qubits is used to purify entangle-

ment between the auxiliary qubits, which can then be used for the remote C-NOT operation. To make the most efficient use of physical qubits, we introduce a new two-level entanglement pumping scheme. Our circuit (Fig. 2.2b) uses raw Bell pairs to repeatedly purify ("pump") against bit-errors, then the bit-purified Bell pairs are used to pump against phase-errors (Fig. 2.2c).

Entanglement pumping, like entanglement generation, is probabilistic; however, failures are detected. Still, in computation, where each logical gate should be completed within allocated time (clock cycle), failed entanglement pumping can lead to gate failure. Therefore, we should analyze the time required for robust initialization, measurement and entanglement generation, and we will show that the failure probability for these procedures can be made sufficiently small with reasonable time overhead.

2.3.1 Robust measurement

The measurement circuit shown in Fig. 2.2a yields the correct result based on majority vote from $2m+1$ consecutive readouts (bit-verification). Since the evolution of the system (C-NOT gate) commutes with the measured observable (Z operator) of the auxiliary/storage qubit, it is a quantum non-demolition (QND) measurement, which can be repeated many times. The error probability for majority vote measurement scheme is:

$$\varepsilon_M \approx \left(\begin{array}{c} 2m+1 \\ m+1 \end{array} \right) (p_I + p_M)^{m+1} + \frac{2m+1}{2} p_L. \tag{2.1}$$

Suppose $p_I = p_M = 5\%$, we can achieve $\varepsilon_M \approx 8 \times 10^{-4}$ by choosing $m^* = 6$ for $p_L = 10^{-4}$, or even $\varepsilon_M \approx 12 \times 10^{-6}$ for $m^* = 10$ and $p_L = 10^{-6}$. Recently, measurement

with very high fidelity (ε_M as low as 6×10^{-4}) has been demonstrated in the ion-trap system [97], using similar ideas as above. The time for robust measurement is

$$\tilde{t}_M = (2m+1)\left(t_I + t_L + t_M\right), \tag{2.2}$$

where t_I, t_L, and t_M are times for initialization, local unitary gate, and measurement, respectively.

2.3.2 Robust entanglement generation

We now use robust measurement and entanglement generation to perform entanglement pumping. Suppose the raw Bell pairs have initial fidelity $F = \langle|\Phi^+\rangle\langle\Phi^+|\rangle$ due to *depolarizing error*. We apply two-level entanglement pumping. The first level has n_b steps of bit-error pumping using raw Bell pairs (Fig. 2.2b) to produce a bit-error-purified entangled pair. The second level uses these bit-error-purified pairs for n_p steps of phase-error pumping (Fig. 2.2c).

For successful purification, the infidelity of the purified pair, $\varepsilon_{E,\text{infid}}^{(n_b,n_p)}$, depends on both the control parameters (n_b, n_p) and the imperfection parameters (F, p_L, ε_M). For depolarizing error, we find

$$\begin{aligned}\varepsilon_{E,\text{infid}}^{(n_b,n_p)} \approx{}& \frac{3+2n_p}{4}p_L + \frac{4+2\left(n_b+n_p\right)}{3}\left(1-F\right)\varepsilon_M \\ &+ \left(n_p+1\right)\left(\frac{2\left(1-F\right)}{3}\right)^{n_b+1} + \left(\frac{\left(n_b+1\right)\left(1-F\right)}{3}\right)^{n_p+1}\end{aligned}$$

to the leading order of p_L and ε_M. The dependence on the initial infidelity $1-F$ is exponentially suppressed at the cost of a linear increase of error from local operations p_L and robust measurement ε_M. Measurement-related errors are suppressed by the prefactor $1-F$, since measurement error does not cause infidelity unless combined

with other errors. In the limit of ideal operations ($p_L, \varepsilon_M \to 0$), the infidelity $\varepsilon_{E,\text{infid}}^{(n_b,n_p)}$ can be arbitrarily close to zero [103]. On the other hand, if we use the standard entanglement pumping scheme [26, 61] (that alternates purification of bit and phase errors within each pumping level), the reduced infidelity from two-level pumping is always larger than $(1-F)^2/9$. Therefore, for very small p_L and ε_M, the new pumping scheme is crucial to minimize the number of qubits per register.

We remark that a faster and less resource intensive approach may be used if the unpurified Bell pair is dominated by *dephasing error*. And one-level pumping may be sufficient (i.e. no bit-error purification, $n_b = 0$). For dephasing error, we have $\varepsilon_{E,\text{infid}}^{(0,n_p)} \approx (1-F)^{n_p+1} + \frac{2+n_p}{4} p_L + 2(1-F)\varepsilon_M$ by expanding to the leading order of p_L and ε_M.

The overall success probability can be defined as the joint probability that all successive steps succeed. We use the model of finite-state Markov chain [144] to directly calculate the *failure probability* of (n_b, n_p)-two-level entanglement pumping using N_{tot} raw Bell pairs, denoted as $\varepsilon_{E,fail}^{(n_b,n_p)}(N_{\text{tot}})$. See Ref. [103] for detailed analysis.

For given F, p_L, and ε_M, the purified pair has minimum infidelity $\Delta_{\min} = \varepsilon_{E,\text{infid}}^{\left(n_b^*,n_p^*\right)}$, obtained by the optimal choice of the control parameters $\left(n_b^*, n_p^*\right)$. Then, we calculate the typical value for N_{tot}, by requiring the failure probability and the minimum infidelity to be equal, $\varepsilon_{E,\text{fail}}^{\left(n_b^*,n_p^*\right)}(N_{\text{tot}}) = \Delta_{\min}$. The total error probability is

$$\varepsilon_E \approx \varepsilon_{E,\text{fail}}^{\left(n_b^*,n_p^*\right)}(N_{\text{tot}}) + \Delta_{\min} = 2\Delta_{\min}. \tag{2.3}$$

The total time for robust entanglement generation $\tilde{t}_E$ is

$$\tilde{t}_E \approx \langle N_{\text{tot}} \rangle \times \left(t_E + t_L + \tilde{t}_M\right), \tag{2.4}$$

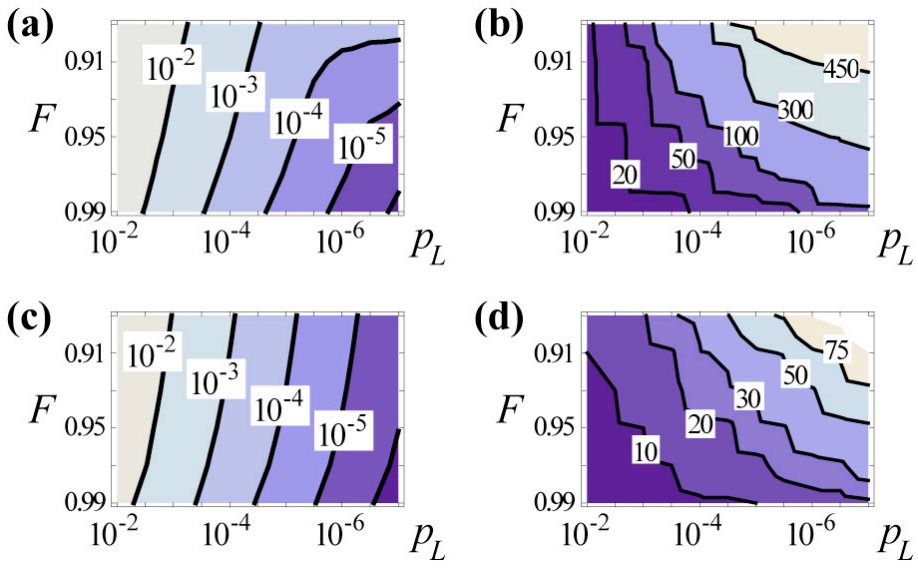

Figure 2.3: Contours of the total error probability after purification ε_E (a,c) and total number of unpurified Bell pairs N_{tot} (b,d) with respect to the imperfection parameters p_L (horizontal axis) and F (vertical axis). (a,b) Two-level pumping is used for depolarizing error, and (c,d) one-level pumping for dephasing error. $p_I = p_M = 5\%$ is assumed.

where t_E is the average generation time of the unpurified Bell pair.

Figure 2.3 shows the contours of ε_E and N_{tot} with respect to the imperfection parameters p_L and $1 - F$. We assume $p_I = p_M = 5\%$ for the plot. The choice of p_I and p_M ($< 10\%$) has little effect to the contours, since they only modifies ε_M marginally. For initial fidelity $F_0 > 0.95$, the contours of ε_E are almost vertical; that is, ε_E is mostly limited by p_L with an overhead factor of about 10. The contours of N_{tot} indicate that the entanglement pumping needs about tens or hundreds of raw Bell pairs to ensure a very high success probability.

2.3.3 Clock cycle time and effective error probability

We introduce the *clock cycle time* $t_C = \tilde{t}_E + 2t_L + \tilde{t}_M \approx \tilde{t}_E$ and the *effective error probability* $\gamma = \varepsilon_E + 2p_L + 2\varepsilon_M$ for general coupling gate between two registers, which can be implemented with a similar approach as the remote C-NOT gate [67]. We now provide an estimate of clock cycle time based on realistic parameters. The time for optical initialization/measurement is $t_I = t_M \approx \frac{\ln p_M}{\ln(1-\eta)} \frac{\tau}{C}$, with photon collection/detection efficiency η, vacuum radiative lifetime τ, and the Purcell factor C for cavity-enhanced radiative decay. We assume that entanglement is generated based on detection of two photons [57, 178], which takes time $t_E \approx (t_I + \tau/C)/\eta^2$. If the bit-errors are efficiently suppressed by the intrinsic purification of the entanglement generation scheme, one-level pumping is sufficient; otherwise two-level pumping is needed. Suppose the parameters are $(t_L, \tau, \eta, C) = (0.1\ \mu\text{s}, 10\ \text{ns}, 0.2, 10)$ [78, 182, 106] and $(1 - F, p_I, p_M, p_L, \varepsilon_M) = (5\%, 5\%, 5\%, 10^{-6}, 12 \times 10^{-6})$. For depolarizing errors, two-level pumping can achieve $(t_C, \gamma) = (997\ \mu\text{s}, 4.5 \times 10^{-5})$. If all bit-errors are suppressed by the intrinsic purification of the coincidence scheme, one-level pumping is sufficient and $(t_C, \gamma) = (140\ \mu\text{s}, 3.4 \times 10^{-5})$. Finally, t_C should be much shorter than the memory time of the storage qubit, t_{mem}. This is indeed the case for both trapped ions (where $t_{mem} \sim 10$ s has been demonstrated [121, 86]) and proximal nuclear spins of NV centers (where t_{mem} approaches 1 s [63]) [103].

This approach yields gates between quantum registers to implement arbitrary quantum circuits. Errors can be further suppressed by using quantum error correction. For example, as shown in Fig. 2.3, $(p_L, F) = (10^{-4}, 0.95)$ can yield $\gamma \leq 2 \times 10^{-3}$, well below the 1% threshold for fault tolerant computation for approaches such as

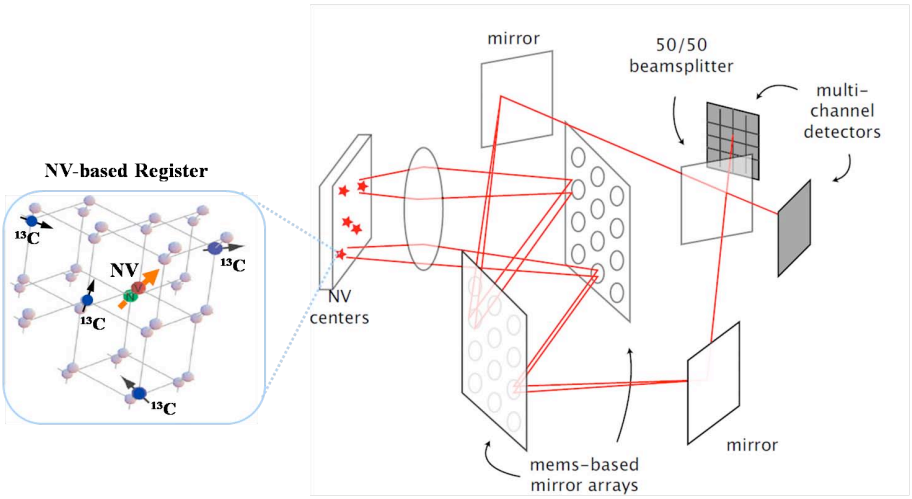

Figure 2.4: The architecture of MEMS-based mirror arrays and multi-channel detectors for quantum computer that supports parallelism. The inset illustrates that we can use both the electronic and nuclear spins for the NV-based quantum register.

the C_4/C_6 code [115] or 2D toric codes [167]; $(p_L, F) = (10^{-6}, 0.95)$ can achieve $\gamma \leq 5 \times 10^{-5}$, which allows efficient codes such as the BCH [[127,43,13]] code to be used without concatenation. Following Ref. [181], we estimate 10 registers per logical qubit to be necessary for a calculation involving 10^4 logical qubits and 10^6 logical gates.

2.4 Architecture Supports Parallelism

It is important that the architecture of the network-based quantum computer supports parallelism. In particular, it should be able to couple many pairs of qubits that grows linearly with the total number of qubits, as well as simultaneous measurements and local unitary gates. In the following, we show an architecture supporting parallelism for the network of NV centers, using MEMS-based mirror arrays and

multi-channel detectors, as illustrated in Fig. 2.4. (A similar architecture has been proposed by Ref. [148].)

The quantum computer operates on a piece of diamond with many NV centers. Each NV center can be used as a quantum register (left inset) consisting of communication, storage, and auxiliary qubits. The emitted photons from each NV centers can be routed by a set of MEMS-based mirrors, split by the beam splitter, and detected by the two detectors from the multi-channel detectors.

There are as many independently controlled mirrors (and detectors) as the number of NV centers we want to manipulate, and it is possible to couple many pairs of NV centers at the same time. Because for each pair of NV center, the emitted photons will trigger only two detectors along the routed optical paths, and a successful click pattern will generate entanglement between the pair of NV centers. Since different pairs do not interfere with each other, many pairs of NV centers (qubits) in the computer can be coupled simultaneously. Recently, large scale MEMS-based optical cross-connect switch with more than 1100 ports has been demonstrated [112]. Since that we only need MEMS response time faster than the clock cycle time t_C (~0.1 ms), MEMS devices with response time less than 0.003 ms [184] should be sufficient.

2.5 Conclusion

In summary, we have analyzed a hybrid approach to fault-tolerant quantum computation with optically coupled few-qubit quantum registers. With a reasonable overhead in operational time and gate error probabilities, this approach enables the reduction of an experimental challenge of building a thousand-qubit quantum com-

puter into a more feasible task of optically coupling five-qubit quantum registers. We have provided an architecture that supports parallel operations for many quantum register pairs at the same time. We further note that it is possible to facilitate fault-tolerant quantum computation with special operations from the hybrid approach such as partial Bell measurement [103] or with systematic optimization using dynamic programming [101].

Chapter 3

Coherence and control of quantum registers based on electronic spin in a nuclear spin bath

3.1 Introduction

The coherence properties of isolated electronic spins in solid-state materials are frequently determined by their interactions with large ensembles of lattice nuclear spins [46, 118]. The dynamics of nuclear spins is typically slow, resulting in very long correlation times of the environment. Indeed, nuclear spins represent one of the most isolated systems available in nature. This allows, for instance, to decouple electronic spin qubits from nuclear spins via spin echo techniques [162, 88]. Even more remarkably, controlled manipulation of the coupled electron-nuclear system allows one to take advantage of the nuclear spin environment and use it as a long-lived quantum

memory [187, 142, 150]. Recently, this approach has been used to demonstrate a single nuclear qubit memory with coherence times well exceeding tens of milliseconds in room temperature diamond [63]. Entangled states composed of one electronic spin and two nuclear spin qubits have been probed in such a system [153]. The essence of these experiments is to gain complete control over several nuclei by isolating them from the rest of the nuclear spin bath. Universal control of systems comprising a single electronic spin coupled to many nuclear spins has not been demonstrated yet and could enable developing of robust quantum nodes to build larger scale quantum information architectures.

In this Letter, we describe a technique to achieve coherent universal control of a portion of the nuclear spin environment. In particular, we show how several of these nuclear spins can be used, together with an electronic spin, to build robust multi-qubit quantum registers. Our approach is based on quantum control techniques associated with magnetic resonance manipulation. However, there exists an essential difference between the proposed system and other previously studied small quantum processors, such as NMR molecules. Here the boundary between the qubits in the system and the bath spins is ultimately dictated by our ability to effectively control the qubits. The interactions governing the couplings of the electronic spin to the nuclear qubit and bath spins are of the same nature, so that control schemes must preserve the desired interactions among qubits while attempting to remove the couplings to the environment. The challenges to overcome are then to resolve individual energy levels for qubit addressability and control, while avoiding fast dephasing due to uncontrolled portion of the bath.

Before proceeding we note that various proposals for integrating these small quantum registers into a larger system capable of fault tolerant quantum computation or communication have been explored theoretically [103, 32] and experimentally [18, 149]. These schemes generally require a *communication* qubit and a few *ancillary* qubits per register, in a hybrid architecture. The *communication* qubits couple efficiently to external degrees of freedom (for initialization, measurement and entanglement distribution), leading to an easy control but also fast dephasing. The *ancillary* qubits instead are more isolated and can act as memory and ancillas in error correction protocols. While our analysis is quite general in that it applies to a variety of physical systems, such as quantum dots in carbon nanotubes [137] or spin impurities in silicon [150], as a specific example we will focus on the nitrogen-vacancy (NV) centers in diamond [63, 153, 88]. These are promising systems for the realization of hybrid quantum networks due to their long spin coherence times and good optical transitions that can be used for remote coupling between registers [100].

3.2 System Model

To be specific, we focus on an electronic spin triplet, as it is the case for the NV centers. Quantum information is encoded in the m_s=$\{0,1\}$ Zeeman sublevels, separated by a large zero field splitting (making m_s a good quantum number). Other Zeeman sublevels are shifted off-resonance by an external magnetic field B_z, applied along the N-to-V axis. The electron-nuclear spin Hamiltonian in the electronic rotat-

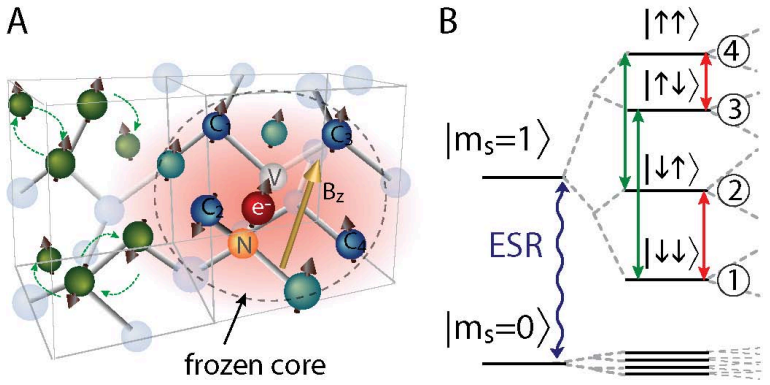

Figure 3.1: a) System model, showing the electronic spin in red and the surrounding nuclear spins. The closest nuclear spins are used as qubits. Of the bath spins, only the spins outside the frozen core evolve due to dipolar interaction, causing decoherence. b) Frequency selective pulses, in a 3-qubit register.

ing frame is

$$\begin{aligned}\mathcal{H} &= \omega_L \sum I_z^j + S_z \sum A_j \cdot \vec{I}^j + \mathcal{H}_{\text{dip}} \\ &= \tfrac{\mathbb{1}-S_z}{2}\omega_L \sum I_z^j + \tfrac{\mathbb{1}+S_z}{2} \sum \vec{\omega}_1^j \cdot \vec{I}^j + \mathcal{H}_{\text{dip}}\end{aligned} \tag{3.1}$$

where S and I^j are the electronic and nuclear spin operators, ω_L is the nuclear Larmor frequency, A_j the hyperfine couplings and $\mathcal{H}_{\text{dip}}$ the nuclear dipolar interaction, whose strength can be enhanced by the hyperfine interaction [140]. When the electronic spin is in the m_s=1 state, nearby nuclei are static (since distinct hyperfine couplings make nuclear flip-flops energetically unfavorable in the so-called frozen core [109]) and give rise to a quasi-static field acting on the electronic spin. The other bath nuclei cause decoherence via spectral diffusion [202, 140], but their couplings, which determine the noise strength and correlation time, are orders of magnitude lower than the interactions used to control the system. While in the m_s=0 manifold all the nuclear spins precess at the same frequency, the effective resonance frequencies in the m_s=1 manifold, ω_1^j, are given by the hyperfine interaction and the enhanced

g-tensor [37, 140], yielding a wide range of values. Some of the nuclear spins in the frozen core can thus be used as qubits. When fixing the boundary between system and environment we have to consider not only frequency addressability but also achievable gate times, which need to be shorter than the decoherence time.

3.3 Control

Control is obtained with microwave (μw) and radio-frequency (rf) fields. The most intuitive scheme, performing single-qubit gates with these fields and two-qubit gates by direct spin-spin couplings, is relatively slow, since rf transitions are weak. Another strategy, requiring only control of the electronic spin, has been proposed [96, 107]: switching the electronic spin between its two Zeeman eigenstates induces nuclear spins rotations about two non parallel axes that generate any single-qubit gate. This strategy is not the most appropriate here, since rotations in the m_s=0 manifold are slow [1]. We thus propose another scheme to achieve universal control on the register, using only two types of gates: 1) One-qubit gates on the electronic spin and 2) Controlled gates on each of the nuclear spins. The first gate can be simply obtained by a strong μw pulse. The controlled gates are implemented with rf-pulses on resonance with the effective frequency of individual nuclear spins in the m_s=1 manifold, which are resolved due to the hyperfine coupling and distinct from the bath frequency [2]. Achievable rf power provides sufficiently fast rotations since the hyperfine

[1] The rotation rates are faster for large external fields, which however reduce the angle between the two axes of rotations, thus increasing the number of switchings and the gate time.

[2] This leaves open the possibility to operate on the bath spins to implement collective refocusing schemes.

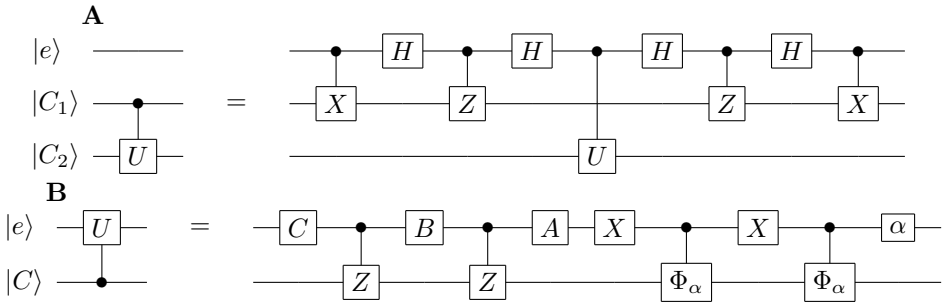

Figure 3.2: Quantum circuits for controlled gates U among two nuclear spins (A) and a nuclear and the electronic spin (B). The gates A, B, C are defined such that $U = e^{i\alpha} AZBZC$ and $ABC = \mathbb{1}$, where Z is a π rotation around z [154]. Φ_α is a phase gate: $|0\rangle\langle 0| + |1\rangle\langle 1| e^{i\alpha/2}$ and the gate α indicates $e^{i\alpha/2}\mathbb{1}$.

interaction enhances the nuclear Rabi frequency when m_s=1 [3]. Any other gate needed for universal control can be obtained combining these two gates. For example, it is possible to implement a single nuclear qubit rotation by repeating the controlled gate after applying a π-pulse to the electronic spin. Controlled gates between two nuclei can be implemented by taking advantage of the stronger coupling to the electron as shown in Fig. 3.2(A). As long as the hyperfine coupling is several times larger than the nuclear coupling, the scheme avoiding any direct nuclear interaction is faster. Although selectively addressing ESR transitions is a direct way to perform a controlled rotation with the electronic spin as a target, this is inefficient as the number of nuclear spin increases. The circuit in Fig. 3.2(B) performs the desired operation with only the two proposed gates on a faster time scale.

When working in the m_s=1 manifold, each nuclear spin qubit is quantized along a different direction and we cannot define a common rotating frame. The evolution

[3]The rf field, being perpendicular to the electronic zero-field splitting, is enhanced by second order electron-nuclear cross-transition [1].

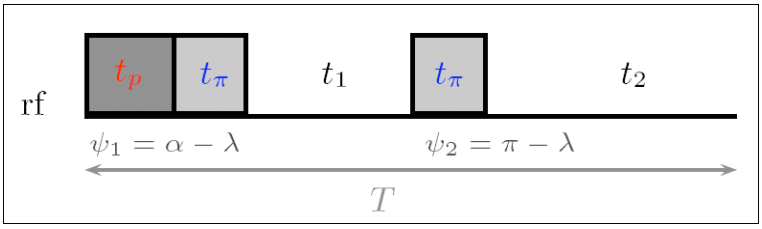

Figure 3.3: Rf pulse scheme for 1 nuclear spin gate in the m_s=1 manifold. With t_p=$\beta/\bar{\Omega}$ and fixing ψ_1=α-λ and ψ_2=π-λ, the time delays are t_1=$\frac{T}{2} - t_p - t_\pi - \frac{\alpha+\gamma}{\omega}$ and t_2=$\frac{T}{2} - t_\pi + \frac{\alpha+\gamma}{\omega}$.

must be described in the *laboratory* frame while the control Hamiltonian is fixed in a given direction for all the nuclei (e.g. along the x-axis). This yields a reduced rf Rabi frequency $\bar{\Omega} = \Omega_{\rm rf}\sqrt{\cos\varphi_1{}^2\cos\theta_1{}^2 + \sin\varphi_1{}^2}$ (where $\{\theta_1, \varphi_1\}$ define local quantization axes in the m_s=1 manifold and $\Omega_{\rm rf}$ is the hyperfine-enhanced Rabi frequency). The propagator for a pulse time t_p and phase ψ is

$$U_L(\Omega_{\rm rf}, t_p, \psi) = e^{-i[\omega t_p - (\lambda-\psi)]\sigma_{\tilde{z}}/2} e^{-i\bar{\Omega} t_p \sigma_{\tilde{x}}/2} e^{-i(\lambda-\psi)\sigma_{\tilde{z}}/2}$$

where $\{\sigma_{\tilde{x}}, \sigma_{\tilde{y}}, \sigma_{\tilde{z}}\}$ are the Pauli matrices in the local frame and λ is defined by $\tan(\lambda) = \tan\varphi_1/\cos\theta_1$. An arbitrary gate $U = R_{\tilde{z}}(\gamma)R_{\tilde{x}}(\beta)R_{\tilde{z}}(\alpha)$ can be obtained by combining U_L with an echo scheme (Fig. 3.3), which not only refocuses the extra free evolution due to the lab frame transformation, but also sets the gate duration to any desired clock time common to all registers. Fixing a clock time is advantageous to synchronize the operation of many registers. This yields a minimum clock time $T \geq 4\pi \times {\rm Max}_{\bar{\Omega}_j, \omega_1^j}\{\bar{\Omega}_j^{-1} + (\omega_1^j)^{-1}\}$.

In order to refocus the fast electronic-spin dephasing given by the frozen core nuclear spins, we need to embed the control strategy described above in a dynamical decoupling scheme [195] without loosing universal control, as explained in the follow-

ing. The electron-bath Hamiltonian is given by Eq. (3.1), where the index j now runs over the spins in the bath. Neglecting for the moment the couplings among nuclei, we can solve for the evolution of the electronic spin under an echo sequence. By defining U_0 and U_1 the propagators in the 0 and 1 manifold respectively and assuming that the nuclear spins are initially in the identity state (high temperature regime), we calculate the dynamics of the electronic spin, $\rho_e(t) = [\mathbb{1} + (|0\rangle\langle 1| f_{ee}(t) + h.c.)]\ \rho_e(0)$, where $f_{ee}(t) = \mathrm{Tr}\left[U_1 U_0 U_1^\dagger U_0^\dagger\right] = \prod [1 - 2\sin^2(\theta_1^j)\sin^2(\omega_1^j t/2)\sin^2(\omega_L t/2)]$ is the function describing the echo envelope experiments [173, 37]. Since in the m_s=0 subspace all the spins have the same frequency, $f_{ee}(2n\pi/\omega_L) = 0$ and the electron comes back to the initial state. Nuclear spin-spin couplings lead to an imperfect echo revival and ultimately to decoherence via spectral diffusion [202, 140]. The energy-conserving flip-flops of remote nuclear spins modulate the hyperfine couplings, causing the effective field seen by the electron to vary in time. The field oscillations can be modeled by a classical stochastic process. The overall evolution of the electronic spin is therefore due to two processes that can be treated separately as they commute: the echo envelope calculated above and the decay due to a stochastic field, approximated by a cumulant expansion [119]. For a Lorentzian noise with autocorrelation function $G(\tau) = G_0 e^{-t/\tau_c}$ we obtain a spin-echo decay $\propto e^{-\frac{2\Omega^2}{3\tau_c}t^3}$ for $t \ll \tau_c$ (or the motional narrowing regime for $\tau_c \ll t$).

By using dynamical decoupling techniques [33] and selecting a cycle time multiple of the bare larmor precession period it is possible to extend the life-time of the electronic coherence. Figure 3.4 shows how to combine the electron modulation with the sequence implementing spin gates. The effectiveness of these techniques relies on the

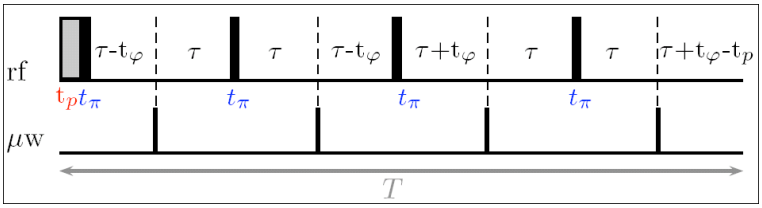

Figure 3.4: Rf and μw pulse sequence to implement a 1 nuclear spin gate while reducing the effects of a slowly varying electronic dephasing noise. The black bars indicate π-pulses, while the first rectangle indicate a general pulse around the x-axis. $\tau = \frac{T}{8} - \frac{t_\pi}{2}$ and $t_\varphi = \frac{\alpha+\gamma}{4\omega}$.

ability to modulate the evolution on a time scale shorter than the noise correlation time. The noise of the electron-nuclear spin system is particularly adapt to these decoupling schemes. Consider for example the NV center. The measured electron dephasing T_2^* time is about $1\mu s$ in natural diamonds [37], as expected from MHz-strong hyperfine couplings. The intrinsic decoherence time T_2 can be orders of magnitude longer ($T_2 \gtrsim 600\mu s$). This reflects the existence of a frozen region, where the spin flip-flops are quenched. The radius of this frozen core is about 2.2 nm [109] and only spins with hyperfine coupling $\lesssim$2.5 kHz contribute to spectral diffusion. Both the inverse correlation time (given by the dipolar coupling among carbon spins) and the noise rms (given by the coupling to the electron) are of order of few kHz. Dynamical decoupling schemes must thus act on time scales of hundreds of μs. This in turns sets achievable constraints on the gate speed.

The time of a conditional single nuclear spin rotation must be set so that the Rabi frequency $\Omega_{\rm rf}$ is much less than the frequency splitting between two *neighboring* spins (in terms of frequencies). Suppose we want to control an n-spin register without exciting bath spins at the Larmor frequency. The minimum frequency

splitting between two nuclei in the m_s=1 manifold will be at best $\delta\omega = \frac{\omega_M}{n}$ for nuclear frequency equally spaced and ω_M the maximum hyperfine-induced effective nuclear frequency. The nuclear frequency spread due to the hyperfine interaction is then $\Delta E_N = \frac{n+1}{2}\omega_M$. We want the Rabi frequencies to satisfy the constraints: $\Delta E_e \gg \Omega_e \gg \frac{n+1}{2}\omega_M > \frac{\omega_M}{n} \gg \Omega_{\rm rf}$, where $\Delta E_e = 2g\mu_B B_z$ is the gap to other Zeeman levels (m_s=-1 for the NVc) and Ω_e the μw power. For a typical choice of 700G magnetic field along the NV axis, we have ΔE_e = 2GHz and ω_L = 0.8MHz. Assuming $\omega_M \approx$ 20MHz and $n = 4$ spins, we obtain the following parameter window (in units of MHz) $2000 \gg \Omega_e \gg 25$, $\Omega_{\rm rf} \ll 5$. The gate clock time can be as short as a few μs, allowing hundreds of gates in the coherence time.

Since the scheme presented is based on selective pulses, the most important (coherent) errors will be due to off-resonance effects. If the Rabi frequency is much smaller than the off-set from the transmitter frequency $\delta\omega$, the off-resonance spin will just experience a shift (Bloch-Siegert shift) of its resonance frequency, $\Delta\omega_{\rm BS} = \delta\omega - \frac{1}{t}\int \sqrt{\Omega_{\rm rf}(t)^2 + \delta\omega^2}\, dt' \approx -\frac{\Omega_{\rm rf}^2}{2\delta\omega} = -\frac{n\Omega_{\rm rf}^2}{2\omega_M}$. This results in an additional phase acquired during the gate time that needs to be refocused. Note that this error grows with the register size and constrains $\Omega_{\rm rf}$. When reducing the Rabi frequency to achieve frequency selectivity, we have to pay closer attention to the rotating-wave approximation and consider its first order correction, which produces a shift of the on-resonance spin $\Delta\omega_{\rm RWA} = \Omega_{\rm rf}^2/4\omega_M$. Other sources of errors are evolution of bystander nuclear spins and couplings among spins. More complex active decoupling schemes [105, 126, 22] can correct for these errors, allowing to use the m_s=1 manifold as a memory.

Advanced techniques like shaped pulses, with amplitude and phase ramping, composite pulses [128], pulses optimized via optimal control theory or with numerical techniques [70, 108, 174] can provide better fidelity. The analytical model of control serves then as an initial guess for the numerical searches. Pulses found in this way correct for the couplings among nuclei and are robust over a wide range of parameters (such as experimental errors or the noise associated with static fields). Table 3.1 shows the results of simulations in a fictitious NV system with 1-4 nuclear spins and effective frequencies in the m_s=1 manifold ranging from 15 to 2MHz. We searched numerically via a conjugate gradient algorithm for a control sequence performing a desired unitary evolution, by varying the amplitude and phase of the μw and rf fields. We then simulated the control sequence in the presence of noise, with contributions from a large, static field and a smaller fluctuating one. The projected fidelities in the absence of experimental errors are very high, a sign that the fast modulation of the electron evolution effectively decouples it from the bath. The pulse robustness with respect to the noise is slightly degraded as the number of spins increases: the noise induces a spread of the electron resonance frequency, and it becomes more difficult to find a sequence of control parameters that drives the desired evolution in this larger Hilbert space for any of the possible electronic frequency. The fidelity degradation is however modest, and can be partially corrected by increasing the control field intensity. Furthermore, combining these pulses in a dynamical decoupling scheme would provide an efficient way to coherently control the registers.

The size of the register is eventually limited by the number of available nuclear spins with a hyperfine coupling strong enough to be separated from the bath. From

	1 spin	2 spins	3 spins	4 spins
F (ideal)	0.9999	0.9999	0.9992	0.9995
F (noise)	0.9994	0.9995	0.9975	0.9925
time	5.0 μs	5.5 μs	6.0 μs	8.5 μs

Table 3.1: Simulated fidelities ($F = |\mathrm{Tr}\left[U_w^\dagger U\right]/2^N|^2$) at the optimal gate time in the presence of noise. The gate is a $\pi/2$ rotation about the local x-axis for qubit 1 in a register of 1–4 nuclear qubits. The noise parameters are $T_2^* = 1.5\mu$s and $T_2 = 250\mu$s; the maximum Rabi frequencies are $2\pi \times 10$MHz and $2\pi \times 20$kHz for the electronic and nuclear spins respectively. As expected, the optimal gate time increases with the register size, reflecting both the more complex control required in a larger Hilbert space and the weaker hyperfine couplings to more distant spins. Similar fidelities were obtained for a CNOT gate between spin 1 and 2.

experiments and ab-initio calculation [74] we expect hyperfine couplings of ~ 130MHz in the first shell, and then a number of about 50 possible nuclear sites with hyperfine values from 15MHz to 1MHz. Even if the concentration of C-13 is increased (and the Nitrogen nuclear spin is used) the size of the register will be limited to about 10 spins. Nevertheless such registers would be very useful for memory storage and error correction purposes.

3.4 Conclusion

In conclusion, we have presented a general approach to the control of a small quantum system comprising an electronic spin and few nuclear spins in the surrounding spin bath. We have shown that several of the bath spins can be isolated and effectively controlled, yielding a few-qubit register. These registers can be employed in many proposals for distributed quantum computation and communication, where coupling among registers could be provided either via photon entanglement [100]

or by a movable reading tip [141]. Our control methods enable algorithms needed for error correction and entanglement purification, while the nuclear spins provide a long-time memory in the $m_s = 1$ manifold, via active refocusing, and the electron dephasing is kept under control by dynamical decoupling methods. We thus develop a modular control scheme, scalable to many registers and applicable to many physical implementations.

Chapter 4

Coherence of an optically illuminated single nuclear spin qubit

4.1 Introduction

Nuclear spins are of fundamental importance for storage and processing of quantum information. Their excellent coherence properties make them a superior qubit candidate even in room temperature solids. Unfortunately, their weak coupling to the environment also makes it difficult to isolate and manipulate individual nuclei. Recently, coherent preparation, manipulation and readout of individual ^{13}C nuclear spins in the diamond lattice were demonstrated [63, 98]. These experiments make use of optical polarization and manipulation of the electronic spin associated with a nitrogen-vacancy (NV) color center in the diamond lattice [4, 37, 73, 89]. This

enables reliable control of the nuclear spin qubit via hyperfine interactions with the electronic spin.

In order to be useful for applications in scalable quantum information processing [4], such as quantum communication [38] and quantum computation [104, 103], the quantum coherence of the nuclear spins must be maintained even when the electronic state is undergoing fast transitions associated with optical measurement and with entanglement generation between electronic spins. In this Letter, we investigate coherence properties of such an optically illuminated nuclear spin–electron spin system. We show that these properties are well-described by a spin-fluctuator model [158, 76, 75, 14], involving a single nuclear spin (system) coupled by the hyperfine interaction to an electron [1] (fluctuator) that undergoes rapid optical transitions and mediates the coupling between the nuclear spin and the environment. We generalize the spin-fluctuator model to a vector description, necessary for single NV centers in diamond [63], and make direct comparisons with experiments. Most importantly we demonstrate that the decoherence of the nuclear spin due to the rapidly fluctuating electron is greatly suppressed via a mechanism analogous to motional narrowing in nuclear magnetic resonance (NMR) [179, 91], allowing the nuclear spin coherence to be preserved even after hundreds of optical excitation cycles. We further show that by proper tuning of experimental parameters it may be possible to completely decouple the nuclear spin system from the electronic environment. The spin-fluctuator model discussed here for NV centers can be generalized to other AMO systems (see Refs. [23, 168] for the recent progress).

[1] More precisely, the optical transitions involve electronic states of several electrons localized at the NV center.

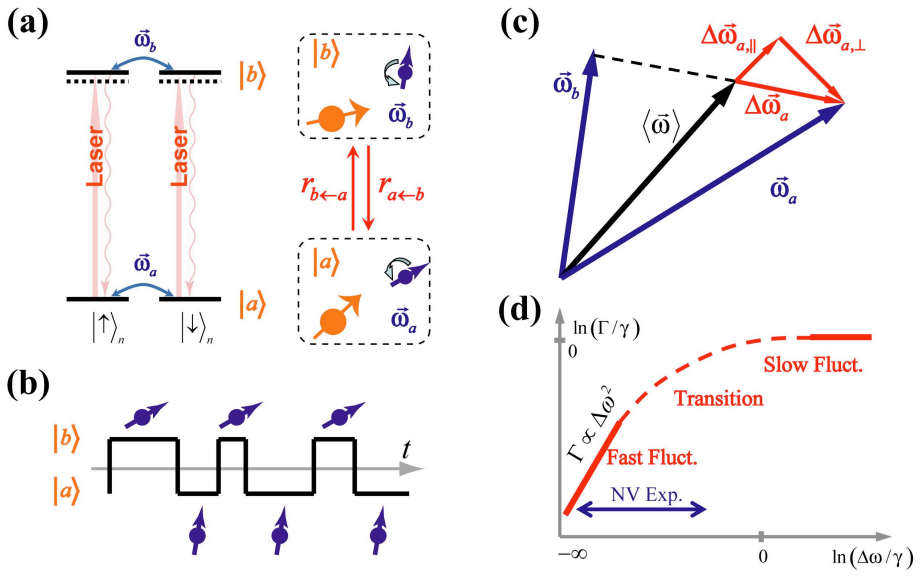

Figure 4.1: (a) Energy levels (left) and schematic model (right) for optical transitions between different electronic states ($|a\rangle$ and $|b\rangle$), with transition rates r_{ba} and r_{ab}. The precession of the nuclear spin ($\vec{\omega}_a$ or $\vec{\omega}_b$) (blue arrow) depends on the electronic state ($|a\rangle$ or $|b\rangle$) (orange arrow). (b) Random telegraph trajectory of the electron, and time-dependent precession of the nuclear spin. (c) Geometric representation of Larmor precession vectors. (d) The decoherence rate Γ as a function of the differential precession frequency $\Delta\omega$, in units of γ.

4.2 Physical Model

The essential idea of this work is illustrated in Fig. 6.1. We consider an individual nuclear spin system ($I = 1/2$, associated with a ^{13}C atom) that is weakly coupled to the electronic spin of an NV center via the hyperfine interaction. The transitions between ground and optically excited electronic states are caused by laser light and spontaneous emission of photons. The strength of the hyperfine interaction differs between the ground and the excited electronic states, because they have different spatial wave functions and thus different overlap with the nucleus. As the electron undergoes rapid optical transitions, the nuclear spin precesses according to a time-dependent effective magnetic field induced by the electron.

This situation can be modeled by considering the electron as a fluctuator with two states, $|a\rangle$ and $|b\rangle$. Let us first assume that the incoherent transitions between these two electronic states $|a\rangle \underset{r_{ab}}{\overset{r_{ba}}{\rightleftharpoons}} |b\rangle$ are described by the random telegraph process as shown in Fig. 6.1(b), which is fully characterized by the classical transition rates r_{ba} and r_{ab} (corresponding to the optical pumping rate and the radiative decay rate, respectively, resulting from an off-resonant optical drive). The nuclear spin will undergo time-dependent precession, characterized by vectors $\vec{\omega}_a$ and $\vec{\omega}_b$ for the electronic states $|a\rangle$ and $|b\rangle$, respectively [Fig. 6.1(a)].

In general, the precession vectors $\vec{\omega}_a$ and $\vec{\omega}_b$ may point along different directions as shown in Fig. 6.1(c). For example, the nuclear spin can precess around different axes for different electronic states. Furthermore, the electron undergoes fast optical transitions and introduces high frequency noise, which, in addition to dephasing, can induce spin-flips [63]. Therefore, we need to consider the nuclear spin precession

around a time-dependent, stochastic vector $\vec{\omega}(t)$, generalizing the earlier scalar model [75, 14].

Let γ and $\Delta\omega$ be the typical scales for the electron transition rates and the *difference* between the qubit precession vectors, respectively. Let us now consider the limiting case of a fast-fluctuator ($\gamma \gg \Delta\omega$). In this case we may use a perturbative approach associated with the small phase shift acquired by the nuclear spin during one excitation cycle $\delta\phi \sim \Delta\omega/\gamma$. On average this phase shift will result in a modification of the precession frequency. In addition, due to random variations in the time spent in different electronic states the phase shift will undergo a random walk with diffusion constant $\sim \delta\phi^2 \times \gamma \sim \Delta\omega^2/\gamma$.

More precisely, to the first order, we have the average precession vector

$$\langle\vec{\omega}\rangle = \frac{r_{ba}^{-1}\vec{\omega}_a + r_{ab}^{-1}\vec{\omega}_b}{r_{ba}^{-1} + r_{ab}^{-1}}, \tag{4.1}$$

where the weights are proportional to the durations of different states for the fluctuator. As illustrated in Fig. 6.1(c), $\langle\vec{\omega}\rangle$ defines the quantization axis of the spin system. The difference between the instantaneous precession vector ($\vec{\omega}_a$ or $\vec{\omega}_b$) and $\langle\vec{\omega}\rangle$, $\Delta\vec{\omega} = \vec{\omega}_a - \langle\vec{\omega}\rangle$ can be decomposed into the parallel and perpendicular components. The perpendicular component introduces spin-flips along the quantization axis at rate $\Gamma_1 \sim (\Delta\omega)_\perp^2/\gamma$. The parallel component causes stochastic phase accumulation, leading to dephasing at the rate $\Gamma_\phi \sim (\Delta\omega)_\parallel^2/\gamma$. Note that both rates are inversely proportional to the fluctuator transition rate γ in the limit of fast electronic transitions. The underlying physics is analogous to the motional narrowing of NMR [179], in which the rapid motion of the environment (corresponding to large γ) averages out the randomly accumulated phase.

In the opposite slow-fluctuator limit ($\gamma \lesssim \Delta\omega$), the decoherence rate is only determined by the fluctuator transition rates. For each fluctuator transition, there is a time variation, $\delta t \sim 1/\gamma$, which induces an uncertainty in the rotation $\delta\phi \sim \Delta\omega\delta t \sim \Delta\omega/\gamma \sim 1$. This implies that a single transition of the fluctuator is sufficient to destroy the coherence of the spin system. The resulting qualitative dependence of the nuclear spin decay upon difference in Larmor precession is illustrated in Fig. 6.1(d).

4.3 Master Equation Formalism

We now introduce the master equation formalism and illustrate that it is possible to reduce the system dynamics to a set of linear differential equations, even in the presence of the non-commutative stochastic precession. We will first solve the spin-fluctuator model with the two-state fluctuator described above. After that, we extend the procedure to include multi-state fluctuators into the formalism.

The incoherent transition of the two-state fluctuator [Fig. 6.1(a)] can be described by the master equations

$$\frac{d}{dt}\begin{pmatrix} p_a \\ \\ p_b \end{pmatrix} = \begin{pmatrix} -r_{ba} & r_{ab} \\ \\ r_{ba} & -r_{ab} \end{pmatrix}\begin{pmatrix} p_a \\ \\ p_b \end{pmatrix}, \tag{4.2}$$

where p_a and p_b are occupation probabilities for states $|a\rangle$ and $|b\rangle$.

The Hamiltonian of the nuclear spin (depending on the state of the fluctuator) is $H = |a\rangle\langle a| \otimes H_a + |b\rangle\langle b| \otimes H_b$, with $H_a = \vec{\omega}_a \cdot \vec{I}$ and $H_b = \vec{\omega}_b \cdot \vec{I}$.

Since there is no coherence between different fluctuator states, we may write the density matrix for the composite system as $\rho = |a\rangle\langle a| \otimes \rho_a + |b\rangle\langle b| \otimes \rho_b$, where

$\rho_j = \begin{pmatrix} \rho_{j,11} & \rho_{j,12} \\ \rho_{j,21} & \rho_{j,22} \end{pmatrix}$ for $j = a$ or b. The unitary evolution of the density matrix ρ with Hamiltonian H can be decomposed into two uncoupled parts: $\frac{d}{dt}\rho_j = -i\left[H_j, \rho_j\right]$ for $j = a, b$. In terms of the Liouville operator, the unitary evolution is

$$\frac{d}{dt}\vec{\rho}_j = \mathcal{L}_j \vec{\rho}_j, \tag{4.3}$$

where the density operator is represented by a column vector $\vec{\rho}_j = \left(\rho_{j,11}, \rho_{j,12}, \rho_{j,21}, \rho_{j,22}\right)^T$ and the Liouville operator by a matrix

$$\mathcal{L}_j \equiv \mathcal{L}\left[\vec{\omega}_j\right] \equiv (-i)\left(H_j \otimes \mathbf{I} - \mathbf{I} \otimes H_j^*\right), \tag{4.4}$$

for $j = a, b$. Notice that the transition matrix depends linearly on the precession vector, and such linearity implies $\mathcal{L}\left[\vec{\omega}_a\right] + \mathcal{L}\left[\vec{\omega}_b\right] = \mathcal{L}\left[\vec{\omega}_a + \vec{\omega}_b\right]$.

Combining the dynamics of the system and the fluctuator, we may write down the following master equations:

$$\frac{d}{dt}\begin{pmatrix} \vec{\rho}_a \\ \vec{\rho}_b \end{pmatrix} = \begin{pmatrix} \mathcal{L}_a - \mathbf{r_{ba}} & \mathbf{r_{ab}} \\ \mathbf{r_{ba}} & \mathcal{L}_b - \mathbf{r_{ab}} \end{pmatrix}\begin{pmatrix} \vec{\rho}_a \\ \vec{\rho}_b \end{pmatrix}, \tag{4.5}$$

where $\mathcal{L}_a$ and $\mathcal{L}_b$ describe the (slow) dynamics of the precession; $\mathbf{r_{ba}} = r_{ba}\ \mathbf{I}_{4\times4}$ and $\mathbf{r_{ab}} = r_{ab}\ \mathbf{I}_{4\times4}$ are associated with the (fast) incoherent optical transitions between electronic states, not affecting the nuclear spin.

4.4 Model with Multi-State Fluctuator

We generalize to a multi-state fluctuator, by introducing r_{ij} the fluctuator transition rate from state j to state i, and $r_{jj} \equiv \sum_{i\neq j} r_{ij}$ the total transition rate from state

j to all other states. For an N-state fluctuator, the generalized form for Eq.(4.5) is

$$\frac{d}{dt}\vec{\rho}_i = (\lambda\mathcal{L}_i - \mathbf{r}_{ii})\,\vec{\rho}_i + \sum_{j\neq i}^{N} \mathbf{r}_{ij}\vec{\rho}_j \tag{4.6}$$

where $\vec{\rho}_j = (\rho_{j,11}, \rho_{j,12}, \rho_{j,21}, \rho_{j,22})^T$ for $j = 1, 2, \cdots, N$, and $\mathbf{r}_{ij} = r_{ij}\mathbf{I}_{4\times 4}$. When there are M fluctuators, with N_j states for the jth fluctuator, we can always reduce it to one composite fluctuator with $N = \prod_{j=1}^{M} N_j$ states.

Given all the parameters $\{\vec{\omega}_i\}$ and $\{r_{ij}\}$, we can solve $\vec{\rho}_i\,(t)$ exactly from the above $4N$ linear differential equations [Eq.(4.6)] with initial conditions for $\{\vec{\rho}_i\,(0)\}$. Finally, the density matrix of the nuclear spin system is $\vec{\rho}(t) = \sum_i \vec{\rho}_i\,(t)$, which together with Eq. (4.6) provides an exact solution to the generalized spin-fluctuator model.

4.5 Experimental Results

The experimental procedure for probing the dynamics of an optically illuminated nuclear spin qubit proximal to NV centers in diamond is described in detail in Ref. [63]. The NV center is a spin triplet in the ground electronic state. In the experiment we optically polarize the electron into $m_s = 0$, in which the hyperfine interaction with the nuclear spin vanishes to leading order. Furthermore, it is believed [95], and is confirmed by experimental evidence reported below, that the electronic spin is a good quantum number during the optical excitation of the NV center. Hence the electron should mostly remain in the $m_s = 0$ manifold during optical excitation.

However, the hyperfine interaction with the electron can dramatically change the precession of the nuclear spin by modifying its effective magnetic moment [37]. The direction and magnitude of the precession vector, which is determined by the effec-

tive g-tensor [37], varies due to the changes in the contact and dipolar interactions associated with different electronic states. Under these experimental conditions, the nuclear precession vectors associated with different electronic states should be proportional to the perpendicular components of the external magnetic field, $B_\perp$, with a proportionality constant and direction that depends upon the electronic state. Thus, we present the experimental data (Fig. 6.2) as functions of the ground state precession frequency ω_g ($\omega_g \propto B_\perp$), which can be accurately measured. Both the optically induced decoherence rate Γ (the decay rate of the nuclear spin Bloch vector) and the change in average Larmor precession frequency $\langle\vec{\omega}\rangle - \omega_g$ were measured for a particular NV center. For the presented data, the optical excitation rate was chosen to correspond to about one half of saturation intensity.

A comparison between first-principle theory and experiment would require precise knowledge of nuclear precession vectors for both the *ground* and *excited* electronic states. The experiments, performed at room temperature, involve excitation of multiple excited states, whose wave functions are not known in great detail. To model quantum dynamics of such a system, we assume that the excited state precession vector has similar order of magnitude to that of the ground state, but might point along a different direction. In the following, we label the ground state as the first state of the fluctuator with precession frequency $\vec{\omega}_g \equiv \vec{\omega}_1$ for the proximal nuclear spin. The jth excited state has precession vector $\vec{\omega}_j$, with its three components drawn from a normal distribution with mean 0 and deviation $\sigma_\omega \sim \omega_g$, for $j = 2, \cdots, N$. We assume that the excitation rate from the 1st to the jth excited state $r_{j1} = R/(N-1)$, the radiative decay rate $r_{1j} = \gamma = 86\ \mu\text{s}^{-1}$ [136], and the total excitation rate $R = \gamma$.

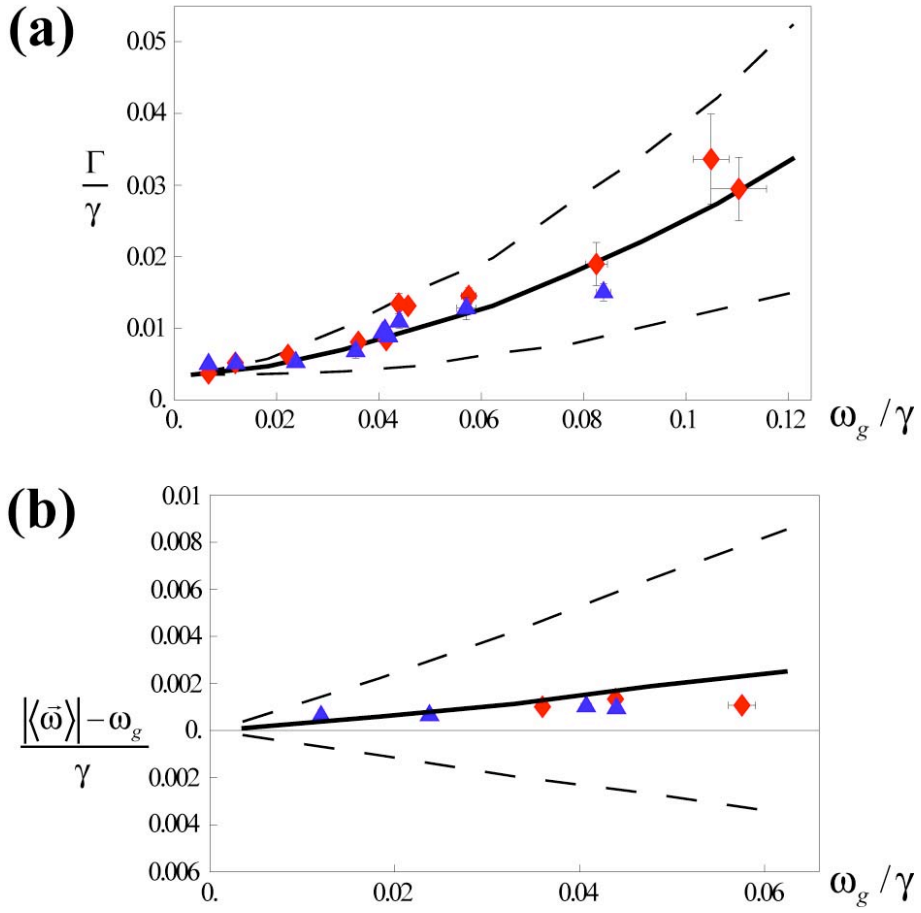

Figure 4.2: Comparison between experimental data (points) and simulation (lines). (a) Optically induced decoherence rate Γ as a function of ground state Larmor precession frequency ω_g (data adopted from Ref. [63]). (b) Shift of average Larmor precession frequency $|\langle\vec{\omega}\rangle| - \omega_g$ as a function of ω_g. For both plots, the axes are also labeled in dimensionless units, normalized by the radiative decay rate $\gamma = 86$ μs^{-1}. Experimental data points (blue triangles, red diamonds) include nuclear spins prepared along both directions ($\hat{x}$, $\hat{z}$) perpendicular to the Larmor precession vector ($\hat{y}$). The full lines are from simulation of the generalized spin-fluctuator model, averaging over 50 different sets of randomly generated excited states, as described in the text. The simulation assumes $N = 3$ for the fluctuator (i.e. one ground state and two excited states [136, 125]). The dashed lines are the statistical standard deviation of the different realizations. In panel (a), the curves from simulation are manually shifted upwards by $\Gamma_0 = 3.4 \times 10^{-3}\gamma$, as described in the text.

The transitions among excited states are neglected. According to [136, 125], there are at least two excited states involved in the optical transition, so we set $N = 3$. By choosing $\sigma_\omega = 2.5\omega_g$, we find good agreement between theory and experiment as shown in Fig. 6.2.

4.6 Discussion

In the fast-fluctuating regime ($\omega_g \ll \gamma$), the experimental decoherence rate increases quadratically with ω_g, consistent with the scaling obtained from the fast-fluctuator limit. When the precession frequency becomes comparable to the fluctuator transition rates ($\omega_g \lesssim 0.2\gamma$), Γ increases sub-quadratically with ω_g. This is because we are in the transition region as indicated in Fig. 6.1(d). In principle, for even higher precession frequency, the decoherence rate should saturate at the optical transition rate. Experimentally, however, it is difficult to manipulate the nuclear spin for very high precession frequency ($\omega_g > 0.2\gamma$) [63].

In addition to the electronic spin-conserving optical transitions analyzed above, the spin-changing transitions between $m_s = 0$ and $m_s = \pm 1$ may also induce decoherence of the nuclear spin. However, the hyperfine field from the electron in spin state $m_s = \pm 1$ is oriented along the well-defined z-axis [63], which introduces decoherence for nuclear spin state $|\uparrow\rangle_X$, but not for $|\uparrow\rangle_Z$. This contradicts the observation that the decoherence rates (with initial states $|\uparrow\rangle_X$ and $|\uparrow\rangle_Z$) are similar for the observed center (see Fig. 6.2). Therefore, we conclude that the spin-changing transitions should not be the dominant process for optically induced nuclear spin decoherence.

By extrapolating the experimental data to zero external magnetic field, we find

that there is still a finite decoherence rate $\Gamma_0 \approx 3.4 \times 10^{-3}\gamma$ (simulation curves are offset with additional fitting parameter in Fig. 6.2(a)). Remarkably, these data indicate that the nuclear spin coherence is still maintained after scattering $\gamma/\Gamma_0 \sim 300$ photons by the electron. This insensitivity, enabled via effects analogous to motional-averaging, is of critical importance for the feasibility of NV-center-based distant quantum communication [38] and distributed quantum computation [104, 103] protocols.

The zero field decoherence rate Γ_0 is still related to optical transitions, because it is much larger than the observed decoherence rate of the nuclear spin in the dark $\Gamma_{dark} \approx 3\times10^{-4}\gamma$ [63]. We attribute this zero field decoherence to the orbital motion of the optically excited states, which produces a "residual" magnetic field at the position of the nucleus. The residual magnetic field can be present for optically excited states, because the orbital motion for these states is not quenched [125, 136]. Considering the nucleus on the second coordination sphere with respect to the vacancy (i.e., $r \approx 2.6$ Å), the magnetic field from the orbital motion is approximately $\mu_B/r^3 \approx 500 \sim 1000$ G. This gives an estimated decoherence rate $\Gamma_0 \approx \Delta\omega^2/\gamma \approx (1 \sim 5) \times 10^{-3}\ \gamma$, which is consistent with the value observed experimentally.

These observations may allow us to develop new methods to further suppress optically induced nuclear decay. Specifically, at low temperatures ($T < 10$ K), it is possible to resolve individual optical transitions and selectively drive the electron between the ground state and one excited state. Under these conditions, it should be possible to eliminate the decoherence Γ_0 by applying an external magnetic field that exactly compensates the residual field from the orbital motion. With the com-

pensation at this "sweet spot", the nuclear spin sees the same total magnetic field, regardless of the state of the electron, and therefore can be completely decoupled from the electronic environment [2] [3].

4.7 Conclusion

In conclusion, we have shown that the vector spin-fluctuator model provides a good description for our observations of coherence properties of the optically illuminated nuclear spin qubit. Our theoretical and experimental results demonstrate a substantial suppression of nuclear spin decoherence due to the mechanism analogous to the motional averaging in NMR. Our analysis further indicated a new approach that may allow us to completely decouple the nuclear spin and the electron during optical excitation. These results are of critical importance for scalable applications of NV-center-based quantum registers [38, 104, 103].

[2] The decoherence associated with the fluctuations of the compensating field (e.g., $\delta B \sim 0.1$ G and $\delta\omega \sim 10^{-3}\Delta\omega$) is approximately $\delta\omega^2/\gamma \sim 10^{-6}\Gamma_0$, negligible compared with other decoherence processes.

[3] Ionization of the NV center caused by green light might also lead to optically induced decoherence of the nuclear spin at B=0. Note that ionization probability should be reduced if resonant red light is used.

Chapter 5

Repetitive readout of single electronic spin via quantum logic with nuclear spin ancillae

5.1 Introduction

Significant efforts have recently been directed towards the manipulation of several qubits in quantum systems, ranging from isolated atoms and ions to solid-state quantum bits [19, 90]. These small-scale quantum systems have been successfully used for proof-of-concept demonstrations of simple quantum algorithms [170, 169, 52]. In addition, they can be used for potentially important practical applications in areas such as quantum metrology [123]. For example, techniques involving quantum logic operations on several trapped ions have been applied to develop an improved ion state readout scheme, resulting in a new class of atomic clocks [97, 171].

In this report we describe and demonstrate a technique to enhance the readout of a single electronic spin in the solid state. Our method makes use of quantum logic between the single electronic spin and nuclear spin qubits in its local environment for repetitive readout. While such nuclear spins are generally the source of unwanted decoherence in the solid-state, recent theoretical [201, 140, 45] and experimental [98, 37, 63, 153, 88] work has already demonstrated that when properly controlled, the nuclear environment can become a very useful resource, in particular, for long-term quantum memory.

Our experimental demonstration makes use of a single nitrogen-vacancy (NV) center in diamond [132]. The electronic ground state of this defect is a spin triplet ($S = 1$) and is a good candidate for a logic qubit, on account of its remarkably long coherence times [7] and fast spin manipulation using microwave fields [152]. Furthermore, the center can be optically spin polarized and measured by combining confocal microscopy techniques with spin-selective rates of fluorescence [99]. In practice, the NV readout is far from perfect, especially under ambient, room temperature conditions. This is because laser radiation at 532 nm for readout re-polarizes the electronic spin to $|m_S = 0\rangle_e$ before a sufficient number of photons can be scattered for the state to be reliably determined.

5.2 Basic Idea

Our approach to improving spin readout is to correlate the electronic spin logic qubit with nearby nuclear spins [103], which are relatively unperturbed by the optical readout, prior to the measurement process. Specifically, we use a single ^{13}C

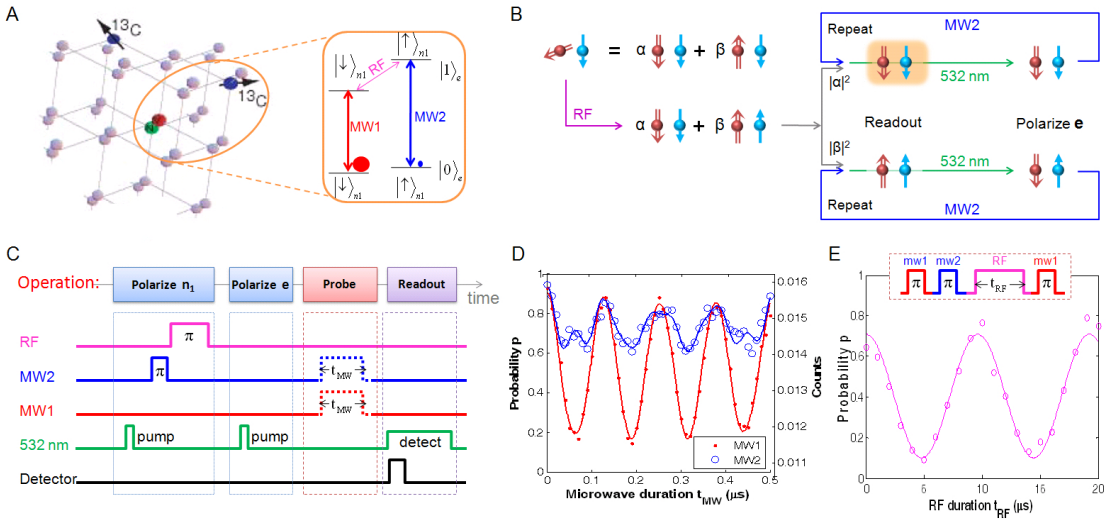

Figure 5.1: (**A**) Illustration of the NV center and its proximal ^{13}C environment. Inset: Energy levels of the coupled spin system formed by the NV electronic spin (**e**) and the first proximal ^{13}C nuclear spin ($\mathbf{n}_1$). With static magnetic field applied along the NV axis, spin $\mathbf{n}_1$ keeps the same quantization axis when spin **e** is $|0\rangle_e$ or $|1\rangle_e$ (see Appendix A). When spin $\mathbf{n}_1$ is $|\downarrow\rangle_{n_1}$ (or $|\uparrow\rangle_{n_1}$), the microwave field MW1 (or MW2) resonantly drives spin **e** between $|0\rangle_e$ and $|1\rangle_e$, which can implement the $\mathrm{C}_{n_1}\mathrm{NOT}_e$ gate. When spin **e** is $|1\rangle_e$, the radio-frequency RF field resonantly drives spin $\mathbf{n}_1$ between $|\downarrow\rangle_{n_1}$ and $|\uparrow\rangle_{n_1}$, which can implement the $\mathrm{C}_e\mathrm{NOT}_{n_1}$ gate. (**B**) Schematic illustration of repetitive readout. The red down (up) arrow represents the electronic spin state $|0\rangle_e$ ($|1\rangle_e$), and blue down (up) arrow represents the nuclear spin state $|\downarrow\rangle_{n_1}$ ($|\uparrow\rangle_{n_1}$). (**C**) Experimental pulse sequences that polarize spin $\mathbf{n}_1$ to $|\downarrow\rangle_{n_1}$ and spin **e** to $|0\rangle_e$, followed by various probe operations, before fluorescence readout of spin **e**. (**D**) Electronic spin Rabi oscillations driven by the MW1 and MW2 fields, for polarized spin $\mathbf{n}_1$. The small wiggles for MW2 in the right panel are due to off-resonant driving of the majority population in the $|\downarrow\rangle_{n_1}$ state. The data is in agreement for finite detunings and microwave power (solid curves). The right vertical axis shows the average counts for a single readout. The left vertical axis shows the probability in the $|0\rangle_e$ state, obtained from the average counts (Appendix A). (**E**) Nuclear spin Rabi oscillation driven by the RF field, with initial nuclear spin polarization $P_{n_1} = 60\,(5)\,\%$. The probe operations in (C) are replaced by the inset pulse sequence.

($I = 1/2$) nuclear spin in the diamond lattice, coupled to the NV electronic spin via a localized hyperfine interaction, as a *memory* ancilla qubit. It has eigenstates $|\uparrow\rangle_{n_1}$ (aligned) or $|\downarrow\rangle_{n_1}$ (anti-aligned) with the local magnetic field. The composite system is first prepared in a fiducial state, $|0\rangle_e|\downarrow\rangle_{n_1}$, using a sequence of optical, microwave and radiofrequency (RF) pulses. Next, the electronic spin is prepared in an arbitrary (unknown) state $|\Psi\rangle_e = \alpha|m_S = 0\rangle_e + \beta|m_S = 1\rangle_e$. Before readout, we perform a sequence of gate operations resulting in the entangled electron-nuclear state $|\Psi\rangle_e|\downarrow\rangle_{n_1} \rightarrow \alpha|0\rangle_e|\downarrow\rangle_{n_1} + \beta|1\rangle_e|\uparrow\rangle_{n_2}$. The optical measurement process projects this state into either $|0\rangle_e|\downarrow\rangle_{n_1}$ or $|1\rangle_e|\uparrow\rangle_{n_2}$. Each of these two states will fluoresce at different rates dependent on the value of m_S. Within a typical measurement period less than one photon is counted before the electron spin is repolarized to $|0\rangle_e$, which indicates that the uncertainty of the spin state measurement is quite large.

The key idea of this work is that the nuclear spin can reveal the former electronic state because of the correlations established before the electronic spin was reset. To achieve this, we perform a controlled-not operation, which maps $|0\rangle_e|\downarrow\rangle_{n_1} \rightarrow |0\rangle_e|\downarrow\rangle_{n_1}$ and $|0\rangle_e|\uparrow\rangle_{n_1} \rightarrow |1\rangle_e|\uparrow\rangle_{n_1}$, and repeat the optical measurement. Fluorescence counting of these two states can be added to prior measurements in order to decrease the uncertainty for state discrimination. If the subsequent readout of the electronic spin does not destroy the orientation of the nuclear spin, it can be determined via repetitive measurements. In this way we can increase the overall signal-to-noise of the measurement process of our logic qubit. While after multiple readout cycles and many quantum logic operations, the nuclear orientation will finally be destroyed, it is possible to further improve the readout scheme by using a pair

of ancillary nuclear spins and imprinting the electronic state into a cat-like state $|\Psi\rangle_e |\downarrow\rangle_{n_1} |\downarrow\rangle_{n_2} \rightarrow \alpha |0\rangle_e |\downarrow\rangle_{n_1} |\downarrow\rangle_{n_2} + \beta |1\rangle_e |\uparrow\rangle_{n_1} |\uparrow\rangle_{n_2}$. In such a case, the state of the first nuclear spin after repetitive sequence can be periodically "refreshed" using the information stored within the second nuclear spin. These schemes are closely related to a quantum non-demolition (QND) measurement [92], as the nuclear spin population operators $\hat{I}_z^{n1,n2}$ do not evolve throughout the electronic spin readout and constitutes good QND observables. Our electronic spin detection is far from perfect, which precludes an ideal QND measurement, but our scheme nevertheless allows us to substantially improve the spin readout, as described below.

To implement our repetitive readout technique we use the NV center coupled to nuclear spins that can be polarized, fully controlled and provide a robust quantum memory even in the presence of optical radiation necessary for electron readout. This is achieved through a combination of optical, microwave, and RF fields, as illustrated in Fig. 1, and discussed in (Appendix A). For the present work, we have chosen a center with a well-resolved ^{13}C hyperfine coupling near 14 MHz. We lift the degeneracy of the $|m_s = \pm 1\rangle_e$ spin states by applying a $B_0 = 30$ gauss magnetic field along the NV axis. Under these conditions, we can selectively address the transitions of the electronic spin ($\mathbf{e}$) within the subspace of $|0\rangle_e, |1\rangle_e\}$, conditioned on a certain nuclear state. The model Hamiltonian for this system, illustrated in Fig. 1A is

$$H = (\Delta + \gamma_e B_0)\hat{S}_z + \gamma_C B_0 \hat{I}_z^{n1} + A\hat{S}_z\hat{I}_z^{n1} \tag{5.1}$$

where $\Delta = 2.87$ GHz is the zero field splitting, γ_e and γ_C are the electronic and nuclear spin gyromagnetic ratios and $\hat{I}_z^{n1}$ and $\hat{S}_z$ are the spin 1/2 angular momentum

operators [1]. Coherent oscillations between the $|0\rangle_e$ and $|1\rangle_e$ states, conditioned on the first proximal nuclear spin ($\mathbf{n}_1$) in $|\downarrow\rangle_{n_1}$ (or $|\uparrow\rangle_{n_1}$), are selectively driven by the microwave field MW1 (or MW2). To control nuclear spin $\mathbf{n}_1$ we use a resonantly tuned RF field to address the levels $|1\rangle_e|\downarrow\rangle_{n_1}$ and $|1\rangle_e|\uparrow\rangle_{n_1}$, which are energetically separated due to the hyperfine interaction (Fig. 1A). With these operations, spin $\mathbf{n}_1$ is polarized by applying MW1 and RF π pulses, which transfer the polarization from spin $\mathbf{e}$ to spin $\mathbf{n}_1$. Fig. 1E demonstrates Rabi oscillations of a spin $\mathbf{n}_1$ using this procedure. This data indicates that we can achieve its preparation (polarization) and readout with combined fidelity $F \equiv \langle\downarrow|\rho'|\downarrow\rangle \geq 80\%$, where ρ' is the reduced density operator for spin $\mathbf{n}_1$.

5.3 Flip-Flop Dynamics of Two Nuclear Spins

To demonstrate control of two nuclear spins, we study the dynamics of spin $\mathbf{n}_1$ after it is polarized to $|\downarrow\rangle_{n_1}$, with electron prepared in the $|0\rangle_e$ state. Fig. 2 indicates that the nuclear population, $p_{n_1,\uparrow}(\tau)$, oscillates between $p_{n_1,\uparrow}(0) \approx 0.2$ and $p_{n_1,\uparrow}(T/2) \approx 0.5$ with a period of $T = 117\,(1)$ μs (Fig. 2AC). The relatively high contrast of these oscillations suggests an interaction with a second nuclear spin ($\mathbf{n}_2$), as the two nuclei "flip-flop" between the states $|\uparrow\rangle_{n_1}|\downarrow\rangle_{n_2}$ and $|\downarrow\rangle_{n_1}|\uparrow\rangle_{n_2}$ Such excitation exchange requires a similar Zeeman splitting for the two spins, indicating that the second nucleus is also a ^{13}C. We note that the interaction strength, $b = \pi/T = 4.27\,(3)$ kHz, is several times that of a bare dipolar coupling (2 kHz for two nuclei separated

[1] As described in [37], the nitrogen nuclear spin (I=1) is a constant of the motion for the NV center and can be ignored. $\hat{S}_z$ is a fictitious spin 1/2 operator for a subspace of the S=1 spin.

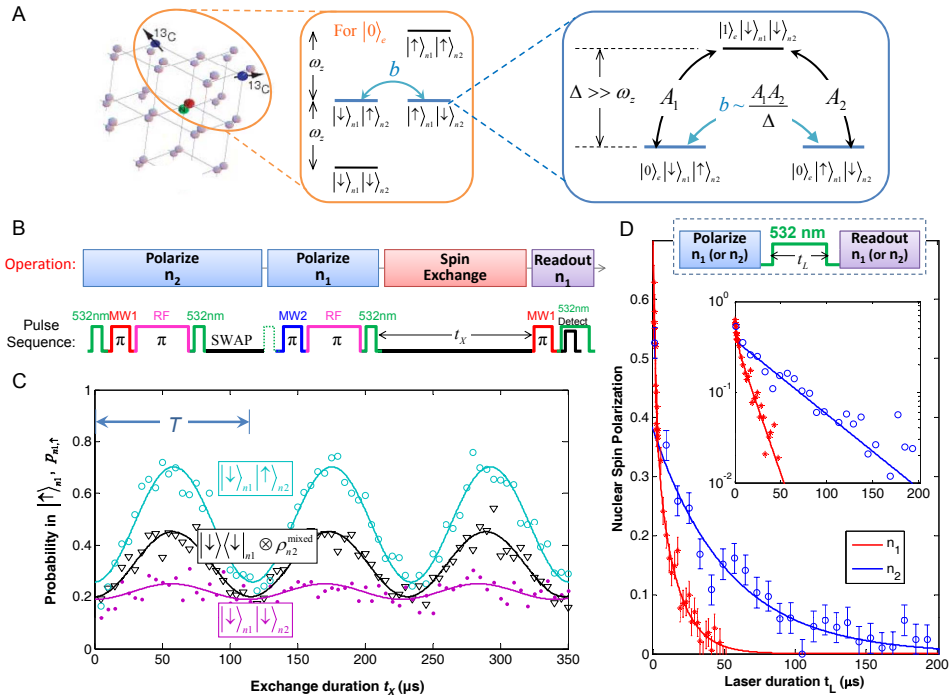

Figure 5.2: (**A**) The coupled spin system formed by the NV electronic spin (**e**) and two proximal ^{13}C nuclear spins ($\mathbf{n}_1$ and $\mathbf{n}_2$). Middle inset: Energy levels for spins $\mathbf{n}_1$ and $\mathbf{n}_2$ when spin **e** is in the $|0\rangle_e$ state. Right inset: Schematics of electron-mediated flip-flop between spins $\mathbf{n}_1$ and $\mathbf{n}_2$, which is mediated by the second-order hopping via $|1\rangle_e |\downarrow\rangle_{n1} |\downarrow\rangle_{n2}$ (or $|-1\rangle_e |\uparrow\rangle_{n1} |\uparrow\rangle_{n2}$, not shown). (**B**) Operations and pulse sequence to probe dynamics between spins $\mathbf{n}_1$ and $\mathbf{n}_2$. The three-spin system is initialized to $|0\rangle_e |\downarrow\rangle_{n1} |\uparrow\rangle_{n2}$, followed by the flip-flop evolution between spins $\mathbf{n}_1$ and $\mathbf{n}_2$, before the final fluorescence readout of spin $\mathbf{n}_1$. (**C**) Spin flip-flop dynamics between spins $\mathbf{n}_1$ and $\mathbf{n}_2$. For three different preparations of the initial state ($|\downarrow\rangle_{n1} |\uparrow\rangle_{n2}$, $|\downarrow\rangle\langle\downarrow|_{n1} \otimes \rho_{n2}^{\text{mixed}}$, and $|\downarrow\rangle_{n1} |\downarrow\rangle_{n2}$, with $\rho_{n2}^{\text{mixed}} = \frac{1}{2}(|\downarrow\rangle\langle\downarrow| + |\uparrow\rangle\langle\uparrow|)_{n2}$), the observed population in state $|\uparrow\rangle_{n1}$, $p_{n1,\uparrow}(t)$, oscillates with the same period $T = 117\,(1)$ μs.. For $|\downarrow\rangle\langle\downarrow|_{n1} \otimes \rho_{n2}^{\text{mixed}}$, spin $\mathbf{n}_1$ becomes fully unpolarized at times $\frac{T}{2}$, $\frac{3T}{2}$ and $\frac{5T}{2}$. For $|\downarrow\rangle_{n1} |\uparrow\rangle_{n2}$ the oscillation amplitude is enhanced by a factor of two, while for $|\downarrow\rangle_{n1} |\downarrow\rangle_{n2}$ it is almost completely suppressed. These observation verifies the theoretical prediction, with flip-flop coupling strength $b = 4.27\,(3)$ kHz. (**D**) Depolarization of spins $\mathbf{n}_1$ and $\mathbf{n}_2$ under optical illumination. For times longer than 1 μs, the polarizations for spins $\mathbf{n}_1$ and $\mathbf{n}_2$ decay exponentially with characteristic times $\tau_{n_1} = 13\,(1)$ μs and $\tau_{n_2} = 53\,(5)$ μs, respectively. These decay times are much longer than the optical readout/pump time of the electronic spin (about 350 ns). Inset: Log-linear plot.

by the nearest neighbor distance, 1.54 $\mathring{A}$) signifying that their interaction is mediated by the NV electronic spin (see inset of Fig. 2A and Appendix A), and is described by the interaction hamiltonian $H_{int} = b(I_{1+}I_{2-} + I_{1-}I_{2+})$.

This interaction can be used to effectively control the state of the second nucleus and of the entire three-spin system. Specifically, a half period of oscillation, $T/2$, constitutes a SWAP operation between the two spins. It can be used, e.g., to polarize the second nuclear spin, as illustrated in Fig. 2BC. In addition, by modifying the initial states of spin $\mathbf{n}_1$, we can prepare the initial state of the two nuclei in any of the four possible configurations: $\{\uparrow\uparrow, \uparrow\downarrow, \downarrow\uparrow, \downarrow\downarrow\}$ (Appendix A). Further control is provided by changing electronic spin state into $|0\rangle_e$ state, in which case the flip-flop dynamics between spins $\mathbf{n}_1$ and $\mathbf{n}_2$ disappears (see Fig. S1). This is because spins $\mathbf{n}_1$ and $\mathbf{n}_2$ have very distinct hyperfine splittings that introduce a large energy difference ($\Delta E \gg b$) between $|\uparrow\rangle_{n_1}|\downarrow\rangle_{n_2}$ and $|\downarrow\rangle_{n_1}|\uparrow\rangle_{n_2}$ and quench the interaction. Therefore, we can implement a controlled-SWAP operation between spins $\mathbf{n}_1$ and $\mathbf{n}_2$, enabling full control over spin $\mathbf{n}_2$.

An important property of the nuclear spin memory that enables the repetitive readout is its robustness under optical illumination. This is illustrated in Fig. 2D. We observe decreased spin polarization for both nuclei when we increase the duration of optical illumination t_L at fixed optical intensity. For t_L longer than 1 μs, the nuclear spins decay exponentially, with decay times $\tau_{n_1} = 13\,(1)$ μs and $\tau_{n_2} = 53\,(1)$ μs (inset). Note that spin $\mathbf{n}_2$ is less perturbed by the optical transitions between different electronic states, as it has a weaker hyperfine coupling to the electron [100]. For t_L less than 1 μs, the decay is slightly faster, which is likely associated with the

dynamics of the spin-fluctuator model that describe optically induced depolarization of single nuclei (see Appendix A and Ref. [100]). Overall, the nuclear spin decay times are much longer than the optical readout/pumping time (350 ns) of the electronic spin.

5.4 Repetitive Readout with One Nuclear Spin

We now turn to experimental demonstration of repetitive readout. As illustrated in Fig. 1D, the direct readout of electronic spin is imperfect, with the signal resulting from different electronic states differing by only about 0.004 detected photons per single readout event. Typical experiments therefore require $> 10^5$ repetitions of the the pulse sequence in Fig. 1C, to clearly resolve the oscillation signal in Fig. 1D. To improve the signal, we first polarize both spins **e** and $\mathbf{n}_1$ to the initial state $|0\rangle_e |\downarrow\rangle_{n_1}$. We next perform some unitary $U(t)$, which prepares the superposition state $|\Psi_1\rangle = (\alpha |0\rangle_e + \beta |1\rangle_e) |\downarrow\rangle_{n_1}$ that we would like to measure. Instead of immediately reading out electronic spin, we use a controlled-not gate ($\mathrm{C}_e\mathrm{NOT}_{n_1}$, achieved by an RF π pulse) to correlate spin **e** with spin $\mathbf{n}_1$(Fig. 3A). Next, we optically readout/pump spin **e**, leaving the spin system in the post-readout state: $\rho_{\mathrm{post}} = |0\rangle\langle 0|_e \otimes \left(|\alpha|^2 |\downarrow\rangle\langle\downarrow| + |\beta|^2 |\uparrow\rangle\langle\uparrow|\right)_{n_1}$. We then read the state of spin $\mathbf{n}_1$ via the electronic spin **e** by performing a controlled-not operation ($\mathrm{C}_{n_1}\mathrm{NOT}_e$, achieved by an MW1 or MW2 π pulse). This completes a one-step readout of spin $\mathbf{n}_1$, which can be repeated until it completely depolarizes due to optical illumination.

As a direct illustration of the enhanced readout technique, we present in Fig. 3, Rabi oscillations of the electronic spin using m subsequent repetitive readouts (Fig. 3B). The accumulation of signal results in a ten-fold enhancement in amplitude. The

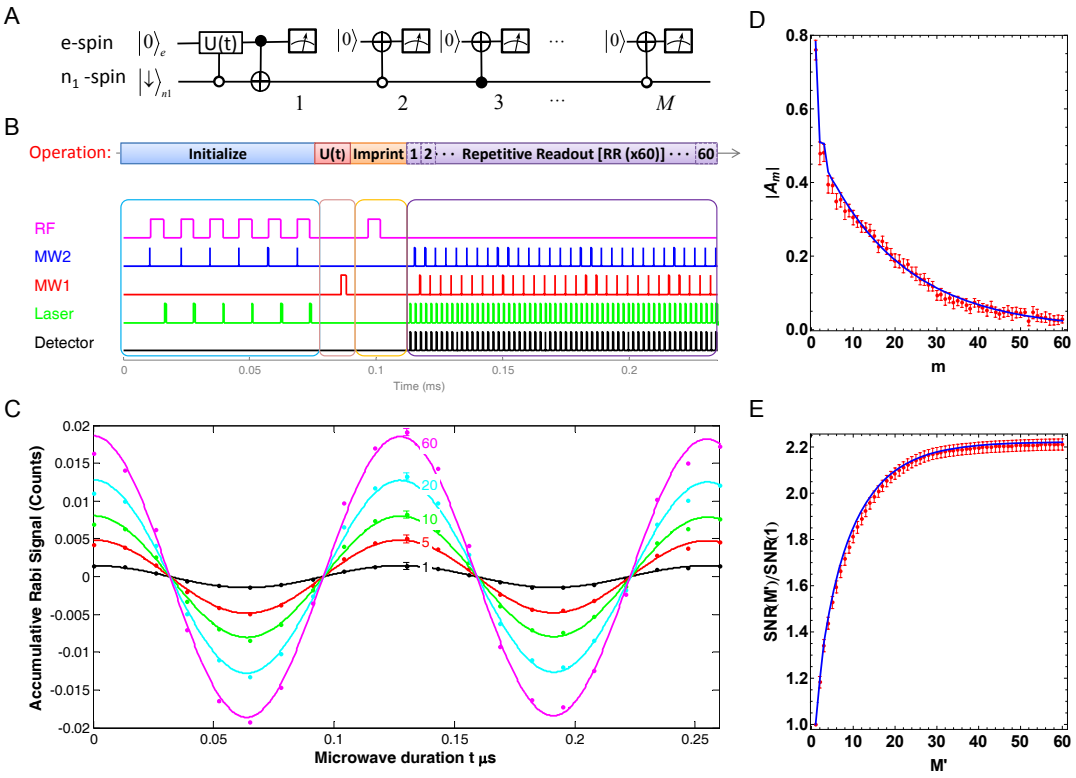

Figure 5.3: (**A**) Quantum circuit for *M-step repetitive readout scheme* assisted by spin $\mathbf{n}_1$. ($M = 60$.) (**B**) Operations and pulse sequences. The initial state $|0\rangle_e |1\rangle_{n_1}$ is prepared with six-step pumping of spins $\mathbf{e}$ and $\mathbf{n}_1$. The MW1 pulse of duration t induces the Rabi rotation $U(t)$ of spin $\mathbf{e}$, whose parity information is imprinted to spin $\mathbf{n}_1$ with an RF π pulse (i.e., the $\mathrm{C}_e\mathrm{NOT}_{n_1}$ gate). After fluorescence readout of spin $\mathbf{e}$, $(M-1)$-repetitive readout of spin $\mathbf{n}_1$ is performed by MW1 or MW2 π pulses (i.e., $\mathrm{C}_{n_1}\mathrm{NOT}_e$ gates) followed by fluorescence readout. (**C**) Cumulative Rabi signal obtained from repetitive readout, summed from $m = 1$ to M', for $M' = 1, 5, 10, 20, 60$ repetitions. The constant background counts are subtracted. (**D**) Normalized amplitudes $|A_m|$ for Rabi oscillation obtained from the m-th readout. $|A_m|$ decreases with m, mostly due to depolarization of spin $\mathbf{n}_1$ under optical illumination. (**E**) Improvement in the SNR using the repetitive readout scheme. Compared to a single readout, the SNR is increased by 220%. The blue curves in (D) and (E) are simulations with imperfection parameters estimated from independent experiments (Appendix A).

performance of the technique is further quantified by using the signal-to-noise ratio (SNR) figure of merit for the cumulative readout signal. The optimal SNR is determined by considering the normalized amplitudes, $|A_m|$, of Rabi oscillations by fitting each of the m-th readouts to a cosine curve and choosing a normalization such that the Rabi oscillation with perfect nuclear spin polarization has $|A| = 1$ (Fig.1B). The signal is defined as the weighted sum of $|A_m|$ up to M' total measurements: $S(M') = \sum_{m=1}^{M'} w_m |A_m|$, with weights $\{w_m\}$. The noise is $N(M') = \sqrt{\sum_{m=1}^{M'} w_m^2 \sigma_m^2}$, where σ_m is the uncertainty of the m-th readout. With optimal choice of weights described in Appendix A, we obtain the optimized SNR as the figure of merit for the repetitive readout scheme:

$$\mathrm{SNR}(M') = \sqrt{\sum_{m=1}^{M'} \left| \frac{A_m}{\sigma_m} \right|^2} \tag{5.2}$$

In the ideal QND case, each repetitive readout would yield the same $|A_m|$ and the SNR would scale with $\sqrt{M'}$. For our experiment, the SNR saturates (Fig. 3E) due to the decay of the normalized amplitudes (Fig. 3D). Nevertheless, experimental data shown in Fig. 3E indicate the enhancement of SNR by more than 220%.

In analyzing this result, we note that several factors contribute to the observed behavior. The sharp decrease of $|A_2|$ can be explained by pulse imperfections, decay under optical illumination, and finite nuclear spin polarization (blue curve in Fig. 3E, as detailed in Appendix A). The subsequent amplitude reduction scales exponentially in m: $|A_m| = |A_2|\eta^{(m-2)}$ with $\eta \approx 0.95$ and is the result of a finite depolarization of spin $\mathbf{n}_1$ induced by each optical readout pulse. Thus the SNR from repetitive readout is limited by three major imperfections (Appendix A): 1) errors from microwave pulses (about 7% error probability for each π pulse), 2) depolarization of nuclear spins under

optical illumination (e.g., about 5% depolarization error to spin $\mathbf{n}_1$ induced by each 350 ns readout laser pulse), and 3) imperfect optical pumping of the electronic spin after each readout. The first two imperfections limit the initial nuclear spin polarization to about 60% (Appendix A). The second imperfection also affects the repetitive optical readout, yielding the overall exponential decay in the amplitude $|A_m|$ with increasing m. The third imperfection could be made very small with sufficiently long optical pumping, but this is not optimal for our repetitive readout scheme, because optical illumination also induces depolarization of the nuclear spins that store useful information. To mitigate the perturbation to the nuclear spins, we choose 350 ns green optical pumping pulses that result in 80% electronic spin polarization in the state $|0\rangle_e$. This affects all readouts immediately proceeded by an optical readout pulse (i.e., $m = 2, \cdots, M$), which attenuates the signal amplitude (Appendix A). Note that the imperfections from microwave π pulses can be effectively suppressed by population transfer via adiabatic passage or pulses with amplitude/phase modulation [128, 194, 108, 34].

5.5 Repetitive Readout with Two Nuclear Spins

As an indication of how the readout can be improved further, we now consider the use of two ancillary nuclear spins. Specifically, we may also correlate the state of spin $\mathbf{e}$ with spin $\mathbf{n}_2$, in addition to spin $\mathbf{n}_1$. Since the decay time of spin $\mathbf{n}_2$ is about four times longer than that of spin $\mathbf{n}_1$ (Fig. 2D), the information stored in spin $\mathbf{n}_2$ persists after spin $\mathbf{n}_1$ has been depolarized under optical illumination. This remaining polarization can be transferred to spin $\mathbf{n}_1$ and repetitively readout

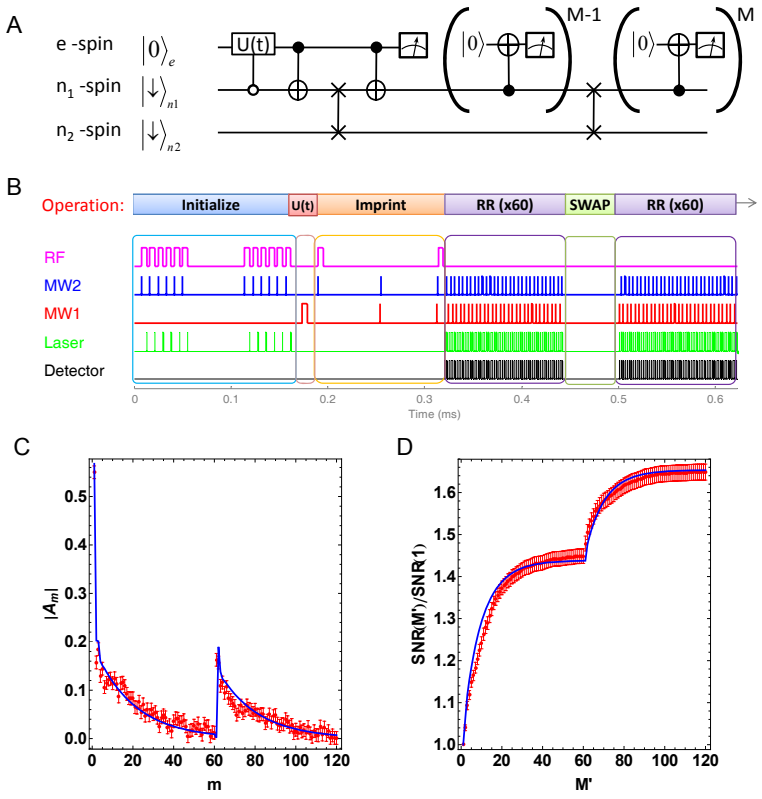

Figure 5.4: (**A**) Quantum circuit for *concatenated M-step repetitive readout scheme* assisted by both spins $\mathbf{n}_1$ and $\mathbf{n}_2$. ($M = 60$.) (**B**) Operations and pulse sequences. Ideally, the GHZ-like state $\alpha\,|0\rangle_e\,|\downarrow\rangle_{n_1}\,|\downarrow\rangle_{n_2} + \beta\,|1\rangle_e\,|\uparrow\rangle_{n_1}\,|\uparrow\rangle_{n_2}$ with the parity information of spin **e** imprinted to both spins $\mathbf{n}_1$ and $\mathbf{n}_2$ is created before the first readout. After the first round of M-step repetitive readout, spin $\mathbf{n}_1$ gets depolarized, but spin $\mathbf{n}_2$ maintains its polarization. The spin state of spin $\mathbf{n}_2$ is swapped to spin $\mathbf{n}_1$, which is then detected during the second round of M-step repetitive readouts. (**C**) Normalized amplitude $|A_m|$ obtained from the m-th readout. There is an "revival" in the signal amplitude starting from $m = M + 1$, after the SWAP operation between spins $\mathbf{n}_1$ and $\mathbf{n}_2$. (**D**) Improvement in the SNR using the double repetitive readout scheme. Compared to a single readout, the SNR is increased by 170%. The blue curves in (C) and (D) are simulations with imperfection parameters estimated from independent experiments (Appendix A).

again. To demonstrate this scheme, we initialize both nuclear spins in the state $|\downarrow\rangle_{n_1}|\downarrow\rangle_{n_2}$ and prepare the electronic spin in a superposition state $(\alpha|0\rangle+\beta|1\rangle)_e$ that we would like to detect. First, we use the operation ($C_eNOT_{n_1}$-SWAP-$C_eNOT_{n_1}$) to prepare the GHZ-type state $|\Psi\rangle = \alpha|0\rangle_e|\downarrow\rangle_{n_1}|\downarrow\rangle_{n_2}+\beta|1\rangle_e|\uparrow\rangle_{n_1}|\uparrow\rangle_{n_2}$. Next, we optically readout/pump spin **e**, leaving the system in state $\rho'_{\text{post}} = |\alpha|^2|0\downarrow\downarrow\rangle\langle 0\uparrow\uparrow| + |\beta|^2|0\uparrow\uparrow\rangle\langle 0\uparrow\uparrow|$. We then perform $M-1$ repetitive readouts of spin $\mathbf{n}_1$, in the manner described above, until spin $\mathbf{n}_1$ is depolarized. At this point, spin $\mathbf{n}_2$ is still directly correlated with the first measurement of the **e** spin. This information can be transferred to spin $\mathbf{n}_1$ by a nuclear SWAP gate. Thus, the parity information can be measured again by performing a second round of M-step repetitive readout. These operations are summarized in the quantum circuit (Fig. 4A) and pulse sequences (Fig. 4B).

Experimentally we demonstrate the "revival" in the signal amplitude $|A_m|$ after the SWAP (Fig. 4C), which leads to an associated jump in the SNR curve (Fig. 4D) for $M = 61$. This shows that we can indeed use the second nuclear spin to further enhance the readout efficiency. While ideally, we expect that the repetitive readout scheme assisted by two nuclear spins should improve the absolute SNR more than a single nuclear spin, experimentally this is not so, as more errors are accumulated due to initialization and pulse imperfections. These errors that reduce the signal amplitudes for the readout assisted by the nuclear spins, compromising the overall SNR improvement. Nevertheless, our experiments clearly demonstrate that it is possible to further boost the relative SNR using additional nuclear spins.

5.6 Conclusion

In conclusion, our work introduces and demonstrates a technique to enhance the readout of individual electronic spins and opens the door to a number of important potential applications in solid-state quantum information science. While we have demonstrated an enhancement for coherent Rabi oscillations, any set of pulses acting on the electronic spin (e.g. a spin echo sequence) can be implemented. This should have immediate applications to NV-based nano-magnetometry [141, 6, 186]. Since the duration of the entire repetitive readout sequence ($\sim 150\mu s$ in Fig. 3B) is shorter than the typical echo duration in pure diamond, SNR improvements directly translate into increased magnetic field sensitivity. In addition, our scheme can also be performed with resonant optical excitations ($\lambda \approx 637$ nm) resolvable for NV centers at cryogenic temperatures. Here we can exploit the spin structure of optical excited-states [136, 72, 8] to readout the electronic spin much more efficiently with reduced perturbation to the nuclear spin [100]. Under these conditions, our technique can be used to achieve a single-shot readout of the electronic spin. In turn, this can be employed to perform robust QND measurements of nuclear spin qubits which will be direct use for distributed quantum networks [103, 63, 55, 9]. Therefore, our experiments demonstrate that manipulation of several nuclear spin ancillae surrounding central electronic spin can be used to implement robust, practically useful quantum algorithms in solid state.

Chapter 6

A fast and robust approach to long-distance quantum communication with atomic ensembles

6.1 Introduction

Quantum communication holds promise for the secret transfer of classical messages as well forming an essential element of quantum networks, allowing for teleportation of arbitrary quantum states and violations of Bell's inequalities over long distances [79]. While experimental and even commercial implementation of simple quantum communication protocols are well established [29, 163], extending these techniques to distances much longer than the attenuation length of optical fiber remains a challeng-

ing goal due to exponential attenuation of transmitted signals. Quantum repeaters [12, 51, 26, 61] overcome the exponential time overhead associated with fiber attenuation and other errors by using a quantum memory and local quantum computation.

Several promising avenues for quantum repeater implementation include both atomic ensembles [59] and using few qubit quantum computers, such as neutral atoms in cavity QED [44, 58], ion traps [20] and solid-state single photon emitters [38, 39]. Experimental progress [41, 35, 65] towards realization of the DLCZ protocol [59] has been especially rapid, with many building blocks demonstrated in the laboratory. The experimental challenge is now shifting towards the realization of scalable quantum repeater systems which could yield a reasonable communication rate at continental distances ($\gtrsim 1000km$). Thus, the DLCZ protocol should be examined and adapted to practical experimental considerations, allowing to remove imperfections such as the finite efficiency of retrieval and single-photon detection and fiber length fluctuations. Our approach extends the DLCZ protocol, keeping the experimental simplicity of the original scheme while avoiding fundamental difficulties due to these expected experimental imperfections.

This paper is organized as follows. In Sec. II we will review the DLCZ protocol and describe our new approach which uses a new basis to encode each qubit. Section III compares both the DLCZ protocol and our approach in the presences of imperfections. Section IV estimates the time scaling of our approach and compares three specific implementations. Section V summarizes our results.

6.2 Atomic-ensemble-based Quantum Repeaters

6.2.1 The DLCZ protocol: a review

The DLCZ protocol [59] starts with entanglement generation (ENG) by counting the interfering Stokes photons scattered from a pair of distant atomic cells x and y. This generates an entangled state

$$|\xi_\phi\rangle_{x,y} = \left(\hat{S}_x^\dagger + e^{i\phi}\hat{S}_y^\dagger\right)/\sqrt{2}\,|\text{vac}\rangle_{x,y} \ , \tag{6.1}$$

with $\hat{S}_x^\dagger$ and $\hat{S}_y^\dagger$ the creation operators of spin-wave modes in the two cells respectively, and ϕ the phase difference between left and right channels for Stokes photons [134]. Then, entanglement connection (ENC) is performed on two pairs of entangled atomic cells $|\xi_{\phi_1}\rangle_{x_L,y_C}$ and $|\xi_{\phi_2}\rangle_{x_C,y_R}$, obtaining a further separated entangled pair $|\xi_{\phi_1+\phi_2}\rangle_{x_L,y_R}$ probabilistically. The ENC step provides built-in purification against many imperfections – photon loss, atomic excitation loss and dark counts. In the final step, post-selection is used to obtain an effectively *polarization entangled state*

$$\left|\Psi^{PME}\right\rangle = e^{i\phi}\left(\hat{S}_{x_1}^\dagger\hat{S}_{y_2}^\dagger + \hat{S}_{x_2}^\dagger\hat{S}_{y_1}^\dagger\right)/\sqrt{2}\,|\text{vac}\rangle \tag{6.2}$$

from two parallel pairs $|\xi_\phi\rangle_{x_1,y_1}|\xi_\phi\rangle_{x_2,y_2}$, which overcomes static phase errors (time independent ϕ's).

There are two important merits of the DLCZ protocol. First, it has intrinsic purification of errors due to photon loss (in the fiber, the quantum memory, and the photon detector) and significantly relaxes the experimental requirement for quantum repeater. In addition, the time scaling of the DLCZ protocol is always sub-exponential and very close to polynomial when the retrieval and detection efficiency is high.

However, the DLCZ protocol does not purify all kinds of errors. For example, time dependent ϕ's (due to fiber length fluctuation) induce phase error, which cannot be taken out as a common factor in Eq.(6.2), since the two pairs of entangled atomic cells are not produced at the same time. Such phase error is accumulated and doubled after each level of ENC. In addition, combined photon loss during ENG and ENC may also induce phase error not purified by the DLCZ protocol. Furthermore, the DLCZ protocol (dashed line in Fig. 6.2) still has a significant time overhead for long distances, because of the super-polynomial scaling in the presence of realistic imperfections. For instance, non-ideal retrieval and detection efficiency ($\eta \equiv \eta_{\text{retrieval}} \times \eta_{\text{detection}} < 1$) during ENC introduces a large vacuum component, suppresses the success probability of later ENC, and consequently slows down the protocol.

Motivated by these issues, we will extend the DLCZ protocol, mitigating the above errors.

6.2.2 New approach

We now consider a different approach in which two atomic cells are used at each node a, labeled (a, H) and (a, V), to store one qubit, a. The qubit is defined as one single spin-wave excitation shared between two cells:

$$\left\{ \left|H\right\rangle_a = S^\dagger_{a,H} \left|\text{vac}\right\rangle, \left|V\right\rangle_a = S^\dagger_{a,V} \left|\text{vac}\right\rangle \right\} . \tag{6.3}$$

When the stored spin waves are converted back into photons, the photons have a polarization (H or V) consistent with that stored in the originating cell. This qubit basis allows projective measurements along any qubit states, e.g., $\left|\pm\right\rangle \equiv \left(\left|H\right\rangle_a \pm \left|V\right\rangle_a\right)/\sqrt{2}$, using linear optical operations and photon counting [117]. We will show that in this

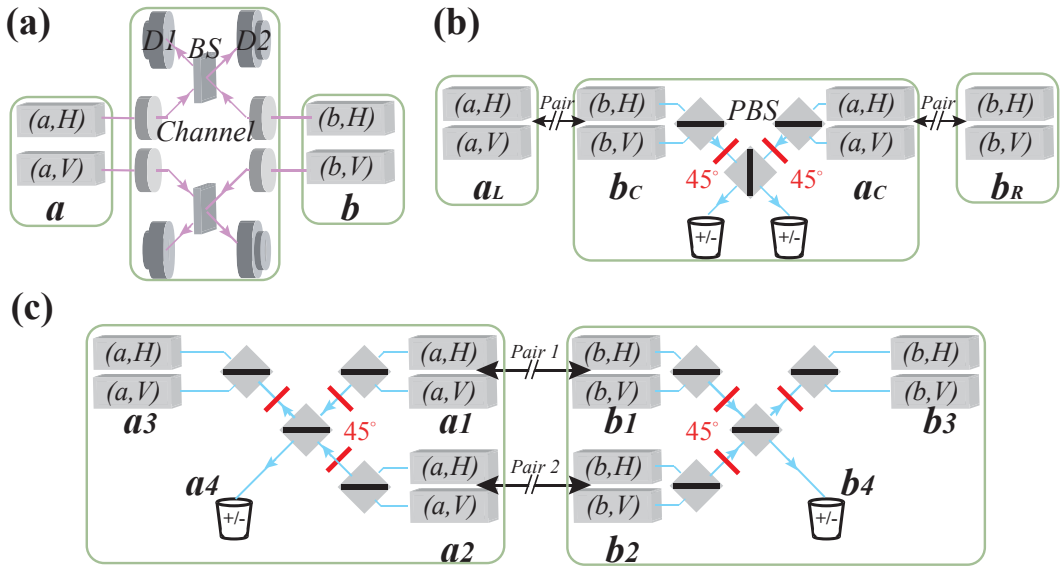

Figure 6.1: Repeater components: (a) Entanglement generation (ENG). (b) Entanglement connection (ENC); indicated operations: retrieve b_C and a_C [additional 45° rotations only for the first level], join on polarizing beam splitter (PBS), detect in $\pm$ basis conditioned on one photon per output, and finally adjust the phase. (c) Entanglement purification (ENP); indicated operations: retrieve a_1, b_1 and a_2, b_2 [additional 45° rotations to purify phase error], interfere a_1, a_2 on PBS (same with b_1, b_2), restore a_3, b_3 conditioned on single photon at a_4 and b_4 respectively, and finally adjust the phase.

logical basis it is possible to perform entanglement purification (ENP) [26, 61] to reduce errors within the logical subspace, including phase fluctuation. Since ENP can suppress errors within the logical subspace which occur with probability q to $O(q^2)$, only a few ENP levels are needed to obtain high fidelity entanglement.

We now describe our procedures for ENG, ENC and ENP. ENG (Fig. 6.1(a)) is similar to that of the DLCZ protocol, but here *two* parallel entangled pairs are generated between a and b:

$$\begin{aligned} \left|\Psi^{ENG}\right\rangle_{a,b} &= \left|\xi_\phi\right\rangle^{+}_{(a,H)(b,H)} \left|\xi_\phi\right\rangle^{+}_{(a,V)(b,V)} \\ &= e^{i\phi}\left(\left|H\right\rangle_a \left|V\right\rangle_b + \left|V\right\rangle_a \left|H\right\rangle_b\right) + \\ &\quad \left|HV\right\rangle_a \left|\mathrm{vac}\right\rangle_b + e^{2i\phi}\left|\mathrm{vac}\right\rangle_a \left|HV\right\rangle_b \ . \end{aligned} \tag{6.4}$$

The entangled states are prepared in the quantum memory, so no simultaneity is required for creating the two states comprising $\left|\Psi^{ENG}\right\rangle$. For small excitation probability p_c, the whole generation only takes time $O(1/p_c)$, in contrast to $O(1/p_c^2)$ for schemes requiring simultaneity, e.g., coupling between trapped atom and photon [20] or parametric down conversion [160]. Errors from multi-photon events occur only with probability p_c^2, and are considered in later analysis of imperfections.

The first level of ENC converts two $\left|\Psi^{ENG}\right\rangle$ states (one between a_L and b_C, the other between a_C and b_R) into polarization entangled states $\left|\Phi^+\right\rangle_{ab} = \left|H\right\rangle_{a_L}\left|H\right\rangle_{b_R} + \left|V\right\rangle_{a_L}\left|V\right\rangle_{b_R}$. Only four out of the sixteen terms in the Schmidt decomposition of $\left|\Psi^{ENG}\right\rangle_{a_L b_C}\left|\Psi^{ENG}\right\rangle_{a_C b_R}$ have any contribution to the output state; the remainder are eliminated by projective measurement during ENC, reducing the probability of success for ENC from 1/2 to 1/8. At higher levels of ENC, the operations correspond

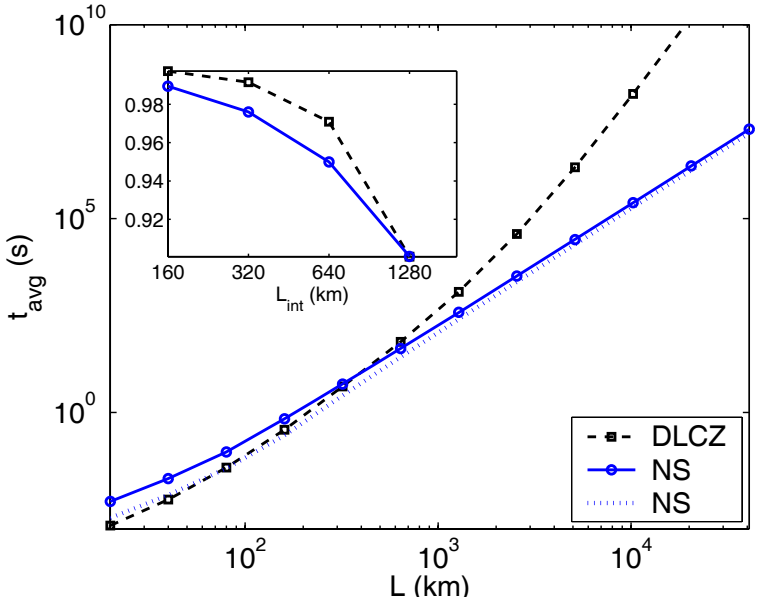

Figure 6.2: Comparison between the DLCZ protocol and the new scheme (NS) (without active entanglement purification (ENP)). For each distance, we optimize over the choice of the control parameters (the half distance between neighboring repeater stations, L_0, and the elementary pair generation probability, p_c). With efficiency $\eta = 90\%$ and targeting fidelity $F = 90\%$, we find the most efficient implementations to create the polarization entangled state (Eq.(6.2)) for both the DLCZ (circled black dashed line) and the new scheme (squared blue solid line). The fiber attenuation length is $L_{att} = 20km$, with no dynamical phase error. The main plot: we show the relationship between the (optimized) average creation time t_{avg} and the final distance L for both schemes, and the empirical estimate (Eq.(6.11)) of the time scaling for the new scheme (blue dotted line). Over long distances ($L \geq 320km$), the polynomial scaling of the new scheme is more favorable than the super-polynomial scaling of the DLCZ protocol. The inset: we plot the fidelities of the intermediate distances ($L_{int} = 160, 320, 640$ and $1280km$), to create polarization entangled states ($L = 1280$, $F = 90\%$), with the optimized choice of the control parameters $(L_0, p_c) = (80, 0.0027)$ and $(40, 0.0081)$ for the DLCZ ($t_{avg} \approx 1900s$) and the new scheme ($t_{avg} \approx 380s$), respectively. The optimized choices of the control paramters are detailed in Table 6.4 and 6.5.

to standard entanglement swapping [12, 51], where

$$\left|\Phi^{\pm}\right\rangle_{a_L b_C} \otimes \left|\Phi^{\pm}\right\rangle_{a_C b_R} \rightarrow \left|\Phi^{+}\right\rangle_{a_L b_R}$$

leads to an entangled pair between L and R with probability 1/2, as detailed below.

The procedure for ENC is illustrated in Fig. 6.1(b). First, the spin waves stored in qubit b_C and a_C are retrieved into photons. At the lowest level of ENC, the polarization of the photons is rotated 45°. The rotations transforms $|HV\rangle_{a_C(\text{or } b_C)}$ into $(|HH\rangle - |VV\rangle)_{a_C(\text{or } b_C)}$, because for bosonic fields [143]

$$S_H^\dagger S_V^\dagger \xrightarrow{45^\circ} \left(S_H^\dagger + S_V^\dagger\right)\left(S_H^\dagger - S_V^\dagger\right) = \left(S_H^\dagger S_H^\dagger - S_V^\dagger S_V^\dagger\right) .$$

Thus, after the polarizing beam splitter (PBS) there will be at least two photons at one output. For incoming state $\left|\Psi^{ENG}\right\rangle_{a_L b_C} \otimes \left|\Psi^{ENG}\right\rangle_{a_C b_R}$, all seven terms containing two excitations in at least one pair of cells in the center repeater node (such as $|HV\rangle_{a_C(\text{or } b_C)}$) do not contribute to the click patterns with one photon at each output. Five terms containing two excitations in one of the left or right repeater nodes (e.g., $|HV\rangle_{a_L(\text{or } b_R)}$) have at most one excitation retrieved from b_C and a_C, which is insufficient to give two clicks. Therefore, only the four terms remaining can give the correct photon detector click patterns.

For all levels of ENC, the photons are then joined on the middle PBS and the number of photons at two outputs are counted in the $\{|+\rangle, |-\rangle\}$ basis. With probability 50%, there is one photon at each output, and the connection is successful; otherwise the process is repeated. If the two photons have orthogonal polarizations, a bit flip $\alpha|H\rangle + \beta|V\rangle \rightarrow \alpha|V\rangle + \beta|H\rangle$ is applied to a_L [1]. At higher levels of ENC,

[1]The bit and phase flips called for in ENC and ENP can be performed using linear optics the

Operation	**Transform of** $\left\|\Phi^{\pm}\right\rangle_{a_L b_C}\left\|\Phi^{\pm}\right\rangle_{a_C b_R}$
Retrieve b_C, a_C	$\left\|0000\right\rangle \pm \left\| 0011\right\rangle \pm \left\| 1100\right\rangle + \left\|1111\right\rangle$
Transform b_C, a_C at PBS	$\left\|0000\right\rangle + \left\|1111\right\rangle$ $\pm \left\|0\right\rangle_{a_L}\left(\left\|HV\right\rangle_{a_C}\right)\left\|1\right\rangle_{b_R}$ $\pm \left\|1\right\rangle_{a_L}\left(\left\|HV\right\rangle_{b_C}\right)\left\|0\right\rangle_{b_R}$
One photon per mode ($p = 0.5$)	$\left\|0000\right\rangle + \left\|1111\right\rangle$
Detect in $\pm$, results m, m'	$\left\|00\right\rangle_{a_L b_R} + mm'\left\|11\right\rangle_{a_L b_R}$
Phase shift mm'	$\left\|\Phi^{+}\right\rangle_{a_L b_R}$

Table 6.1: Entanglement connection procedure applied to $|\Phi^{\pm}\rangle$ inputs for entangled pairs between a_L and b_C, and a_C and b_R. For clarity, we introduce $|0\rangle \equiv |H\rangle$ and $|1\rangle \equiv |V\rangle$ to represent logical states (i.e. states with exactly one excitation), $|HV\rangle$ for non-logical states with two excitations, and $|\text{vac}\rangle$ for states with no excitation (sometimes omitted). We assume H photons pass through and V photons be reflected at the middle PBS.

where the 45° rotations are not necessary, the bit flip is replaced by the phase flip $\alpha\,|H\rangle + \beta\,|V\rangle \rightarrow \alpha\,|H\rangle - \beta\,|V\rangle$, as detailed in Table 6.1 [2].

The third component is ENP (Fig. 6.1(c)) which obtains a high fidelity entangled pair from two pairs. Our procedure uses polarization entangled photons and is similar to recent experimental investigations [160]. During entanglement purification of bit errors (bit-ENP), the qubits from two parallel pairs ρ_{a_1,b_1} and ρ_{a_2,b_2} are retrieved from the quantum memory and joined at PBSs. The photons for two upper outputs are stored into quantum memory a_3 and b_3. The photons for the lower outputs a_4 and b_4

next time the qubits are retrieved from the quantum memory.

[2]ENC can be summarized as $\Theta_{\text{ENC}}^{m,m'}\left|xy\right\rangle_{bc} \rightarrow (x \oplus y \oplus 1)\,(mm')$ where mm' represents the parity of two detected photons and the logical states are $|0\rangle = |H\rangle$ and $|1\rangle = |V\rangle$.

Operation	**Transform of** $\left\|\Phi^n\right\rangle_{a_1b_1}\left\|\Psi^{n'}\right\rangle_{a_2b_2}$
Retrieve a_1b_1, a_2b_2	$\left\|0001\right\rangle + n\left\|1101\right\rangle + n'\left\|0010\right\rangle + nn'\left\|1110\right\rangle$
Interfere a_1, a_2 on PBS; same with b_1, b_2	$\left\|00\right\rangle_{a_3a_4}\left(\left\|HV\right\rangle_{b_4}\right) + n\left(\left\|HV\right\rangle_{a_3}\right)\left\|11\right\rangle_{b_3b_4} + n'\left(\left\|HV\right\rangle_{a_4}\right)\left\|00\right\rangle_{b_3b_4} + nn'\left\|11\right\rangle_{a_3a_4}\left(\left\|HV\right\rangle_{b_3}\right)$
One photon per lower output	**0**

Table 6.2: Bit entanglement purification acting on $\left|\Phi^+\right\rangle\left|\Psi^+\right\rangle$. The same notation as Table 6.1 is used. For such given input states, the click pattern never matches the right pattern, and bit-error of single input qubit can be filtered completely. The remaining steps to preserve the desired Bell states are detection of a_4, b_4 in $\pm$ basis, a phase shift $n \cdot n'$ based on the measurement results, and storing of the traveling photons (a_3, b_3) into atomic ensembles.

are counted in $\{\left|+\right\rangle, \left|-\right\rangle\}$ basis. With probability 50%, there is exactly one photon at each lower output, and the purification is successful; otherwise two new pairs are created by restarting the process. If the two photons have orthogonal polarizations, a phase flip is applied to a_3. An example of purification of bit-error is presented in Table 6.2. During purification of phase errors (phase-ENP), additional 45° rotations are applied to the retrieved qubits and the bit flip is replaced by the phase flip. The addition of 45° rotations effects the basis transform $\left|\Phi^-\right\rangle \leftrightarrow \left|\Psi^+\right\rangle$, leading to purification of errors of the other type. The truth table of phase-ENP is listed in Table 6.3. Bit (or phase) errors can be non-linearly suppressed to the second order during bit-ENP (or phase-ENP) [3].

[3]ENP can be summarized as $\Theta_{ENP}^{m,m'}\left|x\right\rangle_{a_1}\left|y\right\rangle_{b_1}\left|u\right\rangle_{a_2}\left|v\right\rangle_{b_2} \rightarrow (x \oplus u \oplus 1)(y \oplus v \oplus 1)(-1)^{x\cdot\left(mm'+1\right)}\left|x\right\rangle_{a_4}\left|y\right\rangle_{b_4}$ with binary basis $\{\left|0\right\rangle, \left|1\right\rangle\}$ for $\{\left|H\right\rangle, \left|V\right\rangle\}$ during

$\rho_{a_1,b_1} \setminus \rho_{a_2,b_2}$	Φ^+	Φ^-	Ψ^+	Ψ^-
Φ^+	Φ^+	–	Ψ^+	–
Φ^-	–	Φ^-	–	Ψ^-
Ψ^+	Ψ^+	–	Φ^+	–
Ψ^-	–	Ψ^-	–	Φ^-

Table 6.3: Truth table for phase-ENP. Each element give the possible output state after the purification operation. ("–" for cases with no outputs.)

The three components described above for quantum repeater protocol only use atomic cells, linear optics, and photon number counting. We remark that the duration of the retrieved anti-Stokes pulse can be made long ($\gtrsim 1\mu s$) compared to the detector recovery time by adjusting the intensity and duration of the retrieval pulse. This enables photon number counting of the anti-Stokes pulse [66].

6.3 Noise and Imperfections

6.3.1 Non-logical errors

We now examine the performance of our new scheme by considering the role of errors, starting with how imperfections due to inefficiency limit the protocols. Primarily, we find that inefficiency takes logical states into two types of non-logical states – those with too few excitations (*vacuum* type) and those with too many excitations (*multi-excitation* type). We represent these errors by density matrix π_{vac} (a mixed state with at most one excitation between both pairs of cells) or π_{multi} (a mixed state with at least one pair of cells with more than one excitation). The

bit-ENP and $\{|+\rangle, |-\rangle\}$ during phase-ENP, and mm' represents the parity of two detected photons.

normalized density matrix after mth ENC (Fig. 6.1(b)) can be written as

$$\rho_{a_L,b_R}^{(m)} = p_{logic}^{(m)}\rho_{logic}^{(m)} + p_{vac}^{(m)}\pi_{vac}^{(m)} + p_{multi}^{(m)}\pi_{multi}^{(m)} \tag{6.5}$$

where the m-dependent operator $\rho_{logic}^{(m)}$ is the density matrix within logical subspace; $\pi_{vac}^{(m)}$ and $\pi_{multi}^{(m)}$ also depend on m; and the coefficients $p_{logic}^{(m)}$, $p_{vac}^{(m)}$ and $p_{multi}^{(m)}$ are the probabilities for the logical, vacuum and multi-excitation types, respectively.

After the first level of ENC, $p_{vac}^{(1)} \sim 1-\eta$ and $p_{multi}^{(1)} \sim p_c \ll 1$. We can demonstrate that these three probabilities remain stable (see Appendix B) for all higher levels of ENC, by considering the un-normalized state after $(m+1)$th ENC for the new approach: $\tilde{\rho}_{a,b}^{(m+1)} = \tilde{p}_{logic}^{(m+1)}\rho_{logic}^{(m+1)} + \tilde{p}_{vac}^{(m+1)}\pi_{vac}^{(m+1)} + \tilde{p}_{multi}^{(m+1)}\pi_{multi}^{(m+1)}$, with

$$\begin{aligned}
\tilde{p}_{logic}^{(m+1)} &\approx \frac{1}{2}\eta p_{logic}^{(m)} p_{logic}^{(m)} \left(1 + p_{err,new}^{(m+1)} + O\left(p_c\right)\right) \\
\tilde{p}_{vac}^{(m+1)} &\approx \frac{1}{2}\eta p_{logic}^{(m)} p_{vac}^{(m)} \left(1 + O\left(p_c\right)\right) \\
\tilde{p}_{multi}^{(m+1)} &\approx \frac{1}{2}\eta p_{logic}^{(m)} p_{multi}^{(m)} \left(1 + O\left(p_c\right)\right)
\end{aligned}$$

where the probability for the new logical error from the multi-excitation states (accompanied by photon loss) is

$$p_{err,new}^{(m+1)} \sim \left(1-\eta\right) p_c.$$

The total logical error probability $p_{err}^{(m+1)}$ has two contributions: the accumulated logical errors from both input pairs for ENC, $p_{err}^{(m)}$, and the new logical error

$$p_{err}^{(m+1)} - 2p_{err}^{(m)} \sim \left(1-\eta\right) p_c. \tag{6.6}$$

We can calculate for the new scheme,

$$p_{err}^{(m)} \sim \left(2^m - 1\right)\left(1-\eta\right) p_c. \tag{6.7}$$

A more detailed calculation (see Appendix B) , in which π_{vac} and π_{multi} are further divided into subspaces with different number of excitations (e.g. π_{vac} is subdivided into zero-excitation and one-excitation subspaces), verifies the stability of the probability distribution of $p_{logic}^{(m)}$, $p_{vac}^{(m)}$ and $p_{multi}^{(m)}$. (Similarly, dark count can also induce errors in logical subspace with probability $\sim p_{dark}\,(1-\eta_s)$, which is however negligible due to very low dark count probability p_{dark}.)

For the DLCZ protocol, only two cells are used to store entanglement. Besides the logical states (single excitation in two cells), we can similarly define the vacuum states (with no excitation) and multi-excitation states (with two or more excitations). Contrary to our approach, the probability distribution is not stable – both vacuum and multi-excitation probabilities increases with distance (see Appendix A). The vacuum probability soon becomes the dominant term, which reduces the success probability of ENC significantly, resulting in super-polynomial (but still sub-exponential) time scaling (Fig. 6.2). The logical error probability for the DLCZ protocol has the same form as Eq.(6.6) up to the coefficient, but the ratio $p_{multi}^{(m)}/p_{logic}^{(m)}$ (thus $p_{err}^{(m)}$) grows with distance (see Appendix A), which accounts for the sharp decrease of fidelity for the DLCZ protocol (see inset of Fig. 6.2). To maintain good final fidelity, the initial error $p_{multi}^{(1)}$ (and p_c) should be very small, which demands longer generation time of an elementary pair for the DLCZ protocol.

In essence, by requiring at least one excitation in the ensemble, our qubit subspace is automatically purified of vacuum and multi-excitation type errors during ENC. The closest analog to the DLCZ protocol is our new scheme without ENP, i.e., only ENC. At longer distances, our approach is further improved in comparison to the DLCZ

protocol due to the reduced amplitude of vacuum terms.

6.3.2 Logical errors

So far, we have only considered the effects of inefficiency that maps states between logical and non-logical subspace by changing the number of excitations. Besides inefficiency, there are other imperfections, which preserve the number of excitations but induce errors within the logical subspace, such as interferometric pathlength fluctuation and linear optical misalignment. For example, the interferometric pathlength fluctuation leads to a phase difference δ, which changes $\left|\Psi^{ENG}\right\rangle_{a,b}$ into a mixture:

$$\begin{aligned}\left|\Psi^{ENG}\right\rangle_{a,b} \rightarrow e^{i\phi}\left(\left|H\right\rangle_a\left|V\right\rangle_b + e^{i\delta}\left|V\right\rangle_a\left|H\right\rangle_b\right) \\ + \left|HV\right\rangle_a\left|\text{vac}\right\rangle_b + e^{2i\phi+i\delta}\left|\text{vac}\right\rangle_a\left|HV\right\rangle_b \ .\end{aligned} \tag{6.8}$$

where ϕ is static phase difference between left and right channels. Since the last two terms with $|HV\rangle$ will be removed during the first level of ENC, the static phase ϕ has no effect. However, the probability of being in an undesired logical state $|\Psi^-\rangle$ is $\sin^2\frac{\delta}{2}$. The first level of ENC with the combined two inputs of Ψ^- and Ψ^+ gives Φ^-, producing a phase error with probability $2p_{phase-err} = 2\left\langle\sin^2\frac{\delta}{2}\right\rangle$, proportional to the variance of the interferometric phase fluctuation. This error will be amplified during subsequent ENC's, because the survival probability of the state Φ^- (the logical error) is twice as much as that of Φ^+ (the desired component).

We expect that there is little correlation in phase fluctuation between different sections of the fiber, and the variance of the phase fluctuation is proportional to the length of the fiber

$$\left\langle\delta^2\right\rangle = 2DL_0, \tag{6.9}$$

where D is the phase diffusion coefficient of the fiber. If the phase fluctuation satisfies gaussian distribution, the phase error probability

$$p_{phase-err} = \left\langle \sin^2 \frac{\delta}{2} \right\rangle = \frac{1}{2}\left(1 - e^{-DL_0}\right). \tag{6.10}$$

For example, $D = 10^{-3} rad^2/km$, $L_0 = 10km$, and $p_{phase-err} \approx 0.5\%$.

Also, a small probability (p_{err}) of linear optical misalignment per ENC or ENP step is modeled as depolarizing errors. Later, we will demonstrate that errors within the logical subspace restrict the final fidelity of the DLCZ protocol, while for our new approach additional active purification can correct such logical errors to achieve high fidelity.

6.4 Scaling and Time Overhead for Quantum Repeater

6.4.1 Scaling analysis

Based on the calculation of the success probability at each level of connection/purification, we can obtain the estimated average time for various schemes. In Fig. 6.2, we compare our approach to the DLCZ protocol. For the DLCZ protocol, the average creation time for a distant pair contains a super-polynomial contribution (but still sub-exponentially) with distance, due to instability of the vacuum component. For our new scheme, the scaling is strictly polynomial with distance, $t_{avg} \propto L^{\alpha}$, where the exponent $\alpha = \alpha(\eta)$ explicitly depends on the efficiency.

We remark that the DLCZ protocol is slightly more efficient for short final dis-

tances ($L \leq 160km$). The DLCZ protocol can skip the entanglement connection and exploits post-selection to create the polarization entangled state, while the new scheme requires the first level of ENC to eliminate those unwanted components and prepare the polarization entangled state. The post-selection has success probability 1/2, two times more efficient than the success probability 1/4 for the first level of ENC of the new scheme.

For the new scheme (without ENP), we can use the stable probability distribution to estimate the average time:

$$t_{avg} = t_0 \left(L/L_0\right)^{\log_2\left(1.5\ \frac{2(2-\eta)^4}{\eta^2(3-2\eta)}\right)} \tag{6.11}$$

where $t_0 = \frac{1}{p_c\eta}\frac{L_0}{c}e^{L_0/L_{att}}$ is the elementary pair generation time, p_C is the elementary pair generation probability, L_0 is half the distance between neighboring repeater stations, and L is the final distance. The exponent can be understood as an overhead from the finite success probability for ENC, $p_{ENC} \approx \frac{\eta^2(3-2\eta)}{2(2-\eta)^4}$. The constant 1.5 in Eq.(6.11) is the empirical estimate of the overhead from the waiting time to obtain two independent pairs versus the single pair. In Fig. 6.2, the differences between the simulated data and Eq.(6.11) are attributed to the empirical factor (1.5) and an overall factor from the overestimate of the success probability for the first level of ENC. According to Eq.(6.7), one can always reach good final fidelity if the elementary pair generation probability p_c scales as L_0/L. Therefore, the average distant pair generation time scales *exactly polynomially* with distance $t_{avg} \propto L^{\alpha}$, with $\alpha = 1 + \log_2(1.5) + \log_2\left(\frac{2(2-\eta)^4}{\eta^2(3-2\eta)}\right)$.

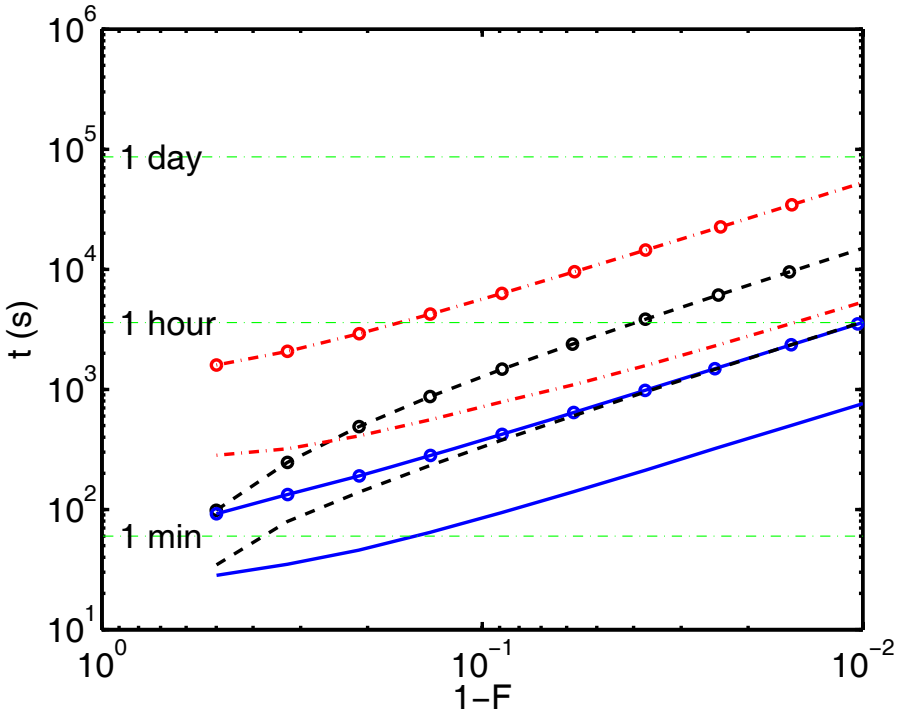

Figure 6.3: Average time versus final fidelity with no phase errors. For fixed final distance $L = 1280$, we plot the (final) fidelity dependence of the (optimized) average pair creation time, for the DLCZ protocol (black dashed lines), new scheme without ENP (blue solid lines), and new scheme with ENP (red dashdotted lines), with efficiency η to be 90% (circles), and 95% (no circles).

6.4.2 Comparison between different schemes

Besides the DLCZ protocol and our new approach without ENP, we now consider a scheme with ENP, which has one phase-ENP after the second level of ENC. We may compare these schemes by using $t - F$ plots – a parametric plot of t_{avg} and F as a function of excitation probability p_c. For given noise model and efficiency η, a repeater scheme corresponds to a curve on $t - F$ plane.

In the absence of interferometric pathlength fluctuation (Fig. 6.3), the new approach without ENP is about 5 times faster than the DLCZ protocol, for $\eta = 90\%$. As given by the previous discussion, this improvement is due to better control of inefficiency-induced imperfections. There is a time overhead for the new approach (with ENP) as compared to the new approach (without ENP). Within each implementation, the higher the efficiency η, the faster the quantum repeater. For high final fidelity ($1 - F \leq 10\%$), the curves approach straight lines with slope -1, because $t \propto p_c^{-1} \propto (1 - F)^{-1}$.

When interferometric pathlength fluctuation (leading to initial phase error) is non-negligible, active ENP is needed. We use a diffusion model for the pathlength fluctuation, as detailed in Sec. 6.3.2. In Fig. 6.4, $t - F$ curves are plotted, assuming the phase diffusion coefficient $D = 10^{-3} rad^2/km$, corresponding to $p_{phase-err} \approx 0.5\%$ over $L_0 = 10km$. Unlike Fig. 6.3 where only inefficiency is considered, there is an upper bound in final fidelity for each implementation. Both the DLCZ protocol and new approach (without ENP) suffer from the initial phase error, with final fidelity no more than 65%, while new approach with ENP maintains high final fidelity up to 97%. For high retrieval and detection efficiency ($\eta = 95\%$), new approach (with ENP)

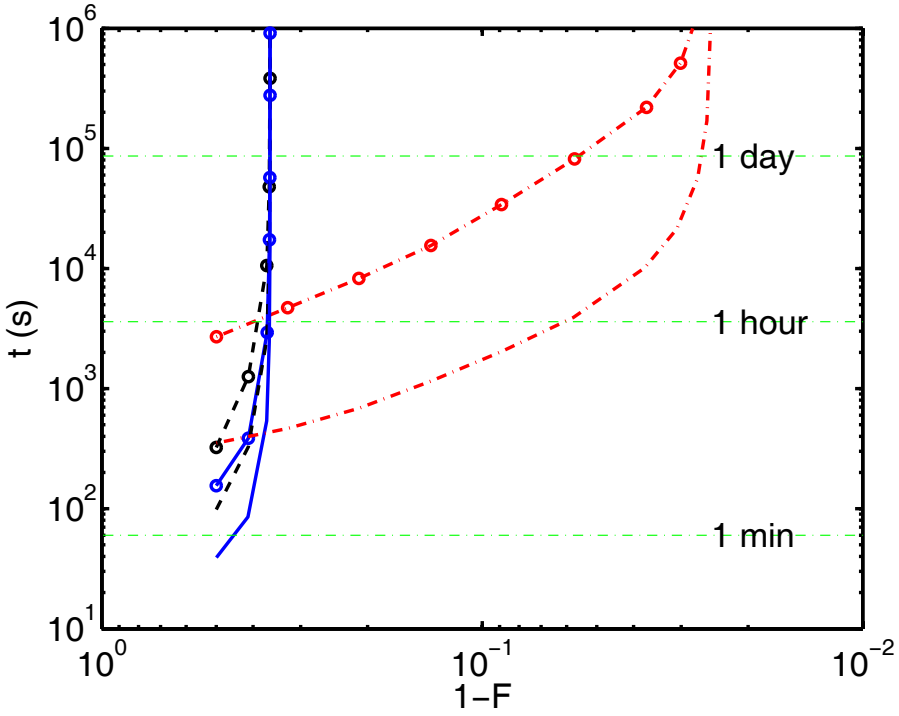

Figure 6.4: Average time versus final fidelity with phase errors. This shows the same optimized approaches as Fig. 6.3 but with finite interferometric pathlength fluctuation characterized by the phase diffusion coefficient $D = 10^{-3} rad^2/km$. Inclusion of ENP (red dashdotted lines) yields a dramatic improvement in time for high fidelity operations.

can produce $1280km$ entangled pairs with fidelity 90% at a rate of 2 pairs/hour, even in the presence of substantial dynamical phase errors.

6.5 Conclusion

In summary, our new approach to long distance quantum communication uses a different qubit basis which prevents the growth of vacuum and multi-excitation probabilities. This keeps the ENC success probability high and error probability low, and leads to true polynomial scaling even in the presence of realistic inefficiencies. We

can achieve a bandwidth of 1 (or 2) entangled pair(s) per six minutes for $F \approx 90\%$ (or 78%) and negligible initial phase error. The new approach also allows active entanglement purification, which combined with built-in purification of transmission loss errors allows purification of arbitrary errors in quantum communication.

Although the present approach shows a dramatic improvement in communication rates and robustness compared to original the DLCZ protocol, the bandwidth remains relatively slow, even when very high efficiencies and very long-lived quantum memory are assumed. While such high efficiencies might ultimately be achievable (see Ref. [188] for recent progress), other approaches need to be considered that can further improve the effective communication bandwidth. For example, we can use many cells per node to improve the bandwidth. In this case, the improvement is at least linear with the number of cells, making it possible to realize long distance ($1280km$) entangled state generation bandwidth of the order of one pair per second.

A simple Monte Carlo optimization of efficient use of the cells shows that we can increase the bandwidth by a factor of $r = M^{1.12}$, where M is the increment of factor of physical resources. Recently, it has also been suggested that multiple cells can be used to further facilitate the quantum repeater, in the presence of memory errors from the quantum memory [47].

$L\,(km)$	20	40	80	160	320	640	1280	2560	5120	10240
$t_{avg}\,(s)$	0.0013	0.0065	0.046	0.44	5.8	95	1900	6×10^{4}	3×10^{6}	3×10^{8}
$L_0\,(km)$	10	20	40	40	40	80	80	80	80	80
p_c	0.26	0.18	0.13	0.040	0.011	0.010	0.0027	7×10^{-4}	2×10^{-4}	5×10^{-5}
F_{fin}	90%	90%	90%	90%	90%	90%	90%	90%	90%	90%

Table 6.4: This table provides detail information for Fig. 6.2. With efficiency $\eta = 90\%$, targeting fidelity $F = 90\%$ and fiber attenuation length $L_{att} = 20km$, the immunized average time t_{avg} and optimized control parameters (L_0, p_c) are listed with respective to various final distances for the DLCZ protocol.

$L\,(km)$	20	40	80	160	320	640	1280	2560	5120	10240
$t_{avg}\,(s)$	0.0051	0.020	0.10	0.68	5.4	45	380	3×10^{3}	3×10^{4}	3×10^{5}
$L_0\,(km)$	5	10	20	40	40	40	40	40	40	40
p_c	0.26	0.17	0.11	0.087	0.037	0.017	0.0081	4×10^{-3}	2×10^{-3}	1×10^{-3}
F_{fin}	90%	90%	90%	90%	90%	90%	90%	90%	90%	90%

Table 6.5: This table provides detail information for Fig. 6.2. With efficiency $\eta = 90\%$, targeting fidelity $F = 90\%$ and fiber attenuation length $L_{att} = 20km$, the minimized average time t_{avg} and optimized control parameters (L_0, p_c) are listed with respective to various final distances for the new scheme.

Chapter 7

Optimal approach to quantum communication using dynamic programming

7.1 Introduction

Sequential decision making in probabilistic systems is a widely studied subject in the field of economics, management science and engineering. Applications range from problems in scheduling and asset management, to control and estimation of dynamical systems [15]. In this paper we make the first use of these techniques for solving a class of decision making problems that arise in quantum information science [154, 21]. Specifically we consider the optimal design of a so-called quantum repeater for quantum communication. Such repeaters have potential application in quantum communication protocols for cryptography [13, 10, 209] and information

processing [82], where entangled quantum systems located at distant locations are used as a fundamental resource. In principle this entanglement can be generated by sending a pair of entangled photons through optical fibers. However, in the presence of attenuation, the success probability for preparing a distant entangled pair decreases exponentially with distance [79].

Quantum repeaters can reduce such exponential scaling to polynomial scaling with distance, and thus provide an avenue to long distance quantum communication even with fiber attenuation. The underlying idea of quantum repeater [26, 61] is to *generate* a backbone of entangled pairs over much shorter distances, store them in a set of distributed nodes, and perform a sequence of quantum operations which only succeed with finite probability. *Purification* operations [11, 51] improve the fidelity of the entanglement in the backbone, while *connection* operations join two shorter distance entangled pairs of the backbone to form a single, longer distance entangled pair. By relying on a quantum memory at each node to let different sections of the repeater re-attempt failed operations independently, a high fidelity entangled state between two remote quantum systems can be produced in polynomial time. A quantum repeater *protocol* is a set of rules that determine the choice and ordering of operations based upon previous results. An optimal protocol is one that produces entangled pairs of a desired fidelity in minimum time within the physical constraints of a chosen implementation.

The complexity of finding the optimal repeater protocols can be understood via the following analogous example problem [15]: given a sequence of rectangular matrices $M_1 M_2 \dots M_n$, such that M_k is $d_k \times d_{k+1}$ dimensional, find the optimal or-

der of multiplying the matrices such that the number of scalar multiplications is minimized. This is a typical example of a nesting problem, in which the order in which operations are carried out effects the efficiency. For example, if $M_1 = 1 \times 10$, $M_2 = 10 \times 1$ and $M_3 = 1 \times 10$, then $(M_1 M_2)M_3$ takes only 20 scalar operations, while $M_1(M_2 M_3)$, requires 200 scalar multiplications. A brute force enumeration of all possible nesting strategies and evaluation of their performance is exponential in n. To solve this problem more efficiently, we observe that the optimal nesting strategy $(M_1 \dots (\dots) \dots M_p)(M_{p+1} \dots M_n)$ should carry out the solution to its subparts optimally, i.e., the nesting $(M_1 \dots (\dots) \dots M_p)$ should represent the best nesting strategy for multiplying $M_1 M_2 \dots M_p$. This is the well-known dynamic programming strategy [15], in which one seeks to optimize a problem by comparing different, already optimized sub-parts of the problem. Dynamic programming enables us to find the optimal solution to the original problem in time that is polynomial in n.

Quantum repeaters also have a nested (self-similar) structure, in which shorter distance entanglement is used to create longer distance entanglement, which is then used in turn for further extending the distance between entangled pairs. This structure allows us to use the methods of dynamic programming to find optimal nesting strategies for designing quantum repeater protocols.

We now proceed to detail the specific optimization problem, then discuss our dynamic programming solution to the problem. We next examine two representative schemes that we wish to optimize [the Briegel-Dur-Cirac-Zoller scheme (BDCZ scheme), Refs. [26, 61], and the Childress-Taylor-Sorensen-Lukin scheme (CTSL scheme), Refs. [38, 39]], and find significant improvements in both preparation time and final

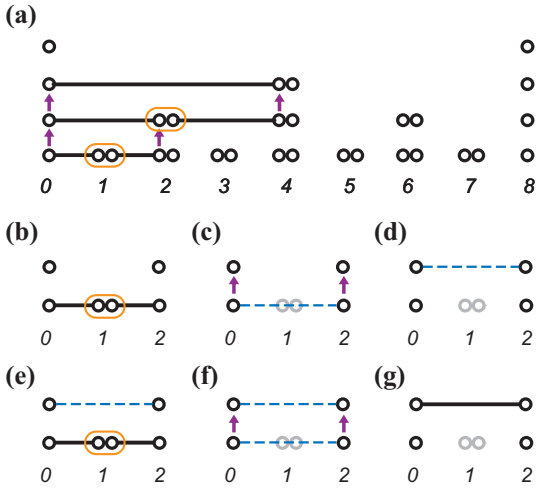

Figure 7.1: Quantum repeater scheme from Refs. [26, 61] (BDCZ scheme). **(a)** In a typical realization with $N + 1 = 9$ nodes, the number of qubits per nodes is bounded by $2 \log_2 2N = 8$. **(b)-(d)** Two entangled pairs with distance 1 are connected (orange rounded rectangle) at node #1 to produce an entangled state with distance 2, which is stored (purple arrows) in the qubits at higher level. **(e)-(g)** Another entangled state with distance 2 is produced to purify (purple arrows) the entangled state stored in qubits at higher level. Similarly, entangled states with distance 2^n can be connected to produce entangled state with distance 2^{n+1}, which may be further purified, as indicated in **(a)**.

fidelity of long distance entangled pairs.

7.2 Dynamic Programming Approach

7.2.1 General quantum repeater protocol

Quantum repeater protocols have a *self-similar structure*, where the underlying operations at each stage of the repeater have the same basic algorithms. In other words, the structure of the problem remains the same at each stage, while the parameters can be different. A generic quantum repeater consists of three kinds of

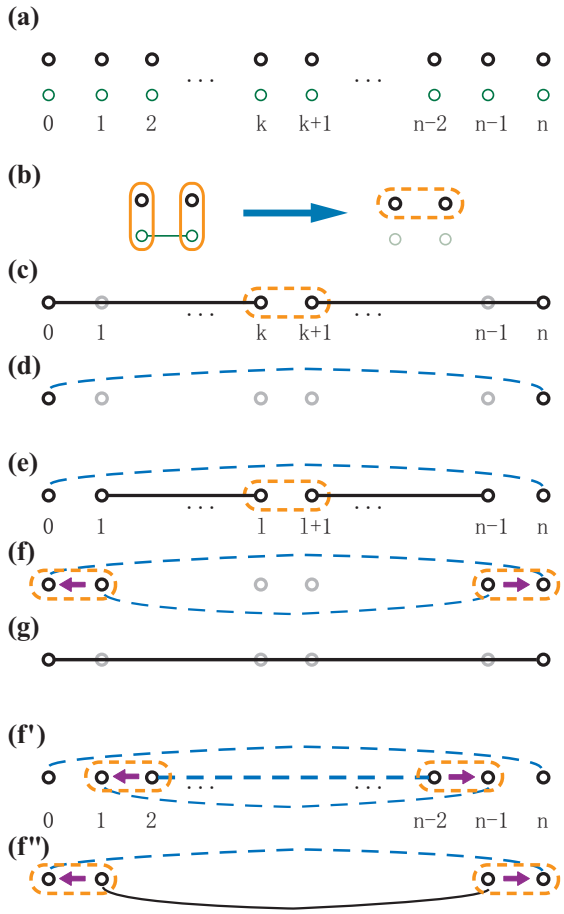

Figure 7.2: Quantum repeater scheme from Refs. [38, 39] (CTSL scheme). **(a)** This scheme has exactly two qubits per node. The communication qubits (green nodes) are used for entanglement generation and short-term storage; the storage qubits (black nodes) are used for long-term storage. **(b)** With the help of local gates (orange solid rounded rectangles) between communication and storage qubits, the entangled state between communication qubits can be used to implement entangling gates (e.g. the Controlled NOT gate) between storage qubits from neighboring nodes. The effective remote gate is highlighted by the orange dashed rounded rectangle. Such remote gate is sufficient for entanglement connection and purification of storage qubits. The communication qubits are omitted in the following plots. **(c)-(d)** Entanglement connection to produce an unpurified entangled state with distance n. **(e)-(g)** Entanglement connection to produce an unpurified entangled state with distance $n-2$ to purify the entangled state with distance n. **(f')(f")** Illustration of multi-level pumping. An entangled state with distance $n-4$ is used to purify an entangled state with distance $n-2$, and the (purified) latter is used to purify an entangled state with distance n. The only difference between (f) and (f") is the fidelity of the entangled state with distance $n-2$. The latter has higher fidelity.

operations: entanglement generation, entanglement connection, and entanglement purification. Entangled pairs are first generated and stored over a short distance L_0. At the first nesting level, two entangled pairs of distance L_0 can be extended to distance $L_1 \sim 2L_0$ via entanglement connection [209]. Due to limited fidelity of the short pairs and the imperfections from the connection operations, the fidelity of the longer pair produced by connection is generally lower than those of the shorter ones. Nevertheless, the fidelity of the longer pair can be improved via entanglement purification, which is able to extract high-fidelity entangled pairs from an ensemble of low-fidelity ones using operations that are local (restricted to qubits within a given node) [11, 51]. An efficient approach of entanglement purification is entanglement pumping [26, 61], which purifies one and the same pair by using low-fidelity pairs with constant fidelity [1]. Thus, at the $(k+1)$th nesting level, the three underlying operations (preparation at distance L_k, connection, and purification) lead to preparation at a distance $L_{k+1} \sim 2L_k$ [2].

7.2.2 Inductive optimization

We now define the optimization problem:

Def: For given physical resources, desired distance L_{final}, and final fidelity F_{final}, an *optimal protocol* minimizes the expected time to have an entangled pair of

[1] In principle, there exist repeater schemes (see [61] and references therein) that work much faster. For those schemes, however, the number of memory qubits per repeater station scales at least linearly with the final distance, which make them impractical.

[2] Since we must wait for entanglement generation and purification to succeed before proceeding to the next nesting level, the overall time for successful pair generation is generally much longer than that of classical communication over the given distance.

fidelity $F \geq F_{\text{final}}$ at a distance $L \geq L_{\text{final}}$.

To solve this optimization problem, the choice of parameters for the quantum operation cannot be viewed in isolation—one has to trade off the desire of low present cost (in terms of time) with the undesirability of high future costs. If one tries to enumerate and test all possible adjustable parameters, the complexity to search for the optimized implementation scales at least exponentially with the number of repeater nodes. A simple example is provided if we make our only adjustable parameter choosing between zero and one purification step at each stage of the protocol. For the BDCZ scheme with $128+1$ repeater nodes, there are already $2^{128} \gtrsim 10^{38}$ possibilities, which is beyond the capability of current computers. Thus a systematic searching method is needed to find the optimized implementation out of such a huge parameter space.

Based on the above self-similar structure, we may express the optimized protocol to produce long entangled pairs in terms of a set of optimized protocols for producing shorter pairs. The general searching procedure can be performed inductively, as detailed in Table 7.1. We make a discrete set of target fidelities (see Sec. 7.2.6), $F = \{f_1, f_2, \ldots, f_q\}$, such that only a finite number of different optimal protocols with shorter distances need to be developed. The complexity for each step of our optimization procedure is shown in the table; the full procedure scales as $\mathcal{O}(q^2n^2)$, where the $\mathcal{O}(n)$ repetitions of step 3 take the most time [3]. In practice, we found the full search of step 3 to be unnecessary—the search can be restricted to pairs of distance $n/2 \pm \mathcal{O}(\log(n))$, leading to complexity $\mathcal{O}(q^2 n \log(n))$.

[3]For the CTSL scheme, there will be another $\mathcal{O}(q)$ overhead, associated with $\mathcal{O}(q)$ possible fidelity choices of the entangled state for the Controlled NOT gate (Fig. 7.2b).

1. Find and store implementations that optimize the average time (for all fidelities $f_1, \ldots, f_q$) with $dist = n = 1$, taking $\mathcal{O}(q)$
2. Assume known optimized implementations (for all fidelities) with $dist \leq n$
3. Find optimized implementations to produce unpurified pairs (for all fidelities) with $dist = n + 1$ by trying (connecting) all combinations of known optimized implementations with $dist \leq n$, with complexity of order $\mathcal{O}(q^2 n)$
4. Find optimized implementations to produce purified pairs (for all fidelities) with $dist = n+1$ by trying all combinations of unpurified pairs with $dist = n + 1$, pumping for $m = 0, 1, 2, 3, \cdots$ times; complexity goes as $\mathcal{O}(m_{\max} q^2)$
5. Store the optimized implementations (for all fidelities) with $dist = n + 1$, based on step 4.
6. Replace n by $n + 1$, and go to step 2.

Table 7.1: Inductive search using dynamic programming.

7.2.3 Repeater schemes and physical parameters

So far, we have only taken a general perspective in explaining quantum repeater protocols and describing the procedure of inductive searching using dynamic programming. In this subsection, we specify the parameters to be optimized by examining the schemes of the quantum repeater, physical restrictions on entanglement generation for current techniques, and the error models of local quantum gates. Only with a functional relationship between physically adjustable parameters and repeater operation outputs, can we find the optimized implementations for procedure 1, 3 and 4 in Table 7.1.

There are several different *schemes* for building a quantum repeater that differ primarily in the amount of physical resources utilized. For example, in the BDCZ scheme [26, 61] (Fig. 7.1), the maximum number of qubits in the quantum memory (to

store intermediate states for connection and purification) required for each repeater node increases logarithmically with the total number of repeater nodes. In the CTSL scheme [38, 39] (Fig. 7.2), an efficient way to use quantum memory is proposed, and only *two* qubits are needed for each node, regardless of the total number of repeater nodes. One of the two qubits is called the *communication qubit*, which is optically active and can be used to generate entanglement with other communication qubits from neighboring nodes. The other qubit is called the *storage qubit*, which can be used to store quantum state over very long time. As shown in Fig. 7.2(b), with the help of local gates (orange solid rounded rectangles) between communication and storage qubits, the entangled state between communication qubits can be used to implement teleportation-based gates (e.g., the Controlled NOT gate) between storage qubits from neighboring nodes [82, 103, 104]. Such remote gates (orange dashed rounded rectangle) are sufficient for entanglement connection and purification of the storage qubits; communication qubits are providing the necessary resource mediating the gates between remote storage qubits. For clarity, we will omit the communication qubits in the following discussion, but still keep track of the mediated operation between remote storage qubits.

To model errors in the physical operations, we need to introduce a number of parameters determined by the quantum hardware. For entanglement generation, the relationship between the fidelity of the elementary pair, F_0, and the generation time, τ_e, depends on the physical parameters (such as the signal propagation speed, c, the fiber attenuation length, L_{att}, the efficiency of single photon collection and detection, ε, and the distance of elementary pair, L_0) and the specific approach to generate en-

tanglement. For example, for the entanglement generation approach using scattering as proposed in Refs. [38, 39], $F_0 = F_0(\tau_e) = \frac{1}{2}\left\{1 + \left[1 - \frac{L_0}{\tau_e c} e^{L_0/L_{att}}\right]^{2(1-\varepsilon)/\varepsilon}\right\}$.

For entanglement connection and pumping, the dominant imperfections are errors from measurement and local two-qubit gate, which we model with a depolarizing channel. In particular, the model for measurement is quantified by a reliability parameter [26, 61], η, which is the probability of faithful measurement. For example, a projective measurement of state $|0\rangle$ would be

$$P_0 = \eta |0\rangle \langle 0| + (1-\eta) |1\rangle \langle 1|.$$

Similarly, the model for local two-qubit gate is characterized by a reliability parameter [26, 61], p. With probability p, the correct operation is performed; otherwise the state of these two qubits is replaced by the identity matrix [26, 61]. For example, the action on a two qubit operation U_{ij} would be

$$U_{ij}\rho U_{ij}^{\dagger} \rightarrow pU_{ij}\rho U_{ij}^{\dagger} + \frac{1-p}{4}\mathrm{Tr}_{ij}[\rho] \otimes I_{ij},$$

where $Tr_{ij}[\rho]$ is the partial trace over the subsystem i and j, and I_{ij} is the identity operator for subsystem i and j. Generally, the reliability parameters (η and p) should be reasonably high (i.e., above some thresholds [26, 61]), so that the suppression of error from entanglement pumping dominates the new errors introduced by entanglement connection and entanglement pumping [4].

[4] We neglect the time associated with local operations, which is usually much shorter than the communication time between neighboring repeater stations. Non-negligible gate operation time can be easily included in our optimization.

7.2.4 Optimization parameters

We now list the adjustable parameters we can optimize over during procedures 1, 3 and 4 in Table 7.1.

1. During the entanglement generation, there is freedom to choose the generation time τ_e, which is determined by the success probability and the communication time. Generally, the higher the success probability, the shorter the generation time and the lower the fidelity of the entangled state, so the generation time and the fidelity should be balanced [38, 39].

2. During the entanglement connection, the distances of two shorter pairs can be adjusted, while the total distance is kept unchanged.

3. During entanglement purification, the number of steps is also adjustable, which should balance the gain in fidelity and the overhead in time.

7.2.5 Additional operations

Besides the above operations from the original quantum repeater schemes, there are some *additional* operations that might be useful. For example, we may skip several intermediate repeater nodes (*node-skipping*) to generate entanglement between distant nodes directly with a substantially lower success probability. Also, during entanglement pumping, we might consider *multi-level pumping* [60], which is to nest several levels of entanglement pumping together before the next level of entanglement connection (Fig. 7.2(f")). Multi-level pumping can produce entangled pair with higher fidelity than single-level pumping. Such additional operations can be easily in-

corporated into the search procedures 1, 3, and 4 in Table 7.1. We will show that the dynamic programming approach can use these additional operations appropriately, to reduce the average time, extend the upper bounds for achievable final fidelity, and even improve the threshold for the reliability parameters of p and η.

7.2.6 Shape parameter approximation and average time approximation

We use two important approximations throughout the analysis: the *shape parameter approximation* and *average time approximation*.

In the shape parameter approximation [61, 38, 39], we use two numbers, the fidelity and the shape parameter (F, v) to classify non-ideal entangled states during our inductive optimization procedure. For a pair of entangled qubits, we assume that the density matrix is diagonalized in the Bell basis $\rho = diag\,(F_1, F_2, F_3, F_4)$, with $F_1 \geq F_2 \geq F_3 \geq F_4$ by an appropriate ordering of the Bell basis. The fidelity $F \equiv F_1$ is the probability of finding the pair in the desired Bell state. The shape parameter $v \equiv \frac{1}{2}\frac{F_3+F_4}{(F_2+F_3+F_4)}$ measures, e.g., the relative ratio of bit error to phase error in the generated pair. We may classify various entangled states according to (F, v), and use this classification to facilitate the bookkeeping of different states. For intermediate distances, we only keep track of the minimum time (and the associated density matrix) for each class of states labeled by (F, v), rather than for each possible state. This significantly alleviates the computational storage requirements of dynamic programming. Meanwhile, since we only use a subset of states to optimize longer distance pairs, the obtained protocol might be a little slower (no more than 10%)

than the optimal one.

In our average time approximation, we only keep track of the average time for entanglement generation, connection and pumping, instead of the full distribution function. This underestimates the time for entanglement connection, because the average time to generate both sub-pairs is longer than the maximum of the average individual times for two sub-pairs. Fortunately, our comparison between the average time approach and the Monte Carlo simulations show that the average times from the average-time approximation and from Monte Carlo simulations only differ by a factor of about 2 for both the BDCZ and the CTSL schemes. In Fig. 7.6, the time distributions from Monte Carlo simulation are plotted.

7.3 Results and Discussion

7.3.1 Improvement of BDCZ and CTSL schemes

With procedure as listed in Table 7.1, we implemented a computer program to examine the mean time to prepare entangled pairs and to search according to our dynamic programming prescription through the parameter space outlined above. We looked for optimal protocols for a quantum repeater for all distances ≤ 1280 km and target fidelities ≥ 0.8. Unless otherwise specified, we use $L_{att} = 20km$, $\varepsilon = 0.2$, and $\eta = p = 0.995$ for the rest of the discussion. We first fix $L_0 = 10km$, and we will consider the optimization of L_0 to justify such choice later. To visualize the results, the profile of the optimized time (smooth surface) is plotted in Fig. 7.3(a)(b) with respect to the final distance (from $10km$ to $1280km$) and the fidelity (from 0.90 to

0.99) for both the BDCZ and the CTSL schemes. The calculation optimizes over the elementary pair generation (both distance and generation time), the connecting positions, and the number of pumping steps, with spacing between neighboring repeater nodes of $10km$; both additional operations (node-skipping and multi-level pumping) are also included for the optimization. For comparison, the unoptimized time profiles (meshes) for the BDCZ and the CTSL schemes are also plotted. The unoptimized protocol assumes fixed elementary pair fidelity ($F_0 = 0.96$ and 0.99 for BDCZ and CTSL, respectively), simple connection patterns (detailed in Ref. [26, 61] and [38, 39]), and constant number of pumping steps.

As expected, the unoptimized protocol always takes longer time than the optimized protocol for the same final distance and target fidelity. Time profiles for the unoptimized protocols have *stair-like jumps* in Fig. 7.3(a)(b). For the BDCZ scheme (Fig. 7.3(a)). The jumps occurring with increasing distance (occurring at distances $L/L_0 = 2^p + 1 = 1, 3, 5, 9, 17, 33, \cdots$) are the results of time overhead from the additional level of connection; the jump occurring with at $F_{final} = 0.98$ is due to the sudden change in the number of pumping steps from 1 to 2. Similarly, for the CTSL scheme (Fig. 7.3(b)), the two jumps are due to the change of the number of pumping steps from 1 to 2 and finally to 3. For the optimized protocols, the time increases smoothly with increasing final distance and fidelity.

The improvement factor (i.e., the ratio between the times for unoptimized and optimized protocols) is plotted for both the BDCZ and the CTSL schemes in Fig. 7.3(c)(d). As we might expect, the previously mentioned jumps lead to sharp *stripes* where the improvement factor changes discontinuously. There are several regions where the op-

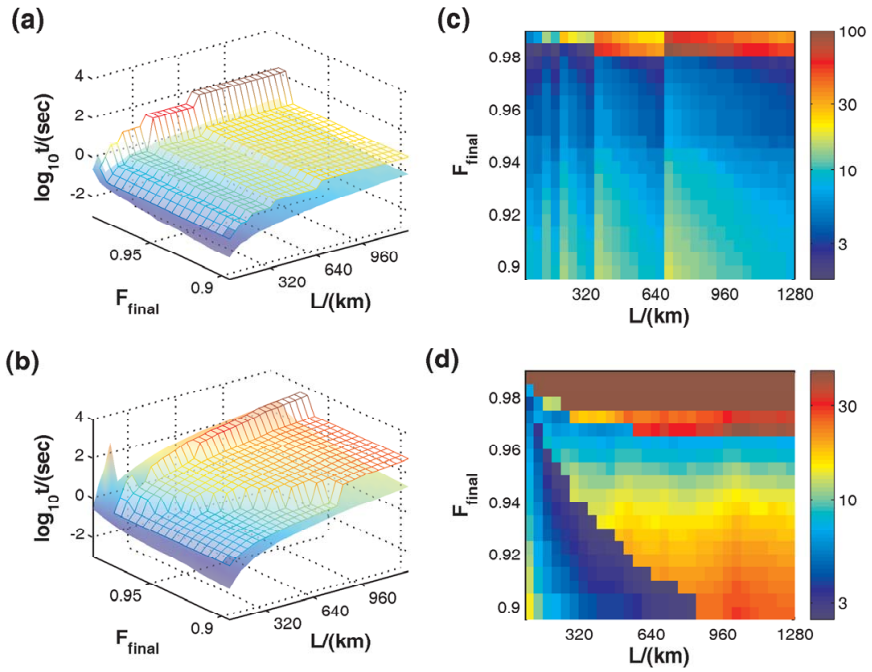

Figure 7.3: Plots of time profiles and improvement factors. Speed-up in time associated with various final distance and fidelity. **(a)** $t\,(F_{final}, L)$ for unoptimized (meshes) and optimized (smooth surface) implementations of the BDCZ scheme; **(b)** for the CTSL scheme. **(c)** Pseudocolor plot of the improvement factor, t_{unopt}/t_{opt}, for the BDCZ scheme; **(d)** for the CTSL scheme, in the region $(F_{final} > 97.5)$, the improvement factor $t_{unopt}/t_{opt} \to \infty$. The default parameters are $L_{att} = 20km$, $\varepsilon = 0.2$, and $p = \eta = 0.995$.

timization gives significant improvement. For example, for the BDCZ scheme, the vertical bright stripes indicate that the optimization provides a time-efficient way to generate entangled pairs for distance $(2^p + \delta_+) L_0$ (with $\delta_+ > 0$), gaining a factor of about 10; the horizontal bright stripes indicate that efficiently arranging the number of pumping steps can also speed up the scheme by a factor of about 30 or even more. For most of the optimized protocols, a distant pair is divided into two shorter pairs with similar distance and fidelity (symmetric partition), but occasional asymmetric partitioning can further reduce the time by about 10%.

For the BDCZ scheme, the correspondence between jumps and stripes essentially accounts for all the features of the improvement plot (Fig. 7.3(c)). For CTSL scheme, however, besides the stripes, there is also a region (with distance $L > 100km$ and fidelity $F \gtrapprox 97.5\%$) where the improvement factor is infinity—optimization not only boosts the speed, but also extends the upper bound of achievable fidelity for distant pairs.

We also study the improvement for other choices of reliability parameters, p and η, especially those values close to the threshold [26, 61]. Suppose the reliability parameters are $p = \eta = 0.990$. In Fig. 7.4(a)(c), we plot the speed-up in time associated with various final distance and fidelity for the BDCZ scheme. For both (optimized and unoptimized) protocols, the highest achievable fidelity is approximately 97.5% (compared to 99% in Fig. 7.3(c)), limited by errors from local operations. The improvement factor ranges between $[1.5, 600]$ (compared to $[1, 100]$ in Fig. 7.3(c)). Apart from these differences, the key features (horizontal and vertical stripes) of improvement from optimization are very similar between Fig. 7.3(c) and Fig. 7.4(c).

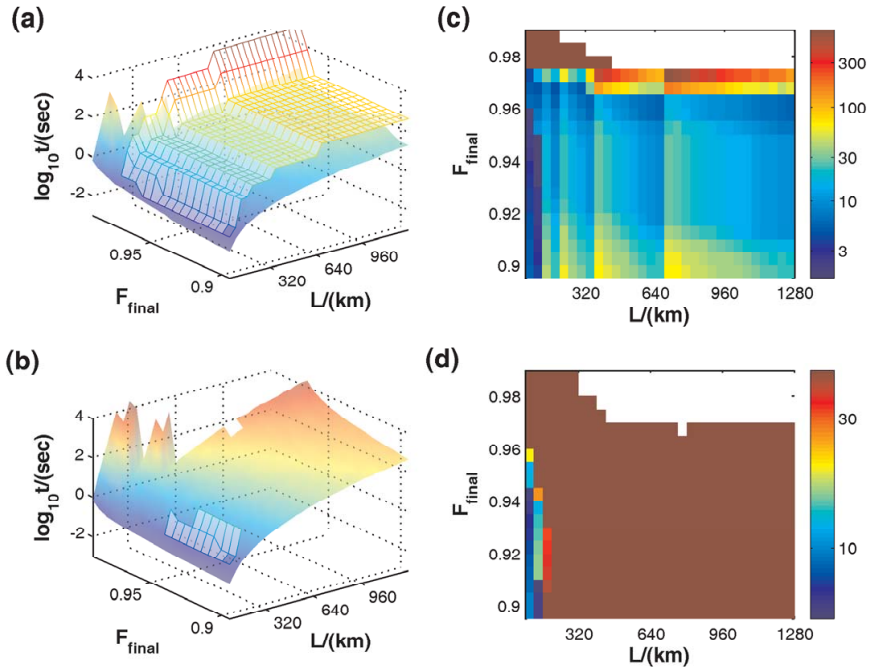

Figure 7.4: Plots of time profiles and improvement factors. The subplots are arranged in the same way as Fig. 7.3. Local operations have lower reliability parameters, $p = \eta = 0.990$. (**a**)(**c**) For the BDCZ scheme, the optimization procedure only improves the speed of the quantum repeater, and does not extend the achievable region in the F-L plot. (**b**)(**d**) For the CTSL scheme, for distances longer than $200km$, the improvement factor, $t_{unopt}/t_{opt} \to \infty$. Here, the reliability parameter ($p = \eta = 0.990$) is *insufficient* to create distant entangled pairs with the unoptimized implementation, but the optimized implementation (with multi-level pumping) is still able to create high-fidelity distant entangled pairs, because multi-level pumping lowers the threshold of the reliability parameters for the CTSL scheme.

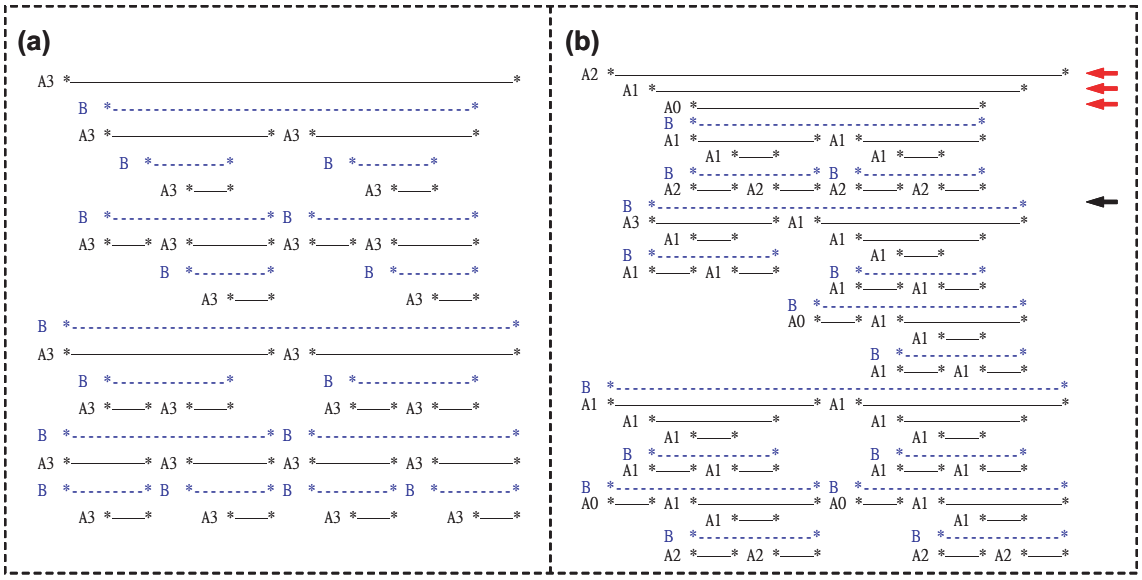

Figure 7.5: Two example implementations with targeting final distance $L = 11L_0$ and fidelity $F_{final} = 0.976$, using the CTSL scheme. Each storage qubit is represented by "*". All the relevant entangled states are shown. The order to produce these entangled states are from bottom to top; states on the same row can be produced simultaneously. There are two kinds of entangled states – purified entangled states (type-A, solid black line) and unpurified entangled states (type-B, dashed blue line). On the left side of each purified entangled state, there is a label "Ak", and this number k indicates that this purified entangled states is obtained from k steps of entanglement pumping. **(a)** The unoptimized (left) implementation has three pumping steps after each entanglement connection, with average time of about 11 sec to produce the pair wanted. **(b)** The optimized (right) implementation is from optimization over pair generation time, connection position, and the number of pumping steps. The optimized choice of connection position does not necessarily break the long pair into two almost identical shorter pairs; for example, the entangled state pointed by the black arrow in the 9th row is obtained by connecting two very different shorter pairs in the row below. In addition, the possibility of multi-level pumping is also taken into account during the dynamic programming. As pointed by the red arrows, the pair of storage qubits in the third row pumps the pair in the second row, and the latter pumps the pair in the first row. The average time is about 1.5 sec for the optimized implementation, about 8 times faster than the unoptimized one.

For the CTSL scheme, however, unoptimized and optimized protocols behave very differently, when $p = \eta = 0.990$. As shown in Fig. 7.4(b)(d), the unoptimized protocol cannot effectively create entangled pairs for distances longer than $200km$, while the optimized protocol is still able to efficiently create distant entangled pairs with very high fidelity. Thus our optimization lowers the threshold requirement for the CTSL scheme of quantum repeater.

To understand the reason for the improvement of the highest achievable fidelity (Fig. 7.3(d)) and the parameter threshold (Fig. 7.4(d)), we examine the optimized protocol of CTSL scheme in the next two subsections.

7.3.2 Comparison between optimized and unoptimized protocols

We first compare the detailed procedures between two (optimized and unoptimized) protocols using CTSL scheme to produce a pair with final distance $L = 11L_0$ and fidelity $F_{final} = 97.6\%$, with default reliability parameters $p = \eta = 0.995$. We choose the highest fidelity achievable by the unoptimized protocol, so that we will see almost all features that give improvements. The results for the unoptimized protocol (Fig. 7.5(a)) follows Refs. [38, 39] exactly, while the optimized one (Fig. 7.5(b)) is from our systematic search using dynamic programming. They differ in the following aspects: (1) during entanglement generation, the optimized implementation generates elementary pairs with fidelity lower than 0.99 to reduce the generation time, and uses entanglement pumping afterwards to compensate the fidelity loss; (2) during entanglement connection, the rule of producing long pair from two almost identical

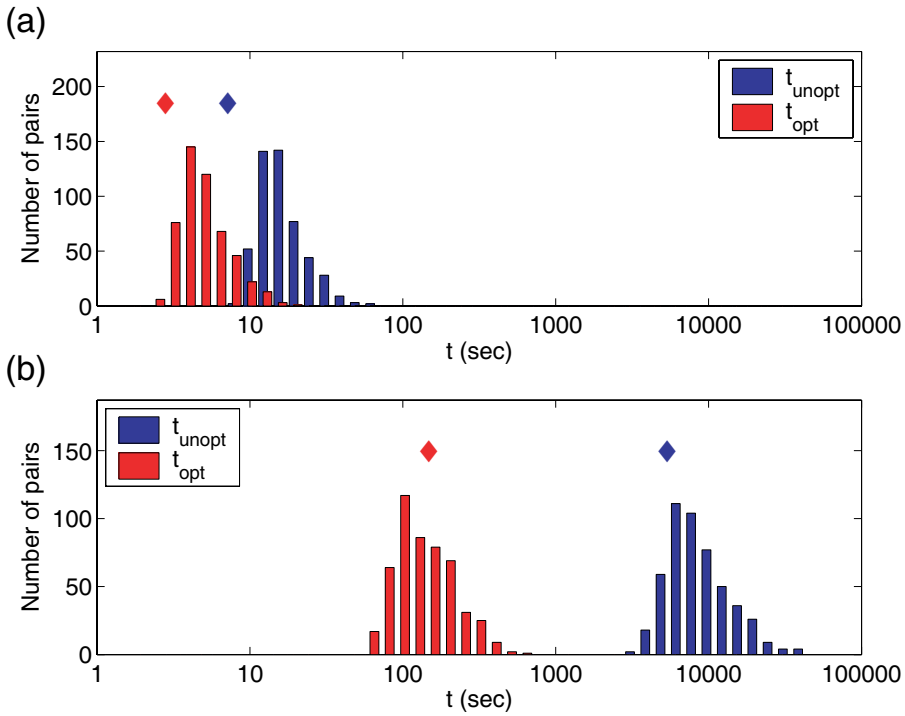

Figure 7.6: Monte Carlo simulation for unoptimized/optimized implementations for **(a)** the BDCZ scheme and **(b)** the CTSL scheme, with final distance $1280km$ and fidelity 0.97. The time distributions for distant pairs are plotted, with red (blue) bars for optimized (unoptimized) implementation. In each plot, the red (blue) diamond indicates the estimated time from average-time approximation (Sec. 7.2.6) for optimized (unoptimized) implementation. The average-time approximation provides a good estimate up to some overall factor ($2 \sim 3$) which is not very sensitive to the implementation.

shorter pairs is slightly modified (e.g., the pair pointed by the black arrow in the 9th row is from connection of two quite different pairs in the 10th row); (3) the number of pumping steps after each connection varies from 0 to 3 for optimized implementation; (4) finally, the optimized implementation uses multi-level pumping, which will be discussed in detail in the next subsection. For clarity, the additional operation of node-skipping is suppressed in the optimization here. The overall average time is reduced from 11 sec to 1.5 sec, improved by a factor of 8.

Note that our optimization results based on average time approximation (see Fig. 7.6 and Sec. 7.2.6) are confirmed by the Monte-Carlo simulation of the optimized protocols, verifying the substantial speed-up.

7.3.3 Multi-level pumping

We now consider the additional operation of multi-level pumping in more detail. We discuss multi-level pumping only for the CTSL scheme, but not for the BDCZ scheme. (In the BDCZ scheme, to introduce multi-level pumping requires additional quantum memory qubits.) In the original unoptimized protocol [38, 39], the purified entangled state with distance n (between the 0th and the nth nodes ($n > 5$)) is produced by entanglement pumping, and the entangled states used for pumping (called pumping-pairs) are *unpurified* entangled states with distance $n-2$ (Fig. 7.2(f)). The fidelity of these pumping-pairs with distance $n-2$ are limited by the connection operation, which imposes an upper-bound for the fidelity of the purified pair with distance n. The underlying restriction is that the pumping-pair is unpurified.

We may lift this restriction by allowing the use of a purified pumping pair. This is multi-level pumping. For example, the pumping-pair with distance $n-2$ may also be produced by entanglement pumping from pumping-pairs with distance $n-4$ (Fig. 7.2(f')), and so on. By doing multi-level pumping, the fidelity of the pumping-pair with distance $n-2$ is increased (Fig. 7.2(f")), and the same for the fidelity upper-bound for the entangled state with distance n. While multi-level pumping can increase the fidelity, it also slows down the repeater scheme.

When the reliability of local operations is above the threshold for the unoptimized

protocol (e.g. $p = \eta = 0.995$), we find that multi-level pumping is necessary only for the last two or three levels to the high-fidelity pair we want to produce. Such multi-level pumping can be identified in the optimized implementation – for example, as indicated by red arrows in Fig. 7.5(b), the pair of storage qubits in the third row pumps the pair in the second row, and the latter pumps the pair in the first row. On the other hand, when the reliability of local operations is below such threshold (e.g. $p = \eta = 0.990$), multi-level pumping is needed almost after every entanglement connection.

If we exclude the possibility of multi-level pumping in dynamic programming, the infinite improvement factor for pairs with distance $L > 100km$ and fidelity $F \gtrapprox 97.5\%$ in Fig. 7.3(d) would disappear. Similarly, in Fig. 7.4(d), without multi-level pumping, there would be no improvement of the parameter threshold, and even the optimized protocol could not efficiently create distant ($L > 200km$) entangled pairs. For the CTSL scheme, multi-level pumping not only enables us to prepare entangled pairs with very high fidelity, but also lowers the required threshold of the reliability parameters (p and η) for local operations. Therefore, the flexibility to include additional operations in our dynamic programming provides a new perspective on the optimization of quantum repeater schemes.

7.3.4 Other improvements

In addition to the previously discussed features in the plots of improvement factor, there is an overall improvement for all final distances and fidelities. Such overall improvement comes from the optimized choice of the distance (by node-skipping)

and the generation time for *each* elementary pair used. Such overall improvement is about 1.5 (or $2 \sim 3$) for the BDCZ (or CTSL) scheme, which indicates that the original choice of uniform distance $L_0 = 10km$ and initial fidelities $F_0 = 96\%$ (or 99%) are quite close to the optimal.

Finally, we consider if it is possible to gain some additional speed-up if we are allowed to choose the location of the nodes of the quantum repeater. In order to answer this question, we discretize the distance into smaller units, e.g. $1km \ll L_{att}$. Since the distance of each elementary pair is determined by the dynamic programming, the optimized location of the nodes can be inferred from the distances of the elementary pairs. We find that the speed-up due to optimization over the location of the nodes is fairly small, no more than 15% in time (for cases with final distances larger than $200km$). Generally we find that as long as the node spacing is less than the attenuation length ($L_0 < L_{att}$), a quantum repeater can be implemented almost optimally.

7.3.5 Experimental implications

Throughout our analysis we have assumed relatively high fidelity of local measurements and operations ($\eta = p = 0.995$ or 0.99) and memory times exceeding total communication times. Recent experiments with tapped ions [124, 97], neutral atoms [16], and solid state qubits [63] are already approaching these values of fidelity and memory times. At the same time, high initial entanglement fidelity ($F_0 \approx 96\%$ or 99%) is also needed for the optimized protocols. Entanglement fidelity of about 90% can be inferred from recent experiments with two ions in independent traps [139].

While optimization procedure can yield protocols compatible with fairly low initial fidelity and high local error rates, in practice these errors introduce a large overhead in communication time.

Besides the schemes considered here, there exist other quantum repeater schemes, in particular the Duan-Lukin-Cirac-Zoller scheme (DLCZ scheme) [59] that requires a smaller set of quantum operation and relatively modest physical resources. The original DLCZ scheme does not use active entanglement purification and hence cannot correct arbitrary errors. In such a case, optimization is straightforward and has been discussed in [59]. Recently, the DLCZ scheme has been extended to include active entanglement purification in order to suppress e.g. phase noises [102, 207]. The extended DLCZ scheme becomes very similar to the BDCZ scheme in terms of the self-similar structure. The technique of dynamic programming can be applied to optimize the extended DLCZ scheme as well.

7.4 Conclusion

We have demonstrated how dynamic programming can be a powerful tool for systematically studying the optimization of quantum repeater protocols. We find substantial improvements to two specific repeater schemes [26, 61, 38, 39]. Beyond searching for optimal choices in previously known elements of the schemes (entanglement generation, connection, and pumping), our systematic study can also incorporate more sophisticated additional operations, such as node-skipping, multi-level pumping, and the flexible location of repeater stations. In particular, our multi-level pumping procedure extends the maximum achievable fidelity for distant pairs. It

should be possible to include additional possibilities to the optimization problem of quantum repeater, such as different choices of entanglement generation and possibly more efficient usage of local qubits [191, 120]. It would also be interesting to study the optimization problem of quantum repeater with finite storage time of the quantum memory [93, 47]. Even the optimized protocols have a rather limited speed (corresponding to generation of one high-fidelity pair over 1280 km in $1 \sim 100$ s (see Fig. 7.6). Therefore, improvement of experimental techniques (to obtain higher local operation fidelities and more efficient atom-photon coupling) as well as development of new theoretical approaches to speed-up quantum repeaters still remain an outstanding goal. Furthermore, the dynamic programming techniques may find application in other outstanding problems in quantum information science, such as the optimization of quantum error correction for fault tolerant quantum computation. In particular, the optimization of the network-based quantum computation scheme with minimal resources [103, 104] might be possible.

Chapter 8

Quantum Repeater with Encoding

8.1 Introduction

Quantum key distribution generates a shared string of bits between two distant locations (a key) whose security is ensured by quantum mechanics rather than computational complexity [79]. Recently, quantum communication over 150 km has been demonstrated [190], but the key generation rate decreases exponentially with the distance due to the fiber attenuation. Quantum repeaters can resolve the fiber attenuation problem, reducing the exponential scaling to polynomial scaling by introducing repeater stations to store intermediate quantum states [26, 39, 191]. Dynamic programming-based search algorithm can optimize the key generation rate and the final-state fidelity of the quantum repeaters [101]. Using additional local resources (i.e., more quantum bits per station), the key generation rate can be further improved by multiplexing different available pairs [47] and banding pairs according to their fidelities [192]. However, since all these protocols use entanglement purification that

requires two-way classical communication, the time to purify pairs increases with the distance and all these protocols are relatively slow. Thus, the finite coherence time of quantum memory ultimately limits the communication distance [93]. As illustrated in Fig. 8.1, the estimated key generation rate sharply decreases as soon as the memory error becomes dominant.

Here we propose a new, fast quantum repeater protocol in which the communication distance is *not* limited by the memory coherence time. Our protocol encodes logical qubits with small CSS codes [154], applies entanglement connection at the encoded level, and uses classical error correction to boost the fidelity of entanglement connection. We eliminate the time-consuming entanglement purification operation over long distances and also avoid the resource-consuming procedure of quantum error correction. We find that the new repeater protocol with small CSS codes can extend the communication distance ($10^3 \sim 10^6$ km) and maintain an efficient key generation rate (above 100 bits/sec) using finite local resources ($30 \sim 150$ qubits/station) that scale logarithmically with distance.

In Sec. 8.2, we describe the idealized quantum repeater protocol to overcome the fiber attenuation problem, emphasizing the possibility of simultaneous entanglement connection and pointing out three other major imperfections (entanglement infidelity, operational errors, and memory errors) that still needs to be suppressed. In Sec. 8.3, we consider an example of quantum repeater with repetition code to suppress the bit-flip errors. In Sec. 8.4, we provide the general protocol for quantum repeater with CSS code that can suppress both bit-flip and dephasing errors. In Sec. 8.5, we compute the final fidelity achievable with our protocol, which in principle can be arbitrarily close

to unity using large and efficient CSS code. In Sec. 8.6, we calculate the maximum number of connections depending on the code and the imperfections, and we also estimate the key generation rate. In Sec. 8.7, we discuss potential improvements and other applications.

8.2 Fast Quantum Communication with Ideal Operations

We start by describing an idealized quantum repeater protocol, where fiber attenuation is the only problem to be overcome. As illustrated in Fig. 8.2, there are L repeater stations, and the separation between the neighboring stations is of the order of the fiber attenuation length. The Bell pairs $|\Phi^+\rangle = \frac{1}{\sqrt{2}}(|0\rangle|0\rangle + |1\rangle|1\rangle)$ between neighboring repeater stations are independently generated and verified. Then *entanglement connection* (swapping) [10, 209] is applied to connect these Bell pairs into a long Bell pair. Each intermediate repeater station measures the two local qubits in the Bell basis (called *Bell measurement*, see the inset of Fig. 8.2) and announces 2 classical bits of information, which uniquely specify the four possible measurement outcomes and enables the determination of the *Pauli frame* for the remaining qubits (i.e., the choice of local Pauli operators that adjust the long Bell pair to $|\Phi^+\rangle$ [115]). This is a deterministic process requiring local operation and (one-way) classical communication.

The entanglement connection can be applied *simultaneously* [1] for all intermediate

[1] We use the rest frame of the repeater stations.

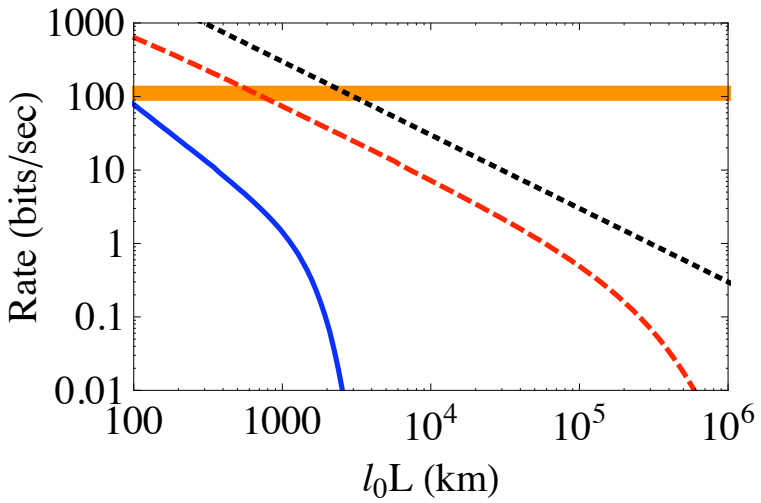

Figure 8.1: Comparison between the conventional and new repeater protocols, in terms of the generation rate of Bell pairs or secret bit pairs (i.e., the sustained bandwidth of the repeater channel). The memory coherence time is assumed to be $t_{coh} = 10$ sec, and the nearest neighbor spacing is $l_0 = 10$ km. (i) The blue curve is the BDCZ protocol (with the maximum number of qubits per station increasing logarithmically with distance, see scheme C in Ref. [61]). The sharp decrease in rate is attributed to blinded connection and purification [93] when the memory error becomes dominant (i.e., time $\gtrsim 0.01\tau_{coh} = 0.1$ sec). (ii) The red dashed curve is the parallel protocol (with the number of qubits per station increasing at least linearly with distance, see scheme B in Ref. [61]). (iii) The black dotted reference curve is the inverse of the classical communication time between the final stations. Since all conventional repeater protocols rely on two-way classical communication, their rates always stay below the reference curve unless parallel or multiplexed [192] repeater channels are used. (iv) The orange horizontal thick line is our new repeater protocol with encoding (with the number of qubits per station increasing logarithmically or poly-logarithmically with distance). Since our protocol runs in the one-way communication mode, the rate is independent of the communication distance, and can reach above the black dashed curve. Our protocol is much more efficient over long distances than conventional protocols.

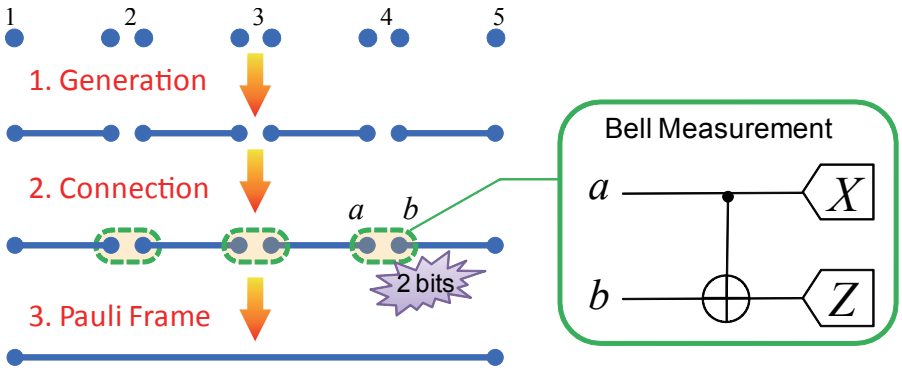

Figure 8.2: Idealized quantum repeater. There are $L = 5$ repeater stations. Each intermediate station has two physical qubits. **Step 1. (Generation)** Bell pairs between neighboring repeater stations are generated. **Step 2. (Connection)** The qubits at the intermediate stations are measured in the Bell basis (see the inset). **Step 3. (Pauli Frame)** The Pauli frame for qubits at the outermost stations is determined, based on the outputs of intermediate Bell measurements. Finally, one remote Bell pair between the outermost stations is created.

stations, because the quantum circuit for Bell measurement does not depend on the Pauli frame. It is the interpretation of the measurement outcome that depends on the Pauli frame. Fortunately, we can wait until we collect all $2(L-2)$ announced classical bits from intermediate stations, and decide the Pauli frame for the final distant Bell pair. In addition, without compromising the security for quantum key distribution, the two final (outermost) stations can measure their qubits in random X and Z basis and announce their choices of the basis even before receiving classical bits from intermediate stations. Half of the time, they will find that they choose the same basis (in the Pauli frame) and obtain strongly correlated measurement outcomes that can be used for secret keys [68]. Thanks to the *simultaneous entanglement connection*, the idealized quantum repeater can be very fast and the *cycle time* τ_c is just the total time for entanglement generation and connection between neighboring repeater

stations.

In practice, however, there are three major imperfections besides the fiber attenuation. (1) The generated entangled state ρ between neighboring repeater stations is not the perfect Bell state $|\Phi^+\rangle$, characterized by the entanglement fidelity

$$F_0 = \left\langle \Phi^+ \right| \rho \left| \Phi^+ \right\rangle \leq 1. \tag{8.1}$$

(2) The local operations for entanglement connection have errors [26, 39, 191, 101]. For example, the local two-qubit unitary operation U_{ij} would be

$$U_{ij}\rho U_{ij}^\dagger \rightarrow (1-\beta)\, U_{ij}\rho U_{ij}^\dagger + \frac{\beta}{4}\,\mathrm{Tr}_{ij}\left[\rho\right] \otimes I_{ij}, \tag{8.2}$$

where β is the gate error probability, $\mathrm{Tr}_{ij}\left[\rho\right]$ is the partial trace over the subsystem i and j, and I_{ij} is the identity operator for the subsystem i and j. The projective measurement of state $|0\rangle$ would be

$$P_0 = (1-\delta)\left|0\right\rangle\left\langle 0\right| + \delta\left|1\right\rangle\left\langle 1\right|, \tag{8.3}$$

where δ is the measurement error probability. (3) The quantum memory decoheres with rate γ. We model the memory error probability for storage time τ_c as $\mu = 1 - e^{-\gamma\tau_c} \approx \gamma\tau_c$. The action of the memory error on the ith qubit would be

$$\rho \rightarrow (1-\mu)\,\rho + \frac{\mu}{2}\,\mathrm{Tr}_i\left[\rho\right] \otimes I_i, \tag{8.4}$$

where $\mathrm{Tr}_i\left[\rho\right]$ is the partial trace over the subsystem i, and I_i is the identity operator for the subsystem i.

In the following two sections, we will present the new repeater protocol. Our new repeater protocol replaces the physical qubits (in Fig. 8.2) with encoded qubits (in

Fig. 8.3), generates the encoded Bell pairs between neighboring stations, connects the encoded Bell pairs at intermediate stations simultaneously, and determines the Pauli frame for the encoded Bell pair shared by the final stations. In Sec. 8.3 we provide an illustrative example of quantum repeater with 3-qubit repetition code that can fix only bit-flip errors. In Sec. 8.4 we propose our new protocol with CSS codes that can fix all imperfections listed above.

8.3 Quantum Repeater with Repetition Code

To illustrate the idea, we first consider an example that uses the 3-qubit repetition code to encode one logical qubit

$$\left|\tilde{0}\right\rangle = |000\rangle \quad \text{and} \quad \left|\tilde{1}\right\rangle = |111\rangle\,, \tag{8.5}$$

which can fix one bit-flip error. Although it cannot fix all the errors given in Sec. 8.2, this example illustrates all other key elements of the new repeater protocol and it can be easily generalized to the CSS encodes that can fix all the errors as discussed in Sec. 8.4.

First, we generate the encoded Bell pair $\left|\tilde{\Phi}^{+}\right\rangle_{12} = \frac{1}{\sqrt{2}}\left(\left|\tilde{0}\right\rangle_1\left|\tilde{0}\right\rangle_2 + \left|\tilde{1}\right\rangle_1\left|\tilde{1}\right\rangle_2\right)$ between neighboring stations 1 and 2, as illustrated in the upper-left panel of Fig. 8.3. We need at least six qubits from each station: three for memory qubits (blue dots) and three for ancillary qubits (gray dots). There are three steps: (i) We locally prepare the encoded state $\frac{1}{\sqrt{2}}\left(\left|\tilde{0}\right\rangle_1 + \left|\tilde{1}\right\rangle_1\right)$ and $\left|\tilde{0}\right\rangle_2$ and store them in the memory qubits (in blue squared boxes); (ii) we generate three copies of the physical Bell pairs $\left(\frac{|0\rangle_1|0\rangle_2+|1\rangle_1|1\rangle_2}{\sqrt{2}}\right)^{\otimes 3}$ between ancillar qubits (gray lines); (iii) we use the entanglement

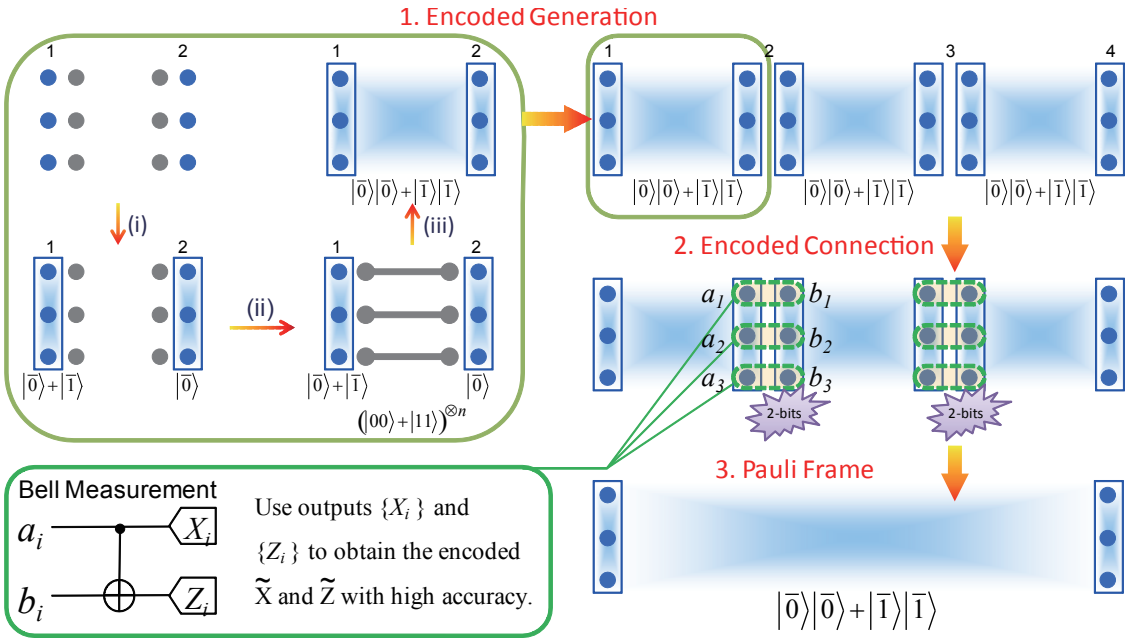

Figure 8.3: Repeater protocol with encoding. Each repeater station has $2n$ memory qubits (blue dots) and $O(n)$ auxiliary qubits (gray dots). Here $n = 3$. **Step 1. (Encoded Generation)** Between two neighboring stations (upper-left panel): (i) memory qubits are fault-tolerantly prepared in the encoded states $|\tilde{0}\rangle$ or $|\tilde{+}\rangle = \frac{1}{\sqrt{2}}\left(|\tilde{0}\rangle + |\tilde{1}\rangle\right)$, (ii) purified physical Bell pairs are generated between auxiliary qubits (connected gray dots), (iii) an encoded Bell pair $\left|\tilde{\Phi}^{+}\right\rangle_{AB} = \frac{1}{\sqrt{2}}\left(|\tilde{0}\rangle_A |\tilde{0}\rangle_B + |\tilde{1}\rangle_A |\tilde{1}\rangle_B\right)$ between neighboring stations is created using encoded CNOT gate (achieved by n pairwise, teleportation-based CNOT gates [82, 208, 103]). **Step 2. (Encoded Connection)** Encoded Bell measurements are simultaneously applied to all intermediate repeater stations, via pairwise CNOT gates between qubits a_i and b_i followed by measurement of the physical qubits (the lower-left panel). Using classical error correction, the outcomes for the encoded Bell measurement can be obtained with a very small effective logical error probability $Q \sim q^{t+1}$ [Eq. (8.11)]. The outcome is announced as 2 classical bits (purple star) at each intermediate repeater station. **Step 3. (Pauli Frame)** According to the outcomes of intermediate encoded Bell measurements, the Pauli frame [115] can be determined for qubits at the outermost stations. Finally, one encoded Bell pair between the final (outermost) stations is created.

resources of 3 physical Bell pairs to implement 3 *teleportation-based CNOT gates* [82, 208, 103], applied *transversally* between the memory qubits storing the encoded states $\frac{1}{\sqrt{2}}\left(\left|\tilde{0}\right\rangle_1+\left|\tilde{1}\right\rangle_1\right)$ and $\left|\tilde{0}\right\rangle_2$:

$$\frac{1}{\sqrt{2}}\left(|000\rangle_1+|111\rangle_1\right)\otimes|000\rangle_2 \tag{8.6}$$

$$\rightarrow\frac{1}{\sqrt{2}}\left(|000\rangle_1|000\rangle_2+|111\rangle_1|111\rangle_2\right), \tag{8.7}$$

which gives us exactly the desired encoded Bell pair $\left|\tilde{\Phi}^+\right\rangle_{12}$. Similarly, we can generate encoded Bell pairs $\left|\tilde{\Phi}^+\right\rangle_{j,j+1}$ between neighboring stations j and $j+1$, for $j=2,\cdots,L-1$.

Then we connect the encoded Bell pairs $\left|\tilde{\Phi}^+\right\rangle_{12}$ and $\left|\tilde{\Phi}^+\right\rangle_{23}$ to obtain the longer encoded Bell pair $\left|\tilde{\Phi}^+\right\rangle_{13}$. The idea is to perform the encoded Bell measurement over the two encoding blocks at station 2. We use $2a$ and $2b$ to refer to the left and the right encoding blocks at station 2, respectively. As shown in Fig. 8.3 (see step 2 and the lower-left panel), we apply three pairwise CNOT gates between the two encoding blocks $\{a_i\}$ and $\{b_i\}$ at station 2. To see the possible outcomes of this procedure, we rewrite the initial state in terms of Bell states between stations 1 and 3,

$$\begin{aligned}
&\left|\tilde{\Phi}^+\right\rangle_{1,2a}\otimes\left|\tilde{\Phi}^+\right\rangle_{2b,3}\\
=&\frac{1}{2}\begin{pmatrix}\left|\tilde{\Phi}^+\right\rangle_{13}\otimes\left|\tilde{\Phi}^+\right\rangle_{2a,2b}+\left|\tilde{\Phi}^-\right\rangle_{13}\otimes\left|\tilde{\Phi}^-\right\rangle_{2a,2b}\\+\left|\tilde{\Psi}^+\right\rangle_{13}\otimes\left|\tilde{\Psi}^+\right\rangle_{2a,2b}+\left|\tilde{\Psi}^-\right\rangle_{13}\otimes\left|\tilde{\Psi}^-\right\rangle_{2a,2b}\end{pmatrix}\\
\rightarrow&\frac{1}{2}\begin{pmatrix}\left|\tilde{\Phi}^+\right\rangle_{13}\otimes\left|\tilde{+}\right\rangle_{2a}\left|\tilde{0}\right\rangle_{2b}+\left|\tilde{\Phi}^-\right\rangle_{13}\otimes\left|\tilde{-}\right\rangle_{2a}\left|\tilde{0}\right\rangle_{2b}\\+\left|\tilde{\Psi}^+\right\rangle_{13}\otimes\left|\tilde{-}\right\rangle_{2a}\left|\tilde{0}\right\rangle_{2b}+\left|\tilde{\Psi}^-\right\rangle_{13}\otimes\left|\tilde{-}\right\rangle_{2a}\left|\tilde{1}\right\rangle_{2b}\end{pmatrix},
\end{aligned}$$

where $\left|\tilde{\Phi}^{\pm}\right\rangle_{13} = \frac{1}{\sqrt{2}}\left(\left|\tilde{0}\right\rangle_1\left|\tilde{0}\right\rangle_3 \pm \left|\tilde{1}\right\rangle_1\left|\tilde{1}\right\rangle_3\right)$, $\left|\tilde{\Psi}^{\pm}\right\rangle_{13} = \frac{1}{\sqrt{2}}\left(\left|\tilde{0}\right\rangle_1\left|\tilde{1}\right\rangle_2 \pm \left|\tilde{1}\right\rangle_1\left|\tilde{0}\right\rangle_2\right)$, $\left|\tilde{\pm}\right\rangle_{2a} = \frac{1}{\sqrt{2}}\left(\left|\tilde{0}\right\rangle_{2a} \pm \left|\tilde{1}\right\rangle_{2a}\right)$. To complete the encoded Bell measurement, we projectively measure the logical qubits of these two encoding blocks as follows: (1) The logical qubit for $2a$ should be measured in the $\{\left|\tilde{\pm}\right\rangle\}$ basis, which can be achieved by measuring the physical qubits $\{a_i\}$ in the $\{|\pm\rangle\}$ basis. Since $\left|\tilde{+}\right\rangle = \frac{1}{2}\left(|+++\rangle + |+--\rangle + |-+-\rangle + |--+\rangle\right)$ and $\left|\tilde{-}\right\rangle = \frac{1}{2}\left(|---\rangle + |-++\rangle + |+-+\rangle + |++-\rangle\right)$, there will be an odd number of $|+\rangle$ outputs if the encoded qubit is in state $\left|\tilde{+}\right\rangle$, and an even number of $|+\rangle$ outputs if the encoded qubit is in state $\left|\tilde{-}\right\rangle$. (2) The logical qubit for $2b$ should be measured in the $\{\left|\tilde{0}\right\rangle, \left|\tilde{1}\right\rangle\}$ basis, which can be achieved by measuring the physical qubits $\{b_i\}$ in the $\{|0\rangle, |1\rangle\}$ basis. There should be three $|0\rangle$ outputs for state $\left|\tilde{0}\right\rangle$, and three $|1\rangle$ outputs for state $\left|\tilde{1}\right\rangle$. The pairwise CNOT gates and projective measurement of physical qubits are summarized in the lower-left panel of Fig. 8.3.

We now show the suppression of bit-flip errors due to the repetition code [Eq. (8.5)]. If one of the physical qubits in $2b$ is bit-flipped, the measurement outcomes for $2b$ will contain two correct outputs and one erroneous output. Choosing the majority output, we can identify and correct the erroneous output, and still obtain the logical bit encoded in $2b$ correctly. We emphasize that only classical error correction is used. If there is one physical qubit in $2a$ that suffers from a bit-flip error, this error will not affect the outputs for $2a$, as bit-flip errors commute with the operators to be measured; this error may affect one corresponding physical qubit in $2b$, which can be identified and corrected using the majority. Therefore, we can obtain the logical outcomes for both $2a$ and $2b$, and the suppressed effective logical error probability

can be

$$Q = \begin{pmatrix} 3 \\ \\ 2 \end{pmatrix} q_b^2 + \begin{pmatrix} 3 \\ \\ 3 \end{pmatrix} q_b^3 \approx 6q_b^2 \ll q_b, \tag{8.8}$$

where $q_b \leq 4\beta + 2\delta + \mu$ is the effective error probability for each b_i to give the wrong output (Appendix. C.1).

To complete the entanglement connection, station 2 announces the outcomes for its two logical qubits from the encoded Bell measurement, which contains *two* classical bits of information and determines the Pauli frame for the encoded Bell pair shared between stations 1 and 3. Note that the detailed outputs of physical qubits are only important to obtain the logical outcomes, but not needed for communication among stations. Similarly, we can perform entanglement connection for all the intermediate stations. Furthermore, these entanglement connections can still be applied simultaneously for all intermediate striations, as described in Sec. 8.2. The final stations share the encoded Bell pair $\left|\tilde{\Phi}^+\right\rangle_{1L} = \frac{1}{\sqrt{2}}\left(\left|\tilde{0}\right\rangle_1 \left|\tilde{0}\right\rangle_L + \left|\tilde{1}\right\rangle_1 \left|\tilde{1}\right\rangle_L\right)$, whose Pauli frame is determined by the $2(L-2)$ announced classical bits from all intermediate stations.

8.4 Quantum Repeater with CSS Code

In this section, we will generalize the repeater protocol from the 3-qubit repetition code to any $[[n, k, 2t+1]]$ *CSS code* [154], which encodes k logical qubits with n physical qubits and fixes up to t (bit-flip and dephasing) errors. For simplicity, we will focus on the CSS codes with $k = 1$, which includes the well studied $[[5, 1, 3]]$, $[[7, 1, 3]]$ (Steane), and $[[9, 1, 3]]$ (Shor) codes. Extension of the protocol to $k > 1$ is straightforward. The CSS code can be regarded as a combination of two classical

error correcting codes C^X and C^Z, which fix dephasing errors and bit-blip errors, respectively. The error syndromes for the code C^X (or C^Z) can be obtained if we have the outputs for the n physical qubits measured in the X (or Z) basis.

The relevant properties of the CSS codes are summarized as follows: (1) The measurement of logical operator $\tilde{X}$ (or $\tilde{Z}$) can be obtained from projective measurement of physical qubits in the X (or Z) basis. (2) The outputs from measurements of physical qubit in the X (or Z) basis should comply with the rules of the classical error correcting code C^X (or C^Z), which can fix up to t^X (or t^Z) errors in the n output bits. (For example, the 3-qubit repetition cod can fix up to $t^Z = 1$ bit-flip error as discussed in Sec. 8.3.) Suppose each output bit has an (uncorrelated) effective error probability $q \sim \beta+\delta+\mu$, after fixing up to t errors the remaining error probability for the logical outcome is $O\left(q^{t+1}\right)$, assuming $t = \min\left\{t^X, t^Z\right\}$. (3) The encoded CNOT gate can be implemented by n pairwise CNOT gates between two encoding blocks [154]. Such pairwise CNOT gates do not propagate errors within each encoding block, and it can be be used for preparation of encoded Bell pairs.

We find that each repeater station needs approximately $6n$ physical qubits (see Appendix C.2 for details), including $2n$ memory qubits to store the two encoded qubits that are entangled with the neighboring stations, and approximately $4n$ ancillary qubits for the fault-tolerant preparation of the encoded qubits and generation of nonlocal encoded Bell pairs between neighboring repeater stations. There are three steps for each cycle of the new repeater protocol:

1. Generate encoded Bell pairs between two neighboring stations (see the upper-left panel of Fig. 8.3): (i) We initialize the memory qubits in logical states $\left|\tilde{0}\right\rangle$ and

$\frac{1}{\sqrt{2}}\left(\left|\tilde{0}\right\rangle + \left|\tilde{1}\right\rangle\right)$ at each station *fault-tolerantly* (with errors effectively uncorrelated among physical qubits from the same encoding block) [2]. (ii) We use entanglement purification to obtain purified Bell pairs between two neighboring stations [61]. Each purified Bell pair can be immediately used for a *teleportation-based CNOT gate* [82, 208, 103]. (iii) According to the property (3) of the CSS code, we need n teleportation-based CNOT gates to implement the encoded CNOT gate and obtain the encoded Bell pair $\left|\tilde{\Phi}^{+}\right\rangle_{j,j+1} = \frac{1}{\sqrt{2}}\left(\left|\tilde{0}\right\rangle_{j}\left|\tilde{0}\right\rangle_{j+1} + \left|\tilde{1}\right\rangle_{j}\left|\tilde{1}\right\rangle_{j+1}\right)$ between neighboring stations j and $j+1$.

2. Connect the encoded Bell pairs, performing encoded Bell measurement at all intermediate stations simultaneously (see step 2 of Fig. 8.3). At each intermediate station, we first apply the pairwise CNOT gates between qubits a_i and b_i, with a_i from the control block and b_i from the target block, for $i = 1, \cdots, n$ (as shown in the lower-left panel in Fig. 8.3). Then we projectively measure the physical qubits in the X basis for a_i and in the Z basis for b_i. According to the property (2) of the CSS code, we can use the classical error correcting code C^X (or C^Z) to fix up to t errors in $\{a_i\}$ (or $\{b_i\}$), leaving only $O\left(q^{t+1}\right)$ for the logical error probability. Thus, the outcomes for the encoded $\tilde{X}$ and $\tilde{Z}$ operators of the encoded Bell measurement can be obtained with high accuracy of $O\left(q^{t+1}\right)$. Similar to the idealized repeater, each intermediate repeater station announces 2 classical bits of information of the encoded Bell measurement.

[2] We can achieve fault-tolerant preparation of the logical state $\left|\tilde{0}\right\rangle$ (or $\left|\tilde{+}\right\rangle$) by two approaches. One approach uses several copies of the logical states to distill a purified logical state with negligible contribution from initial correlated errors [180]. Alternatively, we may start with $|0\rangle^{\otimes n}$ (or $|+\rangle^{\otimes n}$), projectively measure the x-stabilizers using fault-tolerant circuit, and update the stabilizers during entanglement connection. See Appendix C.2 for details.

3. According to the $2(L-2)$ announced classical bits from all intermediate repeater stations, choose the Pauli frame at the final repeater stations for the shared encoded Bell pair.

8.5 Error Estimate

In order to calibrate the encoded Bell pair obtained from the new repeater protocol, we need to generalize the definition of entanglement fidelity, because the encoding enables us to correct small errors that deviate from the logical subspace. We define the *entanglement fidelity* as

$$F = \left\langle \tilde{\Phi}^{+} \right| \mathcal{R}\left[\rho_{\text{fina,Bell}}\right] \left| \tilde{\Phi}^{+} \right\rangle, \tag{8.9}$$

where $\mathcal{R}$ represents the (ideal) recovery operation with quantum error correction [177]. The entanglement fidelity F can calibrate the security for the protocol and bound the maximum information leaked from the final stations [3]. F can also be practically obtained from the correlation measurement between the final repeater station (Appendix C.3).

We emphasize that the property of fault-tolerance can be maintained throughout the entire repeater protocol (fault-tolerant initialization, transverse CNOT gate, and encoded qubit measurement), so the errors for individual physical qubits are effectively uncorrelated. With some calculation (see Appendix. C.1), we estimate that the effective error probability (per physical qubit) is

$$q = 4\beta + 2\delta + \mu, \tag{8.10}$$

[3] According to Ref. [131], if the two final stations share a Bell pair with fidelity $F = 1 - 2^{-s}$, then Eve's mutual information with the key is at most $2^{-c} + 2^{O(-2s)}$ where $c = s - \log_2(2 + s + 1/\ln 2)$.

Note that q does not explicitly depend on F_0, because for level-m purified Bell pairs (see Appendix C.4) the operational errors (β and δ) dominate the super-exponentially suppressed infidelity approximately $(1-F_0)^{2^{m/2}}$. Then the *effective logical error probability* for each encoding block (caused by more than t errors from the encoded block) is

$$Q = \sum_{j=t+1}^{n} \left(\begin{array}{c} n \\ \\ j \end{array} \right) q^j (1-q)^{n-j} \approx \left(\begin{array}{c} n \\ \\ t+1 \end{array} \right) q^{t+1}, \tag{8.11}$$

where the approximation requires small q. Since any logical error from the repeater stations will affect the final encoded Bell pair, the entanglement fidelity is

$$F = (1-Q)^{2L}, \tag{8.12}$$

with infidelity $1-F \approx 2LQ$ for small Q.

For large codes, we may evaluate Eq. (8.11) under the assumptions $n \gg t \gg 1$. Approximating the combinatorial function in this limit yields $Q \approx \frac{1}{\sqrt{2\pi t}} \left(\frac{e^{1+1/2n} nq}{t+1} \right)^{t+1}$, which indicates that for large codes with $n \propto t$, Q can be arbitrarily small when $q \lesssim q_c \approx \lim_{n,t\to\infty} \frac{t+1}{e^{1+1/2n} n}$. Numerically, we can evaluate the complete sum in Eq. (8.11) and we find $q_c \approx 5\%$, which corresponds to $\sim 1\%$ per-gate error rates. In addition, CSS codes with $n \lesssim 19t$ exist for arbitrarily large t (according to the Gilbert-Varsharov bound, see Eq. (30) in Ref. [30]). Therefore, our new repeater protocol with encoding provides a scalable approach for long distance quantum communication.

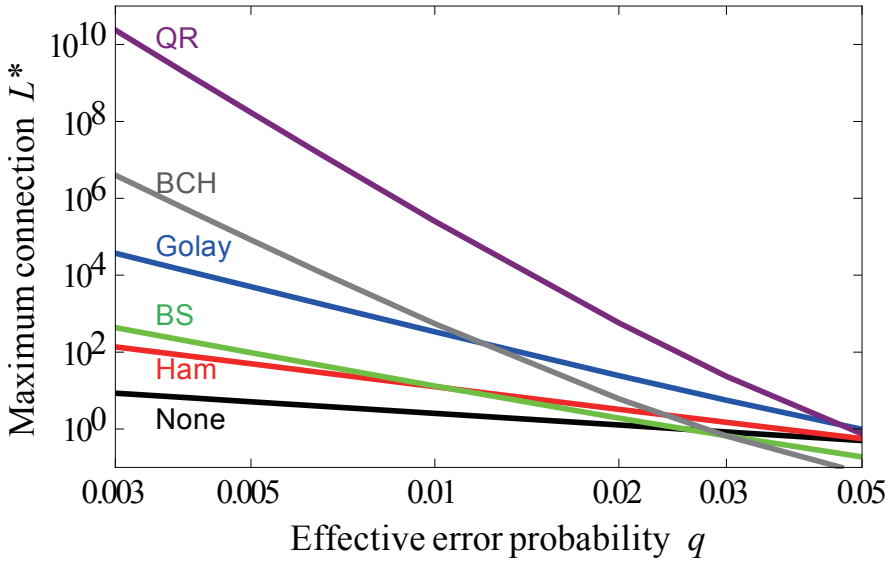

Figure 8.4: From Eqs. (8.11, 8.13), the maximum number of connections L^* is estimated as a function of the effective error probability q, assuming $F^* = 0.95$, for various CSS codes [181] listed in Table 8.1. For $q < 0.03$, L^* scales as $1/q^{t+1}$.

8.6 Example Implementations

We now consider the implementation of the new repeater protocol. Given the effective error probability q and the *target fidelity* F^*, we can use Eq. (8.12) to calculate the *maximum number of connections*

$$L^* = \frac{\ln F^*}{\ln (1 - Q)}. \tag{8.13}$$

This provides a unitless distance scale over which Bell pairs with fidelity F^* can be created. According to Eqs. (8.11,8.13), we can estimate L^* as a function of q, which is plotted in Fig. 8.4 assuming $F^* = 0.95$ for various CSS codes. Since L^* scales as $q^{-(t+1)}$ for $q \lesssim 3\%$, we can significantly increase L^* by considering efficient quantum codes with large t. For example, given $q = 0.3\%$, we estimate the maximum

Name	**Code** $[[n,k,2t+1]]$	**Resources** (qubits/station)	**Distance** (km)
No encoding	–	4	180
Repetition-3	$[3,1,3]$	18	1.0×10^4
Repetition-5	$[5,1,5]$	30	1.0×10^6
Hamming	$[[7,1,3]]$	42	1.4×10^3
Bacon-Shor	$[[25,1,5]]$	150	4.3×10^3
Golay	$[[23,1,7]]$	138	3.7×10^5
BCH	$[[127,29,15]]$	–	4.0×10^7
QR	$[[103,1,19]]$	–	2.4×10^{11}

Table 8.1: Local resources, and maximum communication distance for the new repeater protocol. In the case of no encoding, each station has 2 qubits for entanglement connection, and 2 additional qubits for entanglement purification to obtain high-fidelity purified Bell pairs. For repetition codes (with single square bracket), only one type of errors (bit-flip or dephasing) can be suppressed. For other CSS codes (with double square brackets), both bit-flip and dephasing errors can be suppressed. The local resources are estimated to be $6n$ qubits for each station (Appendix C.2). The distance is estimated from Eqs. (8.11,8.13), assuming parameters $q = 0.3\%$, $F^* = 0.95$ and $l_0 = 10$ km.

number of connections $L^* \approx 9$, 1.4×10^2, and 3.7×10^4 for cases of no encoding, $[[7,1,3]]$ Hamming code, and $[[23,1,7]]$ Golay code, respectively. If we choose the nearest neighbor spacing to be $l_0 = 10$ km (about half the fiber attenuation length), the corresponding maximum distances will be 90 km, 1.4×10^3 km, and 3.7×10^5 km. The new protocol can easily reach and go beyond intercontinental distances. In Table 8.1, we summarize the local resources and maximum communication distance for the new protocol with different encoding.

Besides maximum distances, we also estimate the key generation rate, which is the inverse of the cycle time for the new protocol. For fast local operations (systems such as ion traps [123, 170] and NV centers [98, 63] can achieve almost MHz rate for

local operations), the cycle time is dominated by creating purified Bell pairs between neighboring stations

$$\tau_c \approx \kappa \frac{l_0}{v} \frac{e^{l_0/l_{att}}}{\eta^2}. \tag{8.14}$$

We find that $\tau_c \approx 0.9\kappa$ ms, given the parameters of $l_0 = 10$ km, the fiber attenuation length $l_{att} \approx 20$ km, the signal propagation speed $v \approx 2 \times 10^5$ km/s, and the overall efficiency for collecting and detecting single photon $\eta \approx 0.3$. The dimensionless prefactor κ is the time overhead to ensure that n purified Bell pairs are obtained between neighboring stations. Since there are approximately $4n$ ancillary qubits for entanglement generation at each station, the rate to generate unpurified Bell pairs also increases with n. Thus, κ is not sensitive to the choice of n. As detailed in Appendix C.4, we estimate $\kappa \approx 8$ for $\beta = \delta = 10^{-3}$ and $F_0 = 0.95$ with depolarizing error, and the purified pair has fidelity 0.9984 after three levels of purification. Therefore, for the parameters considered here, approximately $6n$ qubits at each station can achieve $\tau_c \approx 7$ ms, which is sufficient for quantum key generation rate of 100 bits/sec over long distances.

8.7 Discussion

Our new repeater protocol is significantly faster than the standard repeater protocols over long distances [26, 39, 191, 101], because the time-consuming procedure of entanglement purification of distant Bell pairs is now replaced by local encoding with simple CSS code and classical error correction. The new protocol runs in the one-way communication mode, so the key generation rate is independent of the communication distance, and only limited by the cycle time for encoded Bell pair generation and

entanglement connection. The key generation rate can be further improved by having higher efficiency η, improved fidelity F_0, smaller separation between stations l_0, and more qubits per repeater station. In addition, the rate can also be increased by using CSS codes with $k > 1$ (e.g., the $[[127, 29, 15]]$ BCH code mentioned in Fig. 8.4), along with a small modification to the protocol that each intermediate station sends $2k$ classical bits associated with k Bell measurements.

Asymptotically, CSS codes with $n \lesssim 19t$ exist for arbitrarily large t [obtained from the Gilbert-Varsharov bound, see Eq. (30) in Ref. [30]]. Thus, the effective logical error probability Q [Eq. (8.11)] can be arbitrarily small for $q \lesssim 5\%$, and $n \propto t \sim \ln L$ is a small number increasing only logarithmically with L. In practice, however, it is still challenging to initialize large CSS encoding block fault-tolerantly with imperfect local operations. To avoid complicated initialization, we may construct larger CSS codes by concatenating smaller codes with r nesting levels, and the code size scales polynomially with the code distance, $n \propto t^r \sim (\ln L)^r$. Alternatively, we may consider the Bacon-Shor code [5]; the encoding block scales quadratically with the code distance $n = (2t+1)^2 \sim \ln^2 L$, and the initialization can be reduced to the preparation of $(2t+1)$-qubit GHZ states.

If the imperfections are dominated by the dephasing errors, we may use the $[2t+1, 1, 2t+1]$ repetition code [e.g., use the $(2t+1)$-qubit GHZ states $|+\cdots+\rangle \pm |-\cdots-\rangle$ with $|\pm\rangle = \frac{1}{\sqrt{2}}(|0\rangle \pm |1\rangle)$ to encode one logical qubit]. The repetition code has the advantage of small encoding block and efficient initialization (see Table 8.1). For example, given $q = 0.3\%$ and $F^* = 0.95$, we estimate $L^* \approx 1.0 \times 10^3$ and 1.0×10^5 for 3-qubit and 5-qubit repetition codes, respectively. Such simple repetition encoding

can be useful for quantum networks as well [161].

Our repeater protocol can also generate high fidelity entanglement over long distances. For example, $F^* = 0.999$ and $L^* \approx 730$ can be achieved with $q = 0.3\%$ and the $[[23, 1, 7]]$ Golay code. Such high fidelity entanglement might be useful for applications such as quantum state teleportation and distributed quantum computation [103]. Since quantum circuits for state-teleportation or teleportation-based CNOT gate only use Clifford group operations, the generated entanglement can be immediately used in these circuits without waiting for the classical information of the Pauli frame. The adjustment of the Pauli frame has to be postponed until the classical information is received [4].

Suppose good quantum memory (with coherence time longer than the communication time) is available at the final stations, real distant Bell pairs (rather than just strings of secret bits for quantum key distribution) can be generated. For on-demand generation of distant Bell pairs, the time delay $(l_0 L/c)$ associated with the classical communication to specify the Pauli frame is inevitable, and the total time to create one Bell pair on-demand is $\tau_c + l_0 L/c$. For offline generation of distant Bell pairs that are stored in good quantum memory for later use, we have to assume that there are enough qubits at the final stations to store all Bell pair generated, while the number of qubits at each intermediate station remains unchanged. Up to the time delay $(l_0 L/c)$ for the first Bell pair , our quantum repeater channel can create distant Bell pairs at the rate $1/\tau_c$, again corresponding to the flat curve in Fig. 8.1.

[4] Good quantum memory with coherence time longer than the communication time might be needed.

8.8 Conclusion

In summary, we have proposed a new, fast quantum repeater protocol for quantum key distribution over intercontinental distances. Our protocol fault-tolerantly generates a backbone of Bell pairs with CSS encoding, and uses simple procedure of classical error correction during connection. Our protocol using simple CSS code can provide secure quantum communication over thousands or even millions of kilometers, with 0.3% effective error probability per physical qubit and 0.95 target fidelity for the final Bell pair (see Table 8.1). The quantum key generation rate can be above 100 bits/sec, only limited by the Bell pair generation between neighboring stations.

Chapter 9

Anyonic interferometry and protected memory in atomic spin lattices

9.1 Introduction

By definition, topologically ordered states [199] cannot be distinguished by local observables, i.e. there is no local order parameter. They can arise as ground states of certain Hamiltonians which have topological degeneracy and which provide robustness against noise and quasi-local perturbations. These properties of such systems are attractive for quantum memories. However, the local indistinguishability makes measuring and manipulating the topological states difficult because they are only coupled by global operations. One way to access this information is to measure properties of the low lying particle-like excitations. In two dimensions, the quasi-particles act

like punctures in a surface which can have anyonic statistics and their topological properties are probed by braiding different particle types around each other. The existence of anyons also implies a topological degeneracy [64]. Quantum Hall fluids at certain filling fractions are believed to have topological order and there is a vigorous experimental effort to verify anyonic statistics in these systems [151]. A standard approach is to perform some kind of interferometry where one looks for non-trivial action on the fusion state space upon braiding. This is manifested as the evolution of a non-trivial statistical phase in the abelian case, or a change in the amplitude of the participating states in the non-abelian case. Some experimental evidence consistent with observation of abelian anyonic statistics in a $\nu = 2/5$ filled Quantum Hall state has been reported [31] but an unambiguous detection of anyons is still considered an open issue [172].

Spin lattice Hamiltonians can also exhibit topological order [114] and such Hamiltonians can be built with atoms [56] or molecules [145] trapped in an optical lattice [1]. A significant advantage of using atomic systems is that the microscopic physics is well known and there are established techniques for coherent control and measurement. Suggestions have been made for how one would design anyonic interferometers in these systems by using local spin operations to guide excitation along braiding paths [25, 156, 206].

We here present a new approach that directly measures topological degeneracy and anyonic statistics using global operations. The technique involves coupling be-

[1] An optical lattice can be formed by interference from counter-propagating laser beams, which creates a periodic pattern. The resulting periodic potential can trap neutral atoms via the Stark shift.

tween a probe qubit (single ancilla spin qubit or optical mode) and topologically ordered atomic spins in an optical lattice. A many body interaction between spins is mediated by coupling to a common bosonic mode of the radiation field via techniques of cavity QED [135, 84, 48, 24] or, alternatively, via a common phonon mode in ion traps [42]. Our approach avoids localizing and guiding excitations while enabling the measurement of the statistical phase associated with arbitrary braiding paths.

We also note that recent experiments have demonstrated braiding operations on small networks of non-interacting qubits encoded in photon polarization [133, 157], which generates a simulation of anyonic interferometry [87]. However, since the background Hamiltonian vanishes in such systems, they are not protected from noise and the particle interpretation of the "excitations" is ambiguous. In contrast, the technique developed here allows one to probe directly dynamic evolution of anyonic quasi-particles within the parent Hamiltonian. In addition, our mechanism can be used to perform reading and writing of qubits initially encoded in light or atoms into topological memory, which may be useful for offline storage during a computation and for applications in long distance quantum communication [26, 101].

9.2 Atomic and Molecular Spin Lattices in Optical Cavities

We focus on physical systems in which a two-dimensional optical lattice is placed within a high-finesse optical cavity as illustrated in Fig. 9.2a. To be specific, we consider the 2D square lattice Hamiltonian introduced by Kitaev [113] where each

edge of the lattice represents a spin-1/2 particle (see Fig. 9.1a). Each vertex v or each face f is associated with an operator $H_v = \Pi_{j\in \mathrm{star(v)}}\sigma_j^x$ or $H_f = \Pi_{j\in\partial f}\sigma_j^z$. These operators collide on an even number of edges and hence mutually commute. We seek to encode in the $+1$ coeigenspace of these local stabilizers by choosing the so-called *surface-code Hamiltonian*:

$$H_{\mathrm{surf}} = -U\sum_v H_v - J\sum_f H_f. \tag{9.1}$$

$(U, J > 0)$. The ground states of H_{surf} have a degeneracy $\dim\mathcal{H}_{gr} = 2^{2g+h}$ where g is the genus of the surface and h is the number of holes [50]. Designing lattices with genus $g > 0$, such as the surface of a torus, is challenging, but it is possible to create several holes ($h > 0$) in a planar lattice by, for instance, deactivating regions of the lattice with focused far detuned lasers. Alternatively, the planar code with specific boundary as shown in Fig. 9.1a provides a ground state degeneracy of 2. The logical states are coupled by the operators: $\tilde{Z} = \Pi_{j\in\mathcal{C}_Z}\sigma_j^z$ and $\tilde{X} = \Pi_{j\in\mathcal{C}_X}\sigma_j^x$ where the configurations $C_Z(C_X)$ are strings on the lattice (dual lattice) as illustrated in Fig. 9.1a.

There are several experimental proposals to implement the spin lattice Hamiltonians with topological order. For example, Kitaev's honeycomb lattice Hamiltonian H_{hcb} (see Fig. 9.1b)[114] can be designed in optical lattices with ultracold atoms using controlled spin exchange interactions [56, 189], or with molecules using microwave induced dipole-dipole interactions [145]. With an appropriate choice of coupling parameters [114], the honeycomb lattice Hamiltonian has a gapped abelian phase with a low energy effective Hamiltonian locally equivalent to H_{surf}. In the following, we will assume the system interacts via H_{surf}, but our results are also applicable to other

spin lattice Hamiltonians.

We now consider how to implement the global operations for the spin lattice system. In particular, we are interested in a specific type of global operation: products of Pauli operators on a set of spins whose corresponding edges in the lattice form a connected string. Such global operators are called *string operators*. For example, the generators for the encoded qubits ($\tilde{Z}$ and $\tilde{X}$) are string operators (see Fig. 9.1a). All string operators are equivalent to $S^z_{\mathcal{C}} = \prod_{j\in C} \sigma^z_j$ up to local single spin rotations, where $\mathcal{C}$ is the set of selected spins. In particular, $S^x_{\mathcal{C}} = \prod_{j\in C} \sigma^x_j = \left(\prod_j H_j\right) S^z_{\mathcal{C}} \left(\prod_j H_j\right)$, where $\left(\prod_j H_j\right)$ is the global Hadamard rotation on all memory spins with H_j for the jth spin. Thus, we can use two global Hadamard rotations to convert $S^z_{\mathcal{C}}$ into $S^x_{\mathcal{C}}$.

In our setup, the topological memory consists of a spin lattice of trapped atoms or molecules inside an optical cavity as illustrated in Fig. 9.2a. The off-resonant interaction between the common cavity mode and selected spins is described by the quantum non-demolition (QND) Hamiltonian [197, 176]:

$$H = \chi a^\dagger a \sum_{j\in C} \sigma^z_j. \tag{9.2}$$

Here we assume that the cavity mode has a large detuning Δ from a spin-dependent optical transition as shown in Fig. 9.2b. The coupling strength is $\chi = g^2/2\Delta$, where g is the single-photon Rabi frequency for the cavity mode. The QND Hamiltonian preserves the photon number $n_a = a^\dagger a$ of the cavity mode. In addition, the cavity mode also interacts with an ancilla spin, which will be used to probe anyonic statistics associated with quasi-particles.

Similar to the previous schemes [25, 206] to measure anyonic statistics, we assume

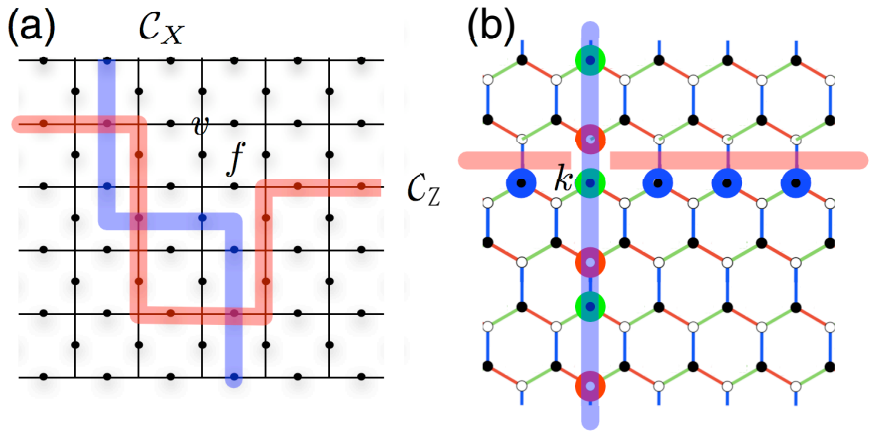

Figure 9.1: Generators for the encoded qubits. (a) A planar code which encodes one logical qubit in the ground states. There is a spin-1/2 particle (filled dot) for each edge of the lattice. The interactions of the local Hamiltonian H_{surf} are along edges that bound a face f, and edges that meet at a vertex v. The strings $\mathcal{C}_{X,Z}$ indicate paths of products of $\sigma^{x,z}$ operators that are logical operators on the code. (b) A nearest neighbor local Hamiltonian H_{hcb} on the honeycomb lattice, with a spin-1/2 particle for each lattice site. The (green, red, blue) edges represent interactions of type $(\sigma^x\sigma^x\ ,\sigma^y\sigma^y\ ,\sigma^z\sigma^z)$ with coupling strength (J_x, J_y, J_z). In the limit that the interactions along the blue links are much stronger than those along the other links, the ground subspace has a gapped $\mathbb{Z}_2$ topological phase [114]. Physical $(\sigma^x, \sigma^y, \sigma^z)$ spin operations as part of the strings $\mathcal{C}_{X,Z}$ are indicated by bold (green, red, blue) circles around the spins. We may implement the vertical string operation in two steps: first apply σ^x rotations to the spins with green circles and then apply σ^y rotations to the spins with red circles. Each step can be implemented with selective addressing [40, 80]. At qubit k, the string crossing, the operation is $\sigma^x_k\sigma^z_k$.

selective addressing of spins in the lattice so that we can perform single spin rotations. The key new ingredient, however, is that we use the common cavity mode to mediate global string operators. We assume that a string of selected atoms can be coupled to the common cavity mode simultaneously, using a control laser beam with appropriately shaped intensity profile [40, 80] as described in Appendix D.1.1. In this way, we avoid problems involving maintaining adiabaticity and localization while braiding quasi-particles. And most importantly, we are able to achieve *controlled-string operations* ($\Lambda\left[S_{\mathcal{C}}^{x,z}\right]$) for an arbitrary string $\mathcal{C}$.

The idea of controlled-string operations can be illustrated by considering a situation when the cavity mode is first prepared in some superposition of zero and one photon states. Within this subspace, the evolution of the QND Hamiltonian for interaction time $\tau = \pi/2\chi$ yields

$$U = \exp\left[-iH\tau\right] = \left[(-i)^{N_C}\prod_{j\in C}\sigma_j^z\right]^{n_a} \tag{9.3}$$
$$= \begin{cases} \mathbf{I} & \text{for } n_a = 0 \\ (-i)^{N_C}\prod_{j\in C}\sigma_j^z & \text{for } n_a = 1 \end{cases},$$

where $N_{\mathcal{C}}$ is the number of elements in $\mathcal{C}$, and the second equality uses the identity $\exp\left[-i\frac{\pi}{2}\sigma_j^z\right] = -i\sigma_j^z$. This unitary evolution will apply the string operator $S_{\mathcal{C}}^z$ to the topological memory, conditioned on one cavity photon. With such controlled-string operations, we can conveniently access the topological memory, and build anyonic interferometry to probe braiding statistics and dynamics of quasi-particles.

In practice, however, it is actually easier to control the ancilla spin rather than to directly manipulate the photon number state. Therefore, in the following, we will

present two approaches to controlled-string operations between the ancilla spin and the topological memory.

9.3 Controlled-string Operations

The key operation of the single photon approach is the evolution of the QND interaction described by equation (9.3). In addition, the cavity mode interacts with a single ancilla spin using spectroscopically resolvable energy levels as shown in Fig. 9.2c. Starting with no photon in the cavity mode $|\text{vac}\rangle$ and ancilla spin in state $\alpha |0\rangle_A + \beta |1\rangle_A$, we can coherently couple the number state of the cavity mode with the state of the ancilla spin by adiabatically increasing the Rabi frequency $\Omega_A(t)$ of the control laser until it is much larger than the single-photon Rabi frequency g'. The intermediate state is then $\alpha |0\rangle_A \otimes |\text{vac}\rangle - \beta |1'\rangle_A \otimes a^\dagger |\text{vac}\rangle$, having the photon number fully correlated with the ancilla spin. Applying the QND interaction with the intermediate state realizes the desired controlled-string operation conditioned on the state of the ancilla spin. Finally, we can reverse the state mapping by adiabatically decreasing the Rabi frequency, which coherently annihilates the photon of the cavity mode and restores the ancilla spin to its logical subspace spanned by $\{|0\rangle_A, |1\rangle_A\}$. Following the procedure summarized in Fig. 9.2d, we can achieve the controlled-string operation:

$$\Lambda[S_{\mathcal{C}}^z] = |1\rangle_A \langle 1| \otimes S_{\mathcal{C}}^z + |0\rangle_A \langle 0| \otimes \mathbf{I}. \tag{9.4}$$

The second approach to controlled-string operations is based on the idea of geometric phase gates [198]. Here, the bosonic field of the cavity mode starts in a coherent state, rather than a superposition of zero and one photon states. If our

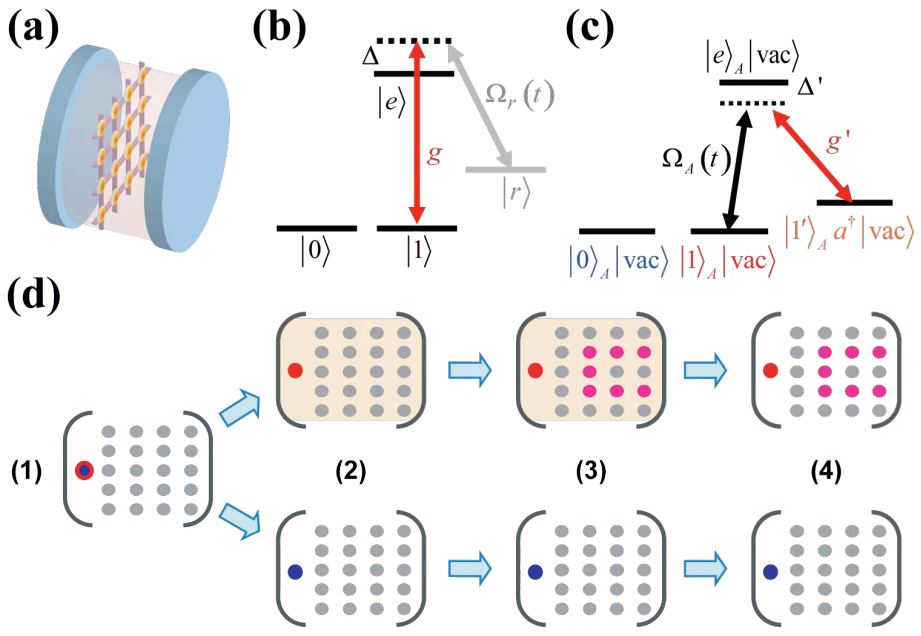

Figure 9.2: Cavity-assisted controlled-string operation based on single photon approach. (a) Inside a cavity, an optical lattice carries spins for topological memory, with individual spin addressability [40, 80]. (b) The energy levels of a selected memory spin ($|0\rangle$ and $|1\rangle$) interacting dispersively with the cavity mode, which implements the QND Hamiltonian of equation (9.2). The coupling coefficient is $\chi = g^2/\Delta$, with single-photon Rabi frequency g and detuning Δ from the excited state $|e\rangle$. A control laser with Rabi frequency $\Omega_r(t)$ couples to the metastable state $|r\rangle$, and it is two-photon resonance with the cavity mode. (c) The energy levels of the ancilla spin (different from memory spins) and the cavity mode for the single photon approach. A different control laser with Rabi frequency $\Omega_A(t)$ connects the states $|1\rangle_A \otimes |\text{vac}\rangle$ and $|1'\rangle_A \otimes a^\dagger |\text{vac}\rangle$, and enables coherent creation and absorption of a cavity photon conditioned on the ancilla spin. (d) Cartoon illustration of the procedure for the implementation of single-photon approach for controlled-string operations: (1) Initialize the ancilla spin (the left highlighted spin) in a superposition state $\alpha|0\rangle_A + \beta|1\rangle_A$ (blue for $|0\rangle_A$ and red for $|1\rangle_A$), with no photon in the cavity and state $|\psi\rangle_S$ for the topological memory. (2) Coherently create a cavity photon (orange shade) for ancilla spin state $|1\rangle_A$ (upper branch); no photon is created for ancilla spin state $|0\rangle_A$ (lower branch). (3) Switch on the interaction between the cavity photon and the selected spins. If there is a cavity photon (orange shade), a non-trivial evolution $S_{\mathcal{C}}^z$ (pink dots) is implemented. (4) Turn off the interaction and coherently absorb the cavity photon into the ancilla spin. Finally the state $\alpha|0\rangle_A \otimes |\psi\rangle_S + \beta|1\rangle_A \otimes S_{\mathcal{C}}^z|\psi\rangle_S$ is prepared.

transformation restores the bosonic field to the initial coherent state, the entire system will accumulate a quantum phase (geometric phase), which is twice the area enclosed by the trajectory in phase space of the bosonic field. We activate the geometric phase gate using an ancilla spin which experiences the QND interaction with the cavity mode that can be selectively turned on and off [40, 80]. As illustrated in Fig. 9.3 and detailed in Appendix D.1.2: if the ancilla spin is in state $|0\rangle_A$, the enclosed area vanishes; if the ancilla spin is in state $|1\rangle_A$, the enclose area has a different sign depending on whether the topological memory is in $+1$ or -1 subspace associated with the string operator $S^z_{\mathcal{C}}$, yielding again equation (9.4).

Various imperfections such as the addressing error, photon loss, and deviation of the QND interaction can degrade the controlled-string operation. The influence from these imperfections can be effectively minimized —deep optical lattice should be applied to suppress the addressing error $N_{\mathcal{C}}\varepsilon_{\text{address}}$, a cavity with high Purcell factor P can be used to reduce the photon loss [165, 146], and quantum control techniques may be introduced to correct the deviation of the QND interaction to arbitrarily high order [194, 27]. In addition, if we use Kitaev's honeycomb lattice model [114] (Fig. 9.1b) to implement the the toric code Hamiltonian, there will be an additional error associated with the string operation, $N_{\mathcal{C}}\varepsilon_{\text{hcb}} \approx N_{\mathcal{C}}\frac{J_x^2+J_y^2}{4J_z^2}$, due to the effective leakage from the low-energy manifold [62]. As discussed in Appendix D.4, the error probability for controlled-string operation is approximately

$$\varepsilon_{\text{string}}\left(N_{\mathcal{C}}\right) \approx \lambda\sqrt{N_{\mathcal{C}}/P} + N_{\mathcal{C}}\left(\varepsilon_{\text{address}} + \varepsilon_{\text{hcb}}\right), \tag{9.5}$$

where the pre-factor $\lambda = \mathbf{2}\pi$ (and $\mathbf{4}\pi^2$) is for the single photon (and geometric phase gate) approach.

9.4 Accessing Topological Quantum Memory

Controlled-string operations provide an interface between the probe qubit which features easy access and efficient manipulation, and the topological memory which provides good storage. To store quantum states we require two operations: the $\mathrm{SWAP}_{\mathrm{in}}$ gate which swaps the state of a probe qubit A to memory M initialized in $\left|\tilde{0}\right\rangle_M$ and the $\mathrm{SWAP}_{\mathrm{out}}$ which swaps back to a probe qubit prepared in $\left|0\right\rangle_A$.

$$\mathrm{SWAP}_{\mathrm{in}} = H_A \cdot \Lambda\left[\tilde{Z}\right] \cdot H_A \cdot \Lambda\left[\tilde{X}\right],$$
$$\mathrm{SWAP}_{\mathrm{out}} = \Lambda\left[\tilde{X}\right] \cdot H_A \cdot \Lambda\left[\tilde{Z}\right] \cdot H_A,$$

where H_A is the Hadamard gate acting on the probe qubit, and $\Lambda\left[\tilde{S}\right]$ represents a controlled-string operation. In addition, universal rotations of the encoded qubit (generally, arbitrary unitaries generated by string operators) over the topological memory can be implemented either by teleportation of quantum gates or by direct geometric phase gate. (See Appendix D.5 for details.) We remark that the ancilla spin can also be entangled with another ancilla spin from a different cavity, and therefore our topological memories can be used for quantum networks [55, 130, 9, 103].

To compare the topological memory and unprotected single-spin memory, we introduce the decoherence rate q for the unprotected spin due to low-frequency noise. The topological memory can significantly reduce the decoherence rate to $q \times (\delta h/J)^N$, where $\delta h \ll J$ is the magnitude of the noise perturbation on individual spins and N is the length of the minimal string associated with the generators for encoded qubits [113]. Meanwhile, errors associated with four controlled-string operations $4\varepsilon_{\mathrm{string}}(N)$ should be taken into account. Therefore, in terms of total error prob-

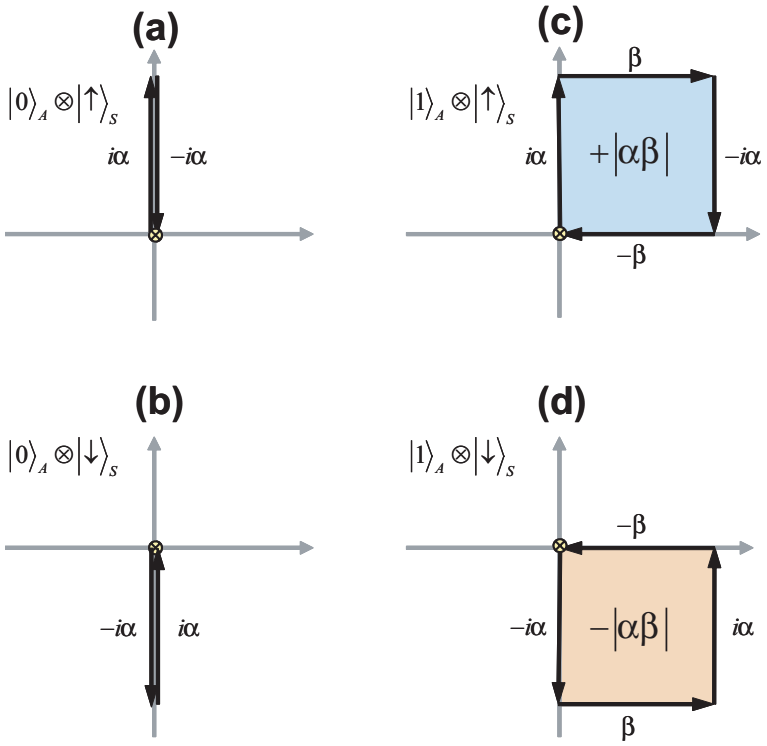

Figure 9.3: Phase accumulation for the approach with geometric phase gate [equation (D.2)]. We use $|\uparrow\rangle_S$ and $|\downarrow\rangle_S$ to represent $+1$ and -1 subspaces of memory spins associated with the string operator $S^z_{\mathcal{C}}$, respectively. (a)(b) When the ancilla spin is in $|0\rangle_A$ state, the enclosed area vanishes. When the ancilla spin is in $|1\rangle_A$ state, (c) for the subspace $|\uparrow\rangle_S$ the enclose area is $|\alpha\beta|$; (d) for the subspace $|\downarrow\rangle_S$ the enclosed area is $-|\alpha\beta|$. The quantum phase accumulated is twice the area enclosed.

ability, the topological memory outperforms the single-spin memory for storage time $t > 4\varepsilon_{\text{string}}(N)/q$. (See Appendix D.4 for details).

9.5 Anyonic Interferometry

We now describe how to use controlled-string operations to extract the statistical phase acquired when braiding abelian anyons. The definition of anyonic statistics usually relies on the adiabatic transport of quasi-particles around each other [3], with

the required condition of adiabaticity to keep the system in the same manifold of excited states and prevent exciting additional degrees of freedom. Note that this procedure relies explicitly on the existence of the Hamiltonian. This is fundamentally different from anyonic simulation approaches [87, 133, 157] not using topological Hamiltonian, which only probe the non-trivial commutation relations of spin operators and initially entangled quantum states. However, anyonic statistics is a property of quasi-particles associated with the Hamiltonian and not just with some specially prepared initial state.

For our spin lattice system with H_{surf}, there are two types of anyons [113]: (1) z-particles on the vertices and (2) x-particles on the faces of the lattice(see Fig. 9.4a,b). These anyons are created in pairs (of the same type) by string operators: $|\psi^z(l)\rangle = S_l^z |\xi\rangle$ and $|\psi^x(l)\rangle = S_{l'}^x |\xi\rangle$, where $|\xi\rangle$ is some ground state of the spins, and $S_l^z = \Pi_{j\in l}\sigma_j^z$ and $S_{l'}^x = \Pi_{j\in l'}\sigma_j^x$ are string operators associated with string l on the lattice and string l' on the dual lattice, respectively (see Fig. 9.4). In our approach, string operators can be used to effectively move quasi-particles quickly along the string trajectory but without exciting other quasi-particles. For example, effective motion of quasi-particles with/without braiding is shown in Fig. 9.4a,b. This evolution is described by

$$S_{l_4'}^x U_{t_3} S_{l_3}^z U_{t_2} S_{l_2'}^x U_{t_1} S_{l_1}^z |\Psi_{\text{initial}}\rangle = e^{i\theta_{\text{tot}}} |\Psi_{\text{initial}}\rangle , \tag{9.6}$$

where we introduce time delays, represented by unitary evolution U_t, between string operations. The goal of these delays is to check that the system stays in the manifold with a fixed number of quasi-particles where time delays lead to only a trivial dynamical phase. On the other hand, if the string operator were to create some complicated

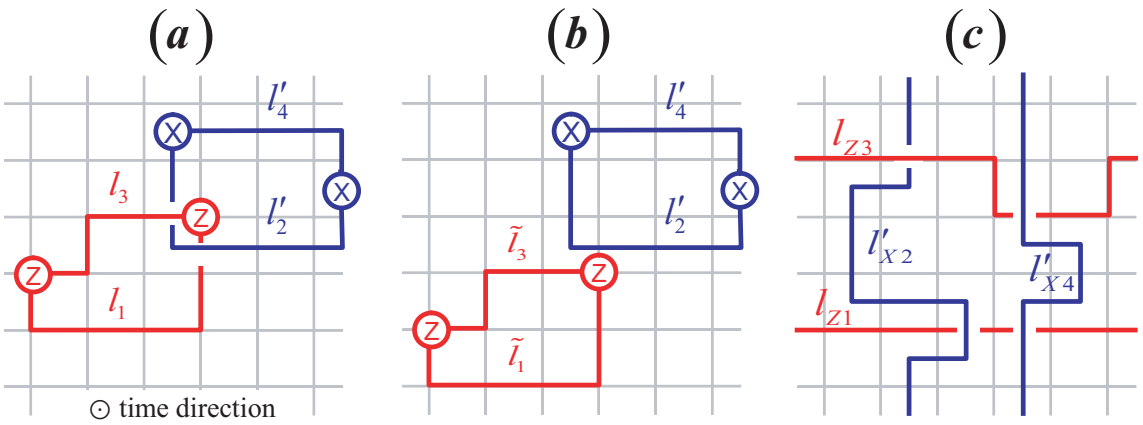

Figure 9.4: Braiding operations. (a)/(b) We can move x-particles and z-particles in tangled/untangled loops using string operators to implement operations with/without braiding of anyons. (c) We can also apply generators for the encoded qubits to achieve the braiding operation. The braiding statistics of anyons should be invariant under non-crossing deformations of the loops [71].

intermediate states, time delays would lead to complete decoherence. The total phase $e^{i\theta_{\text{tot}}}$ includes both the dynamical contribution $e^{i\eta} = e^{i2J(t_1+2t_2+t_3)}$ and the statistical contribution $e^{i\theta} = -1$ (or $+1$) in the presence (or absence) of braiding. Therefore, we can unambiguously measure the statistical phase if we can measure $e^{i\theta_{\text{tot}}}$ for both cases.

The following interference experiment can be used to measure the phase $e^{i\theta_{\text{tot}}}$. First, we prepare the probe qubit in a superposition state $(|0\rangle+|1\rangle)/\sqrt{2}$. We then use controlled-string operations to achieve interference of the following two possible evolutions: if the probe qubit is in state $|0\rangle$, no operation is applied to the memory spins; if the probe qubit is in state $|1\rangle$, the operation $S^x_{l'_4} U_{t_3} S^z_{l_3} U_{t_2} S^x_{l'_2} U_{t_1} S^z_{l_1}$ is applied to the topological memory, which picks up the extra phase $e^{i\theta_{\text{tot}}}$ we want to measure. After the controlled-string operations, the probe qubit will be in state $(|0\rangle + e^{i\theta_{\text{tot}}}|1\rangle)/\sqrt{2}$. Finally, we project the probe qubit to the basis of $|\xi_\pm\rangle \equiv (|0\rangle \pm e^{i\phi}|1\rangle)/\sqrt{2}$ with

$\phi \in [0, 2\pi)$, and measure the operator $\sigma_\phi \equiv |\xi_+\rangle \langle\xi_+| - |\xi_-\rangle \langle\xi_-|$. The measurement of $\langle\sigma_\phi\rangle$ v.s. ϕ should have fringes with perfect contrast and a maximum shifted by $\phi = \theta_{\text{tot}}$. In fact this scheme can be used to measure abelian statistics for an arbitrary finite cyclic group as described in Appendix D.1.4.

It is crucial to verify that the outcome of the anyonic interferometry is invariant under repeated experiments with deformed string operators (see Fig. 9.4) [71]. For example, the two ground states of the 2D compass model [54] are coupled by perpendicular global X and Z string operators and the phase measured using the interferometry scheme above would also yield a phase -1 due to the anti-commutation relations at the crossing spin. Yet the ground states are not topologically ordered because deformed string operators do not preserve the ground subspace. Since our anyonic interferometry can test all possible braiding operations, we can unambiguously verify the topological property of anyons.

Various imperfections will degrade the signature of anyonic statistics. The string operators may have errors that excite unwanted anyons, and the topological memory may not fully restore to the ground state after braiding. In addition, the topological memory may have anyons from imperfect initialization. If these anyons are enclosed by the braiding loops, they will affect the phase factor associated with braiding. However, neither of these imperfections will prevent us from probing anyonic statistics, since they only reduce the contrast of the anyonic interferometry without shifting the fringes of $\langle\sigma_\phi\rangle$. We may even distinguish the two types of imperfections from the contrast. The reduction of the contrast is proportional to the length of the loops for errors from string operators, while it is proportional to the area enclosed by the loops

for errors from imperfect initialization (see discussion in Appendix D.1.3).

9.6 Probing and Control Anyonic Dynamics

Our anyonic interferometry provides a tool to study the dynamics of anyons. First, consider repeating the protocol [equation (9.6)] for anyonic interferometry with the time delays $\{t_j\}_{j=1,2,3}$ between the four controlled-string operations. Processes of anyonic creation, propagation, braiding, and annihilation will induce a time dependence of the final state wavefunction in a general expression: $|\Psi_{\text{final}}\rangle = \alpha(\{t_j\})\,|\Psi_{\text{initial}}\rangle + \beta(\{t_j\})\,|\Psi_{\perp}(\{t_j\})\rangle$, where $\langle\Psi_{\text{initial}}|\Psi_{\perp}(\{t_j\})\rangle = 0$. Since the reduced density matrix of the probe qubit is $\rho = \frac{1}{2}\begin{pmatrix} 1 & \alpha(\{t_j\}) \\ \alpha^*(\{t_j\}) & 1 \end{pmatrix}$, we can measure the complex coefficient $\alpha(\{t_j\})$ using quantum state tomography [154] of the probe qubit.

Probing anyonic statistics can be regarded as special cases, with $\alpha = e^{i(\theta+\eta)}$ or $e^{i\eta}$, and $\beta = 0$. Although the anyons are immobile for the surface code Hamiltonian, the mobility of quasi-particles may change when we include local perturbations, because the excited states with anyons are highly degenerate and any small perturbation to the Hamiltonian can dramatically change the eigen-wavefunctions. Consider for example a specific diffusion model for anyons induced by the local perturbation

$$H_{pert} = \sum_{\alpha\in\{x,y,z\}} \sum_{e\in\text{All spins}} h_e^{\alpha}\sigma_e^{\alpha}, \tag{9.7}$$

where the $h_e^{x,z}$ field components cause diffusion of x(z)-particles and the h_e^{y} field component causes diffusion of fermionic particles (pairs of neighboring x-particle and

z-particle). (See Appendix D.6 for details). The nature of the perturbation (e.g., time independent or changing with time) determines diffusion dynamics of anyons, which can be observed from the coefficient $\alpha(\{t_j\})$ using our anyonic interferometry.

In addition, we can even control the diffusion dynamics of anyons. We introduce the effective time-reversal operations $U_\pi^z \equiv \prod_{e\in\text{All spins}} \sigma_e^z$ and $U_\pi^x \equiv \prod_{e\in\text{All spins}} \sigma_e^x$, which anti-commute with $h_e^x\sigma_e^x$ and $h_e^z\sigma_e^z$ terms of H_{pert}, respectively. The combination of these operations (e.g., $U_\pi^z \overset{\tau/4}{\cdots\cdots} U_\pi^x \overset{\tau/4}{\cdots\cdots} U_\pi^z \overset{\tau/4}{\cdots\cdots} U_\pi^x \overset{\tau/4}{\cdots\cdots}$) is analogous to spin-echo pulses in NMR [129], which can effectively reverse anyonic diffusion caused by static perturbations and consequently extend the fringe contrast of anyonic interferometry to longer time delays, as illustrated in Fig. 9.5. In essence, by applying these global operations, we can localize the anyons without any trapping potential. (See Appendix D.6 for details.) Note that the anyonic interferometry is closely related to the Ramsey experiments in atomic physics, which can now be performed with anyonic quasi-particles.

9.7 Outlook

Controlled-string operations can be applied to other lattice Hamiltonians as well [5, 147], which may provide robust quantum memory with their degenerate ground states. For example subsystem codes [5] can be constructed out of 2D and 3D nearest neighbor spin-1/2 interactions that are realizable with atomic systems [56, 145]. Our approach can be adapted to perform the logical operations generated by strings or planes of Pauli operators in the 2D and 3D subsystem codes, respectively. In addition, the ability to measure global operators on a spin lattice provides a means to probe

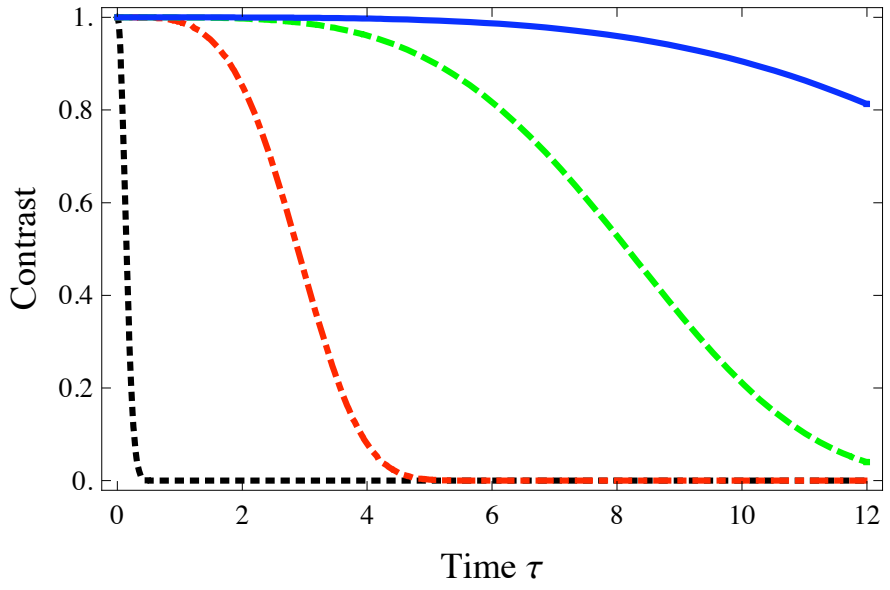

Figure 9.5: Fringe contrast of anyonic interferometry as a function of time (in units of $\left\langle (h_e^x)^2 \right\rangle^{-1/2}$) for anyonic diffusion. The fringe contrast quickly reduces due to anyonic diffusion (black dotted line). However, we can extend the fringe contrast to longer times by applying one (red dotdashed line), four (green dashed line), or ten (blue solid line) pairs of time-reversal operations of U_π^z within the time interval τ. For clarity, we consider only the diffusion of two intermediate x-particles induced by the perturbation $h_e^x \sigma_e^x$ from equation (9.7). We assume that the controlled-string operations are ideal and the random field h_e^x is a Gaussian random process with correlation time $\tau_c = 10$. (See Appendix D.6 for details.)

other properties of topological phases. For example, a class of topologically ordered spin states known as string net states [127], which includes the ground states of H_{surf}, have the property that they are invariant under large closed loop operations. In the present case, these operators are $X_{\text{loop}}(Z_{\text{loop}}) = \prod_{j \in C^{closed}_{X,Z}} \sigma^{x,z}$ which have expectation value 1. A perturbation on H_{surf} in the regime $U \gg J$, by, e.g. a magnetic field, acts like a string tension that reduces the amplitude of large loops (on a vacuum reference state). In fact there are two phases as a function of the strength of the perturbation. For very weak perturbations its has been argued that the loop order parameter scales with the perimeter of the loop while for strong perturbations it scales with the area [94]. These are known as deconfined and confined phases in analogy to lattice gauge theory and are examples of phenomena that could be observed using our protocol. It may also be interesting to consider adapting the present protocol to spin-lattice systems with non-abelian anyons.

Appendix A

Appendices to Chapter 5

Here we present some detailed information for Chapter 5, including the experimental methods, the derivation of the effective Hamiltonian, the model for nuclear spin depolarization under optical illumination, the justification of the optimized SNR, and the simulation for the repetitive readout.

A.1 Methods

A.1.1 Sample

The nitrogen-vacancy color centers used for our repetitive readout experiments are found within a bulk, single crystal type IIa natural diamond with a remarkably low native nitrogen impurity concentration. The lack of paramagnetic defects in this sample is believed to be the primary reason for long ($> 500\mu s$) spin dephasing times of the NV center electronic spin. The ^{13}C nuclei within the lattice are randomly distributed and have a natural isotope fraction, 1.1% relative to all carbon nuclei.

A.1.2 Isolation of single NV centers

We isolate single NV centers using standard confocal microscopy techniques. The NV centers are optically excited using green light (λ_{ex} = 532 nm, sourced from a Coherent Compass 315M-100 laser). We focus the green spot to a nearly diffraction-limited spot-size using an oil immersion objective (Nikon CFI Apochromat TIRF 100X, NA = 1.49) focused within a depth of 50 μm of the diamond surface. Fluorescence emission from the lowest lying excited triplet state (^3E level of NV [136]) is collected within the phonon sideband, starting from the zero phonon line (λ_{ZPL} = 637nm) and extending to 750 nm. This light is focused onto a single-mode optical fiber (NA=.12, MFD = 4.3μm), which acts as a small aperture spatial filter and rejects light emanating from outside the focal plane. Photons incident on the fiber are detected using an avalanche photodiode module (PerkinElmer SPCM-AQR-13).

In order to find a single NV center within the diamond, we image a 50μm x 50μm area within a fixed focal plane by changing the incidence angle of the excitation light wavefronts at the objective. This is accomplished by using a fast, closed-loop XY scanning mirror system (Cambridge Technology, 6215H scanning mirrors). Different focal planes are examined by moving the entire sample, along the tube axis of the objective, using a closed-loop z-axis piezo stage (Physique Instrument, P-620.ZCD). The density of NV centers within the sample is small enough that we can resolve single bright spots and collect light from these emitters. In order to verify that these spots are single centers, we measure the autocorrelation function of the emitted light in a Hanbury-Brown-Twiss style setup ($g_2(\tau)$). Furthermore, we monitor the fluorescence intensity under resonant microwave excitation to verify that these single emitters are

indeed nitrogen-vacancy centers, with a finite ESR response near 2.87 GHz at zero applied magnetic field. If an NV center is strongly coupled to a ^{13}C spin within the lattice, this appears as an additional splitting in the the spectrum of microwave response.

A.1.3 Spin control of the NV centers

At room temperature, the three spin eigenstates of the NV center ($|0\rangle_e$, $|1\rangle_e$, and $|-1\rangle_e$) are equally populated. Optical excitation at 532 nm, excites the ground state triplet of the NV to an excited vibronic state, which decays to the first excited triplet state. The population in these spin states will either radiatively decay back to the ground state or undergo an intersystem crossover to a metastable singlet state. This single state will then decay into the $|0\rangle_e$ state exclusively. This provides a mechanism for optical pumping of the NV center spin. After 1 μs period of illumination (near optical saturation) the $|\pm 1\rangle_e$ states are optically pumped to the $|0\rangle_e$ state in excess of 95%. This conveniently prepares an initial state $|0\rangle_e$ after readout, but barely perturbs the any nuclear spin state.

We apply microwave and radiofrequency (RF) fields to individual NV centers by driving a small copper wire (15μ m diameter) placed on the diamond surface and secured to an impedance matched stripline waveguide. Three separate frequency synthesizers are used to generate the three frequencies needed for generating full spin control of the electronic-nuclear system, identified as MW1, MW2 and RF in Figure 1D of the main text. These values are cited below. Separate amplifiers for the microwave (OphirRF, S-Band, 15W, Model XRF738) and RF (ENI, 10W, Model

310-L) allow us to generate magnetic fields of about 10 gauss. Short microwave pulses, on the order of 10ns, a generated by gating an SPST switch with an extremely short rise time (Custom Microwave Components S0947A-02, rise time 3ns). Timing of the counter gating, RF and microwave pulses and the AOM is coordinated by a multiple channel TTL pulse generator (SpinCore PulseBlaster ESR-Pro, 400MHz), with up to 2.5ns timing resolution.

For pulsed experiments, measurement of the spin state involves counting the NV fluorescent photons after optical pumping. This involves monitoring the phonon side band fluorescence under optical excitation within 100-500ns [136]. Short optical pulses are achieved using an acousto-optic modulator (AOM) with a digital driver (Isomet 1250C-848) setup in a double-pass setup [53]. Rise times of the optical pulses are about 20ns and thus enable sufficient contrast between the two spin states.

In order to remove systematic fluctuations in the counting rates of the fluorescent photons (e.g. heating and defocusing of the NV due to long microwave pulses), we take a series of measurements before *each* run of the experiment. Prior to any of our repeated readout experiments, we measure the fluorescence after the following microwave pulse configurations: (1) no microwave pulse, (2) a single MW1 π-pulse, (3) a single MW2 π-pulse, and (4) a MW1 and MW2 π-pulse. Conditions (1) and (4) set the maximum and minimum count rates for the NV center readout and set the relative scale for the Rabi experiments (Figure 1 of main text).

Random, slow drifting of the counting rates of the NV center (e.g. due to day/night temperature cycles or mechanical perturbations) are accounted for by a software-based feedback mechanism. Prior to each experimental average ($\sim 10^5$ rep-

etitions), we take a reference count rate of the NV fluorescence. If this is outside an allowed threshold, we vary the scanning mirror and piezo stage voltages in order to maximize the counting rate. In this way, defocusing of the NV center can be corrected and stabilized. Over the course of six months, such tracking has enabled us to study the same center exclusively.

A.1.4 Magnetic field tuning

We use three sets of purpose-built orthogonal coil windings in a quasi-Helmholtz configuration to apply the static magnetic field for tuning the spin resonance of the NV. Each winding consists of roughly 100 turns and each pair can generate up to 40 gauss in three orthogonal directions when driven with 4A, direct current. By independently changing the current supplied to each coil pair, we can align the magnetic field vector relative to the axis of symmetry of the NV center ($\hat{z}$). Coarse measurements of the magnetic field amplitudes are made using a three-axis hall sensor (Ametes MFS-3A). For more precise alignment, we measure the ESR response of the NV in both a continuous wave and pulsed (electron spin echo envelope modulation) manner, as described below.

A.1.5 Microwave and RF control pulses

As shown in Fig. 1A, we use MW1 to drive the transition between $|0\rangle_e |\downarrow\rangle_{n1}$ and $|1\rangle_e |\downarrow\rangle_{n1}$, and MW2 for the transition between $|0\rangle_e |\uparrow\rangle_{n1}$ and $|1\rangle_e |\uparrow\rangle_{n1}$. The two transitions differ in energy by $\Delta = 13.675\,(1)$ MHz, mostly contributed from the hyperfine interaction between spins $\mathbf{e}$ and $\mathbf{n}_1$. When the microwave (MW) Rabi

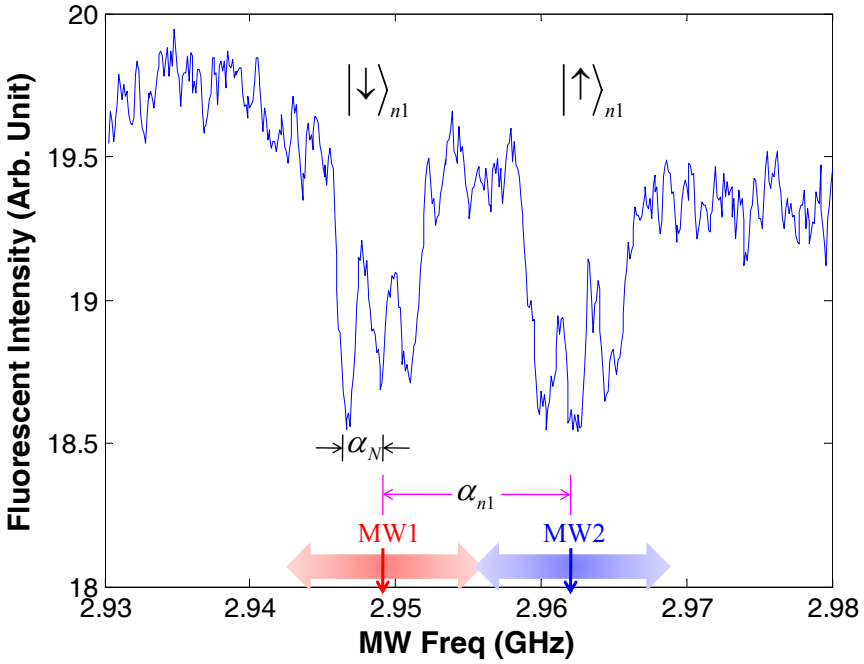

Figure A.1: Fluorescence detected electron spin resonance of the NV center. We monitor the fluorescence under optical excitation at λ_{ex} while sweeping the carrier frequency of the microwave. When the resonance condition is met, we see a drop in the count rate, signifying a transfer of population to the $m_s = \pm 1$ states. Here we show only the portion of the spectrum involving transitions between $m_s = 0$ and 1. In the absence of any nuclear spins, this condition would occur at single frequency, but is split due to the hyperfine interaction with nearby nuclear spins. The six lines shown correspond to coupling of the NV to a nearby ^{13}C ($\mathbf{n_1}, I = 1/2$) and ^{14}N ($I = 1$) with hyperfine couplings α_N and α_{n1} respectively. The two microwave driving frequencies (MW1 and MW2) address the $|\downarrow\rangle_{n1}$ and $|\uparrow\rangle_{n1}$ manifolds and differ in frequency by α_{n1}. The MW Rabi frequency ($\Omega = 7.89$ MHz) is sufficiently large to drive the triplet lineshape for each manifold.

frequency Ω_{MW} is comparable to the detuning Δ, the effect of off-resonant driving should be considered. Fortunately, if we are only interested in π-pulses, the effect of off-resonant driving can be suppressed. For example, we may choose the bare MW Rabi frequency $\Omega_{MW} = \Delta/\sqrt{3} = 7.89$ MHz with pulse duration π/Ω, which performs a π rotation for the resonant transition. For the Δ-detuned transition, the effective Rabi frequency is $\sqrt{\Omega^2 + \Delta^2} = 2\Omega$, and the operation gives a (trivial) 2π rotation. Thus, in principle, we can achieve a perfect $C_{n1}NOT_e$ gate with an MW1 (or MW2) π pulse, despite the finite detuning Δ.

For this experiment the two resonance frequencies of the microwave transitions are $\nu_{MW1} = 2.962$ GHz and $\nu_{MW2} = 2.949$ GHz. The radiofrequency field is tuned to the nuclear spin splitting at $\nu_{RF} = 13.675$ MHz. We note that the duration for a π-pulse on this frequency is about 5μs, which indicates a Rabi frequency of almost 100 kHz. This nuclear Rabi frequency is enhanced from that of a ^{13}C nucleus ($\gamma_C = 1.1$kHz/ Gauss) due to the pseudo-nuclear Zeeman effect [1]. This affect is due to the fact that the field inducing transitions of the nuclear spin is enhanced due to the strong hyperfine coupling between the nucleus and the electronic spin.

In addition, we must also consider the hyperfine interaction with the unpolarized ^{14}N nuclear spin, with $I = 1$ and hyperfine coupling strength $\alpha_N = 2.1\,(1)$ MHz, which gives the triplet splitting for both transition lines in the ESR spectrum (Fig. SA.1). At room temperature, the ^{14}N nuclear spin is in a completely mixed state, with equal probability in the spin states $I_z = 0, \pm 1$.

The splitting associated with ^{14}N nuclear spin can introduce a small detuning $\pm\alpha_N$ to the resonant transition, resulting in an error probability $\sim (\alpha_N/\Omega_{MW})^2$. We

estimate the average error probability for the MW π-pulse to be $\varepsilon_{\text{res}}^{MW} \approx 0.07$ for the resonant transition. In addition, the splitting associated with ^{14}N can also affect the Δ-detuned transition. In the presence of extra detuning $\pm\alpha_N$, the 2π rotation for the Δ-detuned transition is no longer perfect. The estimated average error probability for the MW π-pulse is $\varepsilon_{\text{det}}^{MW} \approx 0.01$ for the Δ-detuned transition.

A.2 Effective Hamiltonian

In this appendix, we start with the full spin Hamiltonian that includes both the electronic spin and the nuclear spins. We obtain the effective Hamiltonian using time-independent perturbation theory. We then study the hyperfine coupling associated with the first nuclear spin ($\mathbf{n}_1$) to justify the claim that the quantization axis of spin $\mathbf{n}_1$ is effectively the same when spin $\mathbf{e}$ is $|m_s = 0\rangle_e$ or $|m_s = 1\rangle_e$. Finally, we use the effective Hamiltonian to study the electron-mediated coupling between the two nuclear spins $\mathbf{n}_1$ and $\mathbf{n}_2$.

A.2.1 Full hamiltonian

To calculate the interaction between nuclear spins, we start with the full spin Hamiltonian for the ground state triplet ($S = 1$) of the NV center electronic spin. We choose a coordinate system with $\hat{z}$ along the NV axis (the [111] crystal axis), $\hat{x}$ and $\hat{y}$ fixed arbitrarily by taking $\hat{x}$ to lie in a horizontal plane with respect to the laboratory coordinates.

First, we start by identifying the physical interactions between the spins of the

system, ordered by their energy (descending):

$$H = H_{ZFS} + H_{EZ} + H_{HF} + H_{NQ} + H_{NZ} + H_{DD}. \tag{A.1}$$

H_{ZFS} is the zero field splitting term, due to the spin-spin interaction of the two unpaired electrons comprising the NV center [136]. H_{EZ} is the Zeeman interaction between the electron and an applied magnetic field B. H_{HF} is the hyperfine interaction between the electronic spin and any nuclear spin within the diamond lattice. In general, it will have an isotropic Fermi contact contribution and a dipole-dipole contribution. H_{NQ} are nuclear quadrupolar splitting for nuclei with spin angular momentum $I \geq 1$. Only the ^{14}N nuclear spin of the NV center ($I = 1$) has a quadrupolar coupling. Since it was shown in [37] that this spin is a constant of the motion, we hereby drop the quadrupolar term from the calculation. H_{NZ} is the nuclear Zeeman interaction between the external magnetic field and a nuclear magnetic moment. Finally, H_{DD} is the dipole-dipole interaction between two nuclear spins.

At static magnetic fields smaller than 100 mT, the symmetry axis of the zero field splitting ($\hat{z}$) defines the quantization axis for the NV center. In this coordinate system the zero field splitting is:

$$H_{ZFS} = \Delta(S_z^2 - \frac{1}{3}S^2) + E(S_x^2 - S_y^2) \tag{A.2}$$

For the ground state of the NV center, $\Delta = 2.87$ GHz and $E \approx 0$ for perfect C_{3v} symmetry. We can then decompose the Hamiltonian into secular ($\|$) and non-secular ($\perp$) terms, depending on whether or not parts of the various interactions commute with S_z^2:

$$H = H_{NV,\parallel} + H_{NV,\perp} + H_B + \sum_{\mathsf{j}} \left(H^{\mathsf{j}}_{\mathrm{hf},\parallel} + H^{\mathsf{j}}_{\mathrm{hf},\perp} \right) + \sum_{\mathsf{j}>\mathsf{k}} H^{\mathsf{j},\mathsf{k}}_{nuc},$$

where the secular ($\parallel$) and non-secular ($\perp$) terms are:

$$\begin{aligned}
H_{ZFS+EZ,\parallel} &= \Delta S_z^2 - \gamma_e B_z S_z \\
H_{EZ,\perp} &= -\gamma_e \left(B_x S_x + B_y S_y \right) \\
H_{NZ} &= -\gamma_0 \sum_{\mathsf{j}} \sum_{n=x,y,z} B_n I_n^{(j)} \\
H^{\mathsf{j}}_{\mathrm{HF},\parallel} &= S_z \sum_{n=x,y,z} \alpha^{\mathsf{j}}_{zn} I^{\mathsf{j}}_n \\
H^{\mathsf{j}}_{\mathrm{HF},\perp} &= \sum_{n=x,y,z} \left(S_x \alpha^{\mathsf{j}}_{xn} + S_y \alpha^{\mathsf{j}}_{yn} \right) I^{\mathsf{j}}_n \\
H^{\mathsf{j},\mathsf{k}}_{DD} &= \sum_{m,n=x,y,z} I^{\mathsf{j}}_m \beta^{\mathsf{j},\mathsf{k}}_{mn} I^{\mathsf{k}}_n,
\end{aligned}$$

Here I^{j} refers to the the j-th nuclear spin, γ_e and γ_0 are the electronic and ^{13}C gyromagnetic ratios, and we note that $\gamma_e < 0$, $\gamma_0 > 0$. (We assume no $\mathbf{g}$ tensor anisotropy for the NV center and have used the convention of $\hbar = 1$.) α^{j}_{mn} is the hyperfine interaction tensor between the electron and the j-th nuclear spin of ^{13}C and β^{jk}_{mn} are the matrix elements for the dipolar coupling tensor between nuclear spins j and k. (Note that sans-serif subscripts demarcate the spin and are not exponents). For remote nuclear spins, the hyperfine interaction is mostly dipolar interaction, while the Fermi contact interaction dominates for nearby nuclear spins [74].

A.2.2 Deriving the effective hamiltonian

Since Δ is the largest energy scale, we may write the effective Hamiltonian in a $1/\Delta$ series. The zeroth order terms commute with ΔS_z^2:

$$H_0 = H_{NV,\parallel} + H_B + \sum_{\mathsf{j}} H^{\mathsf{j}}_{\mathrm{hf},\parallel} + \sum_{\mathsf{j}>\mathsf{k}} H^{\mathsf{j},\mathsf{k}}_{nuc}. \tag{A.3}$$

The next order correction is the virtual transitions between m_s sub-levels driven by either a transverse external magnetic field or by the hyperfine field of a nearby nuclear spin. The total perturbation

$$U = H_{NV,\perp} + \sum_{\mathsf{j}} H^{\mathsf{j}}_{\mathrm{hf},\perp}.$$

Within each m_s subspace (with $m_s = 0, \pm 1$), the first order Hamiltonian $P_{m_s} H_0 + H_1^{m_s}$ can be found by using second order perturbation theory [205]:

$$H_1^{m_s} = P_{m_s} U \frac{1}{E_{m_s} - (\mathbb{1} - P_{m_s}) H_0 (\mathbb{1} - P_{m_s})} U P_{m_s},$$

where $\mathbb{1}$ is the identity operator, $P_{m_s} = |m_s\rangle \langle m_s|_e$ is the projection operator to the subspace with electronic spin projection m_s along the $\hat{z}$ axis, and $E_{m_s} = \Delta m_s^2 - g_e \mu_e B_z m_s$ is the zeroth-order energy of the electronic spin under $H_{NV,\parallel}$. Using this formalism, we obtain the effective Hamiltonian for each m_s subspace:

$$H_1^{m_s} = -\gamma_0 \sum_{\mathsf{j}} \sum_{m,n=x,y,z} B_m \delta g^{\mathsf{j}}_{mn} I^{\mathsf{j}}_n + \sum_{\mathsf{j}>\mathsf{k}} \sum_{m,n=x,y,z} I^{\mathsf{j}}_m \delta \beta^{\mathsf{j},\mathsf{k}}_{mn} I^{\mathsf{k}}_n + \cdots \tag{A.4}$$

where the correction of the g-tensor is

$$\delta g^{\mathsf{j}}_{mn}(m_s) = \frac{(3|m_s| - 2)}{\Delta} \left(\frac{\gamma_e}{\gamma_0}\right) \begin{pmatrix} \alpha^{\mathsf{j}}_{xx} & \alpha^{\mathsf{j}}_{xy} & \alpha^{\mathsf{j}}_{xz} \\ \alpha^{\mathsf{j}}_{yx} & \alpha^{\mathsf{j}}_{yy} & \alpha^{\mathsf{j}}_{yz} \\ 0 & 0 & 0 \end{pmatrix}, \tag{A.5}$$

and the correction of the nuclear spin interaction due to the electron-mediated process is

$$\delta\beta^{\mathsf{j},\mathsf{k}}(m_s) = \frac{(3|m_s|-2)}{2\Delta} \begin{pmatrix} \alpha^{\mathsf{j}}_{xx} & \alpha^{\mathsf{j}}_{xy} & \alpha^{\mathsf{j}}_{xz} \\ \alpha^{\mathsf{j}}_{yx} & \alpha^{\mathsf{j}}_{yy} & \alpha^{\mathsf{j}}_{yz} \\ 0 & 0 & 0 \end{pmatrix}^T \begin{pmatrix} \alpha^{\mathsf{k}}_{xx} & \alpha^{\mathsf{k}}_{xy} & \alpha^{\mathsf{k}}_{xz} \\ \alpha^{\mathsf{k}}_{yx} & \alpha^{\mathsf{k}}_{yy} & \alpha^{\mathsf{k}}_{yz} \\ 0 & 0 & 0 \end{pmatrix},$$

or equivalently

$$\delta\beta^{\mathsf{j},\mathsf{k}}_{mn}(m_s) = \frac{(3|m_s|-2)}{2\Delta} \sum_{l=x,y} \alpha^{\mathsf{j}}_{lm}\alpha^{\mathsf{k}}_{ln}. \tag{A.6}$$

Note we have made the assumption that $\Delta \gg |\gamma_e B_z|$.

The first term in Eq.(A.4) is the pseudo nuclear Zeeman effect, arising from the enhancement of the external magnetic field due to the hyperfine interaction [1]. The enhancement vanishes when we carefully align the external magnetic field along the NV axis (i.e., $\vec{B} = B_z\vec{e}_z$). This is because $\delta g^{\mathsf{j}}_{zn}(m_s) \equiv 0$ (i.e., all elements vanish in the third row of Eq. (A.5)), and consequently there is *no enhancement* for external magnetic field along the z (i.e., NV) axis. Thus, all ^{13}C nuclear spins share the *same* quantization axis (i.e., along the NV axis) and they have the *same* Zeeman splitting $\omega_0 = \gamma_0 B_z \approx 32\,(1)$ kHz, regardless of the individual hyperfine interactions [1]. The second term in Eq.(A.4) is the electron-mediated interaction among the nuclear spins, with the correction to the dipolar interaction tensor.

Therefore, we obtain the effective Hamiltonian of the nuclear spin for each m_s

[1]Note that our earlier experiment [63] explores a different regime, where the external magnetic field has a transverse component with respect to the NV axis. Because of the anisotropy of the g-tensor for proximal nuclear spins, the transverse component can be enhanced depending on the hyperfine interaction. Thus, the proximal nuclear spins can have very different quantization axes, and different effective Zeeman splittings as well [37].

subspace

$$\begin{aligned} H^{m_s} &= H_0^{m_s} + H_1^{m_s} \\ &= \left(\Delta \left|m_s\right| - \gamma_e B_z m_s\right) - \sum_{\mathsf{j}} \omega_0 I_z^{\mathsf{j}} + m_s \sum_{n=x,y,z} \alpha_{zn}^{\mathsf{j}} I_n^{\mathsf{j}} + \sum_{\mathsf{j}>\mathsf{k}} \sum_{m,n=x,y,z} I_m^{\mathsf{j}} \tilde{\beta}_{mn}^{\mathsf{j},\mathsf{k}} \left(m_s\right) I_n^{\mathsf{k}} \end{aligned} \tag{A.7}$$

where $\tilde{\beta}_{mn}^{\mathsf{j},\mathsf{k}} \left(m_s\right) = \beta_{mn}^{\mathsf{j},\mathsf{k}} + \delta\beta_{mn}^{\mathsf{j},\mathsf{k}} \left(m_s\right)$ is the total coupling between the $\mathsf{j}-th$ and $\mathsf{k}-th$ nuclear spins.

For the $m_s = 0$ subspace, the effective Hamiltonian is

$$H_{nuc}^{m_s=0} = -\sum_{\mathsf{j}} \omega_0 I_z^{\mathsf{j}} + \sum_{\mathsf{j}>\mathsf{k}} \sum_{m,n=x,y,z} I_m^{\mathsf{j}} \tilde{\beta}_{mn}^{\mathsf{j},\mathsf{k}} \left(0\right) I_n^{\mathsf{k}}. \tag{A.8}$$

When the Zeeman splitting is large (i.e., $\omega_0 \gg \tilde{\beta}_{mn}^{\mathsf{j},\mathsf{k}} \left(0\right)$), we neglect the non-secular terms of $\delta\beta$ and obtain the simplified Hamiltonian for $m_s = 0$:

$$H_{nuc}^{m_s=0} \approx -\sum_{\mathsf{j}} \omega_0 I_z^{\mathsf{j}} + \sum_{\mathsf{j}>\mathsf{k}} I_z^{\mathsf{j}} \tilde{\beta}_{zz}^{\mathsf{j},\mathsf{k}} \left(0\right) I_z^{\mathsf{k}} + \sum_{\mathsf{j}>\mathsf{k}} \left(b^{\mathsf{j},\mathsf{k}} I_+^{\mathsf{j}} I_-^{\mathsf{k}} + \left(b^{\mathsf{j},\mathsf{k}}\right)^* I_-^{\mathsf{j}} I_+^{\mathsf{k}} \right), \tag{A.9}$$

where $b^{\mathsf{j},\mathsf{k}} = \frac{1}{4}\left(\tilde{\beta}_{xx}^{\mathsf{j},\mathsf{k}} + \tilde{\beta}_{yy}^{\mathsf{j},\mathsf{k}} + i\tilde{\beta}_{xy}^{\mathsf{j},\mathsf{k}} - i\tilde{\beta}_{yx}^{\mathsf{j},\mathsf{k}}\right)$. Both Ising coupling and flip-flop coupling may exist for the $m_s = 0$ subspace.

For the $m_s = 1$ subspace, the effective Hamiltonian is

$$H_{nuc}^{m_s=1} = -\sum_{\mathsf{j}} \omega_0 I_z^{\mathsf{j}} + \sum_{n=x,y,z} \alpha_{zn}^{\mathsf{j}} I_n^{\mathsf{j}} + \sum_{\mathsf{j}>\mathsf{k}} \sum_{m,n=x,y,z} I_m^{\mathsf{j}} \tilde{\beta}_{mn}^{\mathsf{j},\mathsf{k}} \left(1\right) I_n^{\mathsf{k}}. \tag{A.10}$$

where we have dropped the constant $\Delta - \gamma_e B_z$ term for simplicity. The first two terms imply that the jth nuclear spin precesses around the vector $\vec{\omega}^{\mathsf{j}} \equiv -\omega_0 \vec{e}_z + \sum_{n=x,y,z} \alpha_{zn}^{\mathsf{j}} \vec{e}_n$, and the quantization axis is $\vec{e}_z^{\mathsf{j}} \equiv \vec{\omega}^{\mathsf{j}} / \left|\vec{\omega}^{\mathsf{j}}\right|$. When the hyperfine interactions are sufficiently different $\left|\vec{\omega}^{\mathsf{j}} - \vec{\omega}^{\mathsf{k}}\right| \gg \tilde{\beta}_{mn}^{\mathsf{j},\mathsf{k}} \left(1\right)$, all couplings between the

nuclear spins are suppressed except for the Ising coupling. The simplified Hamitonian for $m_s = 1$ is:

$$H_{nuc}^{m_s=1} \approx \sum_{\mathsf{j}} \left|\vec{\omega}^{\mathsf{j}}\right| I_{z_{\mathsf{j}}}^{\mathsf{j}} + \sum_{\mathsf{j}>\mathsf{k}} I_{z_{\mathsf{j}}}^{\mathsf{j}} \tilde{\beta}_{z_{\mathsf{j}} z_{\mathsf{k}}}^{\mathsf{j},\mathsf{k}} (1) I_{z_{\mathsf{k}}}^{\mathsf{k}}, \tag{A.11}$$

where $\tilde{\beta}_{z_{\mathsf{j}} z_{\mathsf{k}}}^{\mathsf{j},\mathsf{k}} (1) = \sum_{m,n=x,y,z} \left(\vec{e}_z^{\,\mathsf{j}}\right)_m \cdot \tilde{\beta}_{mn}^{\mathsf{j},\mathsf{k}} (1) \cdot \left(\vec{e}_z^{\,\mathsf{k}}\right)_m$. For example, with only two proximal nuclear spins $\mathbf{n}_1$ and $\mathbf{n}_2$, and $|\vec{\omega}^{\mathsf{1}} - \vec{\omega}^{\mathsf{2}}| \gg \tilde{\beta}_{mn}^{\mathsf{1},\mathsf{2}} (1)$,

$$H_{nuc}^{m_s=1} \approx \left|\vec{\omega}^{\mathsf{1}}\right| I_{z_1}^{\mathsf{1}} + \left|\vec{\omega}^{\mathsf{2}}\right| I_{z_2}^{\mathsf{2}} + I_{z_1}^{\mathsf{1}} \tilde{\beta}_{z_1 z_2}^{\mathsf{1},\mathsf{2}} (1) I_{z_2}^{\mathsf{2}}. \tag{A.12}$$

If spin $\mathbf{n}_2$ is in the completely mixed state, then spin $\mathbf{n}_1$ has two possible energy splittings $|\vec{\omega}^{\mathsf{1}}| \pm \frac{1}{2}\tilde{\beta}_{z_1 z_2}^{\mathsf{1},\mathsf{2}} (1)$. With a nuclear spin Ramsey experiment (Fig. SA.2), we should be able to either resolve such energy splitting (by observing the beating at frequency $\tilde{\beta}_{z_1 z_2}^{\mathsf{1},\mathsf{2}} (1)$) or give an upper bound on the magnitude of $\tilde{\beta}_{z_1 z_2}^{\mathsf{1},\mathsf{2}} (1)$.

A.2.3 Hyperfine coupling for the first nuclear spin

We now justify the claim that spin $\mathbf{n}_1$ has approximately the same quantization axis for both $m_s = 0$ and $m_s = 1$ subspaces. Since the static magnetic field is along the NV axis $\vec{B} = B_z \vec{e}_z$, there is no enhancement from the g-tensor. Considering only one nuclear spin $\mathbf{n}_1$, we may reduce Eq. (A.7) to

$$H^{\mathsf{1},m_s} = -\omega_0 I_z^{\mathsf{1}} + m_s \sum_n \alpha_{zn}^{\mathsf{1}} I_n^{\mathsf{1}} \tag{A.13}$$

For the $m_s = 0$ subspace, spin $\mathbf{n}_1$ has the quantization axis $\hat{n}_{m_s=0} = \vec{e}_z$. For $m_s = 1$ subspace, we may calculate the quantization axis $\hat{n}_{m_s=1}$ using the hyperfine tensor $\alpha_{mn}^{(\mathsf{1})}$ associated with spin $\mathbf{n}_1$.

If the hyperfine coupling is due to the contact interaction that is isotropic, the hyperfine tensor is proportional to the identity matrix, $\alpha_{mn}^{\mathsf{1}} \propto \delta_{mn}$, and the relevant

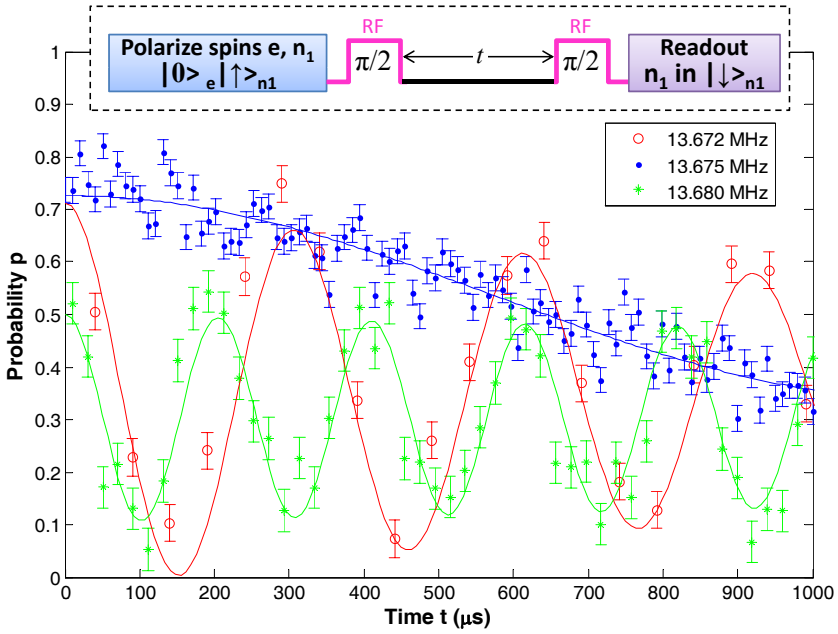

Figure A.2: Ramsey fringes for the nuclear spin $\mathbf{n}_1$. The operations for the nuclear Ramsey experiment are given in the dashed box. Three difference frequencies $\nu = 13.672, 13.675$, and 13.680 MHz are used for the RF field. The frequency for the Ramsey fringes is determined by the detuning of the RF field $\nu - \nu_0$, where $\nu_0 = 13.675\,(1)$ MHz. There is no significant decay in the amplitude of the Ramsey fringes up to 1 ms.

Hamiltonian can be reduced to $-\mu_n B_z I_z^1 + S_z \alpha_{zz}^1 I_z^1$. This implies that the quantization axis $\hat{n}_{m_s=1} = \vec{e}_z$ is also along the NV axis. If the hyperfine coupling also contains a dipolar interaction that is anisotropic, the hyperfine tensor can be characterized by three principle axes with associated principle values. If one of the principle axis is fairly close to the NV axis and the three principle values are also quite similar, then the quantization axis of $\mathbf{n}_1$ can be still very close to the NV axis.

The hyperfine tensors have be calculated with density functional theory (DFT) [74] and obtained from the CW ensemble EPR spectra measurements [69]. In our experiment, we can measured the projection of the hyperfine tensor along the NV axis

$$\alpha_z^1 \equiv \left|\alpha_{zx}^1 \vec{e}_x + \alpha_{zy}^1 \vec{e}_y + \alpha_{zz}^1 \vec{e}_z\right| = \sqrt{\left(\alpha_{zx}^1\right)^2 + \left(\alpha_{zy}^1\right)^2 + \left(\alpha_{zz}^1\right)^2}. \tag{A.14}$$

We perform a Ramsey experiment for spin $\mathbf{n}_1$ in $m_s = 1$ subspace, which measures the level splitting between $|1\rangle_e |\downarrow\rangle_{n1}$ and $|1\rangle_e |\uparrow\rangle_{n1}$ to be $13.675\,(1)$ MHz (see Fig. SA.2). This value also includes $\omega_0 = \pm 32\,(1)$ kHz contribution of Zeeman splitting due to 30 gauss magnetic field parallel/antiparallel to the NV axis [37]. Thus, the projection of the hyperfine tensor along the NV axis is $\alpha_z^1 = 13.675\,(1) \pm 0.032\,(1)$ MHz. On the other hand, the EPR spectra experiment reported by Felton et. al. has also reliably measured the hyperfine tensor, which is axially symmetric with $\alpha_\parallel^1 = 18.95\,(5)$ MHz along the direction 70.8° from the NV axis, and $\alpha_\perp^1 = 13.26\,(5)$ MHz (see Table III in Ref. [69]). Their measurement was performed at 10 K. The matrix representation

for this hyperfine tensor is

$$\alpha^1 = \begin{pmatrix} 17.92\,(5) & 0 & 1.62\,(2) \\ 0 & 13.26\,(5) & 0 \\ 1.62\,(2) & 0 & 13.82\,(5) \end{pmatrix} \text{MHz}, \tag{A.15}$$

in the coordinate system we have chosen, where z-axis is along the NV direction and the $x-z$ plane contains the first proximal ^{13}C determines. The CW ensemble EPR spectra measurements imply $\alpha_z^1 = 13.92\,(6)$ MHz, which matches the value observed in our single NV experiment with only about 0.2 MHz difference (i.e., about 3σ deviation). Beside the distinction of single/ensemble measurement, the temperature difference between the two experiments might attribute to such a small deviation, as both thermal expansion $(1 - a\,(10K)\,/a\,(293K) \sim 10^{-4})$ and vibro-electronic effect may slightly change the electronic spin density distribution and consequently modify the hyperfine coupling. Because the hyperfine coupling varies strongly for proximal ^{13}C spins [74], their projection values along the NV axis can be used to reliably identify the location of the nuclear spin (up to some equivalent lattice sites associated with the C_{3V} symmetric of the NV center).

According the hyperfine tensor α^1, we estimate the quantization axis $\hat{n}_{m_s=1} = \sin\delta\ \vec{e}_x + \cos\delta\ \vec{e}_z$ for $|m_s = 1\rangle_e$, where $\delta = \arctan\frac{\alpha_{xz}^1}{\alpha_{zz}^1} \approx 6.7^\circ$ is the angle between $\hat{n}_{m_s=0}$ and $\hat{n}_{m_s=1}$. Thus, the nuclear spin eigenstates for $m_s = 1$ subspace differ from the nuclear spin eigenstates for $m_s = 1$ subspace by a small angle δ. The difference between these two state is $\sin^2\delta \approx 0.007$, which is too small to be resolved with the current precision. Therefore, we have justified to claim that the quantization axis of

the nuclear spin $\mathbf{n}_1$ almost does not depend on the electronic spin state $|m_s = 0\rangle_e$ or $|m_s = 1\rangle_e$. We may use the simple notation of $|0\rangle_e |\downarrow\rangle_{n1}$, $|0\rangle_e |\uparrow\rangle_{n1}$, $|1\rangle_e |\downarrow\rangle_{n1}$, and $|1\rangle_e |\uparrow\rangle_{n1}$ provides a good approximation for the eigenstates of the Hamiltonian in Eq. (A.13).

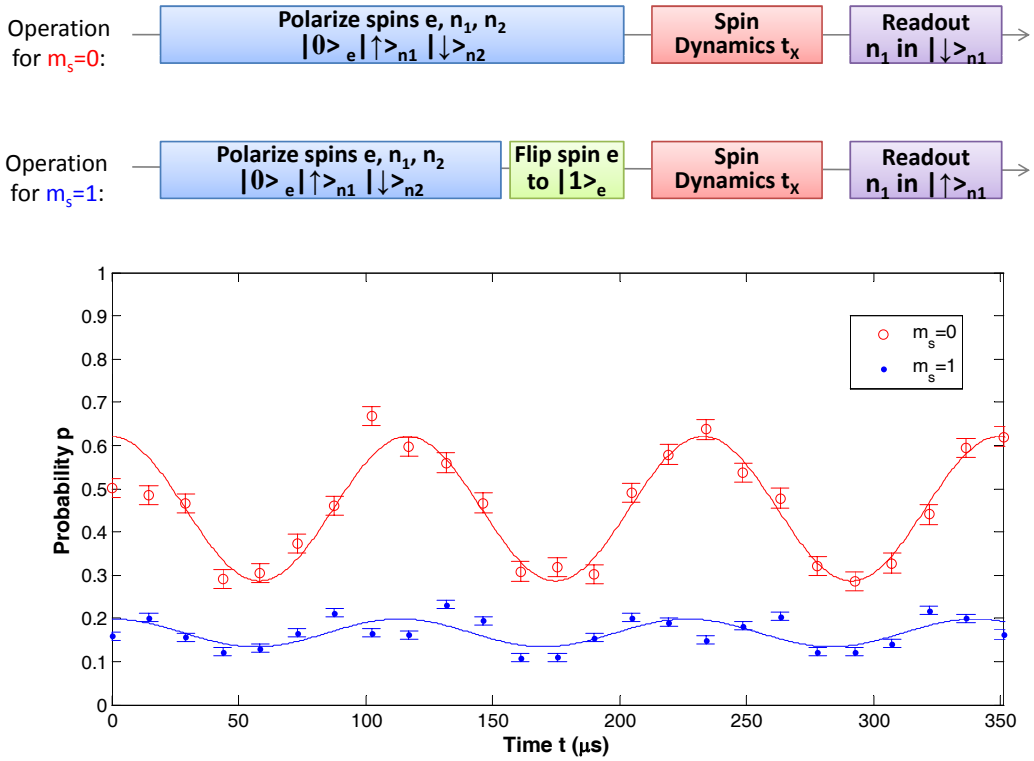

Figure A.3: Dynamics of nuclear spins for $m_s = 0$ and $m_s = 1$ subspaces. The nuclear spins $\mathbf{n}_1$ and $\mathbf{n}_2$ are initialized in $|\uparrow\rangle_{n_1} |\downarrow\rangle_{n_2}$. When the electronic spin is $|m_s = 0\rangle_e$, there is a flip-flop process between the two nuclear spins (red curve). When the electronic spin is $|m_s = 1\rangle_e$, the flip-flop process is strongly suppressed (blue curve).

A.2.4 Spin flip-flop interaction between nuclear spins

We now consider the interaction between two nuclear spins $\mathbf{n}_1$ and $\mathbf{n}_2$. According to Eq. (A.9), the effective spin Hamiltonian between spins $\mathbf{n}_1$ and $\mathbf{n}_2$ for $m_s = 0$ subspace is

$$H_{nuc}^{m_s=0} = \omega_0 I_z^1 + \omega_0 I_z^2 + \tilde{\beta}_{zz}^{1,2} I_1^1 I_z^2 + b^{1,2}(I_+^1 I_-^2 + I_-^1 I_+^2),$$

where we choose $b^{1,2}$ real by absorbing the complex phase into I_+^1. Experimentally, we estimate $\tilde{\beta}_{zz}^{1,2} \lesssim 0.3$ kHz from the nuclear spin Ramsey experiment (as the Ramsey fringes can be observed even up to 3 ms (Fig. SA.2)), which is one or two orders of magnitude smaller than $b^{1,2} = 4.27\,(3)$ kHz or $\omega_0 = 32\,(2)$ kHz, which corresponds to magnetic field of ~ 30 gauss. The observation is also consistent with the theoretical estimate from the hyperfine tensors [2]. For simplicity, we will neglect the $\tilde{\beta}_{zz}^{1,2}$ term and consider the following Hamiltonian:

$$H_f = \omega_0 \left(I_z^1 + I_z^2\right) + b(I_+^1 I_-^2 + I_-^1 I_+^2), \tag{A.16}$$

where $b = b^{1,2} = \left|\frac{1}{4}\left(\tilde{\beta}_{xx}^{1,2} + \tilde{\beta}_{yy}^{1,2} + i\tilde{\beta}_{xy}^{1,2} - i\tilde{\beta}_{yx}^{1,2}\right)\right|$. Neglecting $\tilde{\beta}_{zz}^{1,2}$ may introduce an error with probability $\left(\tilde{\beta}_{zz}^{1,2}/b\right)^2 \lesssim 1\%$, which is actually small compared to other imperfections. In principle, we may also use quantum control techniques [108] to completely compensate the deviation due to finite $\tilde{\beta}_{zz}^{1,2}$.

The nuclear spins $\mathbf{n}_1$ and $\mathbf{n}_2$ have initial poalrization $p_{n_1} \equiv p_{n_1,\uparrow} - p_{n_1,\downarrow}$ and $p_{n_2} \equiv p_{n_2,\uparrow} - p_{n_2,\downarrow}$, respectively. The initial densitiy matrix of the two nuclear spins is $\rho_0 = \rho_{10} \otimes \rho_{20}$, with $\rho_{10} = \frac{1}{2}(1 + p_{n_1} I_z^1)$ and $\rho_{20} = \frac{1}{2}(1 + p_{n_2} I_z^2)$. The evolution of

[2] The hyperfine tensor for n_1 is almost diagonal, with off-diagonal matrix elements much less than the diagonal ones (e.g., $\alpha_{xz}^1 \ll \alpha_{xx}^1, \alpha_{yy}^1, \alpha_{zz}^1$). This suggests that it is very likely that $\delta\beta_{zz}^{1,2} \ll \delta\beta_{xx}^{1,2}, \delta\beta_{yy}^{1,2}$ for the electron-mediated nuclear spin coupling between n_1 and n_2.

the density matrix of spin $\mathbf{n}_1$ is

$$\rho_1(\tau) = \mathtt{Tr}_{\mathbf{n}_2}\{U\rho_0 U^\dagger\} = \frac{1}{2} + I_z^1(p_{n_1} + (p_{n_2} - p_{n_1})\sin^2 b\tau), \tag{A.17}$$

where $U = \exp(-iH_f\tau)$ is the evolution operator and $\mathtt{Tr}_{\mathbf{n}_2}$ traces out the subsystem of spin $\mathbf{n}_2$. Therefore, the polarization of spin $\mathbf{n}_1$ can be written as

$$p_{n_1}(\tau) = p_{n_1} + (p_{n_2} - p_{n_1})\sin^2 b\tau. \tag{A.18}$$

We observe that when the two nuclei are polarized equally ($p_{n_1} = p_{n_2}$) and $p_{n_1} \neq 0$, there is no flip-flop between them. For example, consider the two nuclei prepared in either $\uparrow\uparrow$ or $\downarrow\downarrow$. In this case, flip-flops are suppressed because of the energy gap ($2\omega_0 \gg b$) between the $\uparrow\uparrow$ and $\downarrow\downarrow$ configurations. On the other hand, when both nuclei are prepared with opposite polarizations ($p_{n_1} = -p_{n_2}$), the spin flip-flops are maximized since the energy gap between $\uparrow\downarrow$ and $\downarrow\uparrow$ is zero. After a time of $\tau = \pi/2b$, the $\uparrow\downarrow$ part has evolved to $\downarrow\uparrow$ (i.e., the SWAP operation).

Meanwhile, for $m_s = 1$ subspace, the two nuclear spins have very different energy splittings due to the distinct hyperfine couplings (see the discussion after Eq. (A.10)). This would suppress the spin flip-flop terms. As shown in Fig. SA.3, the flip-flop process between spins $\mathbf{n}_1$ and $\mathbf{n}_2$ are significantly suppressed when the electronic spin is $|m_s = 1\rangle_e$. The residual oscillations are due to the imperfect preparation of the electronic spin (e.g., optical pumping and π pulses) that induces a small probability in $m_s = 0$.

A.3 Nuclear Spin Depolarization for Each Readout

The mechanism for depolarization of nuclear spins under optical illumination is induced by the stochastic electronic optical transitions, which connect multiple electronic states with different hyperfine interactions to the nuclear spins [100, 63]. The process can described by the master equation that accounts for both the classical stochastic transition of the electronic states and the coherent evolution of the nuclear spins with state-dependent hyperfine interaction. For fast optical excitation/relaxation, the depolarization of the nuclear spin is suppressed, which increases the depolarization time for the nuclear spin.

Reducing the transverse magnetic field with respective to the NV axis can further increase the depolarization time of the nuclear spin [100, 63]. The theoretical description for the depolarization of the nuclear spin under optical illumination is detailed in [100]. The same theoretical model can also explain the observed double exponential decay in Fig. 2D, which is associated with the two time scales for dephasing and depolarizing with respective to the motional-averaged quantization axis [100].

Since the power for the laser pulses is almost the same for the experiments presented in Figures 2, 3,and 4, we may use the depolarization curve (Fig. 2D) to estimate the relative reduction in polarization for various operations. For the first nuclear spin, the relative reduction of polarization ε_{n1} is 0.035 ± 0.015 after each 350 ns green laser pulse. For the second nuclear spin, we estimate the relative reduction of polarization ε_{n2} is about 0.3 ± 0.1 after 5 μs green laser pulse, and about 0.5 ± 0.1 after 20 μs

green laser pulse.

A.4 Deriving Optimized SNR

We use the signal-to-noise ratio (SNR) as the figure of merit for the repetitive readout scheme. The signal is defined as the weighted sum of the Rabi oscillation amplitudes obtained from repetitive readout.

$$\text{Signal} = \sum_{m=1}^{M'} w_m \left| A_m \right|, \tag{A.19}$$

with weight w_m for the m-th readout. The corresponding noise is

$$\text{Noise} = \sqrt{\sum_{m=1}^{M'} w_m^2 \sigma_m^2}, \tag{A.20}$$

where σ_m is the noise for the m-th readout, which can also be obtained experimentally. The signal-to-noise ratio [77] is defined as

$$\frac{\text{Signal}}{\text{Noise}} = \frac{\sum_{m=1}^{M'} w_m \left| A_m \right|}{\sqrt{\sum_{m=1}^{M'} w_m^2 \sigma_m^2}}. \tag{A.21}$$

According to the Cauchy-Schwartz inequality, we have

$$\sum_{m=1}^{M'} \left(w_m \sigma_m \right)^2 \sum_{m=1}^{M'} \left(\frac{\left| A_m \right|}{\sigma_m} \right)^2 \geq \left(\sum_{m=1}^{M'} w_m \left| A_m \right| \right)^2, \tag{A.22}$$

where equality is satisfied when $w_m = \left| A_m \right| / \sigma_m^2$. Therefore, the optimized SNR is

$$\text{SNR}_{\text{opt}} \left(M' \right) = \sqrt{\sum_{m=1}^{M'} \left| \frac{A_m}{\sigma_m} \right|^2}. \tag{A.23}$$

A.5 Simulation for the Repetitive Readout

In this appendix, we detail the numerical simulation for both repetitive readout schemes. We use the transition matrix description to keep track of the state evolution. With reasonable choice of imperfection parameters, we are able to obtain A_m and $\mathrm{SNR}_{\mathrm{opt}}(M')$ consistent with the experiment.

A.5.1 Transition matrices

We model $8 = 2^3$ levels associated with the electronic spin and two nuclear spins in the simulation. Because the quantum coherence does not change the outcome of the repetitive readout, it is sufficient to track the probability distribution over these 8 levels. We use the array $\vec{q} = (q_{0\downarrow\downarrow}, q_{0\downarrow\uparrow}, q_{0\uparrow\downarrow}, q_{0\uparrow\uparrow}, q_{1\downarrow\downarrow}, q_{1\downarrow\uparrow}, q_{1\uparrow\downarrow}, q_{1\uparrow\uparrow})^T$ to represent the probability distribution. We consider the transition matrices for various operations characterized by imperfection parameters. For example, if initial state distribution is $\vec{q}_0$ and transition matrix is $\mathcal{T}$, the final state distribution is $\mathcal{T}\vec{q}_0$.

We now list the transition matrices for the operations that are used for spin initialization and repetitive readout.

1) Transition matrix for MW1 π-pulse is

$$\mathcal{T}_{\mathrm{MW1}} = W_{pi} \otimes I_{\downarrow} \otimes \mathbb{1}_2 + W_{id} \otimes I_{\uparrow} \otimes \mathbb{1}_2, \tag{A.24}$$

where

$$W_{pi} = \begin{pmatrix} \varepsilon_{\mathrm{res}}^{MW} & 1-\varepsilon_{\mathrm{res}}^{MW} \\ 1-\varepsilon_{\mathrm{res}}^{MW} & \varepsilon_{\mathrm{res}}^{MW} \end{pmatrix} \qquad W_{id} = \begin{pmatrix} 1-\varepsilon_{\mathrm{det}}^{MW} & \varepsilon_{\mathrm{det}}^{MW} \\ \varepsilon_{\mathrm{det}}^{MW} & 1-\varepsilon_{\mathrm{det}}^{MW} \end{pmatrix}$$

$$I_{\downarrow} = \begin{pmatrix} 1 & 0 \\ 0 & 0 \end{pmatrix} \qquad I_{\uparrow} = \begin{pmatrix} 0 & 0 \\ 0 & 1 \end{pmatrix} \qquad \mathbb{1}_2 = \begin{pmatrix} 1 & 0 \\ 0 & 1 \end{pmatrix}$$

with $\varepsilon_{\rm res}^{MW} = 0.07$ for the resonant transition and $\varepsilon_{\rm det}^{MW} = 0.01$ for the Δ-detuned transition (see Sec. A.1.5). Similarly the transition matrix for MW2 pi-pulse is

$$\mathcal{T}_{\rm MW2} = W_{pi} \otimes I_{\uparrow} \otimes \mathbb{1}_2 + W_{id} \otimes I_{\downarrow} \otimes \mathbb{1}_2. \tag{A.25}$$

2) The transition matrices for nuclear spin depolarization under optical illumination are

$$\mathcal{T}_{n1} = \mathbb{1}_2 \otimes \begin{pmatrix} 1 - \frac{\varepsilon_{n1}}{2} & \frac{\varepsilon_{n1}}{2} \\ \frac{\varepsilon_{n1}}{2} & 1 - \frac{\varepsilon_{n1}}{2} \end{pmatrix} \otimes \mathbb{1}_2 \tag{A.26}$$

for $\mathbf{n}_1$, and

$$\mathcal{T}_{n2} = \mathbb{1}_2 \otimes \mathbb{1}_2 \otimes \begin{pmatrix} 1 - \frac{\varepsilon_{n1}}{2} & \frac{\varepsilon_{n1}}{2} \\ \frac{\varepsilon_{n1}}{2} & 1 - \frac{\varepsilon_{n1}}{2} \end{pmatrix} \tag{A.27}$$

for $\mathbf{n}_2$. The depolarization factors are $\varepsilon_{n1} = 0.05$ for $\mathbf{n}_1$ after $t_{green} = 350$ ns green laser pulse, and $\varepsilon_{n2} = 0.42$ and 0.63 for the second nuclear spin after 5 and 20 μs green laser pulses (see Sec. A.3). During the M-step repetitive readout, the flip-flop evolution between $\mathbf{n}_1$ and $\mathbf{n}_2$ during the short 1.5 μs interval between sequential readouts may occur with probability about 5%, which is also effectively included into ε_{n2}.

3) The transition matrix for optical pumping of the electronic spin is

$$\mathcal{T}_{\rm Pump} = \begin{pmatrix} 1 - \varepsilon_{pump,0} & 1 - \varepsilon_{pump,1} \\ \varepsilon_{pump,0} & \varepsilon_{pump,1} \end{pmatrix} \otimes \mathbb{1}_2 \otimes \mathbb{1}_2, \tag{A.28}$$

where $\varepsilon_{pump,0}$ and $\varepsilon_{pump,1}$ are the error probability for imperfect pumping. The characteristic time for optical pumping of the electronic spin is $\tau_{pump} = 235$ ns, so the 350 ns green laser pulse has $\varepsilon_{pump,1} = 0.25$. In addition, we also assume that there will be $\varepsilon_{pump,0} = 2\%$ of the population from $m = 0$ to $m = 1$ state.

4) The transition matrix for the RF pi-pulse is

$$\mathcal{T}_{\mathrm{RF}} =_2 \otimes \begin{pmatrix} 1-\varepsilon_{RF} & \varepsilon_{RF} \\ \varepsilon_{RF} & 1-\varepsilon_{RF} \end{pmatrix} \otimes \mathbb{1}_2 \tag{A.29}$$

where $\varepsilon_{RF} < 1\%$ based on our calibration, so we assume perfect RF pi-pulse (i.e., $\varepsilon_{RF} = 0$) for simplicity. Similarly we also assume negligible error for the SWAP gate on $\mathbf{n}_1$ and $\mathbf{n}_2$.

A.5.2 Simulation with transition matrices

Using the above transition matrices, we can obtain the evolution in probability distribution for a given pulse sequence. For example, the distribution after k-step repeated pumping of $\mathbf{n}_1$ is

$$\vec{q}_k = \left(\mathcal{T}_{\mathrm{Pump}}\mathcal{T}_{\mathrm{RF}}\mathcal{T}_{\mathrm{MW2}}\right)^k \ \vec{q}_0, \tag{A.30}$$

where $\vec{q}_0$ is the initial distribution. With these parameters, we first simulate and obtain the amplitude of nuclear Rabi oscillation, with amplitude 0.61, consistent with experimental observation of 0.60 ± 0.05.

For the pulse sequence provided in Fig. 3B of the main text, the state for the first readout is

$$\vec{q}^{(\delta)}_{\mathrm{meas},1} = \mathcal{T}_{\mathrm{RF}} \left(\mathcal{T}_{\mathrm{MW1}}\right)^\delta \ \vec{q}_{k=6}, \tag{A.31}$$

where $\delta = 0$ for trivial MW1 pulse with duration $t = 0$, and $\delta = 1$ for MW1 pi-pulse with duration $t = \pi/\Omega_{MW}$. The population difference in $|0\rangle_e$ between $\vec{q}^{(0)}_{\text{meas},1}$ and $\vec{q}^{(1)}_{\text{meas},1}$ gives the normalized amplitude

$$|A_1| = \left|\text{Prob}\left[\vec{q}^{(0)}_{\text{meas},1}\right] - \text{Prob}\left[\vec{q}^{(1)}_{\text{meas},1}\right]\right|, \tag{A.32}$$

where

$$\text{Prob}\left[\vec{q}\right] = q_{0\downarrow\downarrow} + q_{0\downarrow\uparrow} + q_{0\uparrow\downarrow} + q_{0\uparrow\uparrow} \tag{A.33}$$

is the probability in the $|0\rangle_e$ state for distribution $\vec{q}$.

The state for the following readout is

$$\vec{q}^{(\delta)}_{\text{meas},m} = \begin{cases} \left(\mathcal{T}_{\text{Pump}}\mathcal{T}_{\text{MW2}}\right)\vec{q}^{(\delta)}_{\text{meas},m-1} & \text{for even } m \\ \left(\mathcal{T}_{\text{Pump}}\mathcal{T}_{\text{MW1}}\right)\vec{q}^{(\delta)}_{\text{meas},m-1} & \text{for odd } m \end{cases}, \tag{A.34}$$

with $m = 2, 3, \cdots, M$. Finally, the normalized amplitude for the m-th readout is

$$|A_m| = \left|\text{Prob}\left[\vec{q}^{(0)}_{\text{meas},m}\right] - \text{Prob}\left[\vec{q}^{(1)}_{\text{meas},m}\right]\right|. \tag{A.35}$$

And

$$\text{SNR}_{\text{opt}}\left(M'\right) = \sqrt{\sum_{m=1}^{M'} |A_m|^2}. \tag{A.36}$$

The simulation of A_m and $\text{SNR}_{\text{opt}}\left(M'\right)$ for the repetitive readout scheme assisted with one qubits are shown in Fig. 3DE. Similarly, we can also simulate A_m and $\text{SNR}_{\text{opt}}\left(M'\right)$ measured for the repetitive readout scheme assisted with two qubits are shown in Fig. 4CD.

Appendix B

Appendices to Chapter 6

Here we justify two main claims used in the Chapter 6. (1) For the DLCZ protocol, the probability ratios $p_{vac}^{(m)}/p_{logic}^{(m)}$ and $p_{multi}^{(m)}/p_{logic}^{(m)}$ increase with the nesting level m. (2) For the new scheme (without ENP), the probability ratios $p_{vac}^{(m)}/p_{logic}^{(m)}$ and $p_{multi}^{(m)}/p_{logic}^{(m)}$ remain almost independent of the nesting level m. The states of logical, vacuum and multi-excitation types depend on the repeater protocol. For example, the entangled logical state for the DLCZ protocol has total of one excitation stored in two remotely entangled cells (e.g. Eq.(6.1)), while the entangled logical state for the new scheme has two excitations stored in four cells, with one excitation and two cells on each side (e.g. Eq.(6.2)). Thus, the definitions of $p_{logic}^{(m)}$, $p_{vac}^{(m)}$ and $p_{multi}^{(m)}$ are different for the two schemes.

B.1 Non-logical States for the DLCZ Protocol

We start with the DLCZ protocol. First, we decompose the density matrix (for a pair of distant atomic cells x and y) into components with different excitation patterns, neglecting the inter-pattern coherence

$$\rho_{x,y} = p_{00}\pi_{00} + p_{10}\pi_{10} + p_{11}\pi_{11} + p_{20}\pi_{20} + \cdots \tag{B.1}$$

where $p_{ij}\pi_{ij}$ is the projected density matrix to the subspace spanned by the Fock states of the cells $\left\{ |i\rangle_x |j\rangle_y , |j\rangle_x |i\rangle_y \right\}$, with probability p_{ij} and normalized density matrix π_{ij}. For the DLCZ protocol, the vacuum type of state is π_{00}, the logical type of state is π_{10}, and the rest belong to the multi-excitation type. We may also introduce the notation corresponding to Eq.(6.5)

$$\rho_{x,y} = p_{logic}\rho_{logic} + p_{vac}\pi_{vac} + p_{multi}\pi_{multi} \tag{B.2}$$

with $p_{vac} = p_{00}$, $p_{logic} = p_{10}$, and $p_{multi} = p_{11} + p_{20} + \cdots$.

Since we are only interested in the coherence properties for the logical type π_{10}, we only keep track of the probabilities for the vacuum and multi-excitation types and neglect their coherences. From the symmetry for the two cells, we have

$$\pi_{ij} = \pi_{ji} \equiv \frac{1}{2}\left(|i\rangle_x \langle i| \otimes | j\rangle_y \langle j| + |j\rangle_x \langle j| \otimes | i\rangle_y \langle i| \right). \tag{B.3}$$

In the rest of this subsection, we will add a superscript to π_{ij} only when we want to keep track of the coherence for that specific term. For example, $\pi_{10}^{(m)}$ indicates that there is coherence between the states $|1\rangle_x |0\rangle_y$ and $|0\rangle_x |1\rangle_y$, after the mth level of ENC.

Since the DLCZ protocol requires that the probability for the multi-excitation states should always be much smaller than the probability for the logical states (otherwise, a large fraction of multi-excitation states, accompanied by photon loss, can induce significant logical errors), we regard $p_{11}^{(m)}$, $p_{20}^{(m)}(\ll p_{10}^{(m)})$ as perturbations.

We denote the entangled state after the mth ENC as

$$\rho_{x,y}^{(m)} = p_{00}^{(m)}\pi_{00} + p_{10}^{(m)}\pi_{10}^{(m)} + p_{11}^{(m)}\pi_{11} + p_{20}^{(m)}\pi_{20} + \cdots \tag{B.4}$$

We now connect two such entangled states $\rho_{x_L,y_L}^{(m)}$ and $\rho_{x_R,y_R}^{(m)}$ for the $(m+1)$th ENC via the superoperator $\mathcal{E}_{ENC}$

$$\tilde{\rho}_{x_L,y_R}^{(m+1)} = \mathcal{E}_{ENC}\left[\rho_{x_L,y_L}^{(m)}, \rho_{x_R,y_R}^{(m)}\right]. \tag{B.5}$$

where $\tilde{\rho}_{x_L,y_R}^{(m+1)}$ is the unnormalized density matrix for the entangled state after the $(m+1)$th ENC. Since $\mathcal{E}_{ENC}$ is a linear operator and two inputs have the same state,

$$\mathcal{E}_{ENC}\left[\sum_{\alpha} p_\alpha \pi_\alpha, \sum_{\beta} p_\beta \pi_\beta\right] = \sum_{\alpha,\beta} p_\alpha p_\beta \mathcal{E}_{ENC}^{sym}\left[\pi_\alpha, \pi_\beta\right], \tag{B.6}$$

where $\mathcal{E}_{ENC}^{sym}\left[\pi_\alpha, \pi_\beta\right] \equiv \frac{1}{2}\mathcal{E}_{ENC}\left[\pi_\alpha, \pi_\beta\right] + \frac{1}{2}\mathcal{E}_{ENC}\left[\pi_\beta, \pi_\alpha\right]$. Now we calculate $\mathcal{E}_{ENC}^{sym}\left[\pi_\alpha, \pi_\beta\right]$ for $\pi_\alpha, \pi_\beta \in \left\{\pi_{00}, \pi_{10}^{(m)}, \pi_{11}, \pi_{20}, \cdots\right\}$. For example,

$$\mathcal{E}_{ENC}^{sym}\left[\pi_{10}^{(m)}, \pi_{10}^{(m)}\right] = \frac{\eta}{2}\pi_{10}^{(m+1)\prime} + \frac{\eta\left(1-\eta\right)}{2}\pi_{00} \tag{B.7}$$

$$\mathcal{E}_{ENC}^{sym}\left[\pi_{10}^{(m)}, \pi_{00}\right] = \frac{\eta}{2}\pi_{00} \tag{B.8}$$

$$\mathcal{E}_{ENC}^{sym}\left[\pi_{10}^{(m)}, \pi_{11}\right] = \frac{\eta}{2}\pi_{11} + \eta\left(1-\eta\right)\pi_{10} \tag{B.9}$$

$$\mathcal{E}_{ENC}^{sym}\left[\pi_{10}^{(m)}, \pi_{20}\right] = \frac{\eta}{4}\pi_{20} + \frac{\eta\left(1-\eta\right)}{2}\pi_{10} + \frac{3\eta\left(1-\eta\right)^2}{4}\pi_{00} \tag{B.10}$$

$$\mathcal{E}_{ENC}^{sym}\left[\pi_{00}, \pi_{00}\right] = 0 \tag{B.11}$$

$$\mathcal{E}_{ENC}^{sym}\left[\pi_{00}, \pi_{11}\right] = \eta\pi_{10} \tag{B.12}$$

$$\mathcal{E}_{ENC}^{sym}\left[\pi_{0}, \pi_{20}\right] = \eta\left(1-\eta\right)\pi_{00}. \tag{B.13}$$

The logical type of state after the $(m+1)$th ENC, $\pi_{10}^{(m+1)}$, is the average of the states $\pi_{10}^{(m+1)\prime}$ and π_{10}, with relative weights $\frac{\eta}{2}p_{10}^{(m)}p_{10}^{(m)}$ and $2\eta\left(1-\eta\right)p_{10}^{(m)}p_{11}^{(m)} + \eta\left(1-\eta\right)p_{10}^{(m)}p_{20}^{(m)} + 2\eta p_{00}^{(m)}p_{11}^{(m)}$, respectively.

Then we calculate the (unnormalized) density matrix after the $(m+1)$th ENC,

$$\begin{aligned}\tilde{\rho}_{x_L,y_R}^{(m+1)} &= \tilde{p}_{00}^{(m+1)}\pi_{00} + \tilde{p}_{10}^{(m+1)}\pi_{10}^{(m+1)} \\ &\quad + \tilde{p}_{11}^{(m+1)}\pi_{11} + \tilde{p}_{20}^{(m+1)}\pi_{20} + \cdots ,\end{aligned} \tag{B.14}$$

with the probability coefficients

$$\tilde{p}_{00}^{(m+1)} \approx \eta p_{10}^{(m)}\left(p_{00}^{(m)} + \frac{(1-\eta)}{2}p_{10}^{(m)}\right) \tag{B.15}$$

$$\tilde{p}_{10}^{(m+1)} \approx \frac{\eta}{2}p_{10}^{(m)}p_{10}^{(m)} \tag{B.16}$$

$$\tilde{p}_{11}^{(m+1)} \approx \eta p_{10}^{(m)}p_{11}^{(m+1)} \tag{B.17}$$

$$\tilde{p}_{20}^{(m+1)} \approx \frac{\eta}{2}p_{10}^{(m)}p_{20}^{(m+1)}. \tag{B.18}$$

to the leading order with respect to the perturbations of $p_{11}^{(m)}$ and $p_{20}^{(m)}$.

Finally, we divide these probabilities by $\tilde{p}_{10}^{(m+1)}$, and obtain

$$\frac{\tilde{p}_{00}^{(m+1)}}{\tilde{p}_{10}^{(m+1)}} \approx 2\left(\frac{p_{00}^{(m)}}{p_{10}^{(m)}} + \frac{(1-\eta)}{2}\right) > 2\frac{p_{00}^{(m)}}{p_{10}^{(m)}} \tag{B.19}$$

$$\frac{\tilde{p}_{11}^{(m+1)}}{\tilde{p}_{10}^{(m+1)}} \approx 2\frac{p_{11}^{(m)}}{p_{10}^{(m)}} \tag{B.20}$$

$$\frac{\tilde{p}_{20}^{(m+1)}}{\tilde{p}_{10}^{(m+1)}} \approx \frac{p_{20}^{(m)}}{p_{10}^{(m)}}. \tag{B.21}$$

Since the normalization does not change the relative ratio between the probabilities, the above purterbative estimate tells us that the fractions for both the vacuum

state (π_{00}) and the multi-excitation state (π_{11}) are at least doubled, relative to the logical state $\pi_{10}^{(m+1)}$, after each ENC.

In terms of the notation corresponding to Eq.(6.5) ($p_{vac} = p_{00}$, $p_{logic} = p_{10}$, and $p_{multi} = p_{11} + p_{20} + \cdots$), we have

$$\frac{p_{vac}^{(m+1)}}{p_{logic}^{(m+1)}} = \frac{\tilde{p}_{00}^{(m+1)}}{\tilde{p}_{10}^{(m+1)}} > 2\frac{p_{vac}^{(m)}}{p_{logic}^{(m)}} \tag{B.22}$$

$$\frac{\tilde{p}_{multi}^{(m+1)}}{\tilde{p}_{logic}^{(m+1)}} \approx 2\frac{p_{multi}^{(m)}}{p_{logic}^{(m)}} \tag{B.23}$$

The ratio of non-logical states to logical states is at least doubling with distance. As discussed in the main text, it is these unstable non-logical states that leads to the super-polynomial scaling for the DLCZ protocol.

B.2 Non-logical States for the New Scheme

For the new scheme, we can similiarly decompose the density matrix (following Eq.(6.5))

$$\begin{aligned}\rho = p_{00}\pi_{00} + p_{10}\pi_{10} + p_{11}\pi_{11} + p_{20}\pi_{20} \\ + p_{21}\pi_{21} + p_{30}\pi_{30}\cdots\end{aligned} \tag{B.24}$$

where $p_{ij}\pi_{ij}$ is the projected density matrix to the subspace spanned the Fock states with i (or j) photons in a cell-pair and j (or i) photons in b cell-pair, with probability p_{ij} and normalized density matrix π_{ij}. For the new scheme, the vacuum type of states consists of π_{00} and π_{10}, the logical type of state is π_{11}, and the rest belong to the multi-excitation type.

We use a perturbative approach, by assuming $p_{00}\pi_{00}$, $p_{10}\pi_{10}$, and $p_{11}\pi_{11}$ are the dominant terms, and the rest terms are perturbations of order p_c (terms not listed are of order p_c^2). We eliminate those irrelevant perturbation terms (e.g. $p_{30}\pi_{30}$), because after one level of ENC, they are suppressed to $O(p_c^2)$.

Suppose the entangled state after the mth ENC is

$$\begin{aligned}\rho_{a,b}^{(m)} = & p_{00}^{(m)}\pi_{00} + p_{10}^{(m)}\pi_{10} + p_{11}^{(m)}\pi_{11}^{(m)} + p_{20,\|}^{(m)}\pi_{20,\|} \\ & + p_{20,\perp}^{(m)}\pi_{20,\perp} + p_{21,\|}^{(m)}\pi_{21,\|} + p_{21,\perp}^{(m)}\pi_{21,\perp} + \cdots \end{aligned} \tag{B.25}$$

Notice that we need to distinguish two possible types of states for π_{20} because they behave differently during ENC. The first type of states (denoted as $\pi_{20,\|}$) has both photons stored in the same cell, and after retrieval the photons will have the same polarization, follow the same path way, and trigger the photon detector(s) on the same side of the PBS (Fig. 6.1(b)). The second type of states (denoted as $\pi_{20,\perp}$) has two photons stored in different cells, and after the retrieval the photons will have orthogonal polarization, split at the PBS, and trigger photon detectors on both sides of the PBS (Fig. 6.1(b)). Thus, the second type of states are more likely to give the correct click pattern and thus propagate the error to the next level of ENC. Similarly, we introduce $\pi_{21,\|}$ and $\pi_{21,\perp}$.

In the rest of the discussion, we still follow the convention from the previous subsection that $\pi_{ij} = \pi_{ji}$ and we will add a superscript m to π_{ij} only when we want to keep track of the coherence for that specific term.

We now connect two such entangled states $\rho_{a_L,b_C}^{(m)}$ and $\rho_{a_C,b_R}^{(m)}$ for the $(m+1)$th ENC

$$\tilde{\rho}_{a_L,b_R}^{(m+1)} = \mathcal{E}_{ENC}\left[\rho_{a_L,b_C}^{(m)}, \rho_{a_C,b_R}^{(m)}\right] \tag{B.26}$$

where $\tilde{\rho}^{(m+1)}_{a_L,b_R}$ is the unnormalized density matrix for the entangled state after the $(m+1)$th ENC.

Now we calculate $\mathcal{E}^{sym}_{ENC}\left[\pi_\alpha,\pi_\beta\right] \equiv \frac{1}{2}\mathcal{E}_{ENC}\left[\pi_\alpha,\pi_\beta\right] + \frac{1}{2}\mathcal{E}_{ENC}\left[\pi_\beta,\pi_\alpha\right]$ for $\pi_\alpha,\pi_\beta \in \left\{\pi_{00},\pi_{10},\pi^{(m)}_{11},\pi_{20,\|(\text{or }\perp)},\pi_{21,\|(\text{or }\perp)},\cdots\right\}$. For example,

$$\mathcal{E}^{sym}_{ENC}\left[\pi^{(m)}_{11},\pi^{(m)}_{11}\right] = \frac{\eta^2}{2}\pi^{(m+1)\prime}_{11} \tag{B.27}$$

$$\mathcal{E}^{sym}_{ENC}\left[\pi^{(m)}_{11},\pi_{10}\right] = \frac{\eta^2}{4}\pi_{10} \tag{B.28}$$

$$\mathcal{E}^{sym}_{ENC}\left[\pi^{(m)}_{11},\pi_{00}\right] = 0 \tag{B.29}$$

$$\mathcal{E}^{sym}_{ENC}\left[\pi^{(m)}_{11},\pi_{20,\delta}\right] = \eta^2\left(1-\eta\right)\pi_{10} \tag{B.30}$$

$$\mathcal{E}^{sym}_{ENC}\left[\pi^{(m)}_{11},\pi_{21,\delta}\right] = \frac{\eta^2}{4}\pi_{21,\delta} + \frac{\eta^2\left(1-\eta\right)}{2}\pi_{11} \tag{B.31}$$

$$\mathcal{E}^{sym}_{ENC}\left[\pi_{10},\pi_{10}\right] = \frac{\eta^2}{8}\pi_{00} \tag{B.32}$$

$$\mathcal{E}^{sym}_{ENC}\left[\pi_{10},\pi_{00}\right] = 0 \tag{B.33}$$

$$\mathcal{E}^{sym}_{ENC}\left[\pi_{10},\pi_{21,\|}\right] = \frac{\eta^2\left(1-\eta\right)}{4}\pi_{10} + \frac{\eta^2}{8}\pi_{20,\|} \tag{B.34}$$

$$\mathcal{E}^{sym}_{ENC}\left[\pi_{10},\pi_{21,\perp}\right] = \frac{\eta^2}{4}\pi_{1,1} + \frac{\eta^2\left(1-\eta\right)}{4}\pi_{10} + \frac{\eta^2}{8}\pi_{20,\perp} \tag{B.35}$$

$$\mathcal{E}^{sym}_{ENC}\left[\pi_{00},\pi_{21,\|}\right] = 0 \tag{B.36}$$

$$\mathcal{E}^{sym}_{ENC}\left[\pi_{00},\pi_{21,\perp}\right] = \frac{\eta^2}{2}\pi_{10} \tag{B.37}$$

The logical type of state after the $(m+1)$th ENC, $\pi^{(m+1)}_{11}$, is the average of the states $\pi^{(m+1)\prime}_{11}$ and π_{11}, with relative weights $\frac{\eta^2}{2}p^{(m)}_{11}p^{(m)}_{11}$ and $\eta^2\left(1-\eta\right)p^{(m)}_{11}\sum_{\delta=\|,\perp}p^{(m)}_{21,\delta} + \frac{\eta^2}{2}p^{(m)}_{10}p^{(m)}_{21,\perp}$, respectively.

Then we calculate the (unnormalized) density matrix after the $(m+1)$th ENC,

$$\begin{aligned}\tilde{\rho}_{a_L,b_R}^{(m+1)} &= \tilde{p}_{00}^{(m+1)}\pi_{00} + \tilde{p}_{10}^{(m+1)}\pi_{10} + \tilde{p}_{11}^{(m+1)}\pi_{11}^{(m+1)} \\ &+ \tilde{p}_{20,\|}^{(m+1)}\pi_{20,\|} + p_{20,\perp}^{(m+1)}\pi_{20,\perp} + p_{21,\|}^{(m+1)}\pi_{21,\|} \\ &+ p_{21,\perp}^{(m+1)}\pi_{21,\perp} + \cdots \end{aligned} \tag{B.38}$$

with the probability coefficients

$$\tilde{p}_{00}^{(m+1)} \approx \frac{\eta^2}{8} p_{10}^{(m)} p_{10}^{(m)} \tag{B.39}$$

$$\tilde{p}_{10}^{(m+1)} \approx \frac{\eta^2}{2} p_{11}^{(m)} p_{10}^{(m)} \times \left(1 + O\left(p_c\right)\right) \tag{B.40}$$

$$\tilde{p}_{11}^{(m+1)} \approx \frac{\eta^2}{2} \begin{pmatrix} p_{11}^{(m)} p_{11}^{(m)} + p_{10}^{(m)} p_{21,\perp}^{(m)} \\ +2\left(1-\eta\right) p_{11}^{(m)} \left(p_{21,\|}^{(m)} + p_{21,\perp}^{(m)}\right) \end{pmatrix} \tag{B.41}$$

$$\tilde{p}_{20,\delta}^{(m+1)} \approx \frac{\eta^2}{4} p_{10}^{(m)} p_{21,\delta}^{(m)} \tag{B.42}$$

$$\tilde{p}_{21,\delta}^{(m+1)} \approx \frac{\eta^2}{2} p_{11}^{(m)} p_{21,\delta}^{(m)} \tag{B.43}$$

Finally, we divide these probabilities by $\tilde{p}_{11}^{(m+1)}$, and to the leading order (i.e. the zeroth order of p_c) we obtain

$$\frac{\tilde{p}_{00}^{(m+1)}}{\tilde{p}_{11}^{(m+1)}} \approx \frac{1}{4}\left(\frac{p_{10}^{(m)}}{p_{11}^{(m)}}\right)^2 \tag{B.44}$$

$$\frac{\tilde{p}_{10}^{(m+1)}}{\tilde{p}_{11}^{(m+1)}} \approx \frac{p_{10}^{(m)}}{p_{11}^{(m)}} \tag{B.45}$$

$$\frac{\tilde{p}_{20,\delta}^{(m+1)}}{\tilde{p}_{11}^{(m+1)}} \approx \frac{1}{2}\frac{p_{10}^{(m)}}{p_{11}^{(m)}}\frac{p_{21,\delta}^{(m)}}{p_{11}^{(m)}} \tag{B.46}$$

$$\frac{\tilde{p}_{21,\delta}^{(m+1)}}{\tilde{p}_{11}^{(m+1)}} \approx \frac{p_{21,\delta}^{(m)}}{p_{11}^{(m)}} \tag{B.47}$$

Furthermore, all these ratios remain constant (to order p_c), which justifies the claim

that the probabilities for different types of states remain stable for all higher levels of ENC.

If we further introduce $\tilde{p}_{vac}^{(m+1)} = \tilde{p}_{00}^{(m+1)} + \tilde{p}_{10}^{(m+1)}$, $\tilde{p}_{\text{logic}}^{(m+1)} = \tilde{p}_{11}^{(m+1)}$and $\tilde{p}_{multi}^{(m+1)} = \sum_{\delta=\|,\perp} \tilde{p}_{20,\delta}^{(m+1)} + \tilde{p}_{21,\delta}^{(m+1)}$, we have

$$\tilde{p}_{logic}^{(m+1)} \approx \frac{\eta^2}{2} p_{logic}^{(m)} p_{logic}^{(m)} \left(1 + p_{err,new}^{(m+1)} + O\left(p_c\right)\right) \tag{B.48}$$

$$\tilde{p}_{vac}^{(m+1)} \approx \frac{\eta^2}{2} p_{logic}^{(m)} p_{vac}^{(m)} \left(1 + O\left(p_c\right)\right) \tag{B.49}$$

$$\tilde{p}_{multi}^{(m+1)} \approx \frac{\eta^2}{2} p_{logic}^{(m)} p_{multi}^{(m)} \left(1 + O\left(p_c\right)\right) \tag{B.50}$$

where $p_{err,new}^{(m+1)}$ is the probability for the new logical error from the multi-excitation states (accompanied by photon loss)

$$\begin{aligned} p_{err,new}^{(m+1)} &\approx \frac{2\left(1-\eta\right) p_{11}^{(m)} \left(p_{21,\|}^{(m)} + p_{21,\perp}^{(m)}\right) + p_{10}^{(m)} p_{21,\perp}^{(m)}}{p_{11}^{(m)} p_{11}^{(m)}} \\ &\sim \left(1-\eta\right) p_{multi}^{(m)} / p_{\text{logic}}^{(m)} \\ &\sim \left(1-\eta\right) p_c. \end{aligned} \tag{B.51}$$

Appendix C

Appendices to Chapter 8

Here we provide some detailed analysis of imperfections for quantum repeater with encoding presented in Chapter 8, including the estimate of effective error probability, two approaches to initialize the CSS code fault-tolerantly, the relation between the entanglement fidelity and measurement correlation, and the time overhead associated with the entanglement purification process.

C.1 Effective Error Probability

For our quantum repeater protocol, we introduce the effective error probability q, which estimates the odds for obtaining a wrong output of each physical qubit during entanglement connection. The effective error probability combines various imperfections from entanglement generation and entanglement connection. In the following, we will derive the effective error probability q in terms of various error parameters β, δ, and μ as detailed in Sec. 8.2.

First of all, we observe that all relevant operations (local CNOT gates, teleportation-based CNOT gates, and measurements in Z or X basis) never mix bit-flip errors and phase errors. For example, CNOT gates never convert bit-flip errors into phase errors. Measurements in the Z basis are only sensitive to bit-flip errors, but not to phase errors. Therefore, we can use two probabilities (b, p) to characterize the bit-flip and phase errors, respectively.

We will calculate these two probabilities for the physical qubits from the operational step 1(i,ii,iii) and step 2 as illustrated in Fig. 8.3. For state distillation [step 1(i)], it is possible to have $(b', p') = (\beta/4 + \mu/2, \beta/2 + \mu/2)$ for each physical qubit of the encoding block. For entanglement purification [step 1(ii)], it is possible to have $(b'', p'') = (\beta/2, \beta/4)$ for each physical qubit of the physical Bell pairs. For teleportation-based CNOT gates [82, 208, 103] [step 1(iii)], the control and target qubits accumulate errors from the input qubits, with $(b_c''', p_c''') = (b' + \beta/2, 2p' + 2p'' + \beta + \delta)$ for the control, and $(b_t''', p_t''') = (2b' + 2b'' + \beta + \delta, b' + \beta/2)$ for the target. Finally, after entanglement connection [step 2], the accumulated probability for obtaining a wrong output is

$$q_b = b_c''' + b_t''' + \beta/2 + \delta = \frac{15}{4}\beta + 2\delta + \mu \tag{C.1}$$

for measurements in the Z basis, and is

$$q_p = p_c''' + p_t''' + \beta/2 + \delta = 4\beta + 2\delta + \mu \tag{C.2}$$

for measurements in the X basis. For simplicity, we may just use

$$q = \max\{q_b, q_p\} = 4\beta + 2\delta + \mu \tag{C.3}$$

to estimate the effective error probability.

C.2 Fault-tolerant Initialization of the CSS Code

We now consider two possible approaches to fault-tolerant preparation of the logical states $\left|\tilde{0}\right\rangle$ (and $\left|\tilde{+}\right\rangle = \frac{1}{\sqrt{2}}\left(\left|\tilde{0}\right\rangle + \left|\tilde{1}\right\rangle\right)$) of the CSS code, using local operations within each repeater station. Both approaches use the technique of state distillation [180].

To facilitate the discussion, we first briefly review the stabilizer formulism for the CSS code [81, 154]. The error syndromes for the code C^X can be obtained by measuring the operators $\left\{g_j^X\right\}_{j=1,\cdots,m_X}$, and the syndromes for the code C^Z can be obtained by measuring the operators $\left\{g_{j'}^Z\right\}_{j=1,\cdots,m_Z}$. The operators g_j^X and $g_{j'}^Z$ commute $\left[g_j^X, g_{j'}^Z\right] = 0$ for all j and j'. The operators $\left\{g_j^X\right\}$ and $\left\{g_{j'}^Z\right\}$ are called the stabilizer generators. The logical information are stored in the subspace with $+1$ eigenvalues for all stabilizer generators $\left\{g_j^X\right\}$ and $\left\{g_{j'}^Z\right\}$. (E.g., the 3-qubit repetition code is a CSS code with stabilizer generators $\left\{g_1^Z, g_2^Z\right\} = \{Z_1Z_2, Z_2Z_3\}$; any logical state $|\phi\rangle = \alpha\left|\tilde{0}\right\rangle + \beta\left|\tilde{1}\right\rangle$ satisfies the condition $Z_1Z_2\left|\phi\right\rangle = \left|\phi\right\rangle$ and $Z_2Z_3\left|\phi\right\rangle = \left|\phi\right\rangle$.) Note that the stabilizer generator g_j^Z is a product of Z operators, and $g_{j'}^X$ is a product of X operators. In addition, the logical operator $\tilde{X}$ (or $\tilde{Z}$) for the CSS code can also be expressed as a product of X (or Z) operators. (E.g., the 3-qubit repetition code has logical operators $\tilde{X} = X_1X_2X_3$ and $\tilde{Z} = Z_1Z_2Z_3$.)

C.2.1 First approach

In the first approach, we generate several copies of the logical states $\left|\tilde{0}\right\rangle$, which are not fault-tolerant as the errors might be correlated among qubits within each encoding block. For example, one quantum gate (with error probability ε) may induce errors

in the multiple physical qubits; that is the probability for multi-qubit errors can occurs at the order of $O(\varepsilon)$. To suppress such multi-qubit errors, we use the state distillation circuits (i.e., generalization of the entanglement purification circuits) to suppress both the X and Z errors. After each round of distillation, the correlated errors will be suppressed from $O\left(\varepsilon^{l}\right)$ to $O\left(\varepsilon^{l+2}+\varepsilon^{2l}\right)$. The distillation operation does not introduce any new correlated errors. Thus after sufficiently many rounds of distillation, the correlated errors can be suppressed. Meanwhile the uncorrelated errors from the distillation operations are also suppressed by the following distillation operations. Therefore, after sufficiently many rounds of distillation, the probability for uncorrelated errors will reach a steady value, of the order of $\beta+\delta$ for each physical qubit.

C.2.2 Second approach

In the second approach, we try to avoid correlated errors from the beginning. The idea is that we start with n physical qubits initialized in the product state $|0\rangle^{\otimes n}$, and projectively measure the stabilizers, which can be achieved fault-tolerantly using the GHZ states (as described in the next paragraph). We obtain a set of binary numbers associated with the stabilizer measurements. In principle, we can perform error correction to the encoding block to restore it to the $+1$ co-eigenstates for the stabilizers. Alternatively, we may keep track of the values for the stabilizers, and take them into account throughout the entanglement generation and entanglement connection (as detailed below). Finally, we use several copies of the encoding block with uncorrelated error to perform just one round of state distillation to suppress the

error probability per physical qubits to $\sim \beta + \delta$.

To achieve fault-tolerant measurement of the stabilizer, we use l-qubit GHZ states (with $l \leq n$) that can be initialized fault-tolerantly [154]. According to the standard form of the stabilizer code (see Ref. [154], page 470), the error in the value for each stabilizer is equivalent to the error of one physical qubit. We further improve the reliability of the stabilizer measurement by repeating it several times [2].

Since we have included the -1 eigenstates for the stabilizers, we need to generalize the encoded CNOT operation by keeping track of the stabilizers as well as the logical qubits. Suppose the encoding block for the control qubit has eigenvalues $(\mathbf{x}_1, \mathbf{z}_1)$ associated with the X and Z stabilizers, and the block for the target qubit has eigenvalues $(\mathbf{x}_2, \mathbf{z}_2)$. The outputs have eigenvalues $(\mathbf{x}_1, \mathbf{z}_1\mathbf{z}_2)$ for the control block and $(\mathbf{x}_1\mathbf{x}_2, \mathbf{z}_2)$ for the target block. Consequently, when we apply the generalized encoded CNOT operation to entanglement generation, there is additional classical communication to exchange the information of stabilizers between neighboring stations, so that both stations can update the eigenvalues of the stabilizers for their encoding blocks. When we apply the generalized encoded CNOT operation to entanglement connection, the classical error correction need to take into account the eigenvalues of the stabilizers to correct errors. Apart the these modifications, the remaining operations remain the same.

C.2.3 Estimate local resources for second approach

We now estimate the minimum number of qubits needed for each repeater station, which is required by the fault-tolerant preparation of the encoding block with small

error probability. (For simplicity, we assume that local operational time is much faster than the communication time and can be safely neglected.) We focus on the second scheme of fault-tolerant preparation, which first uses the GHZ states to projectively measure the stabilizers and then apply state distillation to suppress individual qubit errors. We emphasize again that both operations of stabilizer measurement and state distillation can be performed fault-tolerantly.

The local resources are split into two categories: the memory qubits to store two encoding blocks ($2n$ qubits), and the ancillary qubits to assist fault-tolerant preparation. The ancillary qubits should fault-tolerantly prepare of the GHZ state (using n_{GHZ} qubits), and store additional two encoding blocks ($2n$ qubits) for the 2-level state distillation. Altogether, there are $4n + n_{GHZ}$ qubits for each station.

We now detail the procedure of prepare the distilled state in the storage block b, using two-level state distillation with two additional blocks $a1$ and $a2$. First, we obtain a level-1 distilled encoding block in b (by projectively preparing the encoded state for $a1$ and b, and using $a1$ to successfully purify b). Then we obtain another level-1 distilled encoding block in $a2$ (by projectively preparing the encoded state for $a1$ and $a2$, and using $a1$ to successfully purify $a2$). Finally, we obtain the level-2 distilled encoding block in b (by using $a2$ to successfully purify b). Generally, we can obtain a level-l distilled block by using l additional blocks (i.e., l n qubits).

C.3 Entanglement Fidelity and Correlation

There are two major sources that will reduce the entanglement fidelity for the final encoded Bell pairs. First, the errors from the Bell measurement from intermediate

stations will lead to the wrong choice of the Pauli frame, and the probability that all $L-2$ Bell measurements are error-free is $(1-Q)^{2(L-2)}$. In addition, unsuccessful local error correction for the final encoded Bell pair will also reduce the generalized fidelity, and the probability to have a successful error correction is approximately $(1-Q)^2$. Therefore, we estimate that the entanglement fidelity to be $F \approx (1-Q)^{2L-2} \gtrsim (1-Q)^{2L}$.

These two sources also affect the correlation of the secret keys. If the secret keys are obtained from the measurement in the X or Z basis, only half of the $2(L-2)$ classical bits from intermediate repeater stations are relevant while the other half do not affect the keys at all. And the probability for successful classical error correction to infer the encoded logical qubit is of the order of $(1-Q)^2$. Therefore, the correlation is approximately $C \approx (1-Q)^L \approx \sqrt{F}$.

C.4 Time Overhead and Failure Probability for Entanglement Purification

We now consider the process of generating n purified Bell pairs between neighboring stations. We will calculate the failure probability P_{fail} for obtaining at least n purified Bell pairs using N_0 unpurified Bell pairs. The failure probability should also depend on the fidelity of unpurified Bell pairs (F_0) and the error probability for local operations (β and δ). Generally, the more unpurified Bell pairs N_0, and the smaller failure probability P_{fail}. For a given P_{fail}, we can estimate the N_0 and consequently the cycle time τ_c that determines the key generation rate.

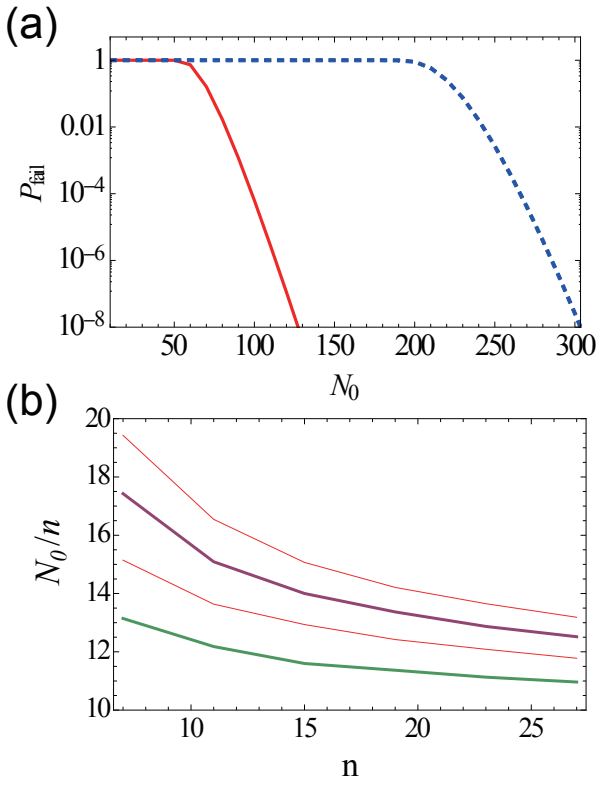

Figure C.1: Failure probability and unpurified Bell pairs. (a) The failure probability P_{fail} decreases exponentially with the number of unpurified Bell pairs N_0 (when N_0 surpasses certain threshold), for $n = 7$ (red solid line) and $n = 23$ (blue dashed line). (b) For fixed P_{fail}, the ratio $N_0/n \sim 15$ for a wide range of n. The four curves from lower left to the upper right correspond to $P_{fail} = 10^{-3}, 10^{-5}, 10^{-7}$ and 10^{-9}, respectively. For both plots, we assume unpurified Bell pairs with fidelity $F_0 = 0.95$ due to depolarizing error. The operational error probabilities are $\beta = \delta = 10^{-3}$. After three levels of purifications, the fidelity of the Bell pair can be 0.9984.

C.4.1 Failure probability

In order to obtain the failure probability, we first calculate the number distribution for purified Bell pairs obtained from N_0 unpurified Bell pairs.

We distinguish the purified Bell pairs according their level of purification. A level-$(i+1)$ pair is obtained from a successful purification using two level-i pairs. Level-0 pairs are the same as unpurified Bell pairs. Level-l pairs are directly used for non-local CNOT gates.

We introduce the number distribution $\left\{p_m^{(i)}\right\}_{m=0,1,2,\cdots}$ for level-i pairs obtained from N_0 unpurified Bell pairs, with $i = 0, 1, \cdots, l$. The number distribution for level-0 pairs is

$$p_m^{(0)} = \delta_{m,N_0}. \tag{C.4}$$

As two level-i pairs are needed for one level-$(i+1)$ pair, we define

$$\tilde{p}_k^{(i)} = p_{2k}^{(i)} + p_{2k+1}^{(i)}, \tag{C.5}$$

which can be used to calculate the number distribution for level-$(i+1)$ pairs

$$p_m^{(i+1)} = \sum_{j=m} \begin{pmatrix} j \\ m \end{pmatrix} r_i^m \left(1 - r_i\right)^{j-m} \tilde{p}_j^{(i)}, \tag{C.6}$$

where r_i is the success probability for obtaining a level-$(i+1)$ pair from two level-i pairs. Thus, the failure probability is

$$P_{fail} = \sum_{j=0}^{n-1} p_j^{(l)}. \tag{C.7}$$

For example, given $\beta = \delta = 10^{-3}$ and $F_0 = 0.95$ with depolarizing error, the fidelity for level-3 purified pair can be 0.9984. In Fig. C.1(a), we plot the failure

probability that decreases exponentially when N_0 surpasses certain threshold. In Fig. C.1(b), we plot N_0/n as a function of n, requiring fixed failure probability P_{fail} ($10^{-3}, 10^{-5}, 10^{-7}$ or 10^{-9}). We note that $N_0/n \approx 15$ is sufficient to ensure $P_{fail} < 10^{-5}$ a wide range of n.

C.4.2 Time overhead and key generate rate

We now estimate the time needed to obtain n purified Bell pairs between two neighboring repeater stations. Each attempt of entanglement generation takes time l_0/v, with success probability $\eta^2 e^{-l_0/l_{att}}$. Since there are n_{EnG} ($= 2n + n_{GHZ}$) qubits available at each station, the generation rate of unpurified Bell pairs is

$$R = \frac{v}{l_0}\eta^2 e^{-l_0/l_{att}} n_{EnG}, \tag{C.8}$$

where the spacing between nearest stations is $l_0 = 10$ km, the fiber attenuation length is $l_{att} = 20$ km, the signal propagation speed is $v = 2 \times 10^5$ km/s, and the overall efficiency for collecting and detecting single photon is $\eta \approx 0.3$. We have $R = n_{EnG} 1.1 \times 10^3 \,\mathrm{sec}^{-1}$.

We can estimate the time to obtain N_0 unpurified Bell pairs $\tau_0 = N_0/R$. Since each station need to connect with both neighboring stations, the total cycle time is twice as long:

$$\tau_c = 2N_0/R = \kappa \frac{l_0}{v} \frac{e^{l_0/l_{att}}}{\eta^2}, \tag{C.9}$$

with

$$\kappa = \frac{2N_0}{n_{EnG}} \approx \frac{2N_0}{4n} \approx 8, \tag{C.10}$$

where the last equality assumes $n_{EnG} \approx 4n$ (i.e., $n_{GHZ} \approx 2n$) and $N_0/n \approx 15$ to ensure $P_{fail} < 10^{-5}$ [see Fig. C.1(b)]. Therefore, for the parameters considered here,

approximately $6n$ qubits at each station can achieve $\tau_c \approx 7$ ms, which is sufficient for quantum key generation rate of 100 bits/sec over long distances.

Appendix D

Appendices to Chapter 9

Here we provide some addition analysis for Chapter 9. We will first present the methods section obtaining some key results used in the main text. Then we discuss some details of addressing multiple nodes, implementing general string operations, estimating the infidelity of controlled-string operations, achieving universal rotations on the topological memory, and modeling the noise for toric-code Hamiltonian.

D.1 Methods

D.1.1 Selective addressing

In order to achieve selective addressing with sub-micron resolution, an additional strong control beam (different from the control beam for the ancilla spin) couples the atomic excited state $|e\rangle$ with the auxiliary metastable state $|r\rangle$, which is initially empty. The control beam is tuned to two photon resonance with the cavity mode as indicated in Fig. 9.2b. Effectively, the strong control field switches off the interaction

of all atoms with the cavity mode by driving them into the "dark state" [40, 80]. Only if the control field vanishes exactly at the position of the atom, will the atom interact with the cavity mode. The problem of selective addressing is thus reduced to the problem of creating the control beam with intensity profile having nodes at desired positions. As detailed in Appendix D.2, the latter can be achieved with a set of Laguerre-Gaussian (LG) modes created by holograms [83].

As discussed in Ref. [80], addressing errors are associated with two effects: (1) Each trapped atom has a finite spread around the lattice points, while the addressing beam vanishes only at the lattice points, and consequently there will always be a tiny but finite coupling between the addressing beam and selected spins. (2) The finite lifetime for the meta-stable state $|r\rangle$ will induce errors for unselected spins. E.g., the estimated error probability associated with each addressing site can be $\varepsilon_{\text{address}} \approx 0.01$ for ^{87}Rb trapped in a deep optical lattice [80]. In addition, for Kitaev's honeycomb lattice model (Fig. 9.1b) the effective leakage error can be $\varepsilon_{\text{hcb}} \approx 0.01$ for parameters $J_x/J_z = J_y/J_z = 0.2$ [62]. For anyonic braiding operations addressing $L = 25$ sites, the overall fidelity $(1 - \varepsilon_{\text{address}} - \varepsilon_{\text{hcb}})^L \approx 0.60$ should provide sufficient contrast for anyonic interferometry.

The addressing error probability can be further suppressed by increasing trapping confinement, using LG beams with larger winding number, applying shaped pulses with optimal control, and choosing long-lived auxiliary state $|r\rangle$. This will enable us to perform braiding operations with longer strings. Alternatively, we may adiabatically expand the entire lattice, perform operations over selected sites, and adiabatically restore the lattice to the initial spacing. The expansion/restoration of

the lattice can be done without changing the trapping wavelength, by either changing the angle between the lattice beams [164] or using holographic techniques to create optical lattices [83]. The addressing errors can be negligibly small for the expanded lattice. The errors associated with the expansion/restoration are dominated by the sites further away from the center of the lattice, because they move faster than those sites close to the center. To suppress such errors, we may freeze all interactions among the lattice sites (by increasing the lattice barriers before the expansion and restoring them after the restoration of the lattice) and perform the expansion/restoration as slowly as possible.

D.1.2 Derivation of the geometric phase gate

We describe the necessary elements to construct the geometric phase gate illustrated in Fig. 9.3. First we require the displacement operator $D(\xi) \equiv e^{\xi a^\dagger - \xi^* a}$ that can be obtained by injecting coherent states through cavity mirrors. The amplitude and phase of the injected field determine the phase space displacement of the bosonic field by ξ.

Second, we need the displacement operation that depends on the state of the memory spins:

$$D(i\alpha S_{\mathcal{C}}^Z) = \begin{cases} D\left(i\alpha\right) & \text{if } \langle S_{\mathcal{C}}^z \rangle = +1 \\ D\left(-i\alpha\right) & \text{if } \langle S_{\mathcal{C}}^z \rangle = -1 \end{cases}, \tag{D.1}$$

where we use $\langle S_{\mathcal{C}}^z \rangle = \pm 1$ to represent the ± 1 subspaces of the memory spins associated with the operator $S_{\mathcal{C}}^z$. We can achieve $D(i\alpha S_{\mathcal{C}}^Z)$ by applying the QND Hamiltonian for time $t_C = \pi/2|\chi|$ with coupling χ before the displacement operation $D(\alpha e^{i\phi})$ followed

by the QND interaction again for time t_C but with coupling $-\chi$. The justification is based on the identity

$$D\left(\alpha e^{i\phi+i\theta O}\right) = R\left(\theta O\right) D\left(\alpha e^{i\phi}\right) R\left(-\theta O\right),$$

with $R\left(x\right) = e^{ixa^\dagger a}$ and the two commuting operators $[O, a] = 0$. For $O = \sum_{j\in C} \sigma_j^z$ and $\theta = \pi/2$, we have $e^{i\phi+i\theta O} = e^{i\phi} \prod_{j\in\mathcal{C}} e^{i\pi/2\sigma_j^z} = e^{i(\phi+m\pi/2)} S_{\mathcal{C}}^z$, with $m = N_C$. Conditioned on $\phi = -(m-1)\pi/2$, we obtain $D\left(\alpha e^{i\phi+i\theta O}\right) = D(i\alpha S_{\mathcal{C}}^Z)$.

Third, we need dispersive coupling between the bosonic field and the ancilla spin (with two levels $\{|0\rangle_A, |1\rangle_A\}$)

$$V_A = \chi_A a^\dagger a \left|1\right\rangle_A \left\langle 1\right|,$$

with coupling strength χ_A, which can be switched on and off via optical control [40, 80] or mechanical displacement of the ancilla spin. With such dispersive interaction, we are able to obtain the displacement operation conditioned on the state of the ancilla spin, $D\left(\beta \left|1\right\rangle_A \left\langle 1\right|\right) = \left|0\right\rangle_A \left\langle 0\right| \otimes \mathbf{I} + \left|1\right\rangle_A \left\langle 1\right| \otimes D\left(\beta\right)$, by the following procedure: (1) apply the interaction V_A for time $t_A = \pi/\chi_A$, (2) displace the bosonic field by $-\beta/2$, (3) apply the interaction V_A again for time t_A, and (4) displace the bosonic field by $\beta/2$. The steps (1-3) displace the bosonic field by $\mp\beta/2$ for the ancilla spin in state $|0\rangle_A$ and $|1\rangle_A$, respectively. Combined with the displacement $\beta/2$ from step (4), we have the operation $D\left(\beta \left|1\right\rangle_A \left\langle 1\right|\right)$.

Finally, the controlled-string operation is a combination of the above elements:

$$U = D\left(-\beta \left|1\right\rangle_A \left\langle 1\right|_A\right) D\left(-i\alpha S_{\mathcal{C}}^z\right) D\left(\beta \left|1\right\rangle_A \left\langle 1\right|_A\right) D\left(i\alpha S_{\mathcal{C}}^z\right). \tag{D.2}$$

The bosonic field is restored to its initial state, while accumulating a phase depending

on both the state of the ancilla spin and the value for the string operator as illustrated in Fig. 9.3.

D.1.3 Fringe contrast of the interferometer in the presence of excitations

We refer to anyons left from the initialization as *quenched anyons*, which can result in measurable effects to the phase measurement associated with braiding [equation (9.6)]. To be specific, we will consider the planar code, and assume that the probability to have one pair of initial anyons is p while neglecting the case with multiple pairs of anyons. If the anyons are immobile (e.g., the braiding operation is much faster than anyonic propagation), the contrast of the phase measurement only depends the probability that the loop $l_1 \cup l_3$ (or $l_2' \cup l_4'$) (see Fig. 9.4a) encloses an odd number of initial x-particles (or z-particles). An extra phase $e^{i\theta} = -1$ will be accumulated from each loop satisfying this condition. Suppose the loop $l_1 \cup l_3$ (or $l_2' \cup l_4'$) encloses m faces (or m' vertices). If one pair of initial x-particles is uniformly distributed among $N^2 \times (N^2 - 1)/2$ possible configurations, the probability for accumulating an extra phase is $q_m \equiv \frac{2m\left(N^2-m\right)}{N^2(N^2-1)}$ for the loop $l_1 \cup l_3$. The probability reaches a maximum value $\approx 1/2$ for $m \approx N^2/2$; meanwhile it vanishes for $m = 0$ or N^2, which is achieved by $l_1 = l_3$. Therefore, the contrast for the fringes of $\langle \sigma_\phi \rangle$ v.s. ϕ will be reduced to $1 - p \times (q_m + q_{m'})$.

If the anyons are highly diffusive (e.g., random anyonic propagation is very fast compared to the intervals between the control operations), we should avoid adding any anyons by applying string operators that act within the ground subspace of

the topological memory. As shown in Fig. 9.4c, we use generators of the encoded qubits associated with strings $\{l_{Z1}, l'_{X2}, l_{Z3}, l'_{X4}\}$ to implement the braiding operation. However, any quenched anyons (if present) will quickly diffuse over the entire torus and completely wash away the fringe of $\langle\sigma_\phi\rangle$. Therefore, the remaining contrast with highly diffusive anyons is $1-p$. Note that imperfect string operators may also reduce the contrast, since they may introduce unwanted anyons to the topological memory with probability approximately proportional to the length of the string.

D.1.4 Extension to $\mathbb{Z}_d$ gauge theories

This interferometric technique can be extended to measure abelian anyonic statistics for any $\mathbb{Z}_d$ gauge theory by introducing the spin lattice Hamiltonian with d levels for each spin [28]. One can still use a probe qubit to measure the statistical phase via controlled-string operations. The mutual statistical phase between a charge $a \in \mathbb{Z}_d$ and flux $b \in \mathbb{Z}_d$ associated with the braiding operation is $\tilde{Z}^{-a}_{\mathcal{C}'_Z}\tilde{X}^{-b}_{\mathcal{C}'_X}\tilde{Z}^{a}_{\mathcal{C}_Z}\tilde{X}^{b}_{\mathcal{C}_X} = e^{i2\pi ab/d}$. Here the string operator $\tilde{Z}^a_{\mathcal{C}_Z}$ ($\tilde{X}^b_{\mathcal{C}_X}$) is a product of Z^a (X^b) operators of all the spins on the string $\mathcal{C}_Z$ ($\mathcal{C}_X$), where Z and X are elements of the generalized Pauli group. The operator Z can be implemented by phasing pairs of spin states at a time using the protocols in the main text for the appropriate duration at each stage. Equivalently, one can choose field polarizations and detunings so that only one of the d levels is strongly coupled to the cavity, then evolve that state for the appropriate time, and swap other states in, evolve, and swap out again. A total of $d-1$ global gates suffice to simulate $\tilde{Z}^a_{\mathcal{C}_Z}$. The same follows for the $X^b_{\mathcal{C}_X}$ operators, but one must perform a parallel Fourier transform operator $F = \prod_{j\in\mathcal{C}_X} f_j$ first on all the spins in

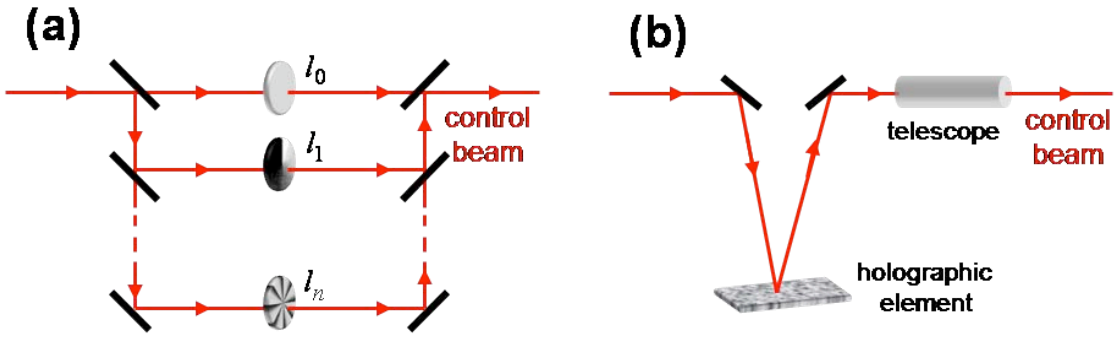

Figure D.1: Creating control beams with multiple nodes for selective addressing. (a) The conceptual idea is illustrated with spiral phase plates [183] and beam splitters, which create and interfere multiple LG beams. The interference pattern will have multiple nodes at the desired positions. (b) The schematic implementation uses holographic techniques to prepare the control beam. The holographic element [e.g., spatial light modulator (SLM)] [83] can imprint the hologram of the desired interference pattern to the control beam.

the configuration, then implement $Z^b_{\mathcal{C}_X}$ then apply F^{-1}.

D.2 Control Beam with Multiple Nodes for Addressing

We now describe how to create the desired control beam with multiple nodes that can be used for selective addressing. The basic idea is to interfere several Laguerre-Gaussian (LG) beams, as shown in Fig. D.1a. These LG beams have the same waist but different orbital angular momentum, which can be generated using spiral phase plates (or holograms). At the beam waist, the electric field distribution for the LG beam with angular momentum l is [159]

$$E_l\left(r_x, r_y\right) = A_l \left(\frac{r_x + i r_y}{w}\right)^l \exp\left[-\frac{r_x^2 + r_y^2}{w^2}\right], \tag{D.3}$$

where (r_x, r_y) are the transverse coordinates, w is the waist, and A_l is the field (complex) amplitude. We introduce the re-scaled complex number $z \equiv \frac{r_x}{w} + i\frac{r_y}{w}$ to represent the transverse coordinates, and we obtain

$$E_l(z) = A_l z^l e^{-|z^2|}. \tag{D.4}$$

When we interfere a set of LG beams $L = \{l_1, l_2, \cdots\}$, the electric field distribution is

$$E_{tot}(z) = \sum_{l \in L} A_l z^l e^{-|z^2|}. \tag{D.5}$$

In practice, one can first calculate the hologram (the inverse Fourier transform) of the desired interference pattern and then use a holographic element [e.g., a spatial light modulator (SLM)] to imprint the hologram on a laser beam [83], as shown in Fig. D.1b.

We now explore the relation between field amplitudes $\{A_l\}_{l \in L}$ and the positions of the nodes $\{z_{0,n}\}_{n=1,\cdots,n_{\max}}$. First, we introduce the polynomial to represent the nodes.

$$P(z) = \prod_{n=1}^{n_{\max}} (z - z_{0,n}) = \sum_{n=0}^{n_{\max}} \alpha_n z^n. \tag{D.6}$$

Then, we assign the (complex) amplitudes of $(n_{\max} + 1)$ LG modes: $A_n = \alpha_n$ for $n = 0, 1, \cdots, n_{\max}$. The electric field distribution of the interference patter is

$$E_{tot}(z) = \sum_{n=0}^{n_{\max}} \alpha_n z^n e^{-|z^2|} = P(z)\, e^{-|z^2|}, \tag{D.7}$$

which vanishes exactly at $\{z_{0,n}\}_{n=1,\cdots,n_{\max}}$. In addition, we may use polynomials with higher degrees to create more robust nodes

$$P'(z) = \prod_{n=1}^{n_{\max}} (z - z_{0,n})^{d_n}, \tag{D.8}$$

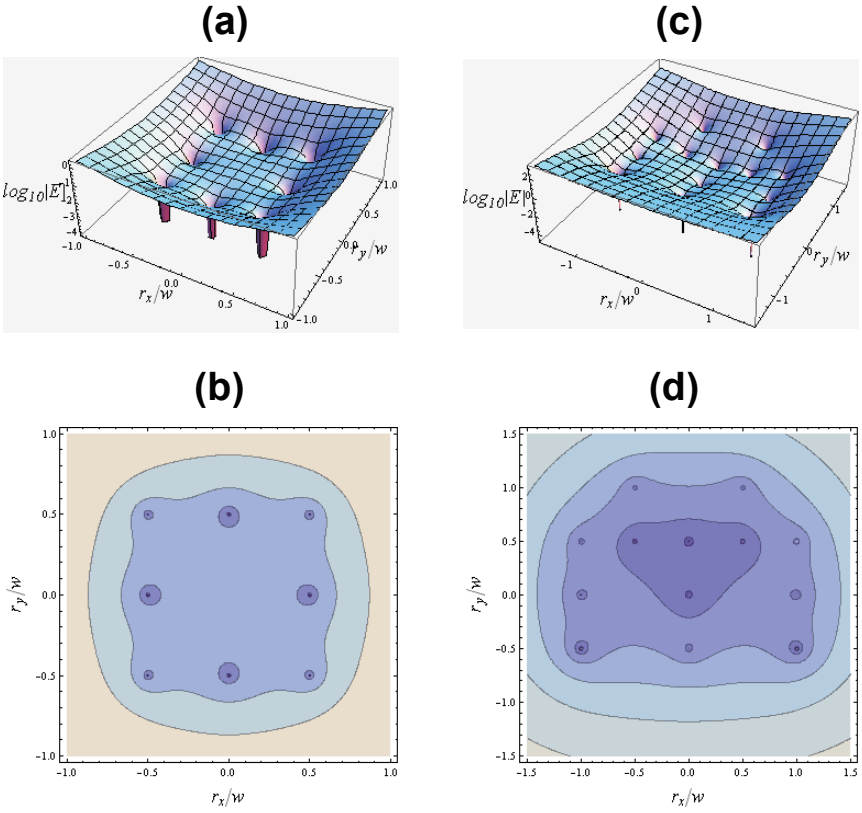

Figure D.2: Selective addressing of multiple sites with interference patterns of the LG modes. The electric field is calculated according to Eq. (D.7). (a,b) Interference pattern addresses (i.e., with vanishing amplitude at) 8 sites that enclose the central site. (c,b) Interference pattern addresses 10 sites that form a letter "M," where we create second-order ($l = 2$) LG nodes at $z = -1 - 0.5i$ and $1 - 0.5i$ to further enhance the selectivity.

where d_n is the vortex winding number associated with the node at $z = z_{0,n}$. Fig. D.2 illustrates two patterns with multiple nodes obtained by the interference technique described here.

D.3 Implementing General String Operations with S_C^z

All string operators are equivalent to $S_{\mathcal{C}}^z = \prod_{j\in C} \sigma_j^z$ up to local single spin rotations, where C is the set of selected spins. In particular, for string operations with x-rotations, we have

$$S_{\mathcal{C}}^x = \prod_{j\in C} \sigma_j^x = \prod_{j\in C} H_j \sigma_j^z H_j = \left(\prod_j H_j\right) S_{\mathcal{C}}^z \left(\prod_j H_j\right), \tag{D.9}$$

with H_j for Hadamard rotation on the jth spin and $\left(\prod_j H_j\right)$ for the global Hadamard rotation on all memory spins. And the last equality uses the properties of Hadamard rotation $H_j H_j = I$ and $H_j \sigma_j^z H_j = \sigma_j^x$. Thus, we can either apply Hadamard rotations on selected spins or use two global Hadamard rotations to convert $S_{\mathcal{C}}^z$ into $S_{\mathcal{C}}^x$.

To apply Hadamard rotations on selected spins requires selective addressing. In contrast, the approach of global Hadamard rotation avoids this issue. Quantum control techniques like robust pulses can significantly improve the fidelity of the global Hadamard rotation.

Note that errors can be introduced to all spins by global Hadamard rotations, but fortunately such errors have only a small effect to the anyonic interferometry. An error from Hadamard rotation can be regarded as having an undesired effect of creating pairs of quasi-particles at the neighboring sites or plaquettes. As long as anyons do not

diffuse during the entire braiding operation, the creation of quasi-particle pairs inside or outside the loops does not reduce the fringe contrast of anyonic interferometry, while only those pairs intersecting with the loops do. Thus, the reduction of the contrast should scale only linearly with the total length of the loops, multiplied by the error probability of Hadamard rotation for each spin (usually much less than addressing error probability per site).

Therefore, using two global Hadamard rotations to convert $S^z_{\mathcal{C}}$ into $S^x_{\mathcal{C}}$ is more favorable than using selective Hadamard rotations, in the case of slow diffusion of anyons and dominant addressing errors. Note that the above discussion also applies to $S^y_{\mathcal{C}} = \prod_{j\in C} \sigma^y_j$, by replacing Hadamard rotation H_j with $R_j = \exp\left[-i\frac{\pi}{4}\sigma^z_j\right]$.

D.4 Fidelity of Controlled-string Operations and Topological Memory

To evaluate the advantage of using topological memory storage, we compare the improvement of storing a qubit in spins prepared in the ground states of $H_{\rm surf}$ (assumed at zero temperature) versus the decoherence rate for encoding a qubit in a single spin. For long-time storage of quantum memory, we expect to gain from the robustness of the topological memory can significantly reduce the decoherence rate by a factor of $(\delta h/J)^N \ll 1$, where δh is the magnitude of the noise perturbation on individual spins and N is the length of the minimal string associated with the generators for encoded qubits [113]. Besides addressing errors ($\sim N_{\mathcal{C}}\varepsilon_{\rm address}$ for string with length $N_{\mathcal{C}}$), controlled-string operations may also be affected by photon loss and non uniform dispersive shifts in the QND interaction. Note that if we use Kitaev's honeycomb lattice model [114] (with coupling strength $J_x, J_y \ll J_z$) to implement the toric code Hamiltonian, there will be an additional error associated with the string operation, $N_{\mathcal{C}}\varepsilon_{\rm hcb} \approx N_{\mathcal{C}}\frac{J_x^2+J_y^2}{4J_z^2}$. This is because the spin operators will create high-energy quasi-particles (different from anyons) with a small probability $\sim \frac{J_x^2+J_y^2}{J_z^2}$, which effectively induces leakage from the low-energy manifold [175, 62].

D.4.1 Errors due to photon loss

The photon loss is attributed to two physical processes: the spontaneous decay with rate γ for the optically excited state $|e\rangle$, and the cavity loss with rate κ during the QND interaction. For single photon approach, the interaction time is $\tau = \pi/2\chi$ and

the effective spontaneous decay rate is suppressed to $\frac{g^2}{\Delta^2}\gamma$ by having large detuning $\Delta \gg g$ for each selected spin. Under the assumption that the selected spins decay independently, the total probability for photon loss is

$$\kappa\tau + N_{\mathcal{C}}\frac{g^2}{\Delta^2}\gamma\tau \geq \mathbf{2}\pi\sqrt{N_{\mathcal{C}}/P} \equiv P_{loss},$$

where we define the Purcell factor $P \equiv g^2/\kappa\gamma$ [165, 146]. And the minimum probability can be achieved by choosing optimal detuning $\Delta = g\sqrt{N_{\mathcal{C}}\gamma/\kappa}$.

For geometric phase gate approach, we can choose $|\alpha|^2 = |\beta|^2 = \pi/2$ so that the total probability for photon loss is $P_{loss} \approx |\alpha|^2 \left(\kappa\tau + N_{\mathcal{C}}\frac{g^2}{\Delta^2}\gamma\tau\right)$ with $\tau \approx \pi\Delta/g^2$. Similar to single photon approach, the probability P_{loss} can be significantly reduced by having a large Purcell factor $P > N_{\mathcal{C}}$. For coherent states, we cannot identify photon loss events unambiguously, but we can still characterize the errors associated with the photon loss.

D.4.2 The deviation of the QND interaction

The dominant deviation of the QND interaction is from the fluctuations of the coupling strength between the cavity mode and selected spins, described by the following perturbation

$$\delta H = \chi a^\dagger a \sum_{j\in C} \delta_j \sigma_j^z,$$

where δ_j is the relative deviation for the jth spin. In the presence of cavity excitation, the implementation of the gate $U_j = \exp\left(i\theta\sigma_j^z\right)$ on the jth spin could lead to the gate $\tilde{U}_j = \exp\left[i\left(1+\delta_j\right)\theta\sigma_j^z\right]$. We define the error by the operator norm $\varepsilon_j \equiv \left\|\tilde{U}_j - U_j\right\| \approx \theta\left|\delta_j\right|$ [17]. Thus we have the error for the QND interaction, $P_{QND} \equiv \left\|\prod_{j\in C}\tilde{U}_j - \prod_{j\in\mathcal{C}} U_j\right\| \leq \sum_j \varepsilon_j$.

This kind of error due to inhomogeneity can be compensated in two ways. First one could add an optical potential to the system which is shaped to equalize the couplings δ_j for all the spins along the configuration path $\mathcal{C}$. A second option is to use composite pulse sequences on the system in which case it has been shown that the error can be reduced to $O\left(|\delta_j|^k\right)$ for $\forall j$ using $O(k^3)$ pulses [27]. Therefore, $P_{QND} \sim N_{\mathcal{C}}\theta\,|\delta|^k$ is effectively suppressed.

D.4.3 Summary

Combining all the decoherence mechanisms, the controlled-string operation with string length $N_{\mathcal{C}}$ has error probability

$$\varepsilon_{\text{string}}\left(N_{\mathcal{C}}\right) \approx \lambda\sqrt{N_{\mathcal{C}}/P} + N_{\mathcal{C}}\varepsilon_{\text{address}} + N_{\mathcal{C}}\varepsilon_{\text{hcb}}, \tag{D.10}$$

where the pre-factor $\lambda = \mathbf{2}\pi$ (and $\mathbf{4}\pi^2$) is for the single photon (and geometric phase gate) approach. The total error probability for the swap-in and swap-out process (4 controlled-string operations with string length N) and memory storage time t is

$$p_{\text{topo-mem}} = \left(\delta h/J\right)^N qt + 4\varepsilon_{\text{string}}\left(N\right).$$

Compared with the storage error without topological encoding $p_{\text{ref-mem}} \approx q \times t$, for storage time $t \gtrsim 4\varepsilon_{\text{string}}\left(N\right)/q$, our topological memory outperforms storage in a single quantum system.

We remark that for single photon approach, photon loss induces leakage errors that can be detected without compromising the state stored in the topological memory. Such detected errors can be overcome by repetition, which is applicable to probabilistic operations such as entanglement generations in quantum repeater [26]

and distributed quantum computer [104, 103]. Detected errors can have a very high tolerable threshold for deterministic quantum computation schemes [116].

D.5 Universal Rotations on the Topological Memory

We can achieve universal rotations of the encoded qubit stored in the topological memory. For example, an arbitrary x-rotation $\tilde{X}_\theta = e^{i\theta\tilde{X}}$ on the topological memory can be achieved via the gate teleportation circuit

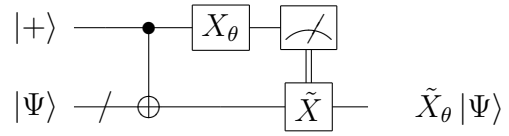

This circuit represents the following procedure: (1) use controlled-string operation $\Lambda\left[\tilde{X}\right]$ to entangle the probe qubit (upper line) and the memory (lower line with a slash), (2) projectively measure the probe qubit in a rotated basis, and (3) perform an encoded Pauli X gate over the topological memory conditioned on the measurement outcome. Similarly, we can also implement arbitrary z-rotation $\tilde{Z}_\theta = e^{i\theta\tilde{Z}}$ on the topological memory via the gate teleportation circuit

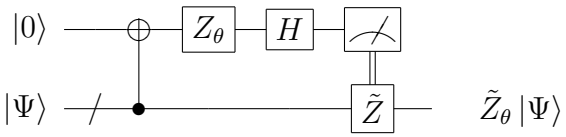

Since any rotation can be decomposed into a sequence of x- and z-rotations, the above two circuits suffice for universal rotations.

The gate teleportation can be generalized to implement arbitrary unitaries generated by string operators. For string operator $\tilde{S}$, the unitary operation $\tilde{S}_\theta = e^{i\theta\tilde{S}}$ can be achieved via the gate teleportation circuit

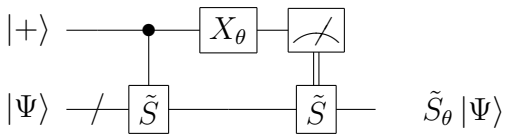

For the geometric phase gate scheme, we can actually implement rotations of the encoded qubit without the probe qubit, e.g., x-rotation of the encoded qubit can be decomposed as $e^{i\theta\tilde{X}} = D\left(-\beta\right) D\left(-\alpha e^{i\frac{\pi}{2}\tilde{X}}\right) D\left(\beta\right) D\left(\alpha e^{i\frac{\pi}{2}\tilde{X}}\right)$ by choosing $|\alpha\beta| = \theta$.

D.6 Noise Model for Toric-Code Hamiltonian

The toric-code Hamiltonian for spins on the edges of $N \times N$ square lattice

$$H_{topo} = -J \sum_{s} A_s - J \sum_{p} B_p, \tag{D.11}$$

is a sum of stabilizer operators $A_s = \Pi_{j \in \text{star}(s)} \sigma_j^x$ and $B_p = \Pi_{j \in \text{boundary}(p)} \sigma_j^z$ associated with the site (vertex) s and the plaquette (face) p, respectively. And the coupling strength J determines the energy gap between the ground and excited states $\Delta \sim J$, which is also the energy associated with the quasi-particle excitations. There are two types of quasi-particles: (1) *z-particles* that live on the vertices of the lattice and (2) *x-particles* that live on the plaquette. The quasi-particles do not change from one type to the other type, but there is a non-trivial topological phase associated with braiding of two quasi-particles of different type. We generate and move these quasi-particles by applying string operators, meanwhile during the interval between the string operators the quasi-particles will evolve under the toric-code Hamiltonian and various local perturbations from the environment. In the absence of perturbations from the environment, the quasi-particles are immobile. However, the mobility of quasi-particles changes when we include local perturbations, because the excited states with quasi-particles are highly degenerate and any small perturbation to the Hamiltonian can change both the energy spectrum and the eigen-wavefunctions.

D.6.1 Perturbation hamiltonian

In this section, we will consider a simple model that will induce diffusion of quasi-particles of the toric-code Hamiltonian. We will consider the case that the perturba-

tion is small compared to the energy gap Δ, so that he number of quasi-particles is still conserved. However, we will show that such small perturbation can lead to non-trivial dynamics in the manifold with fixed number of quasi-particles. The perturbation is described by the Hamiltonian

$$H_{pert} = \sum_{e \in \text{All spins}} h_e \sigma_e^x \tag{D.12}$$

where e is the label for spins that we sum over. The time dependent coefficient h_e is the local field associated with spin e.

We can also write the perturbation Hamiltonian by summing over the plaquettes and their surrounding edges:

$$H_{pert} = \frac{1}{2} \sum_p \sum_{\eta \in \mathcal{N}} h_{p,\eta} \sigma_{p,\eta}^x, \tag{D.13}$$

where p is the label for the plaquette, η is the label for the surrounding edges, $\mathcal{N} = \{(0,1), (0,-1), (1,0), (-1,0)\}$ is the set that includes four edges around the plaquette as illustrated in Fig. D.3a. The combination of (p, η) label the η-edge of plaquette p. We use $h_{p,\eta}$ and $\sigma_{p,\eta}^x$ to represent the local fluctuating field and the spin operator for edge (p, η), respectively. Since each edge is shared by two neighboring plaquettes, both (p, η) and $(p + \eta, -\eta)$ represent the same edge. By definition, we have $h_{p,\eta} \equiv h_{p+\eta,-\eta}$ and $\sigma_{p,\eta}^x \equiv \sigma_{p+\eta,-\eta}^x$. The prefactor $1/2$ in Eq. (D.12) accounts for the double counting of edges.

D.6.2 Effects from perturbation hamiltonian

We now consider the effects from the perturbation Hamiltonian H_{pert}, under the assumption that the number of quasi-particles is conserved. This assumption can

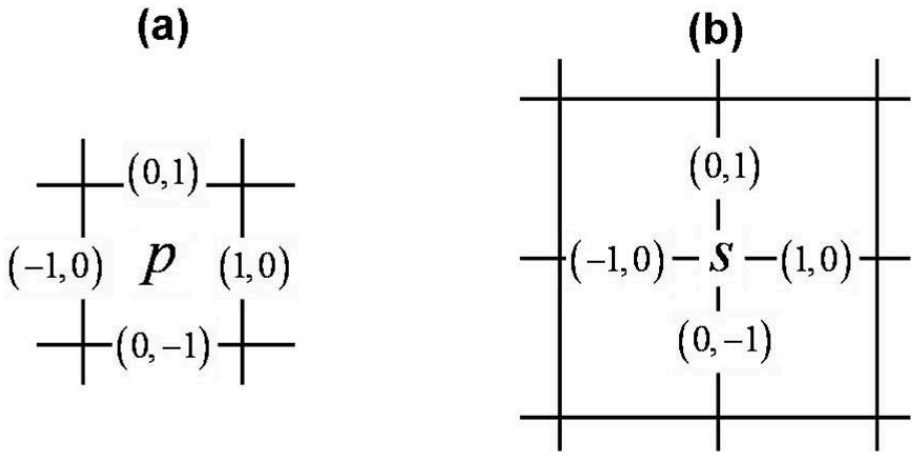

Figure D.3: Relative position of edges with respect to (a) plaquette and (b) site.

be justified as long as the local fluctuating field has a small amplitude and low-frequency noise spectrum, compared with the energy gap from the topological Hamiltonian. For ground states of the toric-code Hamiltonian, there are no quasi-particle excitations. And the perturbation Hamiltonian can only induce *virtual* excitations of quasi-particles. Thus the leading non-trivial effect within the ground-state manifold is the Nth order perturbative process, associated with hopping of virtual quasi-particles along a minimal non-contractible loop of length N. Such Nth order process is suppressed by a factor $(|h|/\Delta)^N$ which decreases exponentially with respect to the system size. As expected, the ground states of the topological Hamiltonian should be robust against these local perturbations.

The perturbation Hamiltonian acts very differently on the excited states. It can induce x-particles to hop to the neighboring plaquettes, while having no influence to z-particles. We may define the creation operator of the x-particle at plaquette p as $b_p^\dagger$, which changes the stabilizer B_p from $+1$ to -1. Similarly, the annihilation

operator b_p changes B_p from -1 to $+1$. By definition, $\left(b_p^\dagger\right)^2 = (b_p)^2 = 0$. The operator $b_p b_p^\dagger - b_p^\dagger b_p$ represents the sign of B_p, and the operator $b_p + b_p^\dagger$ flips the sign of B_p. Since the spin operator $\sigma_{p,\eta}^x$ flips both stabilizers B_p and $B_{p+\eta,-\eta}$ associated with the two neighboring plaquettes, it can be expressed as

$$\sigma_{p,\eta}^x \to \left(b_p + b_p^\dagger\right)\left(b_{p+\eta} + b_{p+\eta}^\dagger\right). \tag{D.14}$$

By conservation of quasi-particles, we can simplify the mapping:

$$\sigma_{p,\eta}^x \to b_p b_{p+\eta}^\dagger + b_p^\dagger b_{p+\eta}. \tag{D.15}$$

Therefore, within the manifold of fixed quasi-particles, the perturbation Hamiltonian can be reduced to

$$H'_{pert} = \frac{1}{2}\sum_p \sum_{\eta\in\mathcal{N}} h_{p,\eta}\left(b_p b_{p+\eta}^\dagger + b_p^\dagger b_{p+\eta}\right), \tag{D.16}$$

where the local field $h_{p,\eta}$ can also be interpreted as the tunneling rate of quasi-particles from p to $p+\eta$, or from $p+\eta$ to p.

We now use H'_{pert} to study the dynamics of quasi-particles. Suppose at time $t = 0$ we create an x-particle at plaquette p

$$|\varphi_0\rangle = b_p^\dagger |vac\rangle . \tag{D.17}$$

This state could be imagined as resulting from a boundary excitation which has moved to plaquette p. For a surface code on a torus, excitations always come in pairs in which case the initial state would be $|\varphi_0\rangle = b_{p'}^\dagger b_p^\dagger |vac\rangle$. In the latter case we focus on the dynamics of a single excitation of the pair assuming the other excitation is far away. Again restricting to the subspace of fixed quasi-particle number, at a later

time τ the state becomes

$$\begin{aligned}|\varphi_\tau\rangle &= \exp\left[-iH'_{pert}\tau\right] b_p^\dagger |vac\rangle \\ &= \left[1 - \frac{1}{2}\sum_{\eta\in\mathcal{N}} \left(h_{p,\eta}\tau\right)^2\right] b_p^\dagger |vac\rangle - i\sum_{\eta\in\mathcal{N}} \left(h_{p,\eta}\tau\right) b_{p+\eta}^\dagger |vac\rangle + O\left(h^3\tau^3\right), \end{aligned} \quad \text{(D.18)}$$

where in the second equality we assume that $h_{p,\eta}$ is *time-independent* and expand only to the second order of $h_{p,\eta}\tau$. The overlap between the initial and final states is

$$\langle\varphi_0|\varphi_\tau\rangle \approx 1 - \frac{1}{2}\sum_{\eta} \left(h_{p,\eta}\tau\right)^2 \approx \exp\left[-\frac{1}{2}\sum_{\eta} h_{p,\eta}^2\tau^2\right]. \quad \text{(D.19)}$$

Therefore, for time-independent perturbation and relatively short waiting time (i.e., $\tau \ll h_{p,\eta}^{-1}$), the probability for a quasi-particle to remain at the same position decreases *quadratically* with time.

Generally, the local field $h_{p,\eta}$ will depend on time and we should replace $h_{p,\eta}\tau$ by $\int_0^\tau h_{p,\eta}\left(t'\right)dt'$ in the equations above. In particular, the local field $h_{p,\eta}\left(t'\right)$ can be a stochastic random variable. In the next section, we will study the dynamics associated with stochastic noise fields $\{h_{p,\eta}\}$.

D.6.3 Time-dependent perturbation

We now consider the local stochastic noise fields characterized by the auto-correlation function

$$f\left(t\right) \equiv \overline{h_{p,\eta}\left(t'\right) h_{p,\eta}\left(t'+t\right)}, \quad \text{(D.20)}$$

where we assume that $h_{p,\eta}$ is steady and the auto-correlation only depends on the time difference between the two sampling points. For simplicity, we will also assume independent local noise for different spins; that is the correlation function $\overline{h_{p,\eta}\left(0\right) h_{p',\eta'}\left(t\right)}$

vanishes unless (p,η) and (p',η') represent the same spin. We can characterize the noise by using the power spectrum density, which is the Fourier transform of the auto-correlation function:

$$\tilde{f}(\omega) \equiv \frac{1}{2\pi}\int_{-\infty}^{\infty} f(t)\, e^{-i\omega t} dt. \tag{D.21}$$

For example, the Gaussian correlation function

$$f(t) = \xi_h^2 \exp\left[-t^2/\tau_c^2\right] \tag{D.22}$$

has power spectrum density

$$\tilde{f}(\omega) = \frac{\xi_h^2}{\sqrt{\pi}\omega_c} \exp\left[-\omega^2/\omega_c^2\right], \tag{D.23}$$

where the typical amplitude of the stochastic field is ξ_h, the correlation time is τ_c, and the cut-off frequency is $\omega_c = 2\tau_c^{-1}$. The power spectrum density vanishes for high frequency $\omega \gg \omega_c$.

We can estimate the probability for a quasi-particle to remain in the same position, in the presence of local stochastic noise,

$$\begin{aligned} p_\tau &= \overline{\left|\langle\varphi_0|\varphi_\tau\rangle\right|^2} \\ &\approx 1 - \sum_{\eta\in\mathcal{N}} \overline{\left(\int_0^\tau h_{p,\eta}(t')\, dt'\right)^2}. \end{aligned} \tag{D.24}$$

We first evaluate the square average of the integral for the fluctuation field

$$\begin{aligned} \overline{\left(\int_0^\tau h_{p,\eta}(t')\, dt'\right)^2} &= \int_0^\tau \int_0^\tau \overline{h_{p,\eta}(t')\, h_{p,\eta}(t'')} dt' dt'' \\ &= \int_{-\infty}^{\infty} \frac{\sin^2(\omega\tau/2)}{(\omega\tau/2)^2} \tilde{f}(\omega)\, d\omega \\ &\approx 2\pi \tilde{f}(\omega = 0)\, \tau, \end{aligned} \tag{D.25}$$

where the last step assumes that we are interested in a time scale much longer than the noise correlation time: $\tau \gg \tau_c$. Plugging Eq. (D.25) into Eq. (D.24), we get the probability

$$p_\tau \approx \exp\left[-z\Gamma\tau\right], \tag{D.26}$$

where $z = |\mathcal{N}| = 4$ is the coordination number of the square lattice, and $\Gamma = 2\pi\tilde{f}\left(\omega = 0\right)$ is the diffusion rate to each neighboring position. For Gaussian correlation [Eq. (D.22)], the diffusion rate is

$$\Gamma = 2\sqrt{\pi}\xi_h^2/\omega_c. \tag{D.27}$$

D.6.4 Fringe contrast for interference experiment

We now consider how diffusion of quasi-particles affect the fringe contrast of the anyonic interferometry. The signal of the anyonic interferometry is attributed to the interference from path-ways with different braiding of anyonic quasi-particles, which is achieved by using controlled-string operations. During the intervals between the controlled-string operations, the quasi-particles excited by the controlled-string operations will diffuse, and the final state of the topological memory will have components orthogonal to the initial state. Since the orthogonal components do not contribute to the fringes, the contrast will be reduced.

The anyonic interferometry is analogous to the Ramsey experiment in the following aspects. For both cases, we start with a superposition state $|0\rangle + |1\rangle$ for some two level system. Then, we let the system evolve, and meanwhile it is also interacting with the environment (e.g., cavity mode and selected spins, or external magnetic field). Finally, we projectively measure the system in some basis $|0\rangle \pm e^{\pm i\phi}|1\rangle$. The

reduction of the measurement signal is attributed to various decoherence processes. For Ramsey experiment, the dominant decoherence is induced by fluctuations of the external magnetic field and it is characterized by the dephasing time T_2^*. For anyonic interferometry, we can define a similar dephasing time

$$T_2^* = \frac{1}{z\Gamma}. \tag{D.28}$$

And the fringe contrast is equal to the averaged overlap function, which can be expressed as

$$\overline{|\langle\varphi_0|\varphi_\tau\rangle|} \approx \exp\left[-\tau/T_2^*\right]. \tag{D.29}$$

For stochastic noise with Gaussian correlation [Eq. (D.22)], we have $T_2^* = \omega_c/\left(z\sqrt{\pi}\xi_h^2\right)$.

D.6.5 Spin echo techniques

Similar to NMR systems, we can also use spin-echo techniques to further suppress the stochastic noise. The essence of spin-echo is to apply an effective time-reversal operation in the middle of the evolution so that the noises from the two intervals cancel each other. For anyonic interferometry, the effective time-reversal operation for the perturbation H_{pert} is

$$U_\pi^z \equiv \prod_{e\in\text{All spins}} \sigma_e^z. \tag{D.30}$$

This is because $\{H_{pert}, U_\pi^z\} = 0$ and $[H_{topo}, U_\pi^z] = 0$. For example, at time $t = 0$ we create an x-particle at plaquette p

$$|\varphi_0\rangle = b_p^\dagger |vac\rangle, \tag{D.31}$$

We apply U_π^z operations at time $\tau/2$ and τ. The final state will be

$$\begin{aligned}\left|\varphi_\tau^{echo}\right\rangle &= U_\pi^z e^{-i\int_{\tau/2}^{\tau} H'_{pert}(t')dt'} U_\pi^z e^{-i\int_0^{\tau/2} H'_{pert}(t')dt'} b_p^\dagger \left|vac\right\rangle \\ &= e^{-i\int_0^{\tau/2}\left[H'_{pert}(t')-H'_{pert}(\tau/2+t')\right]dt'} b_p^\dagger \left|vac\right\rangle . \end{aligned} \tag{D.32}$$

For stochastic noise with Gaussian correlation [Eq. (D.22)], the averaged overlap function now becomes

$$\overline{\left|\langle\varphi_0|\varphi_\tau^{echo}\rangle\right|} \approx \exp\left[-\left(\tau/T_2\right)^4\right] \tag{D.33}$$

where $T_2 \sim \sqrt{\tau_c/\xi_h}$. Since $T_2 \sim T_2^* \times \left(\tau_c\xi_h\right)^{3/2}$, for $\tau_c\xi_h > 1$ we can extend the coherence time by using echo-techniques.

Furthermore, we may introduce n pairs of time-reversal operations within the time interval τ (e.g., the pulse sequence $\underbrace{U_\pi^z \cdot^{\tau/2n} \cdots\cdots U_\pi^z \cdot^{\tau/2n} \cdots\cdots}_{\text{Repeat } n \text{ times}}$). And the time dependence of the contrast becomes

$$\exp\left[-\frac{1}{n^3}\left(\frac{\tau}{T_2}\right)^4\right].$$

The contrast reduction is further slow down by a factor of $n^{3/4}$ and this is illustrated in Fig. 5 of the paper.

D.6.6 General perturbation hamiltonian

We now generalize the perturbation Hamiltonian by including stochastic fields along z direction

$$H_{pert,gen} = \sum_{e\in\text{All spins}} h_e^x\sigma_e^x + h_e^y\sigma_e^y + h_e^z\sigma_e^z. \tag{D.34}$$

We introduce the creation (and annihilation) operators $a_s^\dagger$ (and a_s) for z-particles at site s. Suppose the edge e connects two sites s and $s+\zeta$ and it is also shared by

two plaquettes p and $p+\eta$ (see Fig. D.3). Within the manifold of fixed number of quasi-particles, we have the following mapping:

$$\sigma_e^x \to b_p b_{p+\eta}^\dagger + b_p^\dagger b_{p+\eta} \tag{D.35}$$

$$\sigma_e^z \to a_s a_{s+\zeta}^\dagger + a_s^\dagger a_{s+\zeta} \tag{D.36}$$

Thus, the σ_e^x term leads to hopping of x-particles, while the σ_e^z term leads to hopping of z-particles. The σ_e^y term leads to hopping of *fermionic particles* (paired x-particle and z-particle sharing the same edge, e.g., $a_s^\dagger b_p^\dagger$)

$$\sigma_e^y = i\left[\sigma_e^x, \sigma_e^z\right] \to i\left[b_p b_{p+\eta}^\dagger + b_p^\dagger b_{p+\eta}, a_s a_{s+\zeta}^\dagger + a_s^\dagger a_{s+\zeta}\right]. \tag{D.37}$$

And the effective operator for σ_e^y is still Hermitian. Note that σ_e^y consists of terms like $i\left(b_p b_{p+\eta}^\dagger a_s a_{s+\zeta}^\dagger - a_s a_{s+\zeta}^\dagger b_p b_{p+\eta}^\dagger\right)$, and the minus sign for terms with different order is consistent with the phase associated with the braiding of anyons.

The generalized effective Hamiltonian becomes

$$H'_{pert,gen} = \frac{1}{2}\sum_p \sum_{\eta\in\mathcal{N}} h_{p,\eta}^x \left(b_p b_{p+\eta}^\dagger + b_p^\dagger b_{p+\eta}\right) \tag{D.38}$$

$$+ \frac{1}{2}\sum_s \sum_{\zeta\in\mathcal{N}} h_{s,\zeta}^z \left(a_s a_{s+\zeta}^\dagger + a_s^\dagger a_{s+\zeta}\right) \tag{D.39}$$

$$+ \frac{1}{4}\sum_{e\in\text{All spins}} i h_e^y \left[b_p b_{p+\eta}^\dagger + b_p^\dagger b_{p+\eta}\ ,\ a_s a_{s+\zeta}^\dagger + a_s^\dagger a_{s+\zeta}\right].$$

where the first term induces hopping of x-particles and the second term for z-particles. These two terms commute with each other, except for the situation when (p,η) and (s,ζ) represents the same edge. The third term induces hopping of fermionic particles. If we are studying diffusion property of quasi-particles that are far apart, there is essentially no fermionic particles and we may safely neglect the effect from the third

term. Therefore, as long as the diffusion does not induce braiding of quasi-particles, we can safely treat the diffusion for x-particles and z-particles as independent processes.

We may also introduce the effective time-reversal operation $U_\pi^x \equiv \prod_{e\in\text{All spins}} \sigma_e^x$ for perturbations of $\sum_{e\in\text{All spins}} h_e^z \sigma_e^z$., since they anti-commute $\{h_e^z\sigma_e^z, U_\pi^x\} = 0$. We can combine U_π^z and U_π^x in a nested fashion to suppress the diffusion of **both** x-particles and z-particles:

$$U_\pi^z \left(\cdots\overset{\tau/4}{\cdots} U_\pi^x \cdots\overset{\tau/4}{\cdots} U_\pi^x\right) U_\pi^z \left(U_\pi^x \cdots\overset{\tau/4}{\cdots} U_\pi^x \cdots\overset{\tau/4}{\cdots}\right).$$

which can be further simplified as:

$$U_\pi^z \cdots\overset{\tau/4}{\cdots} U_\pi^x \cdots\overset{\tau/4}{\cdots} U_\pi^z \cdots\overset{\tau/4}{\cdots} U_\pi^x \cdots\overset{\tau/4}{\cdots} \tag{D.40}$$

Since time reversal operations U_π^x and U_π^z also anti-commute with $\sum_{e\in\text{All spins}} h_e^z\sigma_e^z$, the nest combination of the two also suppress the diffusion of fermionic particles. Therefore, we are able to suppress diffusion induced by the general perturbation Hamiltonian of Eq. (D.34) to higher order.

Note that the term $h_e^y\sigma_e^y$ will not impart dynamics to free the x- and z-particles without introducing new particles. Hence by energy considerations we can neglect the presence of fermionic particles and ignore the effect of this term. In this case we can conjugate the perturbed evolution by the "time reversal" operation $U_\pi^y = \prod_{e\in\text{All spins}} \sigma_e^y$, which anti-commutes with σ_e^x and σ_e^z.

D.6.7 Time reversal operations for surface-code hamiltonian with boundaries

We now consider the effective time-reversal operations for the surface-code Hamiltonian with boundaries. For the planar code on a square lattice (see Fig. 1a of the paper), at the left and right are "rough edges" where the stabilizer operator B_p is a product of three σ^x spin operators associated with each boundary plaquette, while at the top and bottom are "smooth edges" where the stabilizer operator A_s is a product of three σ^z spin operators associated with each boundary site. In contrast to the stabilizers associated with interior sites and plaquettes, these boundary stabilizers anti-commute with the previous echo unitary U_π^x or U_π^z. Thus, we have to modify the echo unitaries, so that they commute with all stabilizers.

Let us first consider the modification of U_π^z. We refer to the boundary protruding edges in even rows as "even rough edges," and those in odd row as "odd rough edges." We define $U_\pi^{x,e} \equiv \prod_{\substack{e\in\text{All spins} \\ e\notin\text{Odd rough edges}}} \sigma_e^x$ and $U_\pi^{x,o} \equiv \prod_{\substack{e\in\text{All spins} \\ e\notin\text{Even rough edges}}} \sigma_e^x$, so that $U_\pi^{x,e}$ and $U_\pi^{x,o}$ act on even and odd boundary edges, respectively. After this modification, both $U_\pi^{x,e}$ and $U_\pi^{x,o}$ commute with all stabilizers, especially B_p at the left and right "rough edges." Similarly, we label "even/odd smooth edges" associated the columns for the top and bottom "smooth edges," and modify U_π^x into $U_\pi^{z,e} \equiv \prod_{\substack{e\in\text{All spins} \\ e\notin\text{Odd smooth edges}}} \sigma_e^z$ and $U_\pi^{z,o} \equiv \prod_{\substack{e\in\text{All spins} \\ e\notin\text{Even smooth edges}}} \sigma_e^z$, which commute with all stabilizers.

We introduce the sub-sequence

$$W^{\alpha,\beta}(\tau) \equiv U_\pi^{z,\alpha} \cdot\overset{\tau/4}{\cdots}\cdot U_\pi^{x,\beta} \cdot\overset{\tau/4}{\cdots}\cdot U_\pi^{z,\alpha} \cdot\overset{\tau/4}{\cdots}\cdot U_\pi^{x,\beta} \cdot\overset{\tau/4}{\cdots}\cdot,$$

for $\alpha, \beta = e$ or o. And finally the full echo sequence to suppress anyonic diffusion for the surface-code Hamiltonian with boundaries is

$$W^{e,e}(\tau/4)\, W^{e,o}(\tau/4)\, W^{o,e}(\tau/4)\, W^{o,o}(\tau/4)\,. \tag{D.41}$$

D.6.8 Summary

In summary, we have analyzed a simple noise model on top of the toric-code Hamiltonian. We have found that this noise model can explain diffusion of quasi-particles. For anyonic interferometry, the effect of quasi-particle diffusion is analogous to the dephasing of the Ramsey experiment. Based on this analogy, we have proposed a scheme to extend the spin-echo technique to the topological memory, which will further suppress the diffusion of quasi-particles.

Bibliography

[1] A. Abragam and B. Bleaney. *Electron paramagnetic resonance of transition ions*. Clarendon P., Oxford,, 1970.

[2] P. Aliferis, D. Gottesman, and J. Preskill. Quantum accuracy threshold for concatenated distance-3 codes. *Quantum Inf. Comput.*, 6:97–165, 2006.

[3] Daniel Arovas, J. R. Schrieffer, and Frank Wilczek. Fractional statistics and the quantum hall effect. *Phys. Rev. Lett.*, 53:722–723, 1984.

[4] D. D. Awschalom, R. J. Epstein, and R. Hanson. The diamond age of spintronics - quantum electronic devices that harness the spins of electrons might one day enable room-temperature quantum computers - made of diamond. *Sci. Am.*, 297:84–91, 2007.

[5] Dave Bacon. Operator quantum error-correcting subsystems for self-correcting quantum memories. *Phys. Rev. A*, 73:012340–13, 2006.

[6] Gopalakrishnan Balasubramanian, I. Y. Chan, Roman Kolesov, Mohannad Al-Hmoud, Julia Tisler, Chang Shin, Changdong Kim, Aleksander Wojcik, Philip R. Hemmer, Anke Krueger, Tobias Hanke, Alfred Leitenstorfer, Rudolf Bratschitsch, Fedor Jelezko, and Jorg Wrachtrup. Nanoscale imaging magnetometry with diamond spins under ambient conditions. *Nature (London)*, 455:648–651, 2008.

[7] Gopalakrishnan Balasubramanian, Philipp Neumann, Daniel Twitchen, Matthew Markham, Roman Kolesov, Norikazu Mizuochi, Junichi Isoya, Jocelyn Achard, Johannes Beck, Julia Tissler, Vincent Jacques, Philip R. Hemmer, Fedor Jelezko, and Jorg Wrachtrup. Ultralong spin coherence time in isotopically engineered diamond. *Nat Mater*, advanced online publication, 2009.

[8] A. Batalov, V. Jacques, F. Kaiser, P. Siyushev, Neumann. P., L. J. Rogers, R. L. McMurtrie, N. B. Manson, F. Jelezko, and J. Wrachtrup. Low temperature studies of the excited-state structure of nitrogen-vacancy color centers in diamond. *e-print arXiv:*, 0902.2330v1, 2009.

[9] S. C. Benjamin, D. E. Browne, J. Fitzsimons, and J. J. L. Morton. Brokered graph-state quantum computation. *New Journal of Physics*, 8:141, 2006.

[10] C. H. Bennett, G. Brassard, C. Crepeau, R. Jozsa, A. Peres, and W. K. Wootters. Teleporting an unknown quantum state via dual classical and einstein-podolsky-rosen channels. *Phys. Rev. Lett.*, 70:1895, 1993.

[11] C. H. Bennett, G. Brassard, S. Popescu, B. Schumacher, J. A. Smolin, and W. K. Wootters. Purification of noisy entanglement and faithful teleportation via noisy channels. *Phys. Rev. Lett.*, 76:722–725, 1996.

[12] Charles H. Bennett, Herbert J. Bernstein, Sandu Popescu, and Benjamin Schumacher. Concentrating partial entanglement by local operations. *Phys. Rev. A*, 53:2046, 1996.

[13] Charles H. Bennett, Gilles Brassard, and N. David Mermin. Quantum cryptography without bell's theorem. *Phys. Rev. Lett.*, 68:557, 1992.

[14] J. Bergli, Y. M. Galperin, and B. L. Altshuler. Decoherence of a qubit by non-gaussian noise at an arbitrary working point. *Phys. Rev. B*, 74:024509–11, 2006.

[15] Dimitri P. Bertsekas. *Dynamic programming and optimal control*. Athena Scientific, Belmont, Mass, 2nd edition, 2000.

[16] J. Beugnon, M. P. A. Jones, J. Dingjan, B. Darquie, G. Messin, A. Browaeys, and P. Grangier. Quantum interference between two single photons emitted by independently trapped atoms. *Nature (London)*, 440:779–782, 2006.

[17] Rajendra Bhatia. *Matrix analysis*. Springer, New York, 1997.

[18] K. M. Birnbaum, A. Boca, R. Miller, A. D. Boozer, T. E. Northup, and H. J. Kimble. Photon blockade in an optical cavity with one trapped atom. *Nature (London)*, 436:87–90, 2005.

[19] Rainer Blatt and David Wineland. Entangled states of trapped atomic ions. *Nature (London)*, 453:1008–1015, 2008.

[20] B. B. Blinov, D. L. Moehring, L. M. Duan, and C. Monroe. Observation of entanglement between a single trapped atom and a single photon. *Nature (London)*, 428:153–157, 2004.

[21] Dirk Bouwmeester, Artur K. Ekert, and Anton Zeilinger. *The physics of quantum information : quantum cryptography, quantum teleportation, quantum computation*. Springer, Berlin ; New York, 2000.

[22] M. D. Bowdrey, J. A. Jones, E. Knill, and R. Laflamme. Compiling gate networks on an ising quantum computer. *Phys. Rev. A*, 72:032315, 2005.

[23] M. M. Boyd, T. Zelevinsky, A. D. Ludlow, S. M. Foreman, S. Blatt, T. Ido, and J. Ye. Optical atomic coherence at the 1-second time scale. *Science*, 314:1430–1433, 2006.

[24] Ferdinand Brennecke, Tobias Donner, Stephan Ritter, Thomas Bourdel, Michael Kohl, and Tilman Esslinger. Cavity qed with a bose-einstein condensate. *Nature (London)*, 450:268–271, 2007.

[25] G. K. Brennen and J. K. Pachos. Why should anyone care about computing with anyons? *Proc. R. Soc. London, A*, 464:1–24, 2007.

[26] H. J. Briegel, W. Dur, J. I. Cirac, and P. Zoller. Quantum repeater: The role of imperfect local operations in quantum communication. *Phys. Rev. Lett.*, 81:5932–5935, 1998.

[27] Kenneth R. Brown, Aram W. Harrow, and Isaac L. Chuang. Arbitrarily accurate composite pulse sequences. *Phys. Rev. A*, 70:052318–4, 2004.

[28] S. S. Bullock and G. K. Brennen. Qudit surface codes and gauge theory with finite cyclic groups. *Journal of Physics a-Mathematical and Theoretical*, 40:3481–3505, 2007.

[29] W. T. Buttler, R. J. Hughes, P. G. Kwiat, S. K. Lamoreaux, G. G. Luther, G. L. Morgan, J. E. Nordholt, C. G. Peterson, and C. M. Simmons. Practical free-space quantum key distribution over 1 km. *Phys. Rev. Lett.*, 81:3283, 1998.

[30] A. R. Calderbank and Peter W. Shor. Good quantum error-correcting codes exist. *Phys. Rev. A*, 54:1098, 1996.

[31] F. E. Camino, Wei Zhou, and V. J. Goldman. Realization of a laughlin quasiparticle interferometer: Observation of fractional statistics. *Phys. Rev. B*, 72:075342–8, 2005.

[32] Earl T. Campbell. Distributed quantum-information processing with minimal local resources. *Phys. Rev. A*, 76:040302(R)–4, 2007.

[33] P. Cappellaro, J. S. Hodges, T. F. Havel, and D. G. Cory. Principles of control for decoherence-free subsystems. *J. Chem. Phys.*, 125:044514, 2006.

[34] P. Cappellaro, L. Jiang, J. S. Hodges, and M. D. Lukin. Coherence and control of quantum registers based on electronic spin in a nuclear spin bath. *e-print arXiv:*, quant-ph/0901.0444, 2009.

[35] T. Chaneliere, D. N. Matsukevich, S. D. Jenkins, S. Y. Lan, T. A. B. Kennedy, and A. Kuzmich. Storage and retrieval of single photons transmitted between remote quantum memories. *Nature (London)*, 438:833–836, 2005.

[36] Zeng-Bing Chen, Bo Zhao, Yu-Ao Chen, Jorg Schmiedmayer, and Jian-Wei Pan. Fault-tolerant quantum repeater with atomic ensembles and linear optics. *Phys. Rev. A*, 76:022329–12, 2007.

[37] L. Childress, M. V. G. Dutt, J. M. Taylor, A. S. Zibrov, F. Jelezko, J. Wrachtrup, P. R. Hemmer, and M. D. Lukin. Coherent dynamics of coupled electron and nuclear spin qubits in diamond. *Science*, 314:281–285, 2006.

[38] L. Childress, J. M. Taylor, A. S. Sorensen, and M. D. Lukin. Fault-tolerant quantum repeaters with minimal physical resources, and implementations based on single photon emitters. *Phys. Rev. A*, 72:052330, 2005.

[39] L. Childress, J. M. Taylor, A. S. Sorensen, and M. D. Lukin. Fault-tolerant quantum communication based on solid-state photon emitters. *Phys. Rev. Lett.*, 96:070504, 2006.

[40] Jaeyoon Cho. Addressing individual atoms in optical lattices with standing-wave driving fields. *Phys. Rev. Lett.*, 99:020502–4, 2007.

[41] C. W. Chou, H. de Riedmatten, D. Felinto, S. V. Polyakov, S. J. van Enk, and H. J. Kimble. Measurement-induced entanglement for excitation stored in remote atomic ensembles. *Nature (London)*, 438:828–832, 2005.

[42] J. I. Cirac and P. Zoller. Quantum computations with cold trapped ions. *Phys. Rev. Lett.*, 74:4091–4094, 1995.

[43] J. I. Cirac and P. Zoller. New frontiers in quantum information with atoms and ions. *Physics Today*, 57:38–44, 2004.

[44] J. I. Cirac, P. Zoller, H. J. Kimble, and H. Mabuchi. Quantum state transfer and entanglement distribution among distant nodes in a quantum network. *Phys. Rev. Lett.*, 78:3221–3224, 1997.

[45] W. A. Coish, Jan Fischer, and Daniel Loss. Exponential decay in a spin bath. *Phys. Rev. B*, 77:125329–8, 2008.

[46] W. A. Coish and D. Loss. Hyperfine interaction in a quantum dot: Non-markovian electron spin dynamics. *Phys. Rev. B*, 70:195340, 2004.

[47] O. A. Collins, S. D. Jenkins, A. Kuzmich, and T. A. B. Kennedy. Multiplexed memory-insensitive quantum repeaters. *Phys. Rev. Lett.*, 98:060502, 2007.

[48] Y. Colombe, T. Steinmetz, G. Dubois, F. Linke, D. Hunger, and J. Reichel. Strong atom-field coupling for bose-einstein condensates in an optical cavity on a chip. *Nature (London)*, 450:272–276, 2007.

[49] S. Das Sarma, M. Freedman, and C. Nayak. Topological quantum computation. *Physics Today*, 59:32–38, 2006.

[50] E. Dennis, A. Kitaev, A. Landahl, and J. Preskill. Topological quantum memory. *Journal of Mathematical Physics*, 43:4452–4505, 2002.

[51] D. Deutsch, A. Ekert, R. Jozsa, C. Macchiavello, S. Popescu, and A. Sanpera. Quantum privacy amplification and the security of quantum cryptography over noisy channels. *Phys. Rev. Lett.*, 77:2818–2821, 1996.

[52] L. DiCarlo, J. M. Chow, J. M. Gambetta, Lev S. Bishop, D. I. Schuster, J. Majer, A. Blais, L. Frunzio, S. M. Girvin, and R. J. Schoelkopf. Demonstration of two-qubit algorithms with a superconducting quantum processor. *e-print arXiv:*, 0903.2030, 2009.

[53] E. A. Donley, T. P. Heavner, F. Levi, M. O. Tataw, and S. R. Jefferts. Double-pass acousto-optic modulator system. *Rev. Sci. Instrum.*, 76:063112, 2005.

[54] B. Doucot, M. V. Feigel'man, L. B. Ioffe, and A. S. Ioselevich. Protected qubits and chern-simons theories in josephson junction arrays. *Phys. Rev. B*, 71:024505–18, 2005.

[55] L. M. Duan, B. B. Blinov, D. L. Moehring, and C. Monroe. Scalable trapped ion quantum computation with a probabilistic ion-photon mapping. *Quantum Inf. Comput.*, 4:165–173, 2004.

[56] L. M. Duan, E. Demler, and M. D. Lukin. Controlling spin exchange interactions of ultracold atoms in optical lattices. *Phys. Rev. Lett.*, 91:090402, 2003.

[57] L. M. Duan and H. J. Kimble. Efficient engineering of multiatom entanglement through single-photon detections. *Phys. Rev. Lett.*, 90:253601, 2003.

[58] L. M. Duan and H. J. Kimble. Scalable photonic quantum computation through cavity-assisted interactions. *Phys. Rev. Lett.*, 92, 2004.

[59] L. M. Duan, M. D. Lukin, J. I. Cirac, and P. Zoller. Long-distance quantum communication with atomic ensembles and linear optics. *Nature (London)*, 414:413–418, 2001.

[60] W. Dur and H. J. Briegel. Entanglement purification for quantum computation. *Phys. Rev. Lett.*, 90:067901, 2003.

[61] W. Dur, H. J. Briegel, J. I. Cirac, and P. Zoller. Quantum repeaters based on entanglement purification. *Phys. Rev. A*, 59:169–181, 1999.

[62] Sebastien Dusuel, Kai Phillip Schmidt, and Julien Vidal. Creation and manipulation of anyons in the kitaev model. *Phys. Rev. Lett.*, 100:177204, 2008.

[63] M. V. Gurudev Dutt, L. Childress, L. Jiang, E. Togan, J. Maze, F. Jelezko, A. S. Zibrov, P. R. Hemmer, and M. D. Lukin. Quantum register based on individual electronic and nuclear spin qubits in diamond. *Science*, 316:1312–1316, 2007.

[64] Torbjn Einarsson. Fractional statistics on a torus. *Phys. Rev. Lett.*, 64:1995, 1990.

[65] M. D. Eisaman, A. Andre, F. Massou, M. Fleischhauer, A. S. Zibrov, and M. D. Lukin. Electromagnetically induced transparency with tunable single-photon pulses. *Nature (London)*, 438:837–841, 2005.

[66] M. D. Eisaman, L. Childress, A. Andre, F. Massou, A. S. Zibrov, and M. D. Lukin. Shaping quantum pulses of light via coherent atomic memory. *Phys. Rev. Lett.*, 93:233602, 2004.

[67] J. Eisert, K. Jacobs, P. Papadopoulos, and M. B. Plenio. Optimal local implementation of nonlocal quantum gates. *Phys. Rev. A*, 62:052317, 2000.

[68] A. K. Ekert. Quantum cryptography based on bell theorem. *Phys. Rev. Lett.*, 67:661–663, 1991.

[69] S. Felton, A. M. Edmonds, M. E. Newton, P. M. Martineau, D. Fisher, D. J. Twitchen, and J. M. Baker. Hyperfine interaction in the ground state of the negatively charged nitrogen vacancy center in diamond. *Phys. Rev. B*, 79:075203–8, 2009.

[70] E. M. Fortunato, M. A. Pravia, N. Boulant, G. Teklemariam, T. F. Havel, and D. G. Cory. Design of strongly modulating pulses to implement precise effective hamiltonians for quantum information processing. *J. Chem. Phys.*, 116:7599–7606, 2002.

[71] Michael Freedman, Chetan Nayak, and Kirill Shtengel. Extended hubbard model with ring exchange: A route to a non-abelian topological phase. *Phys. Rev. Lett.*, 94:066401–4, 2005.

[72] G. D. Fuchs, V. V. Dobrovitski, R. Hanson, A. Batra, C. D. Weis, T. Schenkel, and D. D. Awschalom. Excited-state spectroscopy using single spin manipulation in diamond. *Phys. Rev. Lett.*, 101:117601–4, 2008.

[73] Torsten Gaebel, Michael Domhan, Iulian Popa, Christoffer Wittmann, Philipp Neumann, Fedor Jelezko, James R. Rabeau, Nikolas Stavrias, Andrew D. Greentree, Steven Prawer, Jan Meijer, Jason Twamley, Philip R. Hemmer, and Jorg Wrachtrup. Room-temperature coherent coupling of single spins in diamond. *Nature Phys.*, 2:408–413, 2006.

[74] A. Gali, M. Fyta, and E. Kaxiras. Ab initio supercell calculations on nitrogen-vacancy center in diamond: Electronic structure and hyperfine tensors. *Phys. Rev. B*, 77:155206, 2008.

[75] Y. M. Galperin, B. L. Altshuler, J. Bergli, and D. V. Shantsev. Non-gaussian low-frequency noise as a source of qubit decoherence. *Phys. Rev. Lett.*, 96:097009–4, 2006.

[76] Y. M. Galperin, B. L. Altshuler, and D. V. Shantsev. Low-frequency noise as a source of dephasing of a qubit. *e-print arXiv:*, cond-mat/031249, 2003.

[77] Jay Gambetta, W. A. Braff, A. Wallraff, S. M. Girvin, and R. J. Schoelkopf. Protocols for optimal readout of qubits using a continuous quantum nondemolition measurement. *Phys. Rev. A*, 76:012325, 2007.

[78] J. J. Garcia-Ripoll, P. Zoller, and J. I. Cirac. Speed optimized two-qubit gates with laser coherent control techniques for ion trap quantum computing. *Phys. Rev. Lett.*, 91:157901, 2003.

[79] N. Gisin, G. G. Ribordy, W. Tittel, and H. Zbinden. Quantum cryptography. *Rev. Mod. Phys.*, 74:145–195, 2002.

[80] Alexey V. Gorshkov, Liang Jiang, Markus Greiner, Peter Zoller, and Mikhail D. Lukin. Coherent quantum optical control with subwavelength resolution. *Phys. Rev. Lett.*, 100:093005–4, 2008.

[81] D. Gottesman. *Stabilizer Codes and Quantum Error Correction*. PhD thesis, Caltech, 1997.

[82] Daniel Gottesman and Isaac L. Chuang. Demonstrating the viability of universal quantum computation using teleportation and single-qubit operations. *Nature (London)*, 402:390, 1999.

[83] D. G. Grier. A revolution in optical manipulation. *Nature (London)*, 424:810–816, 2003.

[84] S. Gupta, K. L. Moore, K. W. Murch, and D. M. Stamper-Kurn. Cavity nonlinear optics at low photon numbers from collective atomic motion. *Phys. Rev. Lett.*, 99:213601, 2007.

[85] H. Haffner, W. Hansel, C. F. Roos, J. Benhelm, D. Chek-al kar, M. Chwalla, T. Korber, U. D. Rapol, M. Riebe, P. O. Schmidt, C. Becher, O. Guhne, W. Dur, and R. Blatt. Scalable multiparticle entanglement of trapped ions. *Nature (London)*, 438:643–646, 2005.

[86] H. Haffner, F. Schmidt-Kaler, W. Hansel, C. F. Roos, T. Korber, M. Chwalla, M. Riebe, J. Benhelm, U. D. Rapol, C. Becher, and R. Blatt. Robust entanglement. *Applied Physics B-Lasers and Optics*, 81:151–153, 2005.

[87] Y. J. Han, R. Raussendorf, and L. M. Duan. Scheme for demonstration of fractional statistics of anyons in an exactly solvable model. *Phys. Rev. Lett.*, 98:150404–4, 2007.

[88] R. Hanson, V. V. Dobrovitski, A. E. Feiguin, O. Gywat, and D. D. Awschalom. Coherent dynamics of a single spin interacting with an adjustable spin bath. *Science*, 320:352–355, 2008.

[89] R. Hanson, F. M. Mendoza, R. J. Epstein, and D. D. Awschalom. Polarization and readout of coupled single spins in diamond. *Phys. Rev. Lett.*, 97:087601–4, 2006.

[90] Ronald Hanson and David D. Awschalom. Coherent manipulation of single spins in semiconductors. *Nature (London)*, 453:1043–1049, 2008.

[91] W. Happer and A. C. Tam. Effect of rapid spin exchange on magnetic-resonance spectrum of alkali vapors. *Phys. Rev. A*, 16:1877–1891, 1977.

[92] S. Haroche and J. M. Raimond. *Exploring the quantum : atoms, cavities, and photons*. Oxford University Press, Oxford ; New York, 2006.

[93] L. Hartmann, B. Kraus, H. J. Briegel, and W. Dur. Role of memory errors in quantum repeaters. *Phys. Rev. A*, 75:032310–17, 2007.

[94] M. B. Hastings and Xiao-Gang Wen. Quasiadiabatic continuation of quantum states: The stability of topological ground-state degeneracy and emergent gauge invariance. *Phys. Rev. B*, 72:045141–14, 2005.

[95] P. R. Hemmer, A. V. Turukhin, M. S. Shahriar, and J. A. Musser. Raman-excited spin coherences in nitrogen-vacancy color centers in diamond. *Opt. Lett.*, 26:361–363, 2001.

[96] J. S. Hodges, J. C. Yang, C. Ramanathan, and D. G. Cory. Universal control of nuclear spins via anisotropic hyperfine interactions. *Phys. Rev. A*, 78:010303–4, 2008.

[97] D. B. Hume, T. Rosenband, and D. J. Wineland. High-fidelity adaptive qubit detection through repetitive quantum nondemolition measurements. *Phys. Rev. Lett.*, 99:120502–4, 2007.

[98] Fedor Jelezko, T. Gaebel, I. Popa, M. Domhan, A. Gruber, and Jorg Wrachtrup. Observation of coherent osciallation of a single nuclear spin and realization of a two-qubit conditional quantum gate. *Phys. Rev. Lett.*, 93:130501, 2004.

[99] Fedor Jelezko, T. Gaebel, I. Popa, A. Gruber, and Jorg Wrachtrup. Observation of coherent osciallations in a single electron spin. *Phys. Rev. Lett.*, 92:076401, 2004.

[100] L. Jiang, M. V. Gurudev Dutt, E. Togan, L. Childress, P. Cappellaro, J. M. Taylor, and M. D. Lukin. Coherence of an optically illuminated single nuclear spin qubit. *Phys. Rev. Lett.*, 100:073001–4, 2008.

[101] L. Jiang, J. M. Taylor, N. Khaneja, and M. D. Lukin. Optimal approach to quantum communication algorithms using dynamics programming. *Proc. Natl. Acad. Sci. U. S. A.*, 104:17291–17296, 2007.

[102] L. Jiang, J. M. Taylor, and M. D. Lukin. Fast and robust approach to long-distance quantum communication with atomic ensembles. *Phys. Rev. A*, 76:012301–10, 2007.

[103] L. Jiang, J. M. Taylor, A. S. Sorensen, and M. D. Lukin. Distributed quantum computation based-on small quantum registers. *Phys. Rev. A*, 76:062323, 2007.

[104] L. Jiang, J. M. Taylor, A. S. Sorensen, and M. D. Lukin. Scalable quantum networks based on few-qubit registers. *e-print arXiv:*, quant-ph/0703029, 2007.

[105] J. A. Jones and E. Knill. Efficient refocusing of one-spin and two-spin interactions for nmr quantum computation. *J. Magn. Reson.*, 141:322–325, 1999.

[106] M. Keller, B. Lange, K. Hayasaka, W. Lange, and H. Walther. Continuous generation of single photons with controlled waveform in an ion-trap cavity system. *Nature (London)*, 431:1075–1078, 2004.

[107] N. Khaneja. Switched control of electron nuclear spin systems. *Phys. Rev. A*, 76:032326, 2007.

[108] Navin Khaneja, Timo Reiss, Cindie Kehlet, Thomas Schulte-Herbruggen, and Steffen J. Glaser. Optimal control of coupled spin dynamics: design of nmr pulse sequences by gradient ascent algorithms. *J. Magn. Reson.*, 172:296–305, 2005.

[109] G. R. Khutsish. Spin diffusion and nuclear magnetic relaxation in a crystal containing a magnetic impurity. *Soviet Physics Uspekhi-Ussr*, 11:802, 1969.

[110] D. Kielpinski, C. Monroe, and D. J. Wineland. Architecture for a large-scale ion-trap quantum computer. *Nature (London)*, 417:709–711, 2002.

[111] C. Kim, C. Knoernschild, B. Liu, and J. Kim. Design and characterization of mems micromirrors for ion-trap quantum computation. *IEEE Journal of Selected Topics in Quantum Electronics*, 13:322–329, 2007.

[112] J. Kim, C. J. Nuzman, B. Kumar, D. F. Lieuwen, J. S. Kraus, A. Weiss, C. P. Lichtenwalner, A. R. Papazian, R. E. Frahm, N. R. Basavanhally, D. A. Ramsey, V. A. Aksyuk, F. Pardo, M. E. Simon, V. Lifton, H. B. Chan, M. Haueis, A. Gasparyan, H. R. Shea, S. Arney, C. A. Bolle, P. R. Kolodner, R. Ryf, D. T. Neilson, and J. V. Gates. 1100 x 1100 port mems-based optical crossconnect with 4-db maximum loss. *IEEE Photonics Technology Letters*, 15:1537–1539, 2003.

[113] A. Yu Kitaev. Fault-tolerant quantum computation by anyons. *Annals of Physics*, 303:2–30, 2003.

[114] Alexei Kitaev. Anyons in an exactly solved model and beyond. *Annals of Physics*, 321:2–111, 2006.

[115] E. Knill. Quantum computing with realistically noisy devices. *Nature (London)*, 434:39–44, 2005.

[116] E. Knill. Scalable quantum computing in the presence of large detected-error rates. *Phys. Rev. A*, 71:042322–7, 2005.

[117] E. Knill, R. Laflamme, and G. J. Milburn. A scheme for efficient quantum computation with linear optics. *Nature (London)*, 409:46–52, 2001.

[118] F. H. L. Koppens, J. A. Folk, J. M. Elzerman, R. Hanson, L. H. W. van Beveren, I. T. Vink, H. P. Tranitz, W. Wegscheider, L. P. Kouwenhoven, and L. M. K. Vandersypen. Control and detection of singlet-triplet mixing in a random nuclear field. *Science*, 309:1346–1350, 2005.

[119] R. Kubo. A stochastic theory of lineshape and relaxation. In D. ter Haar, editor, *Fluctuation, relaxation, and resonance in magnetic systems*, page 23. Oliver and Boyd, Edinburgh, 1962. Scottish Universities Summer School in Physics (2nd : 1961 : Newbattle, Scotland) Edited by D. ter Haar. diagrs. 25 cm. Includes bibliographies.

[120] T. D. Ladd, P. van Loock, K. Nemoto, W. J. Munro, and Y. Yamamoto. Hybrid quantum repeater based on dispersive cqed interactions between matter qubits and bright coherent light. *New Journal of Physics*, 8:184, 2006.

[121] C. Langer, R. Ozeri, J. D. Jost, J. Chiaverini, B. DeMarco, A. Ben-Kish, R. B. Blakestad, J. Britton, D. B. Hume, W. M. Itano, D. Leibfried, R. Reichle, T. Rosenband, T. Schaetz, P. O. Schmidt, and D. J. Wineland. Long-lived qubit memory using atomic ions. *Phys. Rev. Lett.*, 95:060502, 2005.

[122] Thomas Legero, Tatjana Wilk, Markus Hennrich, Gerhard Rempe, and Axel Kuhn. Quantum beat of two single photons. *Phys. Rev. Lett.*, 93:070503–4, 2004.

[123] D. Leibfried, M. D. Barrett, T. Schaetz, J. Britton, J. Chiaverini, W. M. Itano, J. D. Jost, C. Langer, and D. J. Wineland. Toward heisenberg-limited spectroscopy with multiparticle entangled states. *Science*, 304:1476, 2004.

[124] D. Leibfried, B. DeMarco, V. Meyer, D. Lucas, M. Barrett, J. Britton, W. M. Itano, B. Jelenkovic, C. Langer, T. Rosenband, and D. J. Wineland. Experimental demonstration of a robust, high-fidelity geometric two ion-qubit phase gate. *Nature (London)*, 422:412–415, 2003.

[125] A. Lenef and S. C. Rand. Electronic structure of the n-v center in diamond: Theory. *Phys. Rev. B*, 53:13441, 1996.

[126] Debbie W. Leung, Isaac L. Chuang, Fumiko Yamaguchi, and Yoshihisa Yamamoto. Efficient implementation of coupled logic gates for quantum computation. *Phys. Rev. A*, 61:042310, 2000.

[127] M. A. Levin and X. G. Wen. String-net condensation: A physical mechanism for topological phases. *Phys. Rev. B*, 71:045110, 2005.

[128] M. H. Levitt. Composite pulses. *Prog. Nucl. Magn. Reson. Spectrosc.*, 18:61–122, 1986.

[129] Malcolm H. Levitt. *Spin dynamics : basics of nuclear magnetic resonance*. John Wiley & Sons, Chichester; New York, 2001.

[130] Yuan Liang Lim, Sean D. Barrett, Almut Beige, Pieter Kok, and Leong Chuan Kwek. Repeat-until-success quantum computing using stationary and flying qubits. *Phys. Rev. A*, 73:012304, 2006.

[131] Hoi-Kwong Lo and H. F. Chau. Unconditional security of quantum key distribution over arbitrarily long distances. *Science*, 283:2050, 1999.

[132] J. Loubser and J. A. Vanwyk. Electron-spin resonance in study of diamond. *Reports on Progress in Physics*, 41:1201–1248, 1978.

[133] Chao-Yang Lu, Wei-Bo Gao, Otfried Guhne, Xiao-Qi Zhou, Zeng-Bing Chen, and Jian-Wei Pan. Demonstration of fractional statistics of anyons in the kitaev lattice-spin model. *e-print arXiv:*, 0710.0278, 2007.

[134] M. D. Lukin. Trapping and manipulating photon states in atomic ensembles. *Rev. Mod. Phys.*, 75:457, 2003.

[135] H. Mabuchi and A. C. Doherty. Cavity quantum electrodynamics: Coherence in context. *Science*, 298:1372–1377, 2002.

[136] N. B. Manson, J. P. Harrison, and M. J. Sellars. Nitrogen-vacancy center in diamond: Model of the electronic structure and associated dynamics. *Phys. Rev. B*, 74:104303, 2006.

[137] N. Mason, M. J. Biercuk, and C. M. Marcus. Local gate control of a carbon nanotube double quantum dot. *Science*, 303:655–658, 2004.

[138] D. N. Matsukevich, P. Maunz, D. L. Moehring, S. Olmschenk, and C. Monroe. Bell inequality violation with two remote atomic qubits. *Phys. Rev. Lett.*, 100:150404, 2008.

[139] P. Maunz, D. L. Moehring, S. Olmschenk, K. C. Younge, D. N. Matsukevich, and C. Monroe. Quantum interference of photon pairs from two remote trapped atomic ions. *Nat Phys*, 3:538–541, 2007.

[140] J. Maze, J. M. Taylor, and M. D. Lukin. Electron spin decoherence of single nitrogen-vacancy defects in diamond. *Phys. Rev. B*, 78:094303, 2008.

[141] J. R. Maze, P. L. Stanwix, J. S. Hodges, S. Hong, J. M. Taylor, P. Cappellaro, L. Jiang, M. V. G. Dutt, E. Togan, A. S. Zibrov, A. Yacoby, R. L. Walsworth, and M. D. Lukin. Nanoscale magnetic sensing with an individual electronic spin in diamond. *Nature (London)*, 455:644–647, 2008.

[142] Michael Mehring and Jens Mende. Spin-bus concept of spin quantum computing. *Phys. Rev. A*, 73:052303–12, 2006.

[143] Eugen Merzbacher. *Quantum Mechanics*. John Wiley and Sons, Inc., 3 edition, 1998.

[144] S. P. Meyn and R. L. Tweedie. *Markov chains and stochastic stability*. Springer-Verlag, London ; New York, 1993.

[145] A. Micheli, G. K. Brennen, and P. Zoller. A toolbox for lattice-spin models with polar molecules. *Nature Phys.*, 2:341–347, 2006.

[146] P. Michler, A. Kiraz, C. Becher, W. V. Schoenfeld, P. M. Petroff, L. D. Zhang, E. Hu, and A. Imamoglu. A quantum dot single-photon turnstile device. *Science*, 290:2282–+, 2000.

[147] P. Milman, W. Maineult, S. Guibal, L. Guidoni, B. Doucot, L. Ioffe, and T. Coudreau. Topologically decoherence-protected qubits with trapped ions. *Phys. Rev. Lett.*, 99:020503–4, 2007.

[148] D. L. Moehring, M. J. Madsen, K. C. Younge, R. N. Kohn, P. Maunz, L. M. Duan, C. Monroe, and B. B. Blinov. Quantum networking with photons and trapped atoms (invited). *J. Opt. Soc. Am. B: Opt. Phys.*, 24:300–315, 2007.

[149] D. L. Moehring, P. Maunz, S. Olmschenk, K. C. Younge, D. N. Matsukevich, L. M. Duan, and C. Monroe. Entanglement of single-atom quantum bits at a distance. *Nature (London)*, 449:68–71, 2007.

[150] John J. L. Morton, Alexei M. Tyryshkin, Richard M. Brown, Shyam Shankar, Brendon W. Lovett, Arzhang Ardavan, Thomas Schenkel, Eugene E. Haller, Joel W. Ager, and S. A. Lyon. Solid-state quantum memory using the 31p nuclear spin. *Nature (London)*, 455:1085–1088, 2008.

[151] Chetan Nayak, Steven H. Simon, Ady Stern, Michael Freedman, and S. Das Sarma. Non-abelian anyons and topological quantum computation. *Rev. Mod. Phys.*, 80:1083–77, 2008.

[152] P. Neumann, R. Kolesov, V. Jacques, J. Beck, J. Tisler, A. Batalov, L. Rogers, N. B. Manson, G. Balasubramanian, F. Jelezko, and J. Wrachtrup. Excited-state spectroscopy of single nv defects in diamond using optically detected magnetic resonance. *New Journal of Physics*, 11:013017, 2009.

[153] P. Neumann, N. Mizuochi, F. Rempp, P. Hemmer, H. Watanabe, S. Yamasaki, V. Jacques, T. Gaebel, F. Jelezko, and J. Wrachtrup. Multipartite entanglement among single spins in diamond. *Science*, 320:1326–1329, 2008.

[154] M. A. Nielsen and Isaak Chuang. *Quantum computation and quantum information*. Cambridge University Press, Cambridge, U.K; New York, 2000.

[155] Daniel K. L. Oi, Simon J. Devitt, and Lloyd C. L. Hollenberg. Scalable error correction in distributed ion trap computers. *Phys. Rev. A*, 74:052313–9, 2006.

[156] J. K. Pachos. The wavefunction of an anyon. *Annals of Physics*, 322:1254–1264, 2007.

[157] J. K. Pachos, W. Wieczorek, C. Schmid, N. Kiesel, R. Pohlner, and H. Weinfurter. Revealing anyonic statistics with multiphoton entanglement. *e-print arXiv:*, 0710.0895, 2007.

[158] E. Paladino, L. Faoro, G. Falci, and Rosario Fazio. Decoherence and 1/f noise in josephson qubits. *Phys. Rev. Lett.*, 88:228304, 2002.

[159] F. Pampaloni and J. Enderlein. Gaussian, hermite-gaussian, and laguerre-gaussian beams - a primer. *e-print arXiv:*, physics/0410021, 2004.

[160] Jian-Wei Pan, S Gasparoni, R Ursin, G Weihs, and Anton Zeilinger. Experimental entanglement purification of arbitrary unknown states. *Nature (London)*, 423:417, 2003.

[161] Sebastien Perseguers, Liang Jiang, Norbert Schuch, F. Verstraete, M. D. Lukin, J. I. Cirac, and K. G. H. Vollbrecht. One-shot entanglement generation over long distances in noisy quantum networks. *Phys. Rev. A*, 78:062324, 2008.

[162] J. R. Petta, A. C. Johnson, J. M. Taylor, E. A. Laird, A. Yacoby, M. D. Lukin, C. M. Marcus, M. P. Hanson, and A. C. Gossard. Coherent manipulation of coupled electron spins in semiconductor quantum dots. *Science*, 309:2180–2184, 2005.

[163] A. Poppe, A. Fedrizzi, R. Ursin, H. R. Bohm, T. Lorunser, O. Maurhardt, M. Peev, M. Suda, C. Kurtsiefer, H. Weinfurter, T. Jennewein, and A. Zeilinger. Practical quantum key distribution with polarization entangled photons. *Optics Express*, 12:3865–3871, 2004.

[164] J. V. Porto, S. Rolston, B. L. Tolra, C. J. Williams, and W. D. Phillips. Quantum information with neutral atoms as qubits. *Philosophical Transactions of the Royal Society of London Series a-Mathematical Physical and Engineering Sciences*, 361:1417–1427, 2003.

[165] E. M. Purcell. Spontaneous emission probabilities at radio frequencies. *Physical Review*, 69:681–681, 1946.

[166] R. Raussendorf and H. J. Briegel. A one-way quantum computer. *Phys. Rev. Lett.*, 86:5188, 2001.

[167] Robert Raussendorf and Jim Harrington. Fault-tolerant quantum computation with high threshold in two dimensions. *Phys. Rev. Lett.*, 98:190504–4, 2007.

[168] I. Reichenbach and I. H. Deutsch. Sideband cooling while preserving coherences in the nuclear spin state in alkaline-earth-like atoms. *Phys. Rev. Lett.*, 99:123001, 2007.

[169] R. Reichle, D. Leibfried, E. Knill, J. Britton, R. B. Blakestad, J. D. Jost, C. Langer, R. Ozeri, S. Seidelin, and D. J. Wineland. Experimental purification of two-atom entanglement. *Nature (London)*, 443:838–841, 2006.

[170] M. Riebe, H. Haffner, C. F. Roos, W. Hansel, J. Benhelm, G. P. T. Lancaster, T. W. Korber, C. Becher, F. Schmidt-Kaler, D. F. V. James, and R. Blatt. Deterministic quantum teleportation with atoms. *Nature (London)*, 429:734–737, 2004.

[171] T. Rosenband, D. B. Hume, P. O. Schmidt, C. W. Chou, A. Brusch, L. Lorini, W. H. Oskay, R. E. Drullinger, T. M. Fortier, J. E. Stalnaker, S. A. Diddams, W. C. Swann, N. R. Newbury, W. M. Itano, D. J. Wineland, and J. C. Bergquist. Frequency ratio of al+ and hg+ single-ion optical clocks; metrology at the 17th decimal place. *Science*, 319:1808–1812, 2008.

[172] B. Rosenow and B. I. Halperin. Influence of interactions on flux and back-gate period of quantum hall interferometers. *Phys. Rev. Lett.*, 98:106801–4, 2007.

[173] L. G. Rowan, E. L. Hahn, and W. B. Mims. Electron-spin-echo envelope modulation. *Physical Review*, 137:A61, 1965.

[174] C. A. Ryan, C. Negrevergne, M. Laforest, E. Knill, and R. Laflamme. Liquid-state nuclear magnetic resonance as a testbed for developing quantum control methods. *Phys. Rev. A*, 78:012328–14, 2008.

[175] Kai Phillip Schmidt, Sebastien Dusuel, and Julien Vidal. Emergent fermions and anyons in the kitaev model. *e-print arXiv:*, 0709.3017, 2007.

[176] Marlan O. Scully and Muhammad Suhail Zubairy. *Quantum optics*. Cambridge University Press, Cambridge; New York, 1997.

[177] Peter W. Shor and John Preskill. Simple proof of security of the bb84 quantum key distribution protocol. *Phys. Rev. Lett.*, 85:441, 2000.

[178] Christoph Simon and William T. M. Irvine. Robust long-distance entanglement and a loophole-free bell test with ions and photons. *Phys. Rev. Lett.*, 91:110405, 2003.

[179] Charles P. Slichter. *Principles of magnetic resonance*. Springer-Verlag, Berlin ; New York, 3rd enl. and updated edition, 1990.

[180] A. M. Steane. Efficient fault-tolerant quantum computing. *Nature (London)*, 399:124–126, 1999.

[181] Andrew M. Steane. Overhead and noise threshold of fault-tolerant quantum error correction. *Phys. Rev. A*, 68:042322, 2003.

[182] T. Steinmetz, Y. Colombe, D. Hunger, T. W. Hansch, A. Balocchi, R. J. Warburton, and J. Reichel. Stable fiber-based fabry-perot cavity. *Appl. Phys. Lett.*, 89:111110, 2006.

[183] K. Sueda, G. Miyaji, N. Miyanaga, and M. Nakatsuka. Laguerre-gaussian beam generated with a multilevel spiral phase plate for high intensity laser pulses. *Optics Express*, 12:3548–3553, 2004.

[184] J. Suzuki, A. Komai, Y. Ochuchi, Y. Tezuka, H. Konishi, M. Nishiyama, Y. Suzuki, and S. Owa. Micro-mirror on ribbon-actuator (mor) for high speed spatial light modulator. *Proc. MEMS2008*, pages 762–765, 2008.

[185] Krysta M. Svore, Barbara M. Terhal, and David P. DiVincenzo. Local fault-tolerant quantum computation. *Phys. Rev. A*, 72:022317–17, 2005.

[186] J. M. Taylor, P. Cappellaro, L. Childress, L. Jiang, D. Budker, P. R. Hemmer, A. Yacoby, R. Walsworth, and M. D. Lukin. High-sensitivity diamond magnetometer with nanoscale resolution. *Nature Phys.*, 4:810–816, 2008.

[187] J. M. Taylor, C. M. Marcus, and M. D. Lukin. Long-lived memory for mesoscopic quantum bits. *Phys. Rev. Lett.*, 90:206803, 2003.

[188] James K. Thompson, Jonathan Simon, Huanqian Loh, and Vladan Vuletic. A high-brightness source of narrowband, identical-photon pairs. *Science*, 313:74–77, 2006.

[189] S. Trotzky, P. Cheinet, S. Folling, M. Feld, U. Schnorrberger, A. M. Rey, A. Polkovnikov, E. A. Demler, M. D. Lukin, and I. Bloch. Time-resolved observation and control of superexchange interactions with ultracold atoms in optical lattices. *Science*, 319:295–299, 2008.

[190] R. Ursin, F. Tiefenbacher, T. Schmitt-Manderbach, H. Weier, T. Scheidl, M. Lindenthal, B. Blauensteiner, T. Jennewein, J. Perdigues, P. Trojek, B. Omer, M. Furst, M. Meyenburg, J. Rarity, Z. Sodnik, C. Barbieri, H. Weinfurter, and A. Zeilinger. Entanglement-based quantum communication over 144[thinsp]km. *Nature Phys.*, 3:481–486, 2007.

[191] P. van Loock, T. D. Ladd, K. Sanaka, F. Yamaguchi, K. Nemoto, W. J. Munro, and Y. Yamamoto. Hybrid quantum repeater using bright coherent light. *Phys. Rev. Lett.*, 96:240501, 2006.

[192] R. Van Meter, T. D. Ladd, W. J. Munro, and K Nemoto. System design for a long-line quantum repeater. *e-print arXiv:*, 0705.4128, 2007.

[193] R. Van Meter, K Nemoto, and W. J. Munro. Communication links for distributed quantum computation. *IEEE Transactions on Computers*, 56:1643–1653, 2007.

[194] L. M. K. Vandersypen and I. L. Chuang. Nmr techniques for quantum control and computation. *Rev. Mod. Phys.*, 76:1037–1069, 2004.

[195] Lorenza Viola and Emanuel Knill. Robust dynamical decoupling of quantum systems with bounded controls. *Phys. Rev. Lett.*, 90:037901, 2003.

[196] A. Wallraff, D. I. Schuster, A. Blais, L. Frunzio, R. S. Huang, J. Majer, S. Kumar, S. M. Girvin, and R. J. Schoelkopf. Strong coupling of a single photon to a superconducting qubit using circuit quantum electrodynamics. *Nature (London)*, 431:162–167, 2004.

[197] D. F. Walls and G. J. Milburn. *Quantum optics*. Springer, Berlin; New York, 1994.

[198] Xiaoguang Wang and Paolo Zanardi. Simulation of many-body interactions by conditional geometric phases. *Phys. Rev. A*, 65:032327, 2002.

[199] Xiao-Gang Wen. *Quantum field theory of many-body systems : from the origin of sound to an origin of light and electrons*. Oxford University Press, Oxford, 2004.

[200] Frank Wilczek. *Fractional statistics and anyon superconductivity*. World Scientific, Singapore ; Teaneck, NJ, 1990.

[201] W. M. Witzel and S. Das Sarma. Wavefunction considerations for the central spin decoherence problem in a nuclear spin bath. *Phys. Rev. B*, 77:165319, 2008.

[202] W. M. Witzel, Rogerio de Sousa, and S. Das Sarma. Quantum theory of spectral-diffusion-induced electron spin decoherence. *Phys. Rev. B*, 72:161306–4, 2005.

[203] J. Wrachtrup, S. Y. Kilin, and A. P. Nizovtsev. Quantum computation using the c-13 nuclear spins near the single nv defect center in diamond. *Optics and Spectroscopy*, 91:429–437, 2001.

[204] T. Yamamoto, Yu. A. Pashkin, O. Astafiev, Y. Nakamura, and J. S. Tsai. Demonstration of conditional gate operation using superconducting charge qubits. *Nature (London)*, 425:941, 2003.

[205] Demin Yao and Jicong Shi. Projection operator approach to time-independent perturbation theory in quantum mechanics. *American Journal of Physics*, 68:278–281, 2000.

[206] C. W. Zhang, V. W. Scarola, S. Tewari, and S. Das Sarma. Anyonic braiding in optical lattices. *Proc. Natl. Acad. Sci. U. S. A.*, 104:18415–18420, 2007.

[207] Bo Zhao, Zeng-Bing Chen, Yu-Ao Chen, Jorg Schmiedmayer, and Jian-Wei Pan. Robust creation of entanglement between remote memory qubits. *Phys. Rev. Lett.*, 98:240502–4, 2007.

[208] Xinlan Zhou, Debbie W. Leung, and Isaac L. Chuang. Methodology for quantum logic gate construction. *Phys. Rev. A*, 62:052316, 2000.

[209] M. Zukowski, A. Zeilinger, M. A. Horne, and A. K. Ekert. Event-ready-detectors bell experiment via entanglement swapping. *Phys. Rev. Lett.*, 71:4287, 1993.